SULPHIDE ORE MINERALS: SURFACE CHEMICAL PROPERTIES

STEPHEN RICHARDSON

Doctor of philosophy

THE UNIVERSITY OF ASTON IN BIRMINGHAM

October 1988

Summary.

The surfaces of iron-containing sulphide minerals were oxidised by a range of inorganic oxidants, and the resultant surface alteration products studied using various spectroscopic techniques. The characterisation of surface oxidation is relevant to the alteration of ores in nature and their behaviour during flotation and leaching, of importance to the metallurgical industry.

The sulphides investigated included pyrite (FeS_2), hexagonal pyrrhotine (Fe_9S_{10}), monoclinic pyrrhotine (Fe_7S_8), violarite ($FeNi_2S_4$), pentlandite ($(Fe,Ni)_9S_8$), chalcopyrite ($CuFeS_2$) and arsenopyrite (FeAsS). The surfaces were oxidised by various methods including acid (sulphuric), alkali (ammonium hydroxide), hydrogen peroxide, steam, electrochemical and air/oxygen (in a low-temperature (150°C) furnace). The surfaces were examined using surface sensitive chemical spectroscopic methods including x-ray photoelectron spectroscopy (XPS), Auger electron spectroscopy (AES) and conversion electron Mössbauer spectroscopy (CEMS). Physical characterisation of the surfaces was undertaken using scanning electron microscopy (SEM), spectral reflectance measurements and optical microscopy. Bulk characterisation of the sulphide minerals was undertaken using x-ray diffraction and electron microprobe techniques.

Observed phases suggested to form in most of the sulphide surfaces include Fe_3O_4, $Fe_{1-x}O$, Fe_2O_3, FeOOH, $Fe(OH)_3$, with iron II & III oxy-sulphates. The iron sulphides show variable extents of oxidation, indicating pyrite to be the most stable. Violarite shows a stability to oxidation, suggested to result from both its stable spinel crystal structure, and from the rapid formation of sulphur at the surface protecting the sub-surface from further oxidation. The phenomenon of sub-surface enrichment (in metals), forming secondary sulphides, is exhibited by pentlandite and chalcopyrite, forming violarite and copper sulphides respectively. The consequences of this enrichment with regard to processing and leaching are discussed. Arsenopyrite, often a hindrance in ore processing, exhibits the formation of arsenic compounds at the surface, the dissolution of which is discussed in view of the possible environmental hazard caused by the local pollution of water systems.

The results obtained allow a characterisation of the sulphides in terms of their relative stability to oxidation, and an order of stability of the sulphide surfaces is proposed. Models were constructed to explain the chemical compositions of the surfaces, and the inter-relationships between the phases determined at the surface and in the sub-surface. These were compared to the thermochemically predicted phases shown in Eh/pH and partial pressure diagrams. The results are discussed, both in terms of the mineralogy and geochemistry of natural ores, and the implications for extraction and processing of these ore minerals.

Key words: sulphides, surface oxidation, x-ray photoelectron spectroscopy, Auger electron spectroscopy, conversion electron Mössbauer spectroscopy.

To my parents,

Sylvia and Tony.

Acknowledgements.

I would like to thank my supervisor Prof. David J. Vaughan for his helpful advice and support during this project. Dr. John Ashworth is also thanked for his help.

I would like to express my gratitude to Mr. Andrew Abbot, who provided invaluable assistance in obtaining the XPS and Auger data, and to the Dept. of Electrical and Electronic Engineering and Applied Physics, in which the work was undertaken.

Mr. Narsim Murthy is thanked for advice in the use of the Mössbauer spectrometer, as is Dr. Mike Linskill for advice with associated computer problems. Advice in the use of the SEM, in glass blowing techniques and mineral polishing was provided by Mr. Roger Howell, Mr. Alex Stuart and Mr. Bob Brueton.

Mr. Tim Hopkins is thanked for his help in undertaking the electron microprobe work in the Geology Dept. of Manchester University.

The British Museum (Natural History) is thanked for providing natural samples.

Many thanks are due to the staff of the Dept. of Geological Sciences, Aston University, for their help and advice during this project. I would also like to acknowledge the support of friends and colleagues, both in work and sport, for their active discussion and competition.

Financial support for the project was provided by Aston University.

Contents.

List of tables.

List of figures.

CHAPTER 1.

INTRODUCTION

1. Introduction.

Sulphide ore assemblages are important sources of many metals and for this reason, an understanding of the oxidation characteristics of the major sulphide minerals is important in determining alteration phenomena, both in the natural environment, and during mineral processing.

The objectives of this investigation were to study the surface oxidation of several mineralogically important sulphide ore minerals. An appreciation of the chemical and physical properties of oxidised surfaces is important in understanding the paragenesis of alteration of altered mineral assemblages, and the consequences for flotation and leaching processes of importance in mineral processing.

The minerals studied in this investigation, all of which are major phases in ore assemblages, are all iron-containing sulphides. The three iron sulphide minerals, pyrite (FeS_2), hexagonal pyrrhotine (Fe_9S_{10}) and monoclinic pyrrhotine (Fe_7S_8) were studied. Two iron-nickel sulphides, the primary ore mineral, pentlandite ($(Fe,Ni)_9S_8$), the major ore of nickel, and the secondary sulphide, violarite ($FeNi_2S_4$), were investigated both individually and with regard to the relationship between the minerals in oxidising systems. Chalcopyrite ($CuFeS_2$), the major ore of copper, was investigated with a view to characterising surface properties important in natural environments and in relation to mineral processing and, in particular, flotation. Arsenopyrite (FeAsS), a mineral which often causes problems in ore processing, was investigated in order to determine the oxidised compounds formed and to examine the possibility of the release of toxic compounds into water systems.

The sulphides used were both natural minerals and as synthetic phases. The bulk compositions of the sulphides used in this investigation were characterised using x-ray diffraction and electron microprobe techniques. Attempts were made to ensure that the minerals studied were homogeneous and, as far as possible, free from minor contaminants and compositional variations.

Various methods were used to oxidise the sulphide surfaces, with the intention of producing oxidation phenomena comparable to the

oxidation caused both in natural environments, and in ore processing situations. Acid oxidation, in this investigation produced by sulphuric acid, is an important mechanism in natural systems (and in particular, oxidation by acid mine waters), and in ore processing. Alkalis, in this case ammonium hydroxide, are also important in mineral processing procedures, especially leaching. Hydrogen peroxide was used since it is the ideal oxidant, creating extensive oxidation in aqueous environments without introducing contaminants to the system. Steam and air/oxygen (150°C) oxidation methods similarly do not contain any contaminants that may affect the surface characteristics during oxidation. Electrochemical oxidation is used to determine surface characteristics that may be of importance in natural electrochemical oxidation cells formed in ore deposits.

The two major analytical techniques employed were x-ray photoelectron spectroscopy (XPS) and Auger electron spectroscopy (AES), and were used to provide chemical species characterisation and elemental compositions respectively. XPS and AES are important since they allow surface analysis of 10-15Å depth, being sensitive to the composition of the immediate surface. Conversion electron Mössbauer spectroscopy (CEMS) was used to provide further information on the nature of iron-containing species in the surfaces; however, it is less sensitive compared to XPS and AES, being capable of analysing a surface layer of ∝1000Å depth. This disparity in the depth of analysis can be useful in the determination of the compositions of some surfaces. Other techniques that were used included scanning electron microscopy (SEM), spectral reflectance measurements and optical microscopy.

CHAPTER 2.

ANALYTICAL TECHNIQUES

2. Analytical Techniques.

The techniques used in this investigation can be divided into three groups; those which are sensitive to the chemistry of the surface, those sensitive to the physical characteristics of the surface, and techniques used for bulk characterisation.

2.1. Auger Electron Spectroscopy.

Auger electron spectroscopy (AES) is important in the study of surfaces both from its ability to detect elemental concentrations in the surfaces, and in its limited depth resolution, of the order of 10Å. Further discussion on the use of AES in the study of surfaces is given in Burhop (1952), Davis (1976), Briggs & Seah (1983) and Thompson et al. (1985). Mineralogical applications of AES have been discussed by Urch (1985) and Vaughan & Tossell (1986). One of the first mineralogical applications was presented by Losch & Monhemius (1976) in a study of the surface alteration of a copper-iron sulphide.

The data obtained during this investigation were recorded on a Kratos XSAM 800 XPS/Auger spectrometer after a primary electron beam excitation at an energy of 3keV. A sample chamber vacuum of 10^{-8} to 10^{-9} Torr was maintained.

2.1.1. The Auger Effect.

The Auger effect, illustrated in figure 2.1., is a secondary electron process, occurring as result of primary electron excitation. As a consequence of the electron bombardment, core levels in the elements are excited and eject an electron. The atom relaxes when an electron from an outer orbital fills the vacancy, with the associated photoemission of a quantised Auger electron from an outer orbital or another one of lower energy, leaving the atom in a doubly-ionised state.

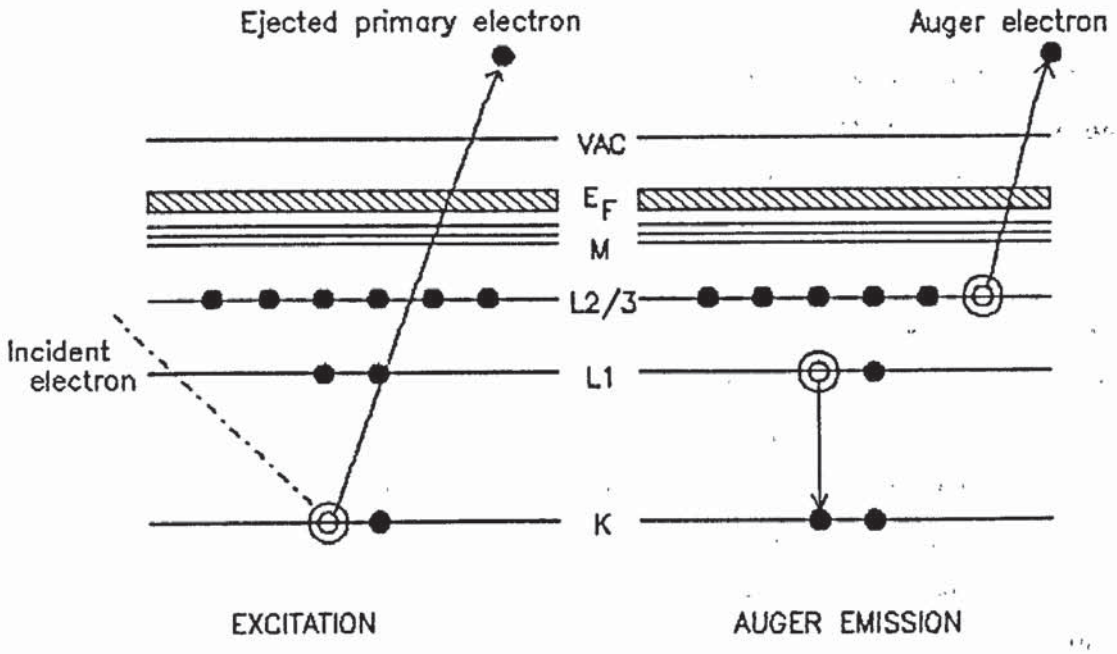

Fig. 2.1. Interpretation of an Auger transition shown by a simplified energy diagram.

Auger transitions for the elements considered in this investigation are included in Appendix 1. By convention, the Auger notation uses the same terminology as in x-ray techniques, for example $KL_1L_{2/3}$, representing ejection of a primary core electron from the K shell, replacement from the L_1 shell, and Auger emission from the $L_{2/3}$ shell (as shown in figure 2.1.).

2.1.2. Data Interpretation.

The kinetic energy of an Auger electron is quantised due to fixed transitions in the atom, and is unique to that atom because of atomic charge effects. A change in the electronic charge around the atom may produce chemical Auger shifts; however, these are not of interest in this investigation since this information can be obtained from x-ray photoelectron spectroscopy. Of more importance, from the viewpoint of this investigation, is the ability to determine elemental compositions from Auger electron spectroscopy.

To determine the concentrations of elements in the 10Å surface layer, with high sensitivity, the differentiated energy function, $dN(E)/dE$, is recorded, although the high signal to noise ratio of the detector masks minor peak details that would have been of compositional interest.

A typical differentiated Auger spectrum is shown in figure 2.2, illustrating a violarite ($FeNi_2S_4$) surface. The peaks detected in this, and in other, differentiated spectra exhibit a peak shape as shown in the inset in figure 2.2. In previous work, the measurement of both negative and full peak heights (figure 2.2. inset), has been used to determine the surface compositions. In this work only the full peak heights are measured.

The peak heights are a function of the elemental composition of the surface, and were corrected for the relative sensitivity (S_x) of the spectrometer to the elements (as discussed in Appendix 1). The corrected peak values were used to determine the element compositions of the surface layer.

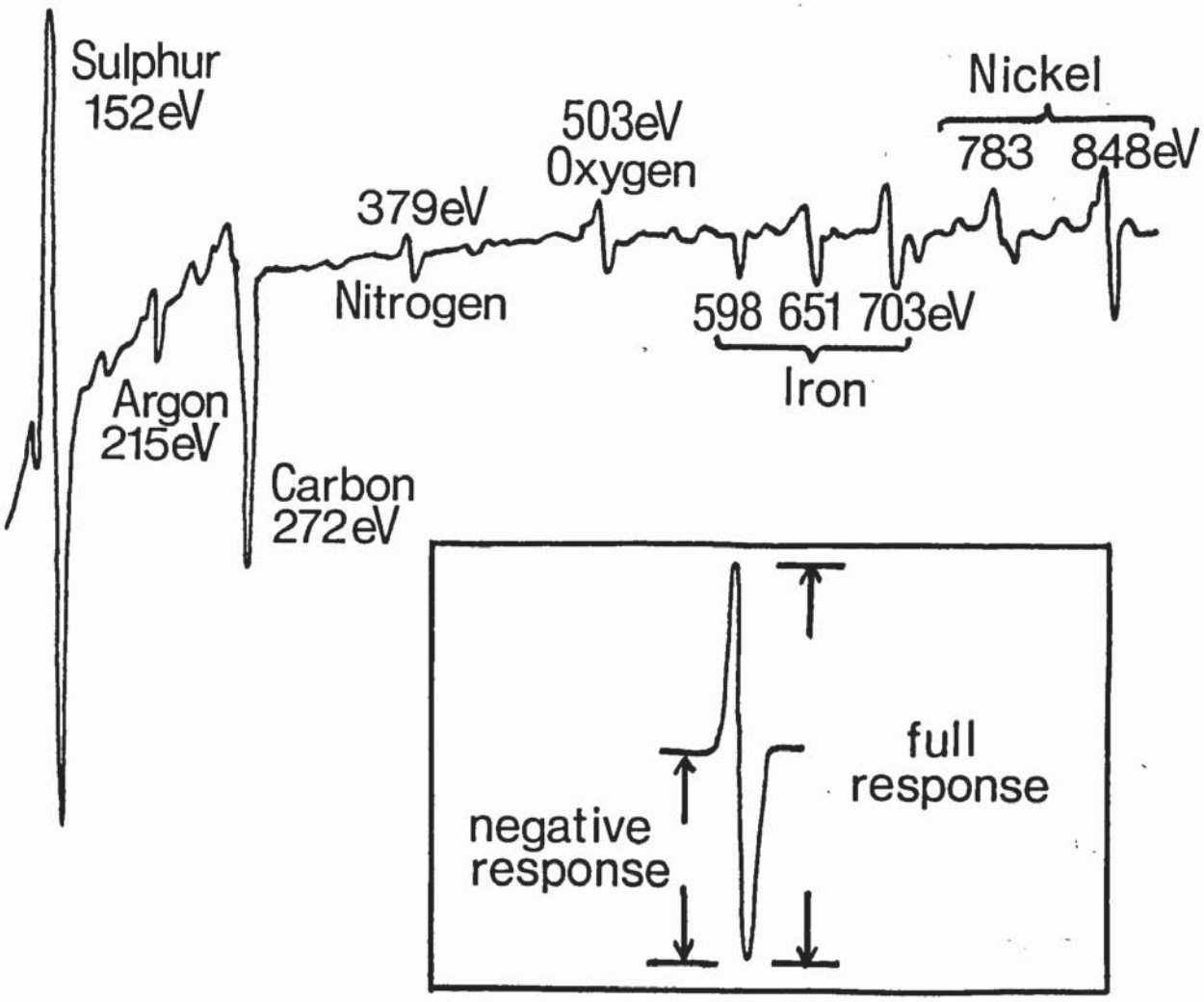

Figure 2.2. A typical differentiated Auger spectrum (for violarite oxidised by sulphuric acid, and sputtered by argon ions for 15 minutes). The inset shows two methods of peak height measurement as discussed in the text.

The element compositions derived for altered and unaltered sulphide surfaces from interpretation of the differentiated Auger spectra, invariably showed a strong feature arising from carbon contamination, a factor inherent in the technique and due to adsorption from the atmosphere and the instrument itself. Major adsorbants are carbon, carbon monoxide, nitrogen and oxygen.

The carbon contamination, although important at the immediate surface, masked the underlying relationships between the major elements in the sulphide surfaces. For this reason, the Auger data, presented in the following chapters, are recalculated for the major elements only.

2.1.3. Argon Ion Sputtering.

In order to investigate the sub-surface elemental compositions, argon ion sputtering, ie. the mechanical erosion (etching) of the sample surface, is used to remove material. Argon ion sputtering may be used in conjunction with Auger electron spectroscopy to produce depth profiles of elemental concentrations in the surface layer analysed.

The sputtering in this investigation was undertaken using a Kratos Minibeam 1 ion gun with a 5 keV operating voltage and 1 μAcm^{-2} sample current, producing an estimated sputter rate of 1 $Amin^{-1}$. This is an approximate rate for sulphides and oxides, as the precise rate will be prone to variation as a result of preferential sputtering in some areas of the surfaces and, in particular, between compounds with relatively large density differences.

The effect of sputtering needs to be considered since, along with the removal of layers of material, the bombardment causes both physical and chemical alteration of the resultant surface. General roughening of the surface occurs, as a result of preferential sputtering in some areas, as indicated by Brundle et al. (1977). Ion enhanced diffusion may occur, along with 'knock-on' effects where small ions, eg. copper ions, are driven back from the surface. Another

major effect of ion bombardment is the the chemical reduction of surface species, and the promotion of chemical reactions as a result of surface heating. Evidence of the chemical effects of sputtering on the surfaces can be inferred in the light of previous work on sputtering in relation to iron-sulphur compounds (Tsang et al., 1979), copper oxides (Panzner et al., 1985), and iron oxides (Mitchell et al., 1981), that demonstrate the reduction of compounds at the surface.

These problems are unlikely to cause effects with regard to measurement of the elemental concentrations using AES that will affect the interpretation of depth profiles. Even so, a reduction of sulphates or oxides must be accompanied by oxygen loss and this must be assessed during the interpretation of the depth profile.

2.2. X-ray Photoelectron Spectroscopy.

X-ray photoelectron spectroscopy (XPS) complements Auger electron spectroscopy in its similar depth of penetration, of the order of 10-15Å. An overview of the technique can be obtained from Siegbahn (1967), Wagner (1979), and Briggs & Seah (1983). Mineralogical applications of XPS have been discussed by Urch (1985). Since the technique is also available on the same Kratos XSAM 800 spectrometer, consecutive analysis by XPS and AES was possible without removing the sample from the sample chamber.

XPS is a valuable technique for the chemical characterisation of surfaces, which when combined with AES, allows an assessment of the phases present in the surface. As this work is concerned with the oxidation of sulphide surfaces, the effect of sputter reduction, as discussed in section 2.1.3., could invalidate any depth profile analysis by inducing reduction in a sub-surface that would be less oxidised with respect to the surface., and for this reason XPS was used to analyse the primary oxidised surfaces only. Even so, in practise it was sometimes necessary to use a few seconds of sputtering in order to remove thin layers of contaminants. Where this was employed, it is noted in the text.

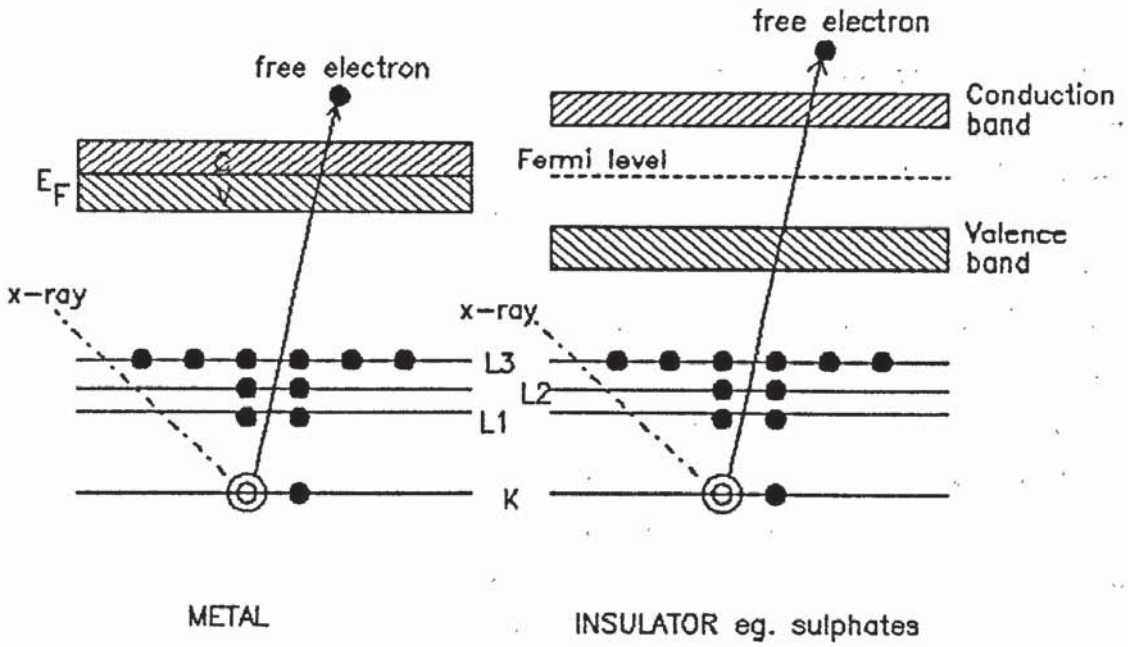

Fig. 2.3. The x-ray photoelectron effect. The two transitions shown are discussed in section 2.2.2.

2.2.1. The X-ray Photoelectron effect.

The x-ray photoelectron effect, illustrated in figure 2.3., occurs when the sample surface is irradiated with soft x-rays, in this case MgKα, causing the ejection of core and valence electrons with quantised kinetic energies. The impinging energies of the x-ray photons are known, and are related to the binding energies of photoelectrons by the following equation;

$$E(B.E.) = h\nu - E(K.E.) - Wf$$

- where E(B.E.) is the original binding energy of the ejected electron, E(K.E.) the kinetic energy of the electron, hν the x-ray photon energy (1253.6eV for MgKα x-rays), and Wf is the calculated work function of the spectrometer.

The work functions for these spectra were calculated with respect to atmospheric carbon, determined from the carbon 1s peak. Although minor organic contaminants were observed, the adsorbed carbon peak with a known binding energy of 284.3eV can be accurately fitted, and the kinetic energy obtained for this peak was used to determine the work function of the spectrometer for each surface investigated. The binding energy of specific electrons can then be determined from their measured kinetic energies.

2.2.2. Surface analysis using XPS.

The peak for the energy level studied is superimposed on a high background, which was removed by a linear background subtraction. Fitting of the peaks for the compounds present in the surface studied was by a non-linear least squares fitting procedure. In most spectra, the original spectrum was used for fitting after linear background subtraction, but where smoothing was necessary on 'noisy' spectra, this was was carried out using a quartic/quintic smoothing procedure.

The particular energy levels for the elements studied have binding energies that are characteristic of the compounds present.

Appendix 2 contains information on the binding energies and peak widths for compounds expected to form on the altered sulphide surfaces. The variation in binding energies is shown in Fig. 2.2. to result from the separation in the valence and conduction bands, causing a greater binding energy in insulators. The binding energy obtained for a specific compound is fixed and and may be used in the deconvolution of the spectra of surfaces containing several compounds.

Often the peaks show considerable overlap, as in the case of the Fe 2p3/2 electron kinetic energies, where a simplified fitting procedure needs to be used to distinguish the phases present. In the simplified fitting, an assessment of the valence states of elements is made, which can be used, with reference to other component elements to identify the surface compounds.

During fitting, account has to be taken of the effect of satellite peaks on the spectrum. X-ray satellites are present, and characteristically for the x-ray source used, a major satellite occurs at 8eV higher kinetic energy above the main line spectrum. This is evident in all of the spectra studied, and is a product of minor x-ray components with higher photon energies. X-ray ghosts, as a result of contamination in the x-ray anode, were not perceived as a major problem in the analyses. An effect which may be important in the spectra studied is the phenomenon of shake-up lines, the result of an ion being excited above the groundstate and the resultant decrease in the electron kinetic energy by a few electron volts, hence causing a higher binding energy addition to the observed spectrum.

In the spectra of the transition metals examined in this study (copper, iron, and nickel) and, for example, the Fe 2p energy level, the spectra exhibit multiplet splitting of the energy level as a result of the spin doublet separation of the Fe 2p3/2 and 2p1/2 energy levels in a ratio of 3:1. Thus in the analyses, the Fe 2p3/2 level is used in fitting due to its greater resolution, as are the respective levels of copper and nickel. Further details concerning the fitting of peaks and peak envelopes to the spectra are considered in the following chapters.

2.3. Conversion Electron Mössbauer Spectroscopy.

Mössbauer spectroscopy is a nuclear gamma resonance technique that can be used to determine surface compositions. The characteristic spectra (presented in appendix 3.) produced using Mössbauer spectroscopy are a result of several interactions with the nuclei of the elements studied, including the effect of valence electrons and hence the electron density surrounding the nucleus, and the effect of ambient internal magnetic fields on the nuclei. An overview of the technique is given by Compton & Schoen (1962), Wertheim (1964), Bancroft (1973), and Hobson (1974), with specific applications of conversion electron Mössbauer spectroscopy discussed by Tricker (1985). Mineralogical applications have been discussed by Vaughan & Craig (1978) and Maddock (1985).

2.3.1. The Mössbauer effect.

The Mössbauer effect is the recoil-free resonant absorption of gamma rays. Although the effect has been observed in over forty elements, the element of importance in this study is Fe^{57}. In order to excite the Fe^{57} nucleus, 14.4keV gamma rays from a Co^{57} source are used. In its groundstate the iron nucleus should absorb 14.4keV gamma rays; however, the nucleus is affected by internal and external fields created by electrical, chemical and magnetic effects. Therefore the gamma rays are absorbed at energies that differ from the groundstate, and these are generated by the Döppler modification of the source.

Conversion electron Mössbauer spectroscopy (CEMS) detects secondary, or conversion, electrons that are emitted with an 89% probability after the absorption of gamma rays. The main conversion electrons are 7.3keV electrons from the K shell (95% produced from within 300nm and 60% from within 54nm) which are emitted in an instantaneous relaxation process after gamma absorption. Effectively, the CEMS spectra are surface sensitive spectra, showing information analogous to the transmission absorption spectra. In CEMS the spectra

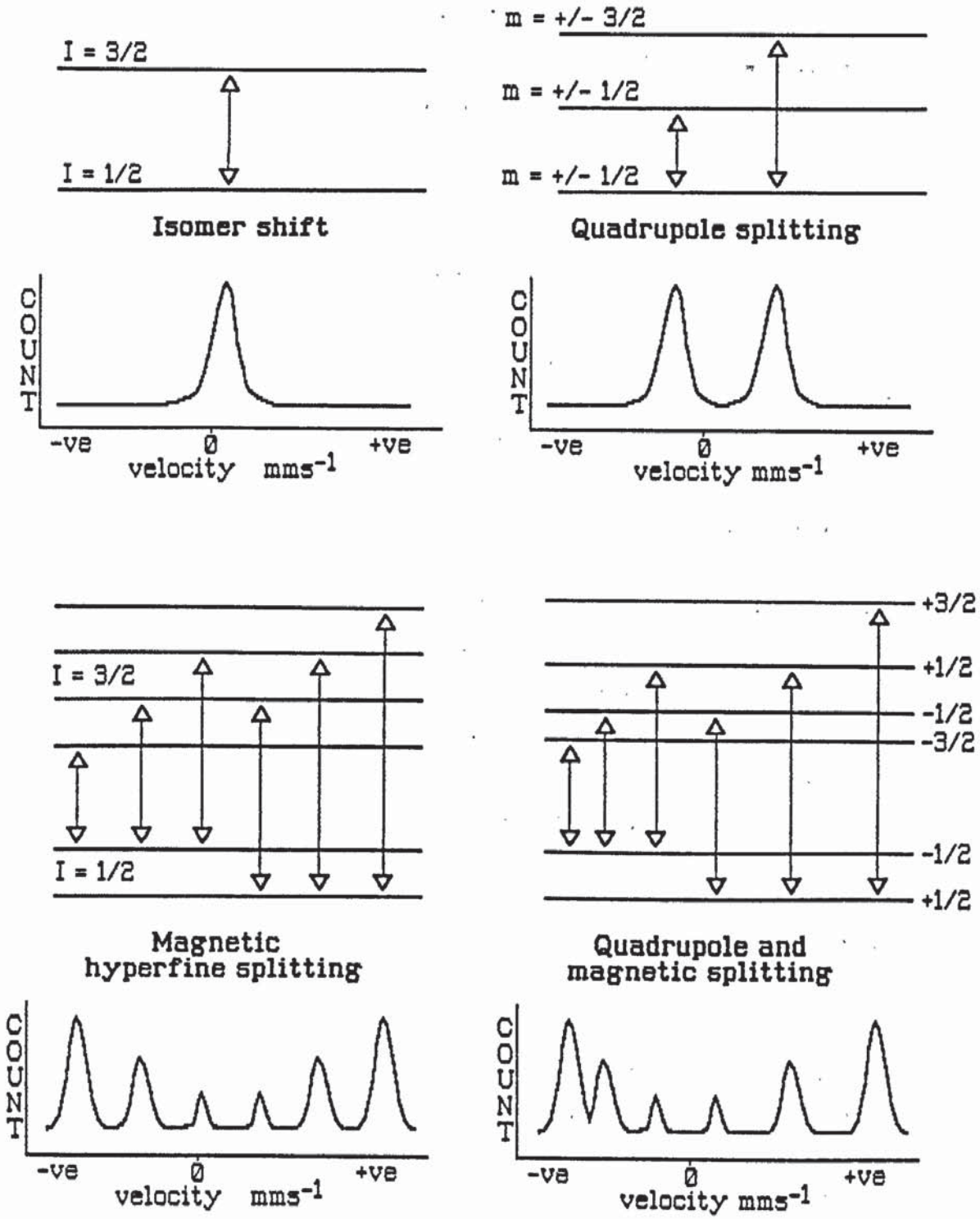

Fig. 2.4. Characteristic spectra showing the effect of the three main hyperfine interactions as observed in Conversion Electron Mössbauer spectra.

show positive emission peaks as shown in fig. 2.4., compared to the negative absorption peaks produced in transmission Mössbauer spectroscopy.

2.3.2. Mössbauer hyperfine interactions.

The fine linewidth generated in Mössbauer spectroscopy enables the differentiation of small energy separations in the nuclei. The resultant peaks are fitted and parameters are determined with respect to standards, in this case, iron foil. The spectra observed are produced all, or in part, by the three major hyperfine interactions, illustrated in figure 2.4.

Firstly, the isomer shift (IS), also known as the chemical shift, arises as a consequence of a change in the s-electron density around the nucleus, produced by valence state changes. The isomer shift occurs as a result of an indirect effect of 3d-electron removal on the 3s-electrons. The result of shielding, and consequently of changes in the charge density at the nucleus, cause isomer shifts that can be characteristic of the valence state. For example, isomer shifts of 0 mms^{-1} for Fe^{o}, 0 - 0.7 mms^{-1} for Fe^{3+}, and 0.6 - 1.5 for Fe^{2+}, have been recorded. An accurate determination of the isomer shift may be indicative of the valence state and can be used, along with other parameters, to identify the chemical phases present.

The second hyperfine interaction is quadrupole splitting (QS). Quadrupole splitting results from splitting of the nuclear levels as a consequence of a distortion in the electron cloud and charge density surrounding the nucleus. Considering Fe^{2+}, in the low spin configuration the t2g energy levels are full and valence effects are minimal, so the splitting is due to largely to site distortion; in the high spin configuration, neither the t2g or eg levels are full, and splitting is due to valence effects. For Fe^{3+} low spin there is a valence contribution, but for high spin both the t2g and eg levels are half-filled, thus any quadrupole splitting will be a result of lattice effects.

The third interaction is magnetic hyperfine splitting, caused by internal (or induced) magnetic fields interacting with the nuclear magnetic dipole moment. For Fe^{57}, magnetic splitting produces a six line spectrum for magnetic phases, with a degree of splitting proportional to the ambient magnetic field.

2.3.3. Data collection and fitting of the Mössbauer spectra.

Mössbauer spectra were recorded using an Harwell spectrometer with an INO-TECH (IT-5200) multi-channel analyser. Conversion electrons were detected in a backscattered electron counter (Harwell MBSC 200) using a helium/methane (5% CH_4) counter gas. The CEM spectra were recorded at room temperature, in the absence of an external magnetic field.

The Mössbauer spectra were fitted using a computer program designed to fit a sum of Lorentzian lines to the spectra. The original program was written by Dr. A.J.Stone, after the method described in the appendix to Bancroft et al. (1967). The program uses a Gauss linear regression procedure and allows the fitting of free or fixed parameters for the baselines, peak positions, widths and areas of the spectra, and has the facility to fix parameters for equivalent pairs of peaks.

The sulphides investigated were analysed unaltered, by both CEMS and transmission Mössbauer spectroscopy. Subsequent alteration, and the formation of new phases on the surfaces, were studied using CEMS.

2.4. Spectral Reflectance Measurements and Optical Microscopy.

The sulphides were prepared in polished blocks in order to measure the reflectance of the surfaces before and after oxidation, and where appropriate to determine the oxidation rates from the change in reflectance during the oxidation period. The reflectance (R%) measured (the percentage of light reflected from the surface at normal incidence) was determined such that for each sulphide a

uniformity of crystallographic orientation was maintained. Thus, for samples from large crystals (eg. pyrite and pyrrhotines) the optic axis was maintained in the same orientation for all surfaces. This is not possible for some sulphides as discussed in section 2.4.1. For the synthetic minerals (pentlandite and violarite) the samples contained a random orientation of grains, and the analyses were undertaken on several grains in random crystallographic orientation, producing an average reflectance for the surfaces.

2.4.1. Reflectance measurement.

Quantitative reflectance measurements were carried out using a Reichert reflex spectral microphotometer, with calibration using a WTiC standard, as approved by the Commission on Ore Microscopy of the International Mineralogical Association. The reflectance of light perpendicular to the sample surface was measured from 400 to 700nm wavelengths (within the visible spectrum), at 20nm intervals, with additional measurements at the COM standard wavelengths of 470,546,589 and 650nm.

The reflectance measurements were used as an indication of the degree of oxidation of the surface measured in terms of the reduction in reflectance, and if possible to determine chemical reasons for changes in specific spectral regions. In practice, it was found that the results were less indicative of chemical changes, and caution was also exercised in inferring the rates of reaction from reflectance changes. In general terms, the decrease in reflectance across the spectral range after a period of oxidation indicates the degree of alteration. However, these empirical changes cannot be interpreted directly because of other effects, which include; (1) the character of the oxidised phases formed on the surface and their reflectances, (2) the extent to which the light is scattered by the oxidised layer as a result of roughening of the surface and partial transmission through the oxidised layer (characterised by the formation of thin film interference on some surfaces), (3) the extent to which the resultant subsurface still reflects light, and finally (4) the reduction in

reflectance as a consequence of surface cracking. Nevertheless, after considering these problems, it was observed that the final reflectance values measured were consistently proportional to the depth of oxidation determined using chemical spectroscopic methods.

In chapters 4 to 9 the reflectance data are presented in table form. For each mineral, at each stage of oxidation, the reflectance value given represents an average of several points of analysis. Where marked bireflectance is present, eg. In arsenopyrite, the reflectance value represents an average of the reflectance in different orientations, since the bireflectance ceases to be a distinguishable feature after slight oxidation.

2.4.2. Features of Optical Microscopy.

In preliminary examination, optical microscopy was used to determine the homogeneity of the sulphides. In combination with the reflectance measurements, optical microscopy is important in inferring the nature of the surface alteration. Characteristically, oxidised sulphide surfaces showed evidence of several important features, including the formation of oxidised areas partially covering the sample surface, evidence of thin film interference as a result of the formation of thin layers of oxidation products, and cracking of sample surfaces.

Although the average reflectance values determined for the oxidised sulphide surfaces are a good indicator of the degree of alteration of the surface, in agreement with the spectroscopic analyses, the surfaces of some oxidised sulphides are far from uniform. The oxidation effects observed have been used to show the presence of compositional variations (in hexagonal pyrrhotine) and twinning (in arsenopyrite). Particular surface phenomena observed using optical microscopy (and where relevant, shown in photomicrographs) have been related to both SEM and spectroscopic data in order to produce a chemical characterisation of the visible surface alteration.

2.5. Scanning Electron Microscopy (SEM).

Scanning electron microscopy (undertaken on a Stereoscan S150 SEM) was used largely as an auxiliary technique, yielding information on the physical nature of the oxidised surfaces. The surfaces studied were both polished prior to oxidation, and cleaved before oxidation, for comparison. For the polished surfaces, the unoxidised sulphides showed no visible defects in the surfaces at magnifications greater than 2000x.

SEM has applications in determining several important features, including the nature of the oxidised surface with respect to argon ion sputtering. Other important uses are the determination of oxidation products forming on the surface, and from this, the interpretation of amorphous or crystalline growth, and also whether the oxidation is causing other physical defects in the oxidised surfaces.

2.6. Bulk characterisation.

The sulphides used in this work were characterised by optical microscopy, x-ray diffraction (XRD) and electron probe micro-analysis (EPMA). Optical microscopy was used primarily to determine the homogeneity of the sulphides used.

2.6.1. X-ray Diffraction.

XRD was used to characterise the bulk samples. Analyses of material from the oxidised surfaces were obtained using both diffractometer and Debye-Scherrer camera techniques.

The techniques showed all the unoxidised sulphides to be homogeneous. After oxidation, small samples from the oxidised surfaces were analysed using a Debye-Scherrer camera; however, it was not possible to separate a thick enough oxidised layer from the bulk sample, even in the case of hexagonal pyrrhotine, for which the oxidation extent is greatest.

2.6.2. Electron microprobe analysis.

The bulk composition of the sulphides was determined using electron microprobe techniques. The sulphides were prepared in polished blocks which were ground using carborundum grits and then polished using tin oxide on wet laps. Final polishing was carried out using 1/4μm diamond paste on dry laps. Prior to analysis the samples were coated with a 20nm carbon film.

Analyses were undertaken using a CAMECA microprobe with wavelength dispersive spectrometers (with the following operating conditions; 20kV accelerating potential, 14.5 nA sample current). Data interpretation were carried out using Link Systems software. The sulphides were analysed for the elements given in table 2.1.

Table 2.1. Elements analysed (elmt) and standards used in the electron microprobe characterisation of the sulphides.

elmt	Line	Standard		elmt	Line	Standard	
S	Kα	pyrite	FeS_2	Zn	Kα	sphalerite	(Zn,Fe)S
Mn	Kα	Mn metal		As	Kα	arsenopyrite	FeAsS
Fe	Kα	pyrite	FeS_2	Ag	Lα	Ag metal	
Co	Kα	Co metal		Cd	Lβ	greenockite	CdS
Ni	Kα	Ni metal		Sb	Lα	chalcostibite	$CuSbS_2$
Cu	Kα	chalcopyrite	$CuFeS_2$				

2.7. Discussion of uncertainties.

The data derived from the different techniques, as presented in chapters 2 to 9, have accuracies which are dependent on various factors, such as the degree of reproducibility, surface inhomogeneity, and fitting accuracies etc., as noted below.

Technique	Main cause of inaccuracy	Accuracy (+/- %)
Reflectance	Surface inhomogeneity (mineral dependent)	2 - 5
AES	Peak subtraction from background	@ 1 - 2
XPS	Fitting accuracy	0.5 - 1
CEMS	Fitting and background subtraction	2 - 5

CHAPTER 3.

SAMPLE PREPARATION: SURFACES & OXIDATION METHODS

3. Sample preparation.

3.1 Sulphide minerals.

This investigation is concerned with the surface oxidation characteristics of seven major sulphide minerals. The sulphides studied are commonly occurring minerals in natural ores, and as for most of the major sulphide ore minerals, are iron-containing. The sulphides investigated are listed in table 3.1.

Table 3.1. Sulphide minerals investigated.

Sulphide	Formula	Source	Chapter
Pyrite	FeS_2	natural	4
Hexagonal pyrrhotine	Fe_9S_{10}	natural	5
Monoclinic pyrrhotine	Fe_7S_8	natural	5
Violarite	$FeNi_2S_4$	synthetic	6
Pentlandite	$(Fe,Ni)_9S_8$	synthetic	7
Chalcopyrite	$CuFeS_2$	natural	8
Arsenopyrite	FeAsS	natural	9

From table 3.1. it can be seen that the sulphides studied included both natural and synthetic samples. In order to study the effects of oxidation on the sulphides it was necessary to know the compositions of the samples, and information on any contaminants which might affect the rate, extent and products of oxidation. For this reason, synthetic sulphides are ideal since there is a compositional control. All of the sulphides shown were produced synthetically; however, the characteristics of some of the synthetic minerals made them unsuitable for oxidation and analysis. The reasons for the use of natural samples rather than synthetic minerals for some mineral analyses are outlined in section 3.2.

3.2. Sulphide synthesis.

Ideally, considering the contamination problems encountered using natural samples, all of the sulphides studied should have been synthetic, thus precisely controlling chemical compositions. In practice it was found that with the procedures used, mono-mineralic homogeneous phases were only produced for the iron-nickel sulphides (violarite and pentlandite). For the other sulphides, problems were encountered due to the formation of mixtures of phases, skeletal textures and charges composed of small grains. Other factors affecting the suitability of synthetic minerals included the quantity of sample produced (not always enough to produce duplicate samples), and the size of surface available (especially for conversion electron Mössbauer spectroscopy which requires a relatively large ($>1cm^2$) surface area). For these reasons, natural sulphides were used (for pyrite, the pyrrhotines, chalcopyrite and arsenopyrite).

The synthesis procedure involved the dry, evacuated silica tube method, as described by Scott (1976). The step-wise production of charges for synthesis is shown in figure 3.1. A length of silica tube, of 4mm internal diameter, was melted in an oxy-propane flame from a welding torch and two sealed sample tubes produced. The ends were sealed such that the glass walls are of uniform thickness, which limits the effects of temperature gradients in the tube during heating in the furnace. After cleaning, the required elements were weighed into the sample tube and mixed thoroughly. Tightly packed silica wool was added to the tube to prevent the loss of sample in the vacuum system and during the necking down of the tube. The tube was heated rapidly (to avoid the loss of volatiles), above the silica wool, in order to draw out a thin capillary. The tube was then attached to a vacuum system and evacuated slowly to prevent the loss of material in the system. The capillary was then collapsed under a vacuum using a welding torch, producing a vacuum-sealed charge.

The charge was heated in a horizontal tube furnace (as shown in figure 3.2b., but without the oxidation equipment). The details of the

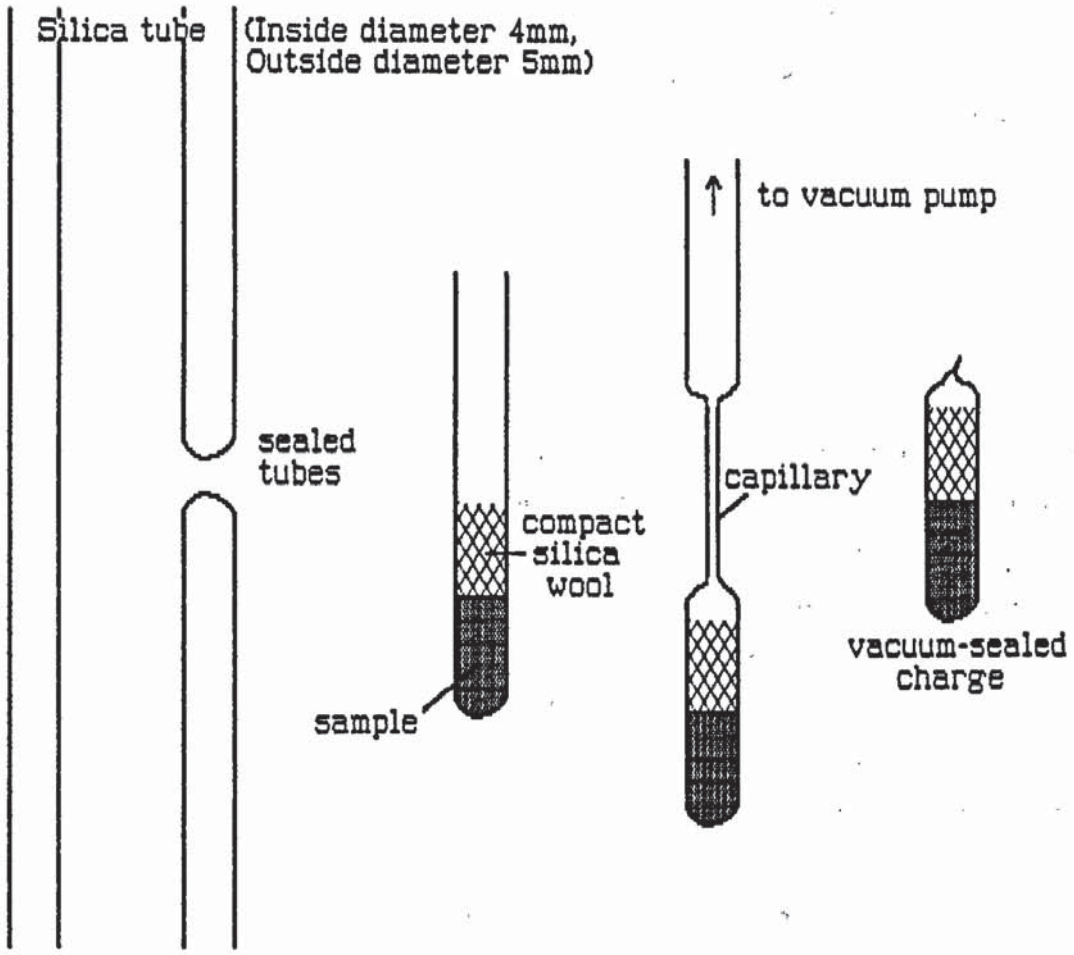

Figure 3.1. Step-wise production of a vacuum-sealed charge, used in the synthesis of sulphides.

temperatures and charge compositions for the iron-nickel sulphides are given in chapters 6 and 7.

Table 3.2. Element purity in the starting materials used in the synthesis of iron-nickel sulphides.

Element	Purity	Source
Fe	99.999 %	Johnson-Matthey Specpure
Ni	99.999 %	Johnson-Matthey Puratronic
S	99.9999 %	Johnson-Matthey Specpure

3.3. Surface preparation.

Prior to oxidation, the mineral surfaces were prepared both in polished form and as cleaved surfaces. Using polished surfaces there is greater control over the crystallographic orientation of the sample, which may have an effect on the oxidation of the surfaces. A drawback of using polished surfaces is the uncertainty regarding the mechanical effects of polishing and the possible alteration of the oxidation characteristics. Polished surfaces were also necessary to follow the oxidation changes resulting from oxidation by using reflectance measurements.

The same polishing techniques were used on all of the polished surfaces. Preliminary steel lapping with 400 mesh carborundum grit was followed by grinding with 600, 800 and 1200 mesh carborundum grits. Polishing was carried out by machine lapping using tin oxide on wet laps, followed by final polishing using 1/4μm diamond paste on dry laps.

The cleaved surfaces are comparable to the surfaces observed in nature, and as such, are probably better surfaces to use to characterise the surface alteration. Throughout the measurements, the polished and cleaved surfaces showed similar oxidation phenomena when analysed spectroscopically, and both preparation methods were

used to produce standard x-ray photoelectron and CEM spectra for unoxidised sulphides (showing similar spectra for both cleaved and polished surfaces). The optimum methods of sample preparation, and in particular, storage methods, were determined and are discussed section 3.5.

3.4. Oxidation methods.

The alteration of the sulphide surfaces was promoted by the use of various oxidation methods. These were chosen to represent both the environments of oxidation observed in nature (shown in figure 10.3.) and during mineral processing. The oxidation methods used allow characterisation of the oxidised surface produced in varying Eh/pH conditions and in oxidation by air/oxygen (at 150°C in a furnace). The methods used are shown in table 3.3.

Table 3.3. Oxidant strengths, temperatures, and time of exposure.

Oxidation method	Strength	pH*	T(K)	pO_2	time
Air/oxygen (150°C)	-	-	423	0.2-1.0	48 hours
Steam	-	-	348-368	<0.2	2.5 hours
NH_4OH	10M	10.5	298	(v.low)	30 min
H_2SO_4	3M	1.4	298	(v.low)	20 min
H_2O_2	25vol(**)	7	298	(low)	20 min
Electrochemical (0.8V)		7	298	(v.low)	20 min

* Measured using indicators and a pH meter.
** 25% H_2O_2/75% H_2O by volume.

The original strengths and times of exposure for the oxidants chosen were determined in the light of preliminary investigations into the effects of oxidation on pyrite and pyrrhotine surfaces,

a.

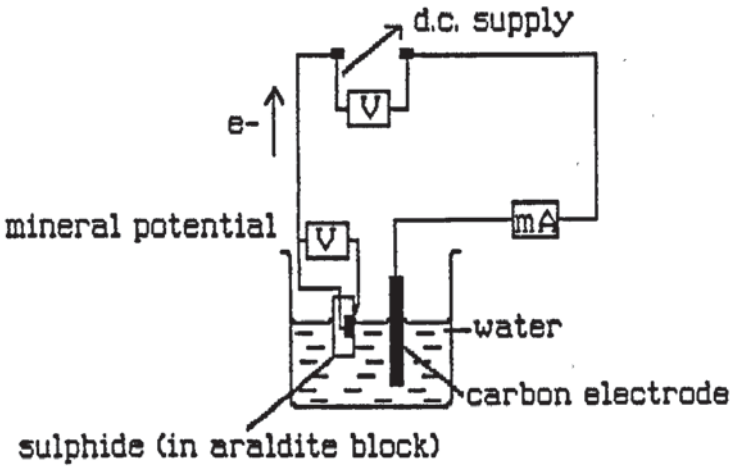

b.

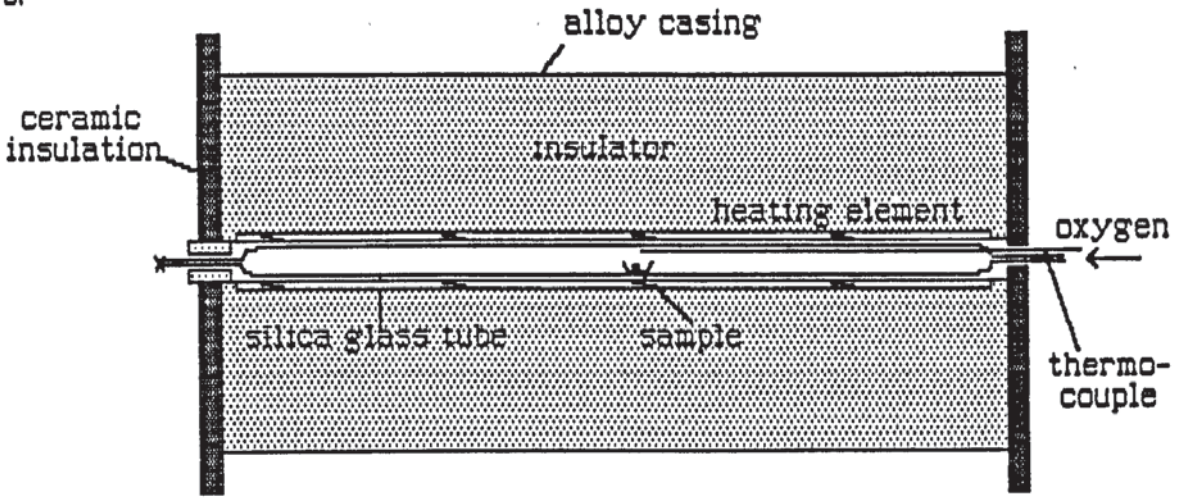

Figure 3.2. a. Diagrammatic representation of the electrical circuit for electrochemical oxidation. b. Furnace apparatus for oxidation by air/oxygen at 150°C.

sulphides showing varying extents of oxidation. The chemical effects of the oxidation methods used are discussed in chapter 10 (section 10.2.), where the mechanisms of oxidation are considered.

Oxidation by ammonium hydroxide, sulphuric acid and hydrogen peroxide was carried out by direct exposure of the surfaces in beakers at room temperature. The solutions were agitated during the oxidation. The volume of solution ($100cm^3$) with respect to the area of sample surface ($0.5cm^2$) ensured that the solution remained relatively unchanged throughout the oxidation period. Detailed discussion of the effects of these oxidation techniques is included in chapter 10, section 10.2.

Steam oxidation was carried out with a jet of steam directed continuously at the surface. Condensation occurred at the edges of the sample; however, the jet of steam kept most of the analysed surface free from condensation. The temperature of the sample surface was measured at between 75 and 95°C. Further details of the chemical processes involved are presented in chapter 10, section 10.2.2.

The apparatus used for oxidation by air/oxygen at 150°C is shown in figure 3.2b. The sample was placed in a calibrated temperature region, monitored by a thermocouple, within a silica-glass tube. The tube was filled with oxygen at the start of the oxidation period, and to account for leaking and diffusion from the system, the oxygen was replaced after 24 hours.

The circuit for electrochemical oxidation is shown in figure 3.2a. and was arranged such that the sulphide surface formed the anode and the carbon electrode formed the cathode. More detailed discussion of electrochemical oxidation is included in chapter 10, section 10.2.4.

Most of the oxidation methods are easily reproduced such that the strength of each oxidant is similar on each sulphide surface, and the differing effects on the sulphide surfaces can be assessed with respect to the relative oxidation stabilities of the minerals. In the case of electrochemical oxidation the extent of surface alteration may differ since there are several variables in the system used, including the surface area, mineral potential (although attempts are made to maintain 0.8V for each sulphide), mineral conductivity and

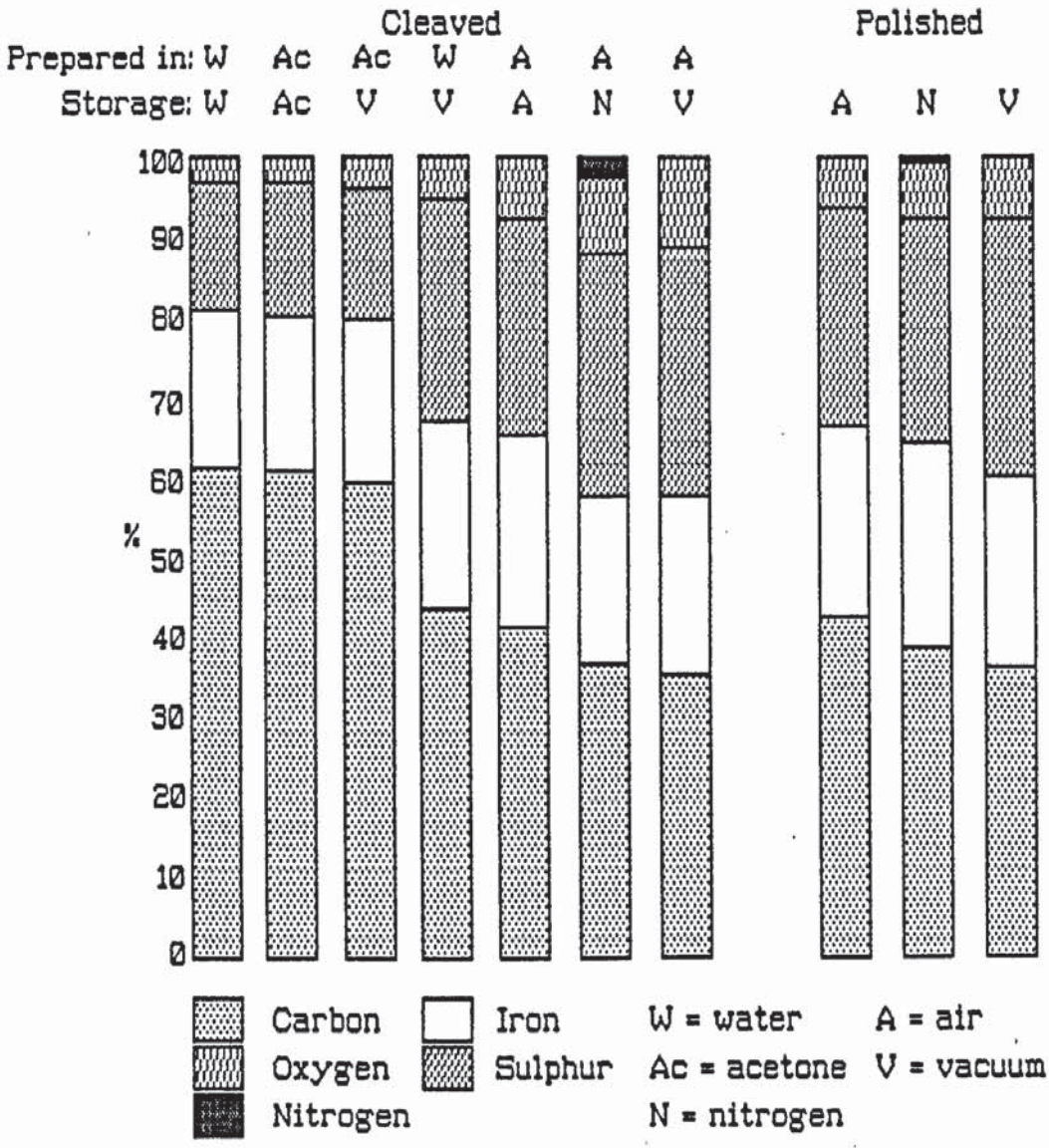

Figure 3.3. Compositions of unoxidised pyrite surfaces prepared by various methods and determined using differentiated Auger spectra, showing the effects of contamination in the 10Å surface layer.

the general resistance in the circuit. For this reason it was necessary to use several duplicate samples in order to assess the average effects of electrochemical oxidation.

3.5. Sample storage.

Storage of the samples was also a major consideration after preparing the mineral surfaces, and also after oxidation, since the surface should ideally remain in an unaltered state between the polishing or cleaving of the sulphides and the oxidation of the surfaces, and also between the oxidation of the surface and the spectroscopic analysis.

Media considered for use during preparation of the surfaces and during storage included acetone, water, nitrogen, air and vacuum, as shown in figure 3.3, indicating the surface changes after one week. The relative "efficiency" of the different methods of storing the samples after polishing or cleaving were determined using an XPS/Auger analysis of surfaces stored in various media. From the Auger analysis it was determined that the main contaminants were carbon, oxygen and nitrogen. On most surfaces, these were determined by XPS to constitute a monolayer of adsorbed species including carbon, carbon monoxide, oxygen, water and nitrogen.

It was determined that the ideal method of storage was a compromise between oxygen and carbon contamination of the surface, which show an inverse relationship (shown for pyrite in figure 3.3., and also determined for hexagonal pyrrhotine). The cleaved surfaces were prepared in air and stored in either air-filled or evacuated desiccators prior to oxidation. The polished surfaces were stored similarly. An evacuated desiccator was used for long-term (more than two days) storage of prepared surfaces. In order to limit the alteration of the surfaces after oxidation the samples were stored in an evacuated desiccator. Loss of volatile components from the surface in the evacuated desiccator was not important, since the samples would inevitably be placed in ultra-high vacuum conditions during the spectroscopic analyses.

The alteration of the unoxidised surfaces in evacuated conditions with time was minimal and as such, the length of storage was not an important factor. After oxidation it was necessary to allow the surface to dry before analysis, and the drying time was decreased in the vacuum conditions of the desiccator. The oxidised surfaces may alter with time, and for this reason, were analysed as soon as possible after the oxidation process.

CHAPTER 4.

PYRITE

4. Pyrite

4.1. Introduction.

Pyrite (FeS_2) is a mineral found in many ore associations (Ramdohr, 1980; Craig & Vaughan, 1981) and, as such, has been the subject of numerous investigations concerning both its stability and its oxidation characteristics. An understanding of the Fe-S system, represented by pyrite and pyrrhotine in this investigation, is also esssential for understanding the other systems that have been studied in the present work (Cu-Fe-S, Fe-Ni-S and Fe-As-S). For this reason, the characterisation of the iron sulphides and their oxidation products in terms of the analytical techniques used and the range of oxidants employed was necessary.

The use, in the present work, of a range of oxidants permitted the determination of the effects of Eh and pH on oxidation phenomena, factors that have not been quantitatively studied in previous work. In view of the greater sensitivity to the immediate surface layer of the techniques employed, it was expected that the products of oxidation found in the present work would not always be in agreement with the results of previous workers (largely obtained from studies of weathered ores and from bulk laboratory analyses).

In order to compare the results of previous investigations to this work, the surface analysis data are preceded by a brief review of past work.

4.2. Previous work on pyrite stability and oxidation.

Pyrite is a very stable mineral in the Fe-S system, below its maximum thermal stability of 742°C determined by Arnold, 1962 (cf. 743°C determined by Kullerud & Yoder, 1959). The stability of pyrite results from its electron configuration which involves a pairing of the six d-electrons, filling the t_{2g} orbitals, confirmed by its diamagnetic character (Nickel, 1967; Tossell et al., 1981; Vaughan & Craig, 1978). The structural stability with respect to marcasite (similarly FeS_2) is evident from the relative free energies of

formation, of $-160.23 kJmol^{-1}$ for pyrite and $-158.42 kJmol^{-1}$ for marcasite (Robie et al., 1978). This indicates that pyrite is slightly the more stable phase.

An overview of pyrite oxidation has been presented by Lowson (1982) and the variations in oxidation products and suggested modes of formation are numerous. In considering the published work on pyrite oxidation, it is evident that although previous workers generally agree as to the alteration products, there is disagreement regarding the formation of several phases. In aqueous oxidation it is generally accepted that H_2S, HS^-, SO_4^{2-}, and Fe^{2+} are major products, with the associated formation of iron oxides and sulphates, as predicted thermochemically. Although in terms of the thermodynamics of oxidation, the oxy-hydroxides such as goethite and lepidocrocite (α & γ FeOOH) are unstable with respect to hematite (as illustrated by partial pressure and Eh/pH diagrams, figures 4.10. and 4.11.) they are the predominant alteration products in naturally oxidised pyritic ores (Ramdohr, 1980) and would be expected to constitute a major component of the oxidised surfaces.

Additional compounds that have been reported are largely a result of the particular conditions of oxidation. Precursor compounds have been predicted to account for the formation of sulphates, reported either as a direct oxidation product, or as a result of a step-wise formation via sulphites and thiosulphates (Lowson, 1982). Similarly, wüstite has been cited by Burkin (1966) as a precursor to the formation of hematite (Fe_2O_3) and magnetite (Fe_3O_4).

The presence of sulphur as an oxidation product has not been conclusively demonstrated, although it has been suggested (Biegler & Swift, 1979; Mathews & Robins, 1972; Banerjee, 1971) that sulphur formation is dependent on the conditions during oxidation. These authors report the formation of sulphur during various conditions ranging from thermal oxidation in air, and acid perchlorate, to oxidation by ferric sulphate. The uncertainty as to sulphur formation after pyrite oxidation may result from detection problems encountered with the techniques used previously, or the consequent removal of sulphur from the system by further oxidation.

The formation of ferric ions has been shown to be a promoter of increased oxidation, as discussed by Dutrizac & MacDonald (1974) and Mathews & Robins (1972). In electrochemical oxidation, the alteration products reported depend on the electrode used. Cathodic oxidation of pyrite was reported to produce ferric hydroxide, ferric ions and sulphur (Peters & Majima, 1968). In acid solutions the formation of ferric hydroxide at the cathode was not observed, and hydrogen sulphide, and ferric ions are reported. Anodic oxidation (Biegler & Swift, 1979) is reported to produce ferric ions and sulphur. In a single case, pyrrhotine has been reported as an oxidation product of pyrite (Molchanov, 1982) after milling of superfine pyrite powder in water, with magnetite reported as an end-product.

The uncertainties raised by the variation in reported products of pyrite oxidation, emphasise the need for a detailed study of pyrite oxidation in various oxidants.

4.3. Characterisation of the pyrite.

The surface analyses were undertaken on a single pyrite crystal, of unknown provenance. The bulk pyrite was examined using XRD, SEM (EDS) and by electron microprobe. All techniques indicated the pyrite to be very pure, although there were very small inclusions of minerals rich in Si and Ti. These phases comprised less than 0.1% of the sample, and were assumed to be of no relevance to the surface study, and to have no effect on the oxidation rates.

Apart from the impurities noted, the pyrite contained no further elemental impurities. Electron microprobe results for the average of several analyses are contained in table 4.1.

Table 4.1. Electron microprobe characterisation of the pyrite.

	Fe (At %)	S (At %)	Impurity
Pyrite	33.39 +/- 0.20	66.53 +/- 0.21	None detected
Formula	1.000	1.993	

4.4. Optical Properties.

The spectral reflectance spectrum obtained for unoxidised pyrite agrees with the spectrum described in the IMA/COM data file (Stanley & Criddle, 1986). Table 4.2. shows reflectance data for the unoxidised pyrite surface and after oxidation in various media. Each reflectance value is an average of five points on the isotropic pyrite surface.

Table 4.2. Reflectance measurements for unoxidised pyrite and for pyrite surfaces after oxidation by a range of oxidants.

	Reflectance (R%)				
Oxidation method	470nm	546nm	589nm	650nm	ΔR(*)
Unoxidised (R^o)	45.6	51.7	53.5	54.4	
Air/oxygen (150°C)	43.2	48.4	50.1	51.0	7.3
Steam	41.7	47.3	48.9	49.7	8.6
H_2O_2	40.3	45.7	47.3	48.1	11.6
H_2SO_4	37.6	42.7	44.1	44.9	17.5
NH_4OH	33.4	37.8	39.2	39.8	27.8
Electrochemical (0.8V)	32.1	36.4	37.7	38.3	29.6

* ΔR = average change in reflectance = $(R^o - R')/R^o \times 100$

After oxidation by all methods used, the spectra showed a uniform reduction in reflectance across the visible region. The average changes in reflectance observed can be regarded as an indication of the extent of alteration of the surface because the degree of oxidation deduced from the reflectance measurements is roughly proportional to the depths of oxidation derived from spectroscopic measurements. The physical effects of alteration are shown by a photomicrograph (figure 4.6.) and by SEM photographs (figures 4.7 to 4.9), that are discussed in section 4.9. with respect to the determined chemical characteristics of the surfaces.

4.5. Auger Electron Spectroscopy.

Variations in elemental composition with depth were derived from differentiated Auger spectra of the oxidised pyrite surfaces. Theoretically, the unoxidised pyrite should produce spectra showing a composition of 33.3% iron and 66.7% sulphur. Figure 4.1. shows profiles of two typical oxidised surfaces, which illustrate a convergence to the expected composition of pyrite, and show a depth of oxidation limited to approximately 100Å or less. In the steam oxidised pyrite (Fig 4.1a.), and similarly both for pyrite oxidised by hydrogen peroxide and by air/oxygen (at 150°C in a furnace), the oxygen concentration decreases rapidly with depth. It seems unlikely that the oxygen present in a surface that is only slightly oxidised would react to the depths shown in these profiles and this may be evidence of differential sputtering and mixing of the surface components, which will have an effect on all of the profiles.

For more heavily oxidised pyrite samples, after oxidation by ammonium hydroxide (Fig 4.1b.), or sulphuric acid, or after electrochemical oxidation, the profiles indicate a greater content of oxygen incorporated in the surface. In the pyrite surfaces oxidised by NH_4OH and H_2SO_4, the Auger profiles indicate an initial decrease in oxygen followed by a significant increase. This is interpreted as a subsurface oxygen-rich layer, possibly sulphate, protected from dissolution by a chemically different surface.

Previous analysis of pyrite after sputtering (Tsang et al., 1979) indicate that the iron sulphides are prone to considerable chemical reduction, even to the point of producing metallic iron. This was not observed to be a major problem in the surfaces studied here, the Fe:S ratio determined at depth being consistent with FeS_2. This has led to the assumption that the sulphide subsurface was not subject to measurable reduction, although the extent to which the oxygen-containing phases in the surface have been reduced is uncertain. This reduction does not invalidate the results obtained, but they must be treated with caution, since an induced reduction creating a loss of volatile oxygen (or less volatile sulphur) would result in an apparently less oxidised surface.

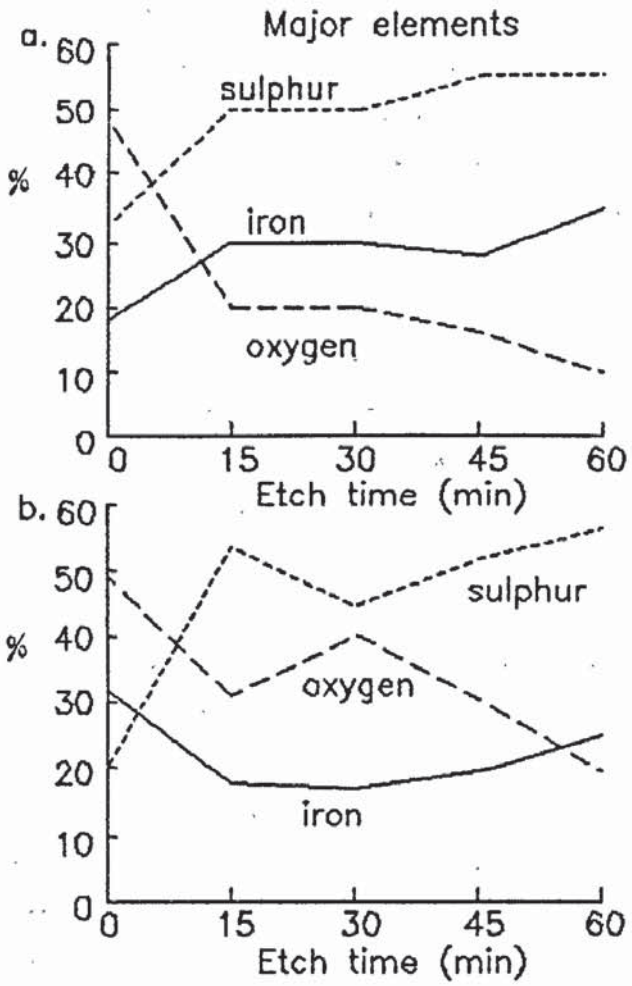

Fig. 4.1. Auger depth profiles for pyrite oxidised by (a) steam and (b) ammonium hydroxide, showing the major elements only. Carbon contamination was a major factor at the surface, but diminished rapidly with depth. (The etch rate is approximately 1Å per minute, thus the scale can be interpreted as a depth scale in Angstroms).

4.6. X-ray Photoelectron Spectroscopy.

Sputtering was not used extensively in combination with XPS, because of the chemical reduction effects discussed in Section 4.5. Even so, it was sometimes necessary to use sputtering for a few seconds to remove adsorbed contaminants, largely carbon, carbon monoxide, nitrogen and oxygen. In the case of pyrite, this was important since the limited oxidation resulted in surfaces with relatively large contamination, when considered with respect to the amount of oxidation products formed. By a comparison between unsputtered and slightly sputtered surfaces oxidised by similar methods, it was established that the peak envelope for the oxygen 1s photoelectrons remains unchanged, thus indicating no detectable reduction of the oxygen-containing phases.

A preliminary investigation of unaltered surfaces produced binding energy information for pyrite from the fitted peaks, of 707.1eV for Fe 2p(3/2), and 161.5eV for S 2p. This is comparable with previous data compiled by Wagner (1979), and obtained by Clifford et al. (1975), and Remond et al. (1981). Data for the peak positions derived from previous work and from this investigation are presented in Appendix 2.

Figure 4.2. shows representative Fe 2p(3/2) spectra for pyrite. The spectrum for unoxidised pyrite may indicate a minor effect of shake-up (discussed in chapter 2, section 2.2.2.) in the spectrum resulting in a broadening of the peak on the high binding energy edge. This effect is minimal, and taking this into consideration, it was inferred that the contribution of shake-up to the oxidised region of the spectrum was minimal. Slightly oxidised samples, as illustrated by the spectrum of steam oxidised pyrite, show pyrite (in the 10-15Å surface layer) as still a major component of the surface, and that either the oxidised surface is limited in depth, or the oxidised layer only partly covers the surface.

After extensive oxidation the surface was altered to a combination of oxides, hydroxides and sulphates. Difficulty in assigning peaks to particular compounds because of the overlap between peaks was overcome by fitting peaks for representative Fe(II)

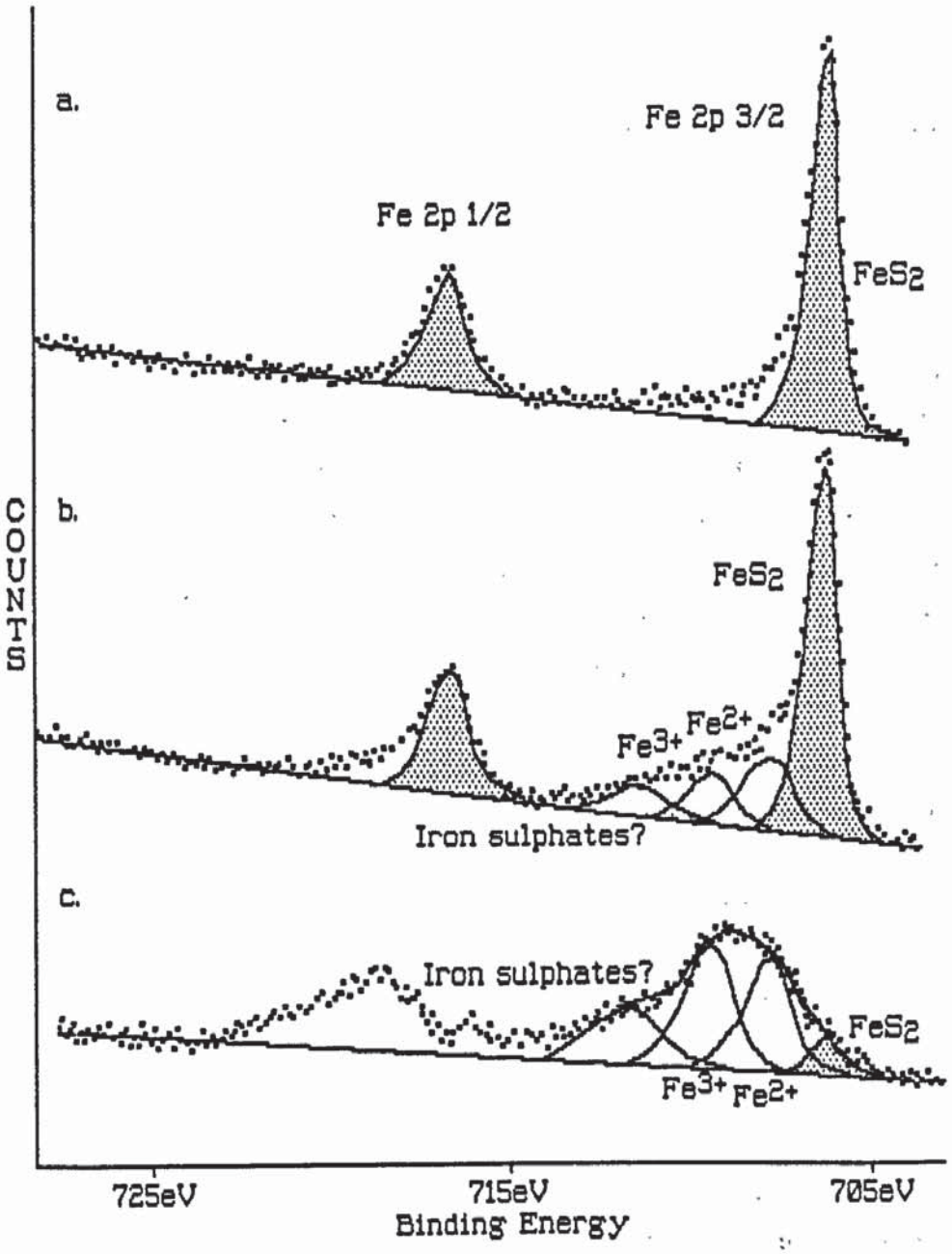

Fig. 4.2. Iron 2p (1/2 and 3/2) x-ray photoelectron spectra obtained for (a) unoxidised pyrite and for pyrite oxidised by (b) steam and following (c) electrochemical oxidation.

and Fe(III) species, with associated sulphates. On the evidence of the Fe 2p(3/2) spectra, it is apparent that the oxidation produces a range of oxidised phases.

Considerable changes are observed between the different oxidised pyrite samples when fitting the sulphur 2p spectra. The unoxidised pyrite (Fig. 4.3.) shows a broadening on the high energy side of the peak that can be attributed to the formation of S(0). As discussed later, it may be valid to infer that this contribution to the spectrum is from elemental sulphur.

The spectra of the surfaces altered by steam, hydrogen peroxide, and by air/oxygen at 150°C (Fig 4.3.) exhibit the formation of sulphur (0) and a peak due to sulphite or thiosulphate indicative of a sulphide surface that is partly oxidised (evident from the lack of sulphate in the spectra.) The heavily oxidised surfaces show a contribution to the spectra from sulphate, in addition to an increase in the concentration of sulphur (0). For surfaces oxidised in sulphuric acid (Fig 4.3) the sulphate is a major component of the surface, and this is also the case for electrochemical oxidation and oxidation by NH_4OH, with the latter showing a very low sulphur (0) content.

Oxygen was investigated by fitting the oxygen 1s spectra. As a volatile component in the oxidants, oxygen is a component of most of the oxidised phases detected. The variations in the binding energies of the oxygen 1s spectra for the compounds observed are very small and do not permit easy resolution, and for the Fe 2p(3/2) spectra, the fitting procedure was simplified to fit a contribution from both iron II and III oxides and hydroxides, and sulphates. For the oxygen 1s spectra, the term sulphate is used to refer to sulphates, sulphites and thiosulphates.

The oxygen spectra observed indicate a variation in the ratios of the fitted peaks, attributable to the oxygen-containing compounds, that is complementary to the proportions of oxygen-containing compounds shown by the Fe 2p(3/2) and S 2p spectra. Two spectra are shown in Fig. 4.4., which illustrate the compositional differences, in terms of simplified peak fitting, that are observed as a result of oxidation. The small variation in the the binding energies of the

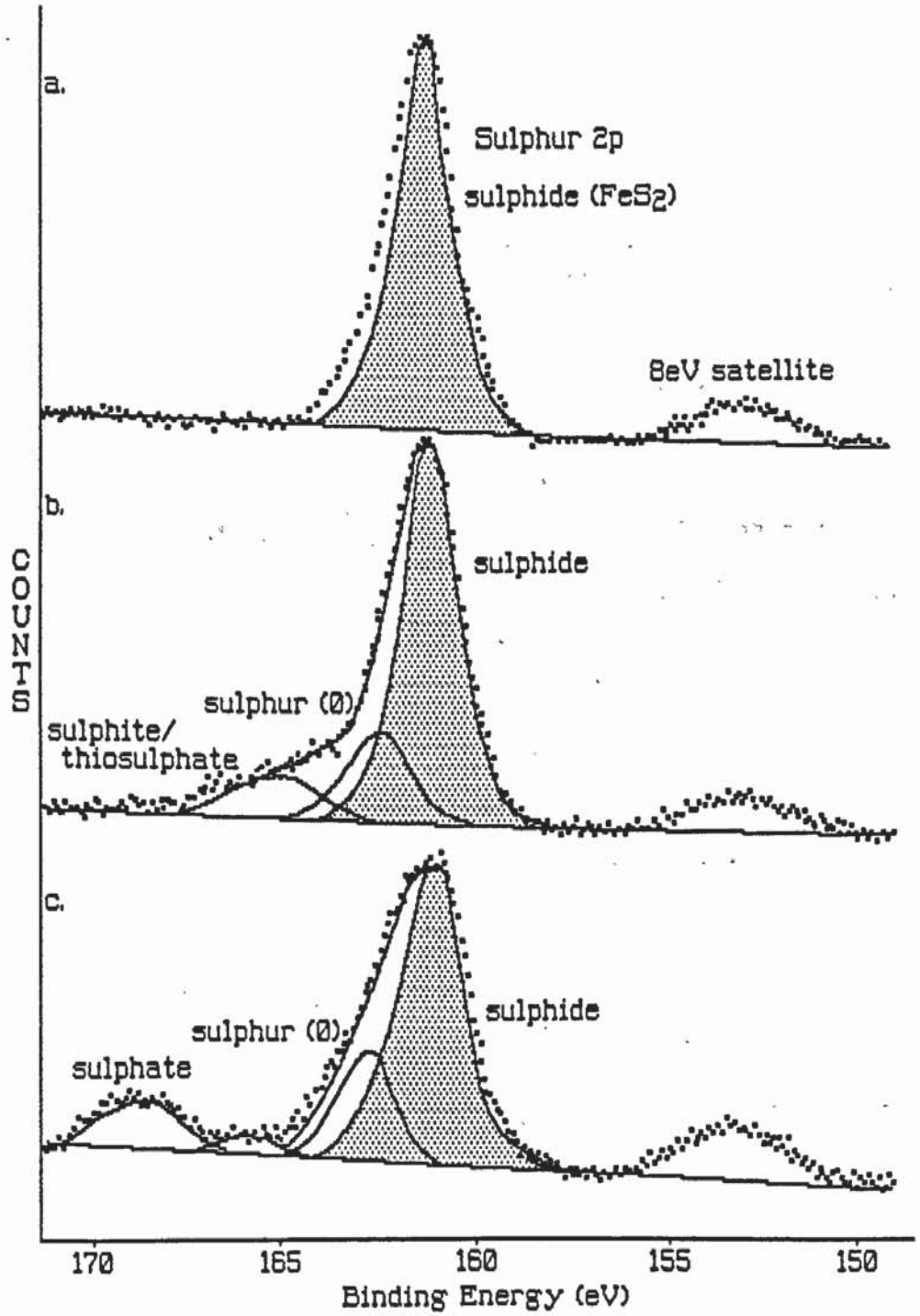

Fig. 4.3. Sulphur 2p x-ray photoelectron spectra observed for (a) an unoxidised pyrite surface, and pyrite surfaces oxidised (b) by air/oxygen (at 150°C in a furnace), and (c) by sulphuric acid.

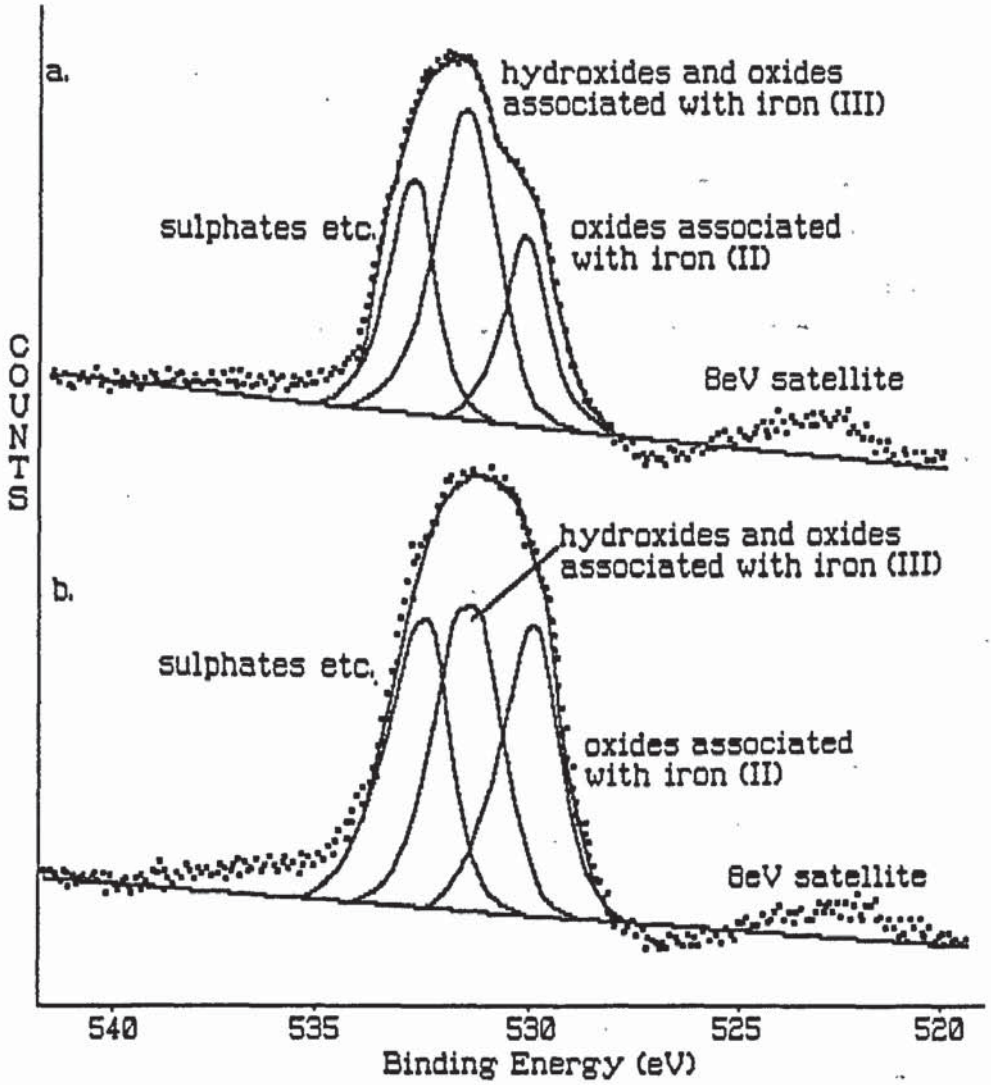

Fig. 4.4. Oxygen 1s x-ray photoelectron spectra observed for pyrite surfaces after oxidation by (a) ammonium hydroxide and (b) hydrogen peroxide.

oxygen 1s peaks, resultant from oxygen-containing compounds, prohibits the separation of individual compounds. The interpretation of the oxygen spectra, and the deconvolution of the peaks into possible compounds is discussed in Section 4.10.

4.7. Compositional interpretation of the XPS and AES spectra.

Using the fitted x-ray photoelectron spectra and the elemental compositions inferred from the differentiated Auger electron spectra, surface compositions were estimated. General compositions, restricted in terms of the valence states determined, are given in table 4.3. and are the bulk composition for a surface layer of approximately 10-15Å depth, as determined by the depth resolution of the XPS.

Table 4.3. General surface compositions from XPS/AES analyses (estimated molecular percentages).

	Method of oxidation					
Phase	air/oxygen	steam	H_2O_2	H_2SO_4	elec.chem	NH_4OH
Fe II/III sulphate	-	5.0	9.3	24.2	25.7	27.3
Fe II sulphite etc.	9.6	14.0	7.4	3.2	-	-
Fe III (oxides & Fe II hydroxides)	16.1 23.2	14.3 15.6	24.9 15.5	26.1 17.3	31.8 27.4	36.8 27.4
S (0)	12.1	14.2	7.3	8.9	7.3	2.7
Pyrite - FeS_2	39.0	36.9	35.6	20.3	7.8	5.8

It is also possible to provide an assessment of the actual phases present in the oxidised surfaces. For example, the detection of sulphur (0) in the x-ray photoelectron spectra was interpreted as an indication of the presence of elemental sulphur. This was justified by the lack of any indication of polysulphide formation from the Fe 2p(3/2) spectra, or any supportive evidence for the presence of

thionates, such as $(SO_3\text{-}S_n\text{-}SO_3)^{-2}$. The peak attributable to sulphur (0) was in evidence in surfaces with no thionate, sulphite or thiosulphate detected. However, this is not discounting that where the latter are found in the oxidised surfaces there is a contribution to the sulphur (0) peak. However, where thiosulphates have been identified in the oxidised surfaces, the presence of sulphur (0) that is not attributable to elemental sulphur, may be a factor.

The modal proportions of Fe II and Fe III sulphates were difficult to ascertain, partly because they are not clearly defined in the sulphur 2p spectra, and also because the iron 2p spectra are subject to shake-up phenomena in this region of the spectrum (as discussed in chapter 2, section 2.2.2.). Consequently the sulphates were mainly fitted as one peak.

The phases that are most difficult to determine are the mixtures of Fe II and Fe III hydroxides and oxides . In previous work concerning the deconvolution of the peaks attributable to these phases, the problems have been outlined. These are largely concerned with the number of possible compounds involved, namely Fe_2O_3, Fe_3O_4, FeOOH, $Fe(OH)_2$, $Fe(OH)_3$, and metastable $Fe_{1-x}O$. The Fe 2p3/2 and O 1s binding energies measured previously for these compounds are listed in Appendix 2.

In the past, two approaches have been used to identify the oxide and hydroxide phases present, involving either the individual contributions to the spectrum from each compound, or comparison of the overall peak envelopes for like compounds. Comparison of the overall peak envelopes is practical only for surfaces containing one, or a limited number of iron oxides/hydroxides. Nevertheless, it has been used in several studies e.g. Stout et al. (1980), Brion (1980) and Brion et al. (1980). Problems were also encountered with the fitting of peaks for individual compounds to the spectra of the oxidised surfaces. The individual phases with peak contributions previously measured by McIntyre and Zetaruk (1977), Harvey and Linton (1981), and Mills and Sullivan (1983), are well defined, but fitting such data to a complex mixture of surface compounds is not practical. The problems encountered were resolved by assessing the

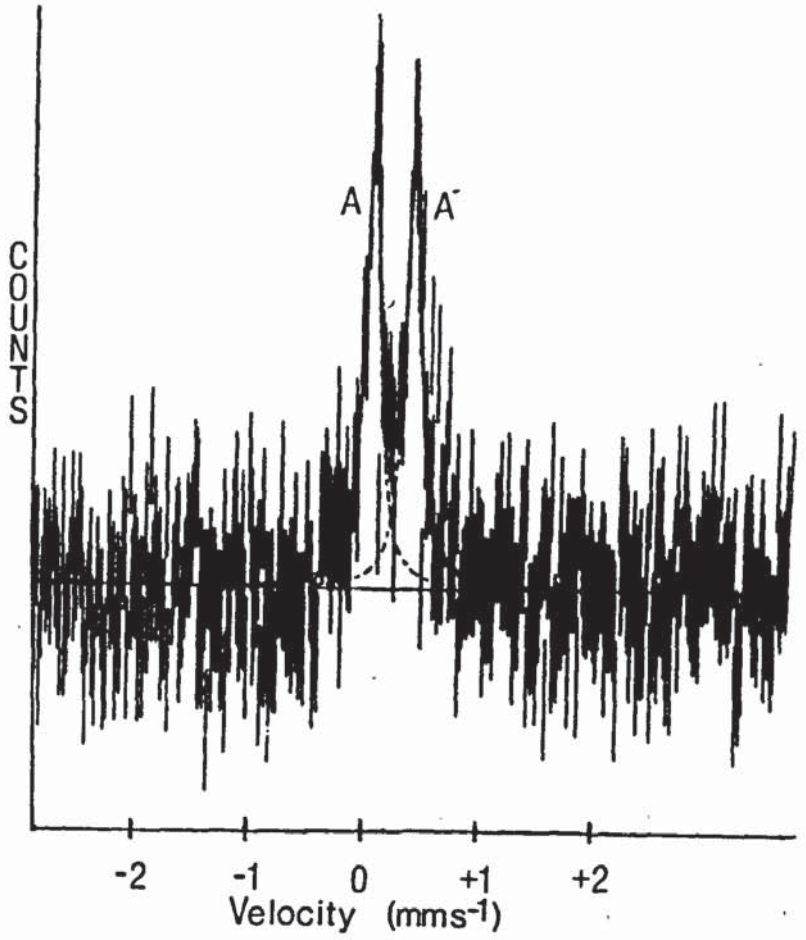

Figure 4.5. Conversion electron Mössbauer spectrum for pyrite oxidised by ammonium hydroxide.

Fe II/III hydroxide and oxide contributions in the light of both the relative proportions determined by XPS, and the compounds predicted on the basis of their thermodynamic stabilities as discussed in section 4.10.

4.8. Conversion Electron Mössbauer Spectroscopy.

The information on surface compositions shown in table 4.3. indicates that surface alteration is limited to a level that would be below the resolution of CEMS. Even so, it was necessary to determine whether the subsurface had been altered chemically, a factor detectable by CEMS.

The unoxidised pyrite surfaces produced a conversion electron Mössbauer spectrum with a characteristic quadrupole doublet. This indicated an isomer shift of 0.262 mms^{-1} and quadrupole splitting of 0.638 mms^{-1}. The parameters determined were in agreement with previous recorded parameters for pyrite (Morice et al., 1969; Finklea & Cathey, 1976; Montano & Seehra, 1976; Evans et al., 1982;).

After the oxidation of the pyrite surfaces to the same extent as those surfaces analysed by XPS and AES, the CEM spectra did not exhibit further features. This indicates that there was no structural alteration of the pyrite surface below the depths of analysis obtainable by XPS and AES. After extensive oxidation using NH_4OH, the oxidant that produced the most oxidation of pyrite, the surface as studied by CEMS (Fig. 4.5) did not show any evidence of alteration.

4.9. Relating spectroscopic results to SEM and photomicrographs.

The chemical characterisation of the surfaces determined in the previous section can be related to the physical nature of the surfaces, as shown in the reflectance spectra, reflected light photomicrographs and SEM photographs.

Figure 4.6. shows a typically oxidised pyrite surface which exhibits characteristics that are observed on several pyrite surfaces. After oxidation a brown tarnish predominates which is partially obscurred by a blue sheen overlying the surface.

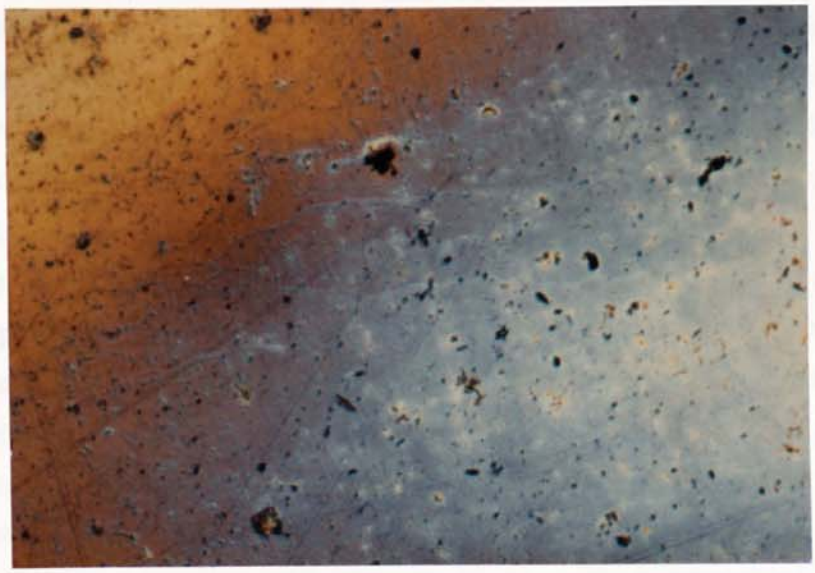

Figure 4.6. Reflected light photomicrograph of pyrite after oxidation by sulphuric acid. (Width of field = 3 mm, magnification = 33x)

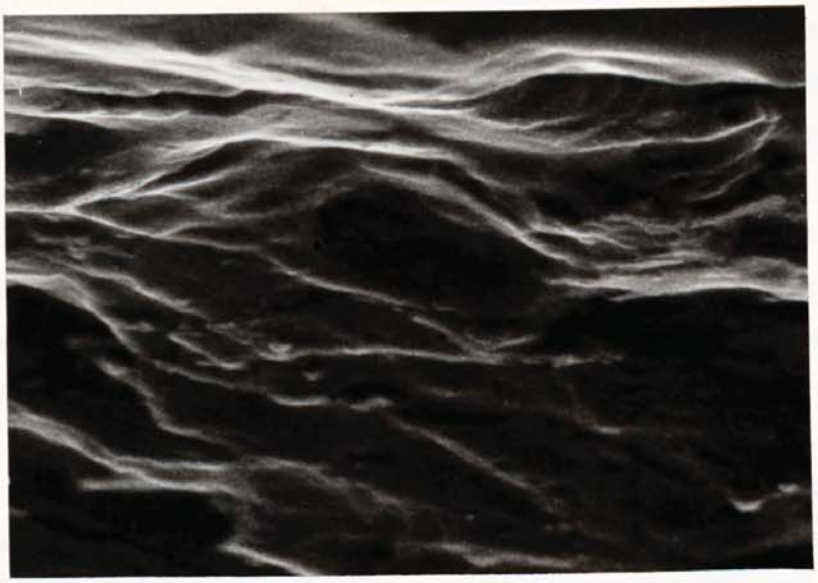

Figure 4.7. Unoxidised pyrite surface after cleaving. (Width of field = 60μm, magnification = 1680x)

The brown tarnish is probably caused by iron oxides and hydroxides. The nature of the blue colouration is uncertain, but may be related to either the formation of sulphates on the surface, or alternatively related simply to the thickness of the oxidised layer and the consequent interference of the reflected light transmitted through the oxidants.

Under the optical microscope, the surface does not appear to have any physical topography, but this can be seen using the SEM. For comparison with further SEM photographs, an unoxidised cleaved pyrite surface is shown in figure 4.7. Figure 4.8. shows a cleaved surface of pyrite oxidised by ammonium hydroxide, the strongest oxidant (as determined spectroscopically). The oxidation products occur as scales (peeling off the surface) and clusters of oxidation products. The surface components appear mainly amorphous, and the products form over large areas of the sample surface.

With regard to the colour change observed in the photomicrograph (fig. 4.6.) the SEM photographs of similar areas show increased formation of oxidation products in the 'blue' zones. Within these zones, there is evidence of formation of rhombic crystals, of up to 10μm in length, as shown in figure 4.9 (after sulphuric acid oxidation). These are probably sulphates, since these are most likely to show such crystal forms, whereas the oxides etc. tend to be amorphous.

No determination of sulphur, inferred to be present in the XPS spectra, was made from these surfaces using the scanning electron microscope, although on other sulphide minerals it may be postulated from the forms on the surfaces.

The SEM photographs shown are for cleaved surfaces, although polished surfaces show similar oxidation products, although with reduced topography. Considering the pyrite surfaces, the topography determined from the SEM photographs is greater than the depth of spectroscopic analysis. The consequence of this, is the detection of oxidised phases in localised areas, with some areas of the surfaces showing little alteration. For this reason, it is not possible to infer layering characteristics from the pyrite surfaces.

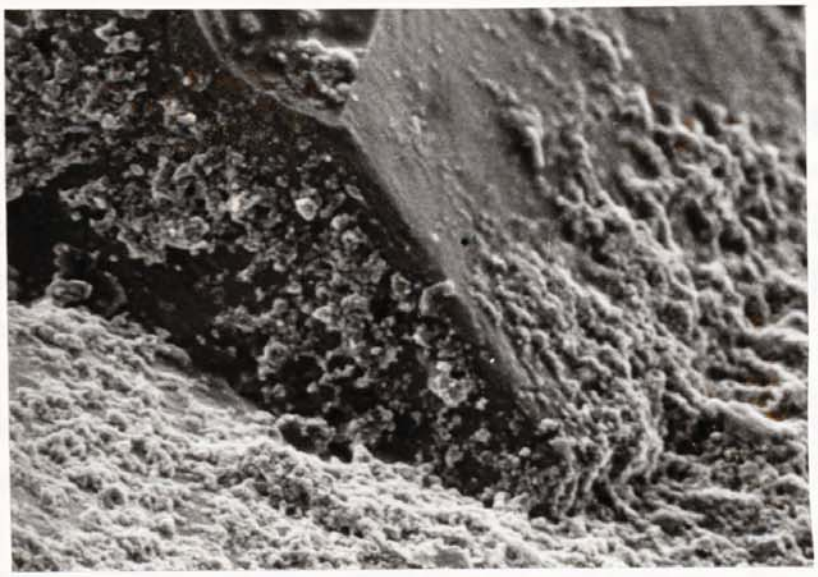

Figure 4.8. SEM photograph of a cleaved pyrite surface oxidised by ammonium hydroxide. (Width of field = 240μm, magnification 420x)

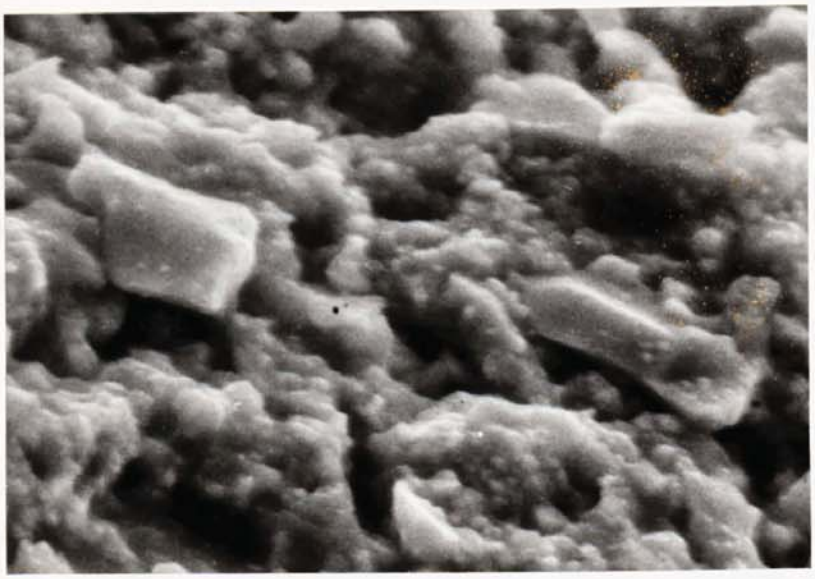

Figure 4.9. Evidence for the formation of crystalline forms within the largely amorphous oxidised layer of a cleaved pyrite surface oxidised by ammonium hydroxide. (Width of field = 24μm, magnification = 4200x)

4.10. Interpretation and Discussion.

The interpretation of the altered pyrite surfaces in terms of the XPS analyses, showed a range of products, that are a function of the strengths and pHs of the oxidants. The AES analyses revealed surfaces that were limited in depth of oxidation, and which showed in some cases, evidence of partial layering, as indicated in figure 4.1b. Consequent with the limited oxidation the analyses by CEMS failed to determine any oxidants on the sample surfaces.

The oxidised phases on the pyrite surfaces were compared to the thermochemically predicted products of oxidation as interpreted using a partial pressure diagram (Figure 4.10.) and an Eh/pH diagram (Figure 4.11.). The Eh/pH diagram is constructed with fixed concentrations of dissolved species, however these may differ in the oxidising solutions. In particular, the concentration of dissolved sulphur could be expected to be much lower, thus decreasing the stability field of elemental sulphur. Some phases are less affected by dissolved species concentrations, and it can be shown that the stability zones of certain phases are confined to fixed conditions (eg Fe_3O_4 in alkaline solutions), and these were used to aid the determination of the iron hydroxides/oxides present.

In these diagrams, FeOOH is thermodynamically unstable with respect to Fe_2O_3, but, as indicated by natural samples (Ramdohr, 1980) FeOOH is undoubtedly a product of pyrite oxidation. A similar problem occurs because, according to the Eh/pH diagram, Fe_3O_4 is unstable in acid environments; however, in the oxidised subsurface the conditions might have been such that Fe_3O_4 is stable. This is shown by its stability in terms of partial pressure diagrams, and the limitation of the oxidising effect of solutions on the sub-surface, due to sub-surface oxidation being largely a diffusive process. In view of the surface compositions proposed from the XPS spectra in table 4.3. it appears that there was a major component of Fe_3O_4 or metastable iron oxide ($Fe_{1-x}O$) in all of the altered surfaces.

The sulphur phases are inter-related in the surfaces; as the oxidation extent increases (shown by a decrease in the pyrite content of the surface) the proportion of sulphates also increases, and

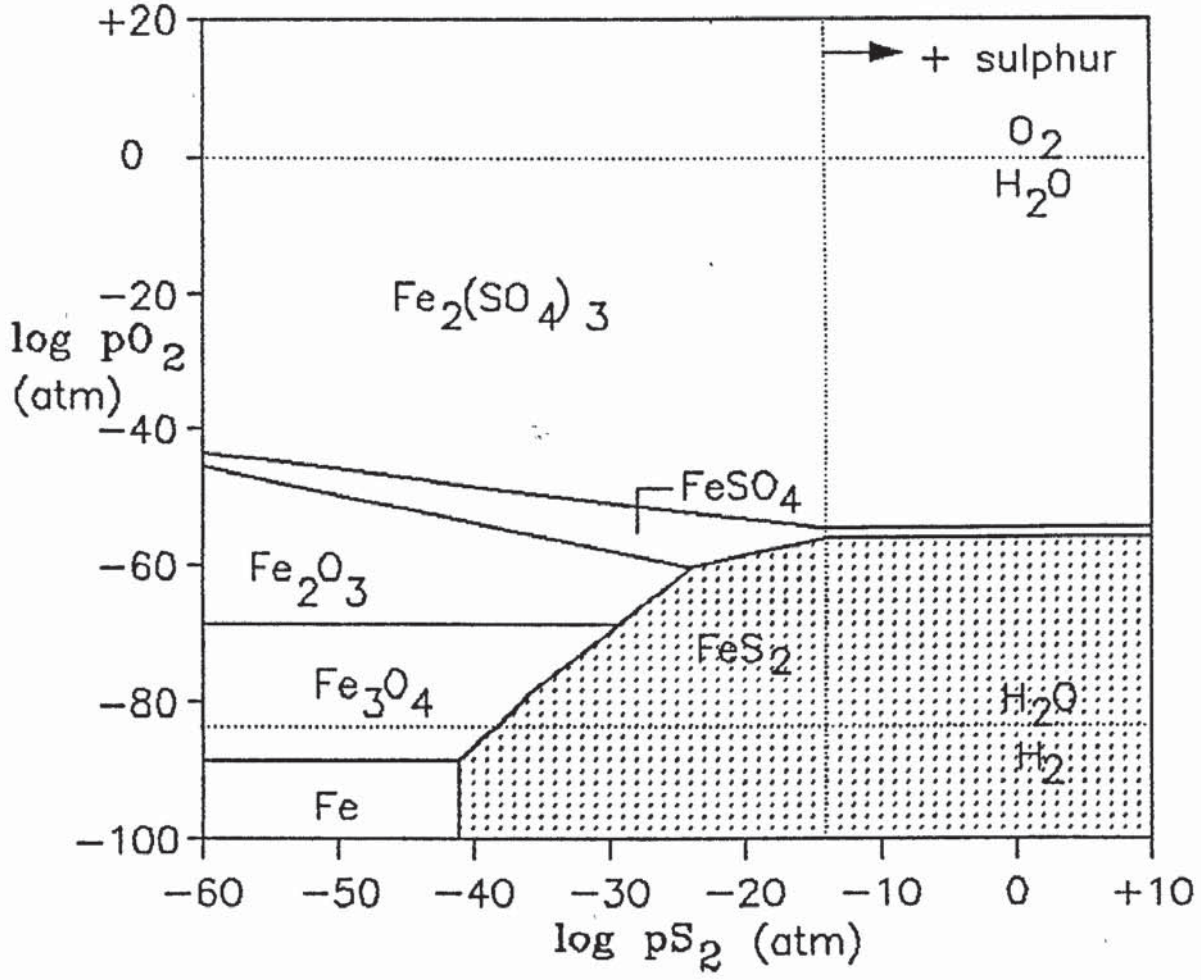

Figure 4.10. Partial pressure diagram (log pO_2/log pS_2) for oxidised pyrite. (Equations and free energies of formation for the component phases contained in Appendix 4.)

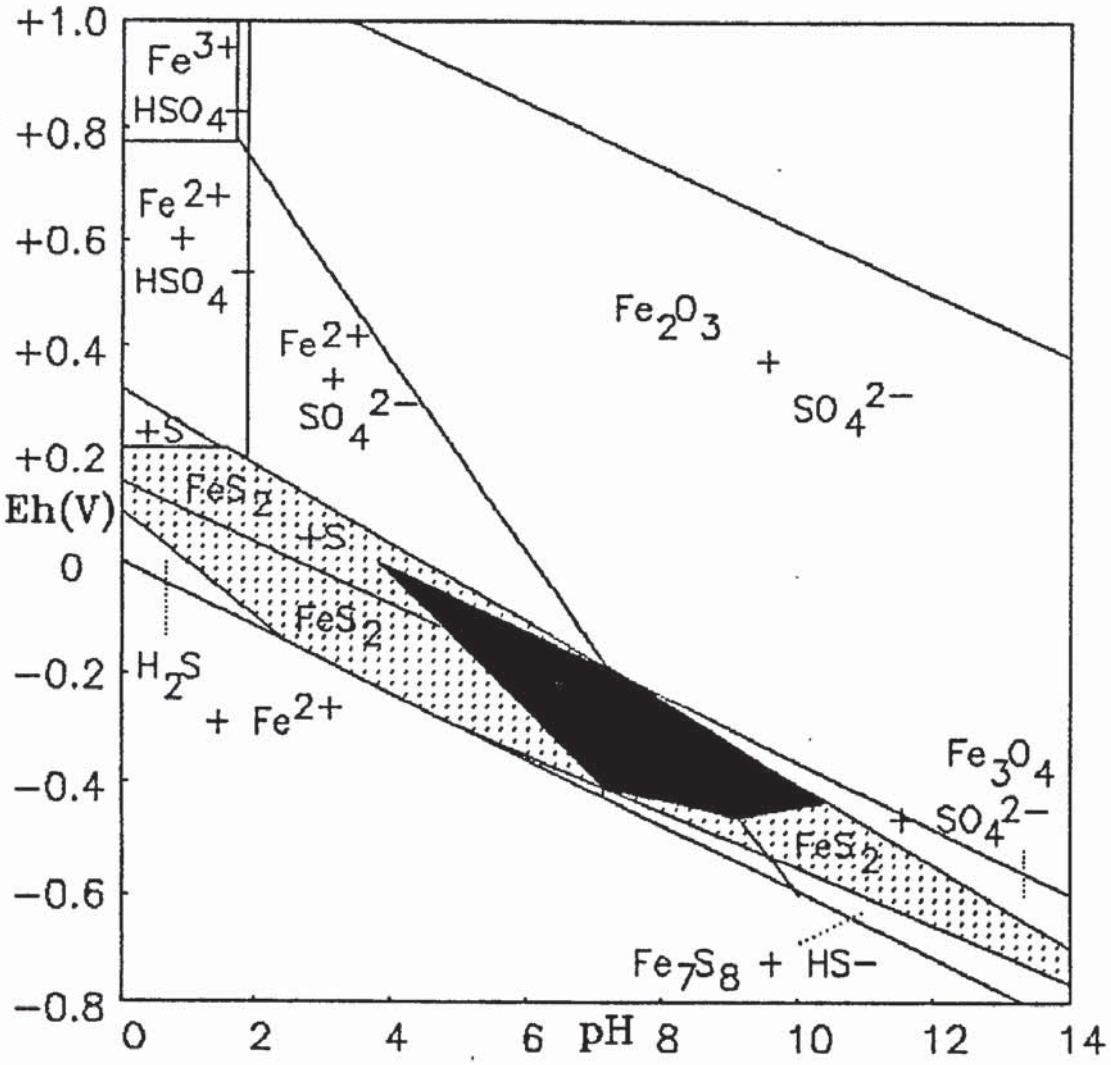

Figure 4.11. Eh/pH diagram for oxidised pyrite with respect to pyrrhotine (Fe_7S_8) and the oxidised phases. The phase boundaries and the shaded area were determined for log[Fe]=-6 and log[S]=-1, and the filled area for log[Fe]=-6 and log[S]=-6. (Equilibria and free energies for the phases contained in Appendix 4.)

significantly this is associated with a decrease in both sulphites (and thiosulphates) and elemental sulphur. The sum of sulphur-containing oxidised phases increases with the increased oxidation.

Treating the oxidation of pyrite surfaces in general terms, the oxidation is observed to be slow in anhydrous environments. In neutral solutions the oxidation rate increases, but not to a significant extent. With reference to Eh/pH diagrams this is expected because pyrite is predicted to be most stable in such solutions. In acid solutions, pyrite oxidises further, and with respect to oxidation to a similar extent in other media, shows an increase in both sulphate and sulphur formation. The most effective oxidation occurs in alkaline solution, e.g. one containing ammonium hydroxide.

Considering the oxidation of pyrite in terms of acid and the alkali oxidants; in sulphuric acid the initial oxidation of the pyrite surface is probably by hydrogen ion attack;

$$xFeS_2 + yH_2O + (4x-2y)H^+ + (4x-2y)e \rightarrow Fe_xO_y + 2xH_2S$$

$$FeS_2 + yH_2O + (4-y)H^+ + (4-y)e \rightarrow Fe(OH)_y + 2H_2S$$

$$FeS_2 + 2H_2O + H^+ + e \rightarrow FeOOH + 2H_2S$$

and in alkaline solution, by hydroxyl ions;

$$xFeS_2 + yOH^- + (2x-y)H^+ + (4x-2y)e \rightarrow Fe_xO_y + 2xHS^-$$

$$FeS_2 + yOH^- + 2H^+ + (4-y)e \rightarrow Fe(OH)_y + 2HS^-$$

$$FeS_2 + 2OH^- + H^+ + e \rightarrow FeOOH + 2HS^-$$

After oxidation of pyrite by ammonium hydroxide, the Auger analyses show no change in the minimal nitrogen content detected with respect to pyrite oxidised by other media, indicating that ammonium ions were unlikely to have initiated the oxidation.

In aqueous solutions, sulphates are easily dissolved, but the presence of the sulphates in aqueous environments suggests an oxygenation of pyrite in both acid and alkali solutions.

$$FeS_2 + 2O_2 \rightarrow FeSO_4 + 0.5S_2$$

Another point raised by the presence of sulphur in alkaline solutions, and sulphates in aqueous oxidation, is the role played by the subsurface in allowing phases to form where, if they were in contact with the solution, they would be unstable. The processes leading to this are discussed in more detail in Chapter 10, along with further discussion on the mechanisms and characteristics of pyrite oxidation, presented with respect to the alteration observed on other mineral surfaces. A general view of iron sulphide stability with respect to hexagonal and monoclinic pyrrhotine is given in section 5.10.

CHAPTER 5.

HEXAGONAL AND MONOCLINIC PYRRHOTINE

5. Hexagonal and Monoclinic Pyrrhotine.

5.1. Introduction.

The pyrrhotines (approximate composition range FeS to Fe_7S_8) have been observed in many ore associations, often as major minerals (Ramdohr, 1980; Craig & Vaughan, 1981). In this investigation, hexagonal pyrrhotine ($\simeq Fe_9S_{10}$) and monoclinic pyrrhotine ($\simeq Fe_7S_8$) were selected in order to study the surface oxidation characteristics of this group of minerals.

Although similar in composition and crystal structure, the stabilities of hexagonal and monoclinic pyrrhotine are markedly different. Both for this reason, and because of their common occurrence, they have been the subject of many investigations concerning their stabilities (Carpenter & Desborough, 1964; Desborough & Carpenter, 1965; Arnold, 1969; Morimoto et al., 1975; Kissin & Scott, 1982; including a review of work on the iron-sulphur system by Power & Fine, 1976). The pyrrhotines exhibit variable stoichiometry which is due to site ordering and vacancies within a hexagonally close-packed structure. Crystallographically, the monoclinic and hexagonal pyrrhotines show 4C and 5C (or 4.94C) structures respectively. The 4C structure has the greater concentration of site vacancies.

As shown by Kissin & Scott (1982), and others, the stability field of monoclinic pyrrhotine is at low temperatures (stable at room temperature, maximum thermal stability $\simeq$254°C) and hexagonal pyrrhotine is a higher temperature phase (minimum thermal stability varying between 100 and 220°C as reported by Nakazawa & Morimoto, 1971).

The relative instability of hexagonal pyrrhotine at room temperature is suggested by the mineralogy of natural ores in which it has altered to monoclinic pyrrhotine, or, in supergene environments, to pyrite and marcasite. The ordering of the structure in the hexagonal to monoclinic pyrrhotine transformation suggests the greater instability of hexagonal pyrrhotine at room temperature. Thus,

during laboratory oxidation hexagonal pyrrhotine would be expected to be more reactive.

5.2. Previous work.

Pyrrhotine oxidation has been studied previously on a range of naturally occurring samples under various oxidation conditions. Ramdohr (1980) reports the natural oxidation of pyrrhotines to be accompanied by sulphur enrichment, leading to pyrite and marcasite formation and associated magnetite and iron sulphates. Alteration lamellae formed as result of compositional variations in the samples, and the formation of aggregate replacement fabrics are also reported.

Vanyukov & co-authors have studied the oxidation of pyrrhotine, as noted in abstracts of papers available only in Russian (Vanyukov & co-authors, 1977; 1978a; 1978b; 1979). These report the formation of oxide films that limit the oxidation, leading to the coalescence of oxide spheres. The oxidation of finely milled pyrrhotines is reported to proceed by an oxidation of the surfaces followed by a contraction of the original sulphide nuclei. Iron diffusion through the oxide layer was considered to be the rate determining process in oxidation. At high temperatures (400 - 600°C) the products were reported to be hematite and magnetite, with no sulphate formation. The oxidation of a monoclinic pyrrhotine in a fluidised bed, was reported to produce Fe_2O_3, Fe_3O_4, FeO, FeS_2 and $FeSO_4$.

Steger & Desjardins (1978) used x-ray diffraction and chemical methods to determine the oxidation products of monoclinic pyrrhotine (in a temperature/humidity chamber at 52°C) and concluded the major products to be goethite and elemental sulphur, with ferric sulphate present as a minor Fe^{3+} component. Steger (1980) reported that pyrrhotine under similar conditions produced a predominance of FeOOH and ferric oxides, and also sulphates. In the case of sulphates they were assumed to form via intermediary thiosulphate..

Pyrrhotines have been investigated spectroscopically in previous work, but not in detail. Clifford et al. (1975) inferred that after grinding and flotation, XPS spectra indicate sulphate formation to be predominant. Buckley & Woods (1985a) also used XPS to characterise

pyrrhotine oxidation. After exposure to air the surfaces indicated the presence of iron hydroxy-oxide, sulphates and elemental sulphur. In aqueous solutions, Buckley & Woods (1985b) suggested the major products to be iron oxides and sulphates, and the possibility of polysulphide formation was considered. Buckley & Woods (1985a&b) used the term 'metal-deficient sulphide' to account for the consequent metal depletion as a result of the formation of oxidised phases.

5.3. Characterisation of the pyrrhotines used in this study.

For this investigation, pyrrhotines were selected that appeared to be, as far as possible, compositionally homogeneous. Due to problems in synthesizing homogeneous pyrrhotines, the sulphides used were both natural, and were supplied by the British Museum of Natural History (hexagonal pyrrhotine BM 57565 from Beer Alston, Devon and monoclinic pyrrhotine BM 1910,497 from Morro Velho, Minas Geraes, Brazil).

Initial characterisation by x-ray diffraction using previous data from Graham (1969), Morimoto et al. (1975) and the JCPDS powder data file to identify the pyrrhotines, showed the phases to be monomineralic 5C hexagonal pyrrhotine and 4C monoclinic pyrrhotine. Further confirmation was derived from electron microprobe analyses of several points on polished sample surfaces. For each pyrrhotine, consistent measurements were obtained as shown in table 5.1.

Table 5.1. Bulk characterisation of the pyrrhotines.

Pyrrhotine	Fe (At %)	S (At %)	Impurity
Hexagonal 5C	47.19 +/- 0.21	52.54 +/- 0.29	<0.20% Ni
Monoclinic 4C	46.26 +/- 0.26	53.54 +/- 0.34	<0.17% Ni

	Fe_xS	FeS_x		
Hexagonal 5C	0.898	1.114	89% Fe_9S_{10}	11% Fe_7S_8
Monoclinic 4C	0.864	1.157	98% Fe_7S_8	2% FeS_2
(Pure Fe_9S_{10}	0.900	1.111)		
(Pure Fe_7S_8	0.875	1.143)		
(Pure FeS_2	0.500	2.000)		

5.4. Optical Properties.

The spectral reflectance data obtained for hexagonal and monoclinic pyrrhotine both show slight bireflectance, more evident in the monoclinic pyrrhotine, in agreement with the spectra for monoclinic pyrrhotine in the IMA/COM data file (Stanley & Criddle, 1986). The data recorded in table 5.2. show average reflectance values for unaltered pyrrhotines and pyrrhotines oxidised by various methods. Photomicrographs and SEM photographs of altered hexagonal and monoclinic pyrrhotine surfaces are shown in figs. 5.7 to 5.14.

Table 5.2. Reflectance measurements for unoxidised pyrrhotines and for surfaces after oxidation by various methods.

Oxidation method	Reflectance (R%) 470nm	546nm	589nm	650nm	ΔR(*)
Monoclinic pyrrhotine.					
Unoxidised (R^o)	33.0	38.1	40.7	43.2	
Air/oxygen (150°C)	31.2	35.8	37.9	41.1	5.9
Steam	28.1	33.2	35.4	38.2	13.0
H_2O_2	20.2	25.9	31.4	35.1	27.4
H_2SO_4	19.6	23.4	25.0	27.3	38.5
NH_4OH	9.8	10.5	10.0	8.3	75.9
Electrochemical (0.8V)	12.1	9.8	7.6	6.3	76.9
Hexagonal pyrrhotine.					
Unoxidised (R^o)	31.8	34.2	37.5	39.9	
Air/oxygen (150°C)	27.3	30.9	35.1	38.2	8.3
Steam	25.7	30.6	33.6	36.7	11.7
NH_4OH	18.2	21.7	23.1	25.4	38.4
H_2SO_4	11.1	8.9	8.2	7.6	75.0
H_2O_2	6.3	7.2	7.4	7.6	81.1
Electrochemical (0.8V)	5.7	6.3	5.2	5.1	84.5

* ΔR = average change in reflectance = $(R^o-R')/R^o \times 100$

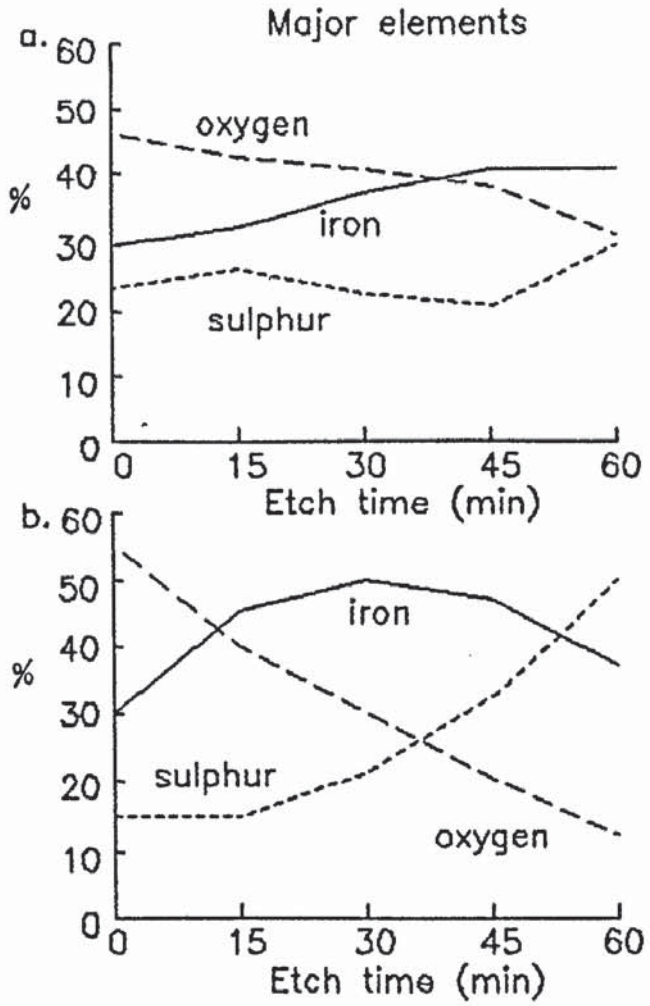

Fig. 5.1. Auger depth profiles for hexagonal pyrrhotine oxidised by (a) sulphuric acid and (b) ammonium hydroxide.

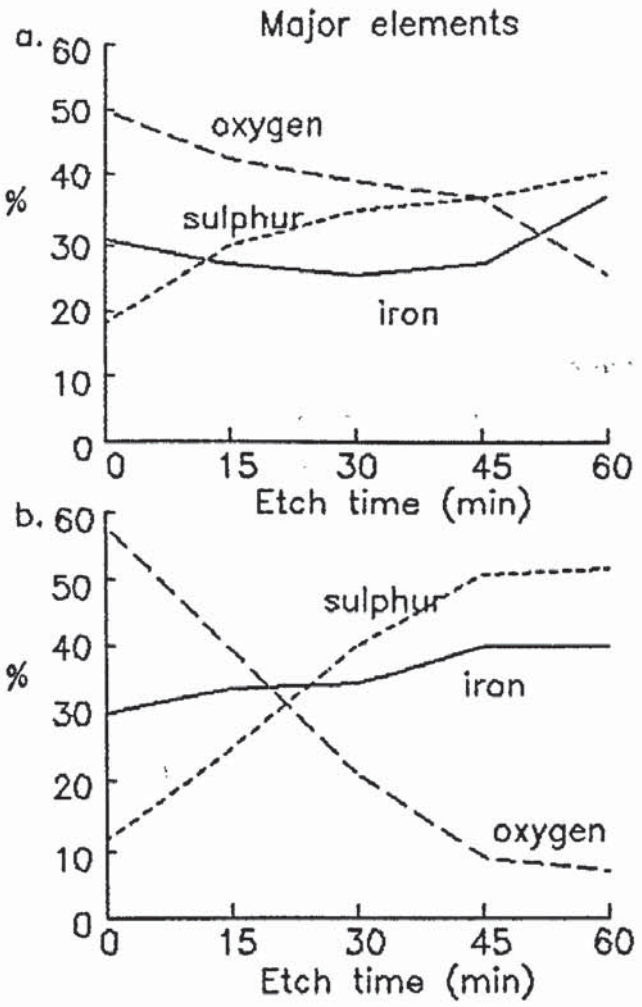

Fig. 5.2. Auger depth profiles for monoclinic pyrrhotine oxidised by (a) sulphuric acid and (b) ammonium hydroxide.

5.5. Auger Electron Spectroscopy.

Auger electron spectroscopy was used to determine elemental depth profiles of the oxidised pyrrhotines. Assuming the stoichiometric proportions of iron and sulphur in the pyrrhotines to be as indicated in table 5.1., the Auger profiles would be expected to converge to these values in the unoxidised sub-surfaces.

Figure 5.1. shows profiles of hexagonal pyrrhotine surfaces oxidised by sulphuric acid (5.1a.) and ammonium hydroxide (5.1b.). Depth profiles are shown in Fig 5.2. for monoclinic pyrrhotine oxidised using the same two methods.

The oxidation of both pyrrhotine types by sulphuric acid is characterised by the presence of a considerable oxygen concentration at depth in the surfaces. Conversely, the oxidation in ammonium hydroxide produced a surface where oxygen decreases rapidly width depth. It would appear that sulphuric acid causes a depth of oxidation much greater than 60Å (as determined from the Auger depth profiles). Although the depth profiles for the pyrrhotines oxidised by NH_4OH show less oxidation, oxygen is still a major component after 60 minutes of sputtering.

There are several factors that are common to the Auger profiles obtained for the pyrrhotines. At the immediate surface the relative oxygen proportions of both hexagonal and monoclinic pyrrhotine oxidised by a particular method are similar, but at depth it is evident that the oxygen-containing phases are present to greater depths in the hexagonal pyrrhotine surfaces. Also observed is a generally greater sulphur-concentration in the surfaces of monoclinic pyrrhotine with respect to hexagonal pyrrhotine. This is partially a response to the greater oxygen content of the hexagonal pyrrhotine lowering the proportion of sulphur, although it is more a result of sulphur-rich compounds forming in the monoclinic pyrrhotine surface.

In general, the depth profiles tend to show uniform decreases and increases in elemental concentrations, suggesting an oxidation without layering. A convergence to the atomic proportions of iron and sulphur expected in the bulk pyrrhotines is observed, evidence negating a sputter-induced reduction of the pyrrhotines.

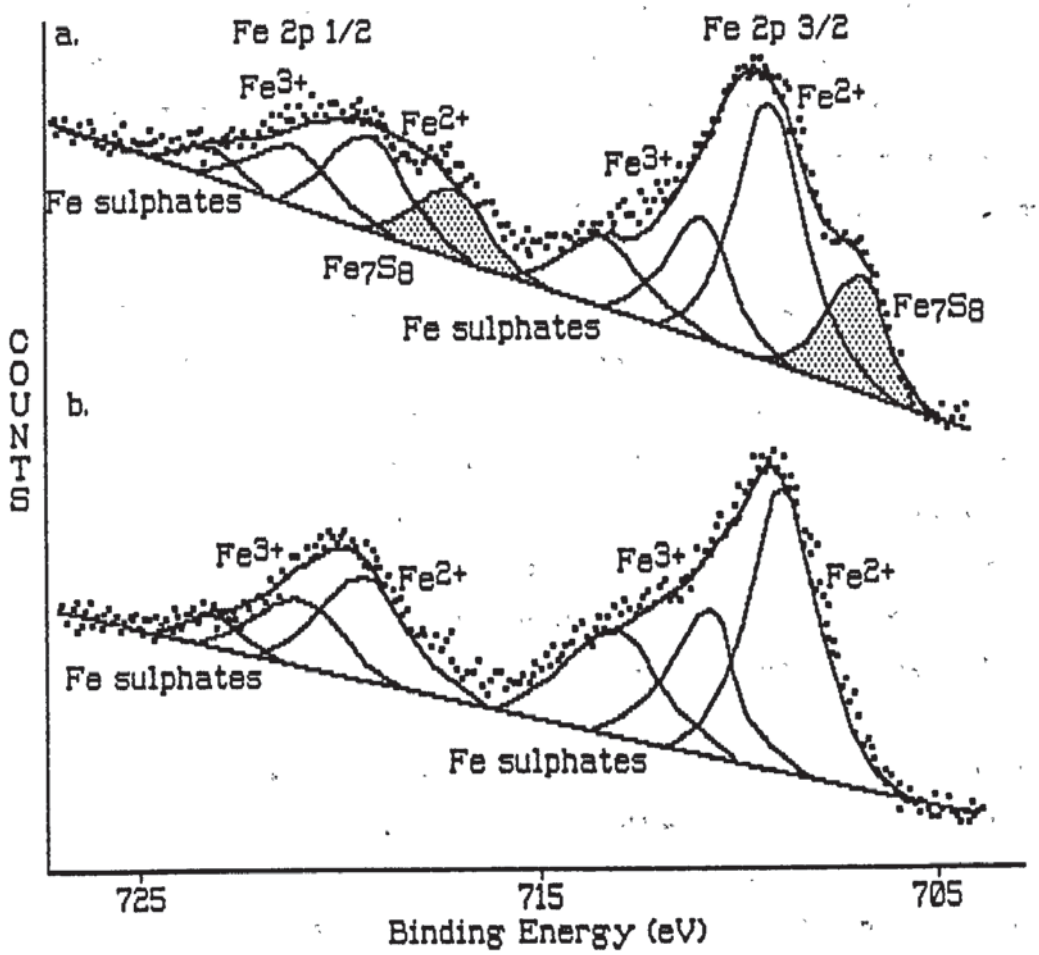

Fig. 5.3. Fe 2p (1/2 & 3/2) x-ray photoelectron spectra showing comparative oxidation of (a) monoclinic and (b) hexagonal pyrrhotine oxidised by sulphuric acid.

5.6. X-ray Photoelectron Spectroscopy.

As indicated by the Auger and reflectance analyses, the oxidised surfaces of both hexagonal and monoclinic pyrrhotine were considerably altered. The contamination of these surfaces was limited and the surfaces were analysed without prior sputtering to remove contaminants.

In preliminary work, the binding energies of relevant energy levels were calculated for hexagonal and monoclinic pyrrhotines. For both minerals the Fe 2p(3/2) binding energies are 707.1eV, and S 2p binding energies are 161.4eV. The Fe 2p(3/2) binding energies are comparable to the value of 'near 707eV' determined by Buckley & Woods (1985a&b).

Fig. 5.3. illustrates comparative Fe 2p(3/2) spectra observed for monoclinic and hexagonal pyrrhotine oxidised by sulphuric acid. The spectra indicate the greater oxidation of hexagonal pyrrhotine, evident from the lack of pyrrhotine in the analysed surface. As for pyrite (section 4.6.), no observable shake-up phenomena were identified in the pyrrhotine spectra. These spectra indicate extensive oxidation, and although most of the other spectra show less evidence of extensive oxidation, the pyrrhotines are heavily oxidised by all oxidation methods.

A range in the degree of oxidation is shown by the sulphur 2p spectra in fig. 5.4. for pyrrhotines oxidised by ammonium hydroxide and after electrochemical oxidation. The increase in oxidation, as observed between oxidants, is accompanied by both an increase in sulphate (or oxy-sulphate) and a comparable increase in the sulphur (0) peaks. This sulphur (0) peak is interpreted as a result of elemental sulphur formation, and although strictly there may be a contribution from polysulphides or thionates, this can be discounted because of the lack of evidence from the iron 2p(3/2) and oxygen 1s spectra for such compounds.

In the sulphur 2p spectra of hexagonal pyrrhotine oxidised by sulphuric acid there is evidence of a sulphide peak, not shown in the Fe 2p(3/2) spectra, which indicates the greater escape depths of the

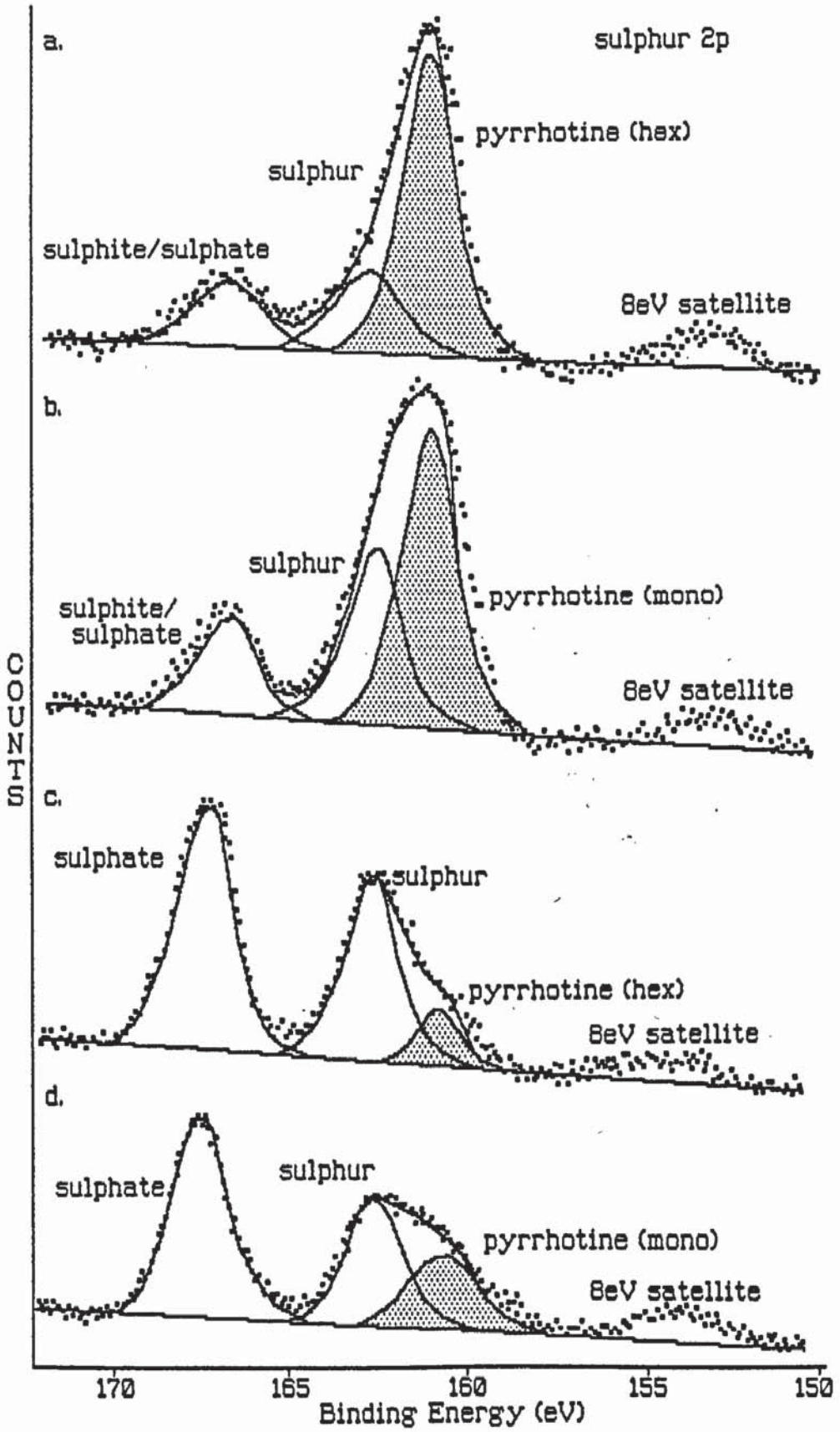

Fig. 5.4. Sulphur 2p x-ray photoelectron spectra for pyrrhotines oxidised in ammonium hydroxide (a & b) and by electrochemical oxidation (c & d).

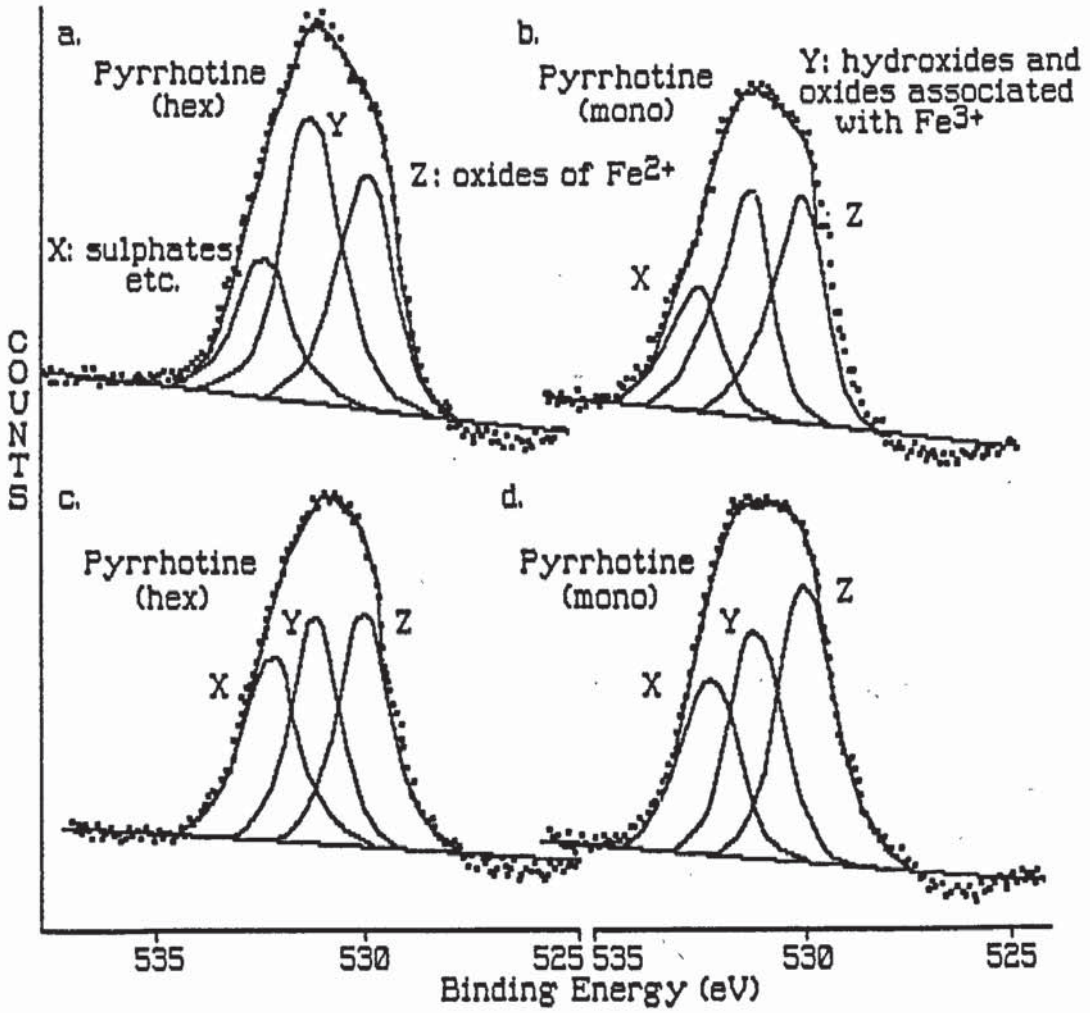

Fig. 5.5. Oxygen 1s x-ray photoelectron spectra for hexagonal and monoclinic pyrrhotine oxidised by air/oxygen at 150°C (a & b) and by hydrogen peroxide (c & d).

sulphur 2p photoelectrons resulting from their higher kinetic energies.

The oxysulphate phase observed in the spectra of pyrrhotines oxidised by steam and by air/oxygen at 150°C indicate binding energies consistent with the formation of sulphites or thiosulphates. Since the binding energies of the sulphites and thiosulphates are not clearly defined a definite identification cannot be made. In NH_4OH oxidation a peak with a slightly lowered binding energy from that of sulphates is observed, and may result from both sulphates and sulphites.

The pyrrhotine oxidation observed from the oxygen 1s spectra is in agreement with the interpretations of the other spectra. In fig. 5.5. oxygen 1s spectra are shown for pyrrhotines oxidised by air/oxygen at 150°C in a furnace and by hydrogen peroxide. The oxygen spectra observed show a lot of variation, but similarities are observed for hexagonal and monoclinic pyrrhotines oxidised by the same method.

5.7. Compositional Interpretation of the XPS and AES spectra.

Surface compositions were estimated from the x-ray photoelectron spectra and the Auger depth profiles. An interpretation, in terms of the specific valence states is given in table 5.3., arranged in order of the oxidation extent determined from the pyrrhotine remaining in the analysed layer.

The values shown in table 5.3. represent the bulk composition for a surface layer of approximately 10-15Å depth, as determined by the depth resolution of XPS.

It is possible to further characterise the actual surface compounds present. With regard to the detection of S (0) in the surface, it is interpreted as elemental sulphur. Spectroscopically, this is justified since there is no indication of polysulphide formation in the Fe 2p(3/2) spectra (that would be indicated by a sulphide and sulphur peak shifts), and the oxygen spectra give no evidence for the presence of thionates. (From chemical analyses it

was observed that when finely powdered hexagonal or monoclinic pyrrhotine were reacted with hydrogen peroxide, there was a violent reaction, caused partly by a release of oxygen and partly by the rapid breakdown of pyrrhotine. On completion, the remaining oxidised pyrrhotine was covered by a layer of sulphur, providing further evidence for an elemental sulphur peak.)

Table 5.3. General surface compositions from XPS/AES analyses (estimated molecular percentages).

	Method of oxidation					
Phase	air/oxygen	NH_4OH	Steam	Elec.	H_2O_2	H_2SO_4
Hexagonal pyrrhotine						
Fe II/III sulphate	-	3.6	-	27.8	26.2	24.0
Fe II sulphite etc.	12.8	3.6	21.3	-	-	-
Fe III (oxides & Fe II hydroxides)	28.3	37.3	25.2	34.2	29.6	23.6
	23.4	24.9	28.4	26.8	30.4	38.2
S (0)	9.6	6.3	10.3	8.2	11.3	12.2
Pyrrhotine - Fe_9S_{10}	25.9	24.3	14.8	3.0	2.5	2.0
	air/oxygen	NH_4OH	H_2SO_4	H_2O_2	Steam	Elec.
Monoclinic pyrrhotine.						
Fe II/III sulphate	-	4.4	20.8	20.6	-	25.5
Fe II sulphite etc.	11.2	4.4	-	-	27.3	-
Fe III (oxides & Fe II hydroxides)	23.8	31.1	21.2	23.7	24.6	33.2
	24.0	25.2	28.5	27.4	17.0	27.2
S (0)	14.4	12.8	13.2	13.0	16.2	7.8
Pyrrhotine - Fe_7S_8	26.6	22.1	16.3	15.3	14.9	6.3

The determination of the Fe^{2+} and Fe^{3+} hydroxides and oxides is complex due to the overlapping peaks. The problems encountered are outlined in the chapter on pyrite (Ch. 4 Sec. 4.7.). Even so, the information in table 5.3. and from the thermochemically predicted phases allow some deconvolution of the relevant spectra. For the hexagonal and monoclinic pyrrhotines, their oxide to hydroxide ratios are similar largely because the oxidation method is responsible for the phases formed on the surface, shown, in particular, in the interpretation of the NH_4OH with an increase in the ferric hydroxide and ferric oxy-hydroxide formation.

A notable anomaly occurs with both pyrrhotines, in regard to their oxidation in sulphuric acid. The x-ray photoelectron spectra show a relative increase in Fe^{2+} with respect to Fe^{3+}, contrary to the expected oxidation of iron to Fe^{3+}. The major component of Fe^{2+} observed, may be a result of oxides forming in a protected sub-surface.

5.8. Conversion Electron Mössbauer Spectroscopy.

The CEM spectra for pyrrhotines show evidence of the oxidised phases, expected from the depth of oxidation observed. These are shown in fig. 5.6. for hexagonal pyrrhotine oxidised by sulphuric acid. Similar oxidation products are determined from the spectra of monoclinic pyrrhotine.

The unoxidised hexagonal pyrrhotine shows two six-peak magnetically split spectra indicative of two iron sites (represented in fig. 5.6. by peaks A & B, which showed a 4:1 ratio in the unoxidised spectrum). After oxidation there was a further contribution to the spectrum observed in the outer peaks of site B (labelled C and C'), with a magnetic splitting of approximately 305 kOe, an isomer shift 0.3mms^{-1}, and quadrupole splitting of 0.3mms^{-1}, and new peaks (D and D') with a magnetic splitting of approximately 450 kOe. Similar measurements for the oxidised phases are obtained from the spectra of monoclinic pyrrhotine. By a comparison of the parameters obtained for the oxidised phases to possible compounds

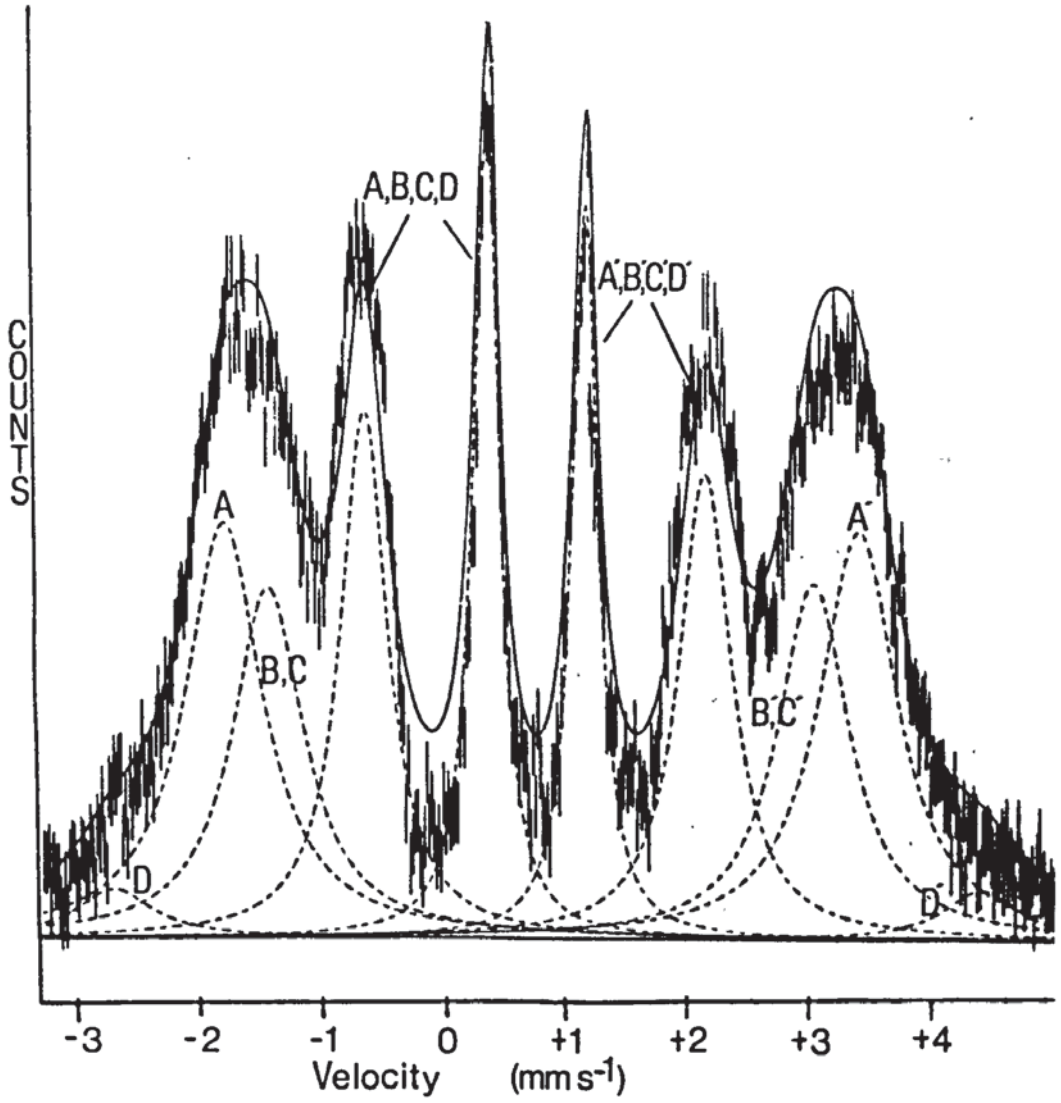

Fig. 5.6. Conversion electron Mössbauer spectrum for hexagonal pyrrhotine oxidised by sulphuric acid. Some peaks are representative of more than one phase or site and are discussed in the text.

(given in appendix 3.) it is suggested that peaks CC' are produced by αFeOOH (goethite) and peaks DD' are produced by Fe_3O_4 (magnetite). This information helps in the identification of the Fe^{2+} and Fe^{3+} oxides and hydroxides that were difficult to confirm from the XPS/Auger data, and this evidence is discussed in section 5.10.

5.9. SEM and optical microscopy.

The evidence from optical microscopy and SEM photography agrees with the information on oxidation of hexagonal and monoclinic pyrrhotines inferred from the spectroscopic techniques, in so far as the depths of oxidation are concerned; however, it is difficult to relate specific phases, determined spectroscopically, to the phenomena observed in these photographs

The hexagonal pyrrhotine exhibits extensive alteration of the surface after oxidation by all the methods used. In figure 5.7. the surface shows evidence of cracking, which, along with further information derived from SEM photographs (eg. figure 5.9.) suggested that the cracking was caused by leaching of the pyrrhotine surface. This is shown by the apparent stability of surfaces covered by alteration products.

Alteration products on the hexagonal pyrrhotine surfaces have caused a range of chemical alteration effects. In figure 5.7. the orange/brown alteration (probably related to oxides and hydroxides) changes to blue oxidation near the surfaces cracking (which is a result of oxidation). Surface oxidation products in these zones (figure 5.9.) are shown to be largely amorphous. The lamellar texture observed may be due to minor compositional differences in the pyrrhotine, resulting from exsolution to monoclinic pyrrhotine (although the electron micro-probe data do not show this).

Similar textures are observed after oxidation by sulphuric acid and by electrochemical methods. The sulphuric acid oxidation gave rise to a surface that was dissimilar to any other sulphide surface investigated. SEM photographs (figure 5.10) exhibited the formation

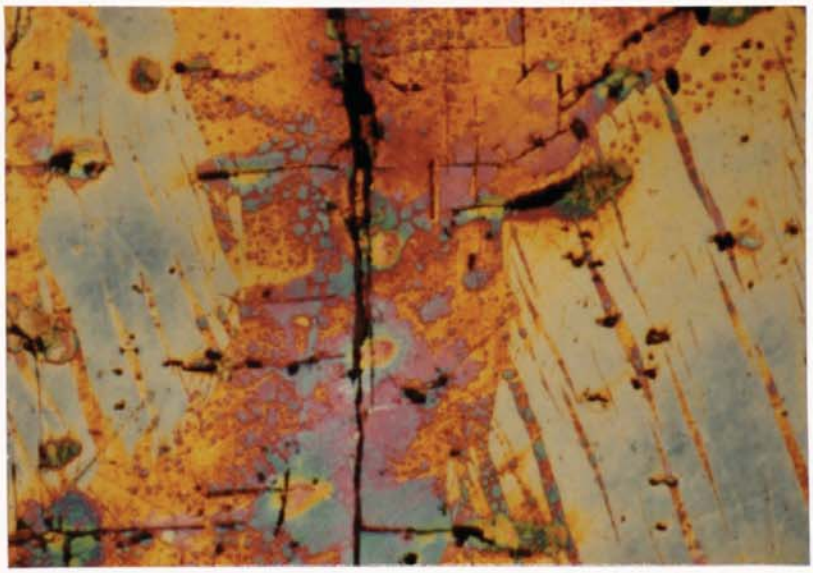

Figure 5.7. Photomicrograph of a hexagonal pyrrhotine surface oxidised by hydrogen peroxide. (Width of field = 1.5mm, magnification = 67x)

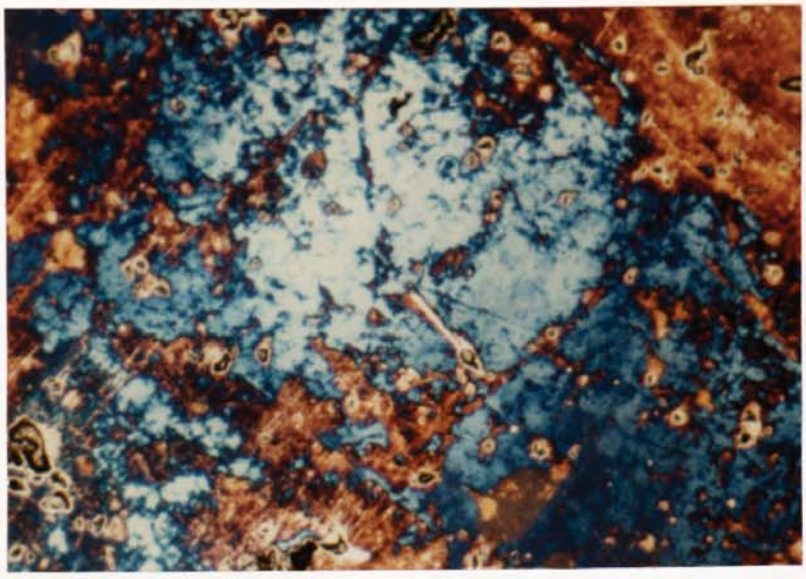

Figure 5.8. Photomicrograph of steam oxidised hexagonal pyrrhotine. (Width of field = 1.5mm, magnification = 67x)

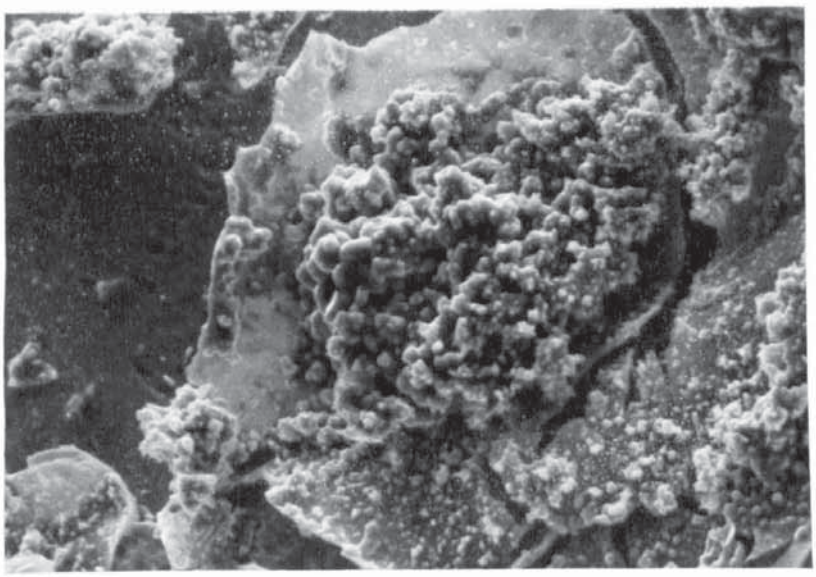

Figure 5.9. SEM photograph of a hexagonal pyrrhotine surface oxidised by hydrogen peroxide. Edge of a fracture zone on an surface that was originally polished. (Width of field = 240μm, magnification = 420x)

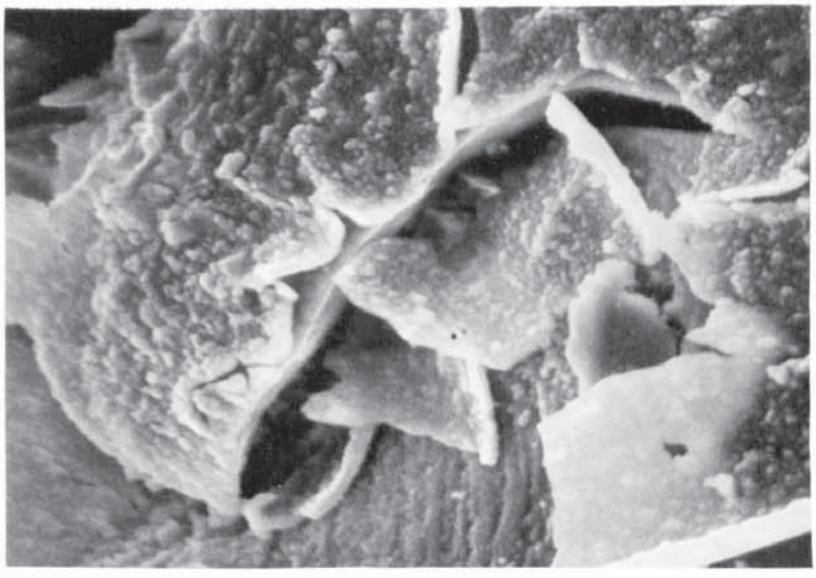

Figure 5.10. SEM photograph of a hexagonal pyrrhotine surface oxidised by sulphuric acid. (Width of field = 60μm, magnification = 1680x)

of an oxidised platy surface. This suggests a process involving sub-surface oxidation and the consequent expansion of these layers producing the topography observed.

The hexagonal pyrrhotine surface after steam oxidation (figure 5.8.) exhibits a uniform brown tarnish that is overlain by 'blue' oxidation products. A similar alteration is observed after ammonium hydroxide oxidation. The blue tarnish is not present after air/oxygen (150°C) oxidation, suggesting it to be related to aqueous oxidation. This may be evidence that the blue colouration is due to a hydrated phase at the surface

The photomicrographs and SEM photographs of monoclinic pyrrhotine suggest that, for the most part, the oxidation is not as extensive as that observed for hexagonal pyrrhotine. Nevertheless, figure 5.11 indicates a surface comparable to that of hexagonal pyrrhotine (figure 5.7.), although there is an absence of cracking. A cracked surface is only observed for the electrochemically oxidised sample of monoclinic pyrrhotine, as shown in figure 5.13.

Also noted is the absence of a blue layer on the monoclinic pyrrhotine oxidised by steam (figure 5.12., with comparison to figure 5.8). In comparing this difference to the spectroscopic results, the only major chemical difference is a variation in the Fe^{2+}:Fe^{3+} ratios of the surface products (1.12:1 for hexagonal and 0.69:1 for monoclinic pyrrhotine), suggesting a far greater Fe^{2+} content in the hexagonal pyrrhotine surface products.

Typically, the monoclinic pyrrhotine showed limited oxidation in most oxidants. The phases formed on the surface were generally aggregates of amorphous phases, the characteristic surface observed shown by the SEM photograph in figure 5.14.

5.10. Interpretation and Discussion.

The characteristics of hexagonal and monoclinic pyrrhotine oxidation involve a rapid alteration of the surfaces by most oxidation methods, and greater overall oxidation observed for the hexagonal pyrrhotine. Comparatively large oxidation depths (in comparison to other sulphides) were indicated by the Auger profiles,

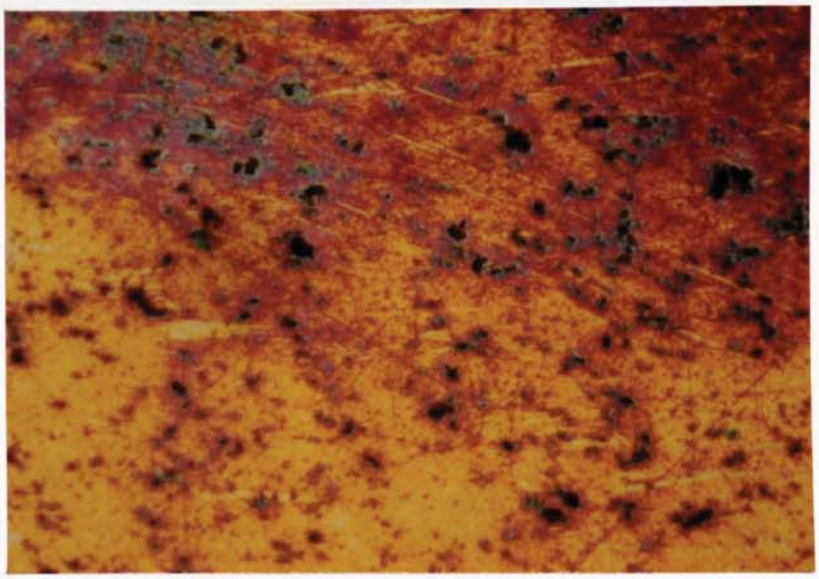

Figure 5.11. Photomicrograph of monoclinic pyrrhotine oxidised by hydrogen peroxide. (Width of field = 1.5mm, magnification = 67x)

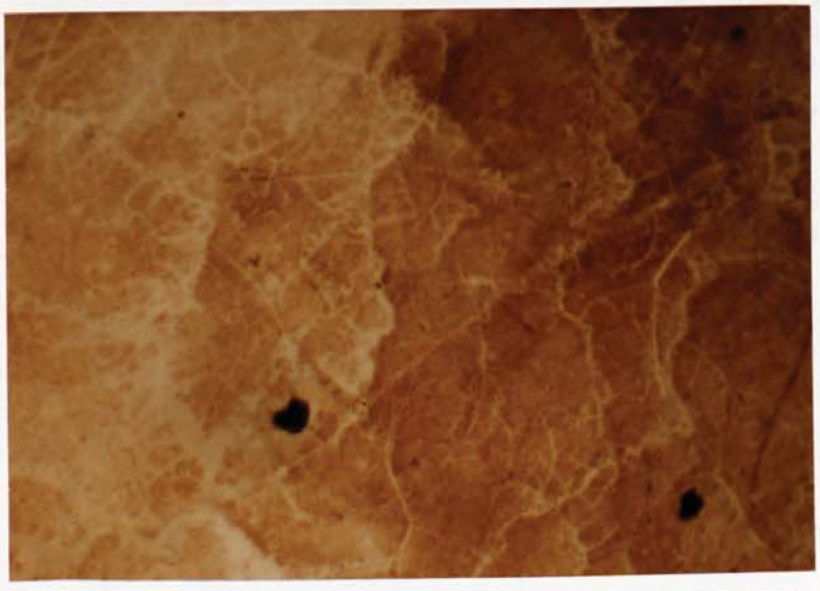

Figure 5.12 Photomicrograph showing the surface of monoclinic pyrrhotine after oxidation by steam. (Width of field = 1.5mm, magnification = 67x)

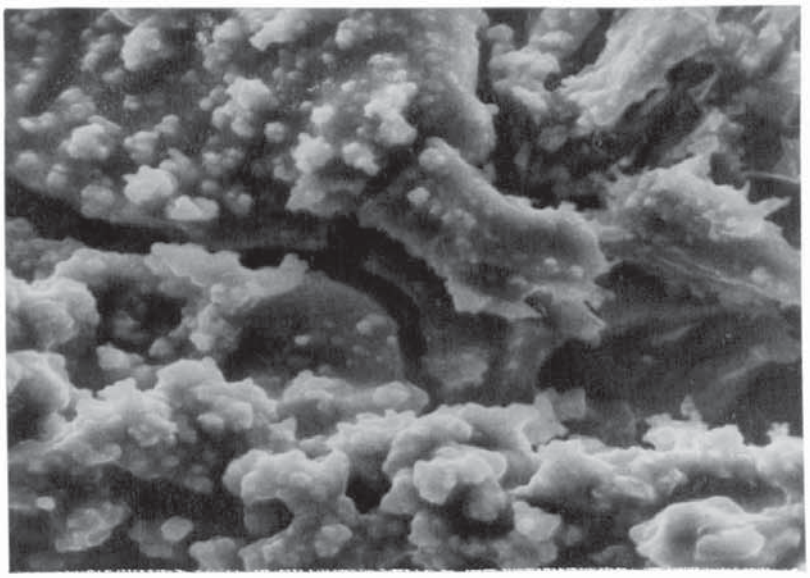

Figure 5.13. SEM photograph of monoclinic pyrrhotine oxidised electrochemically. (Width of field = 60μm, magnification = 1680x)

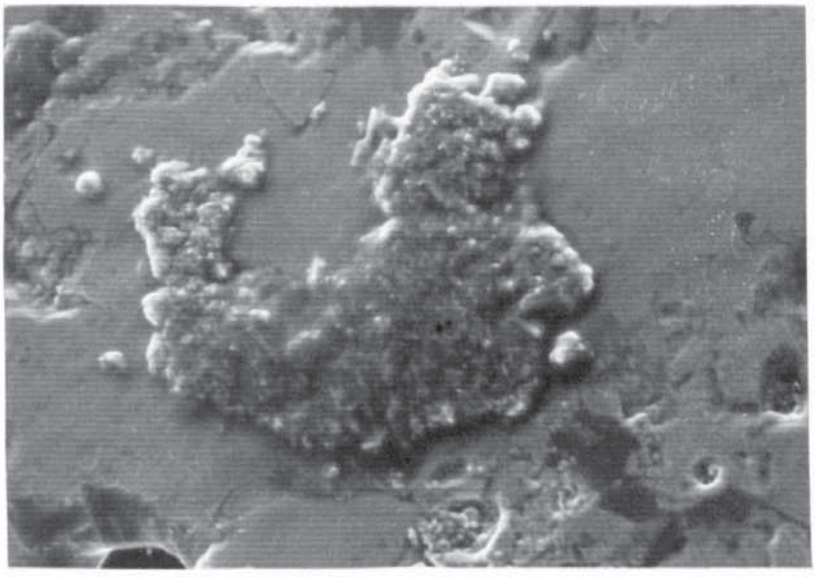

Figure 5.14. SEM photograph of monoclinic pyrrhotine oxidised by ammonium hydroxide. (Width of field = 240μm, magnification = 420x)

suggesting an extensive oxidation. SEM photographs show the formation of oxidised layers on the surfaces, although these may not be directly related to any layering determined spectroscopically. The compositions were suggested by the XPS analyses, which, in conjunction with thermochemical predictions, were used to determine the chemical compositions of the oxidised surfaces.

The thermochemically stable phases are shown by the Eh/pH diagram (illustrated in figure 4.11. of the pyrite chapter) and in the partial pressure diagram shown in figure 5.15. The stability of FeOOH in natural environments as an alteration product of pyrrhotines is accepted, although in these diagrams Fe_2O_3 is shown as the stable phase. From both XPS and Mössbauer analysis, it was shown that the main oxidation products were FeOOH and Fe_3O_4, with associated sulphur and oxysulphates. The iron oxide/hydroxide components suggested above are supported by the greater proportion of Fe^{2+} to Fe^{3+} in most of the surfaces, excepting the ammonium hydroxide oxidation, where ferric hydroxides and oxy-hydroxides are expected to predominate.

Although thermochemical stability is important in determining the chemical products of oxidation, the use of chemical equations to show the reactions involved in the oxidation of iron sulphides is important in explaining the observed extent of oxidation.

The following equations are related the oxidation of the pyrrhotines and of pyrite in both acid and alkali solutions.

$$xFe_nS_m + (2xm-2ny)H^+ + nyH_2O + (2xm-2ny)e \rightarrow nFe_xO_y + xmH_2S$$

$$xFe_nS_m + nyOH^- + (xm-ny)H^+ + (2xm-2ny)e \rightarrow nFe_xO_y + xmHS^-$$

Comparing the oxidation of the pyrrhotines (which show extensive oxidation) to pyrite, the equations can be used to explain the relative degree of oxidation. Using the equations above for the iron sulphides, the electron balance shows the pyrite reaction to be cathodic, whilst the pyrrhotine reaction is an anodic reaction. This

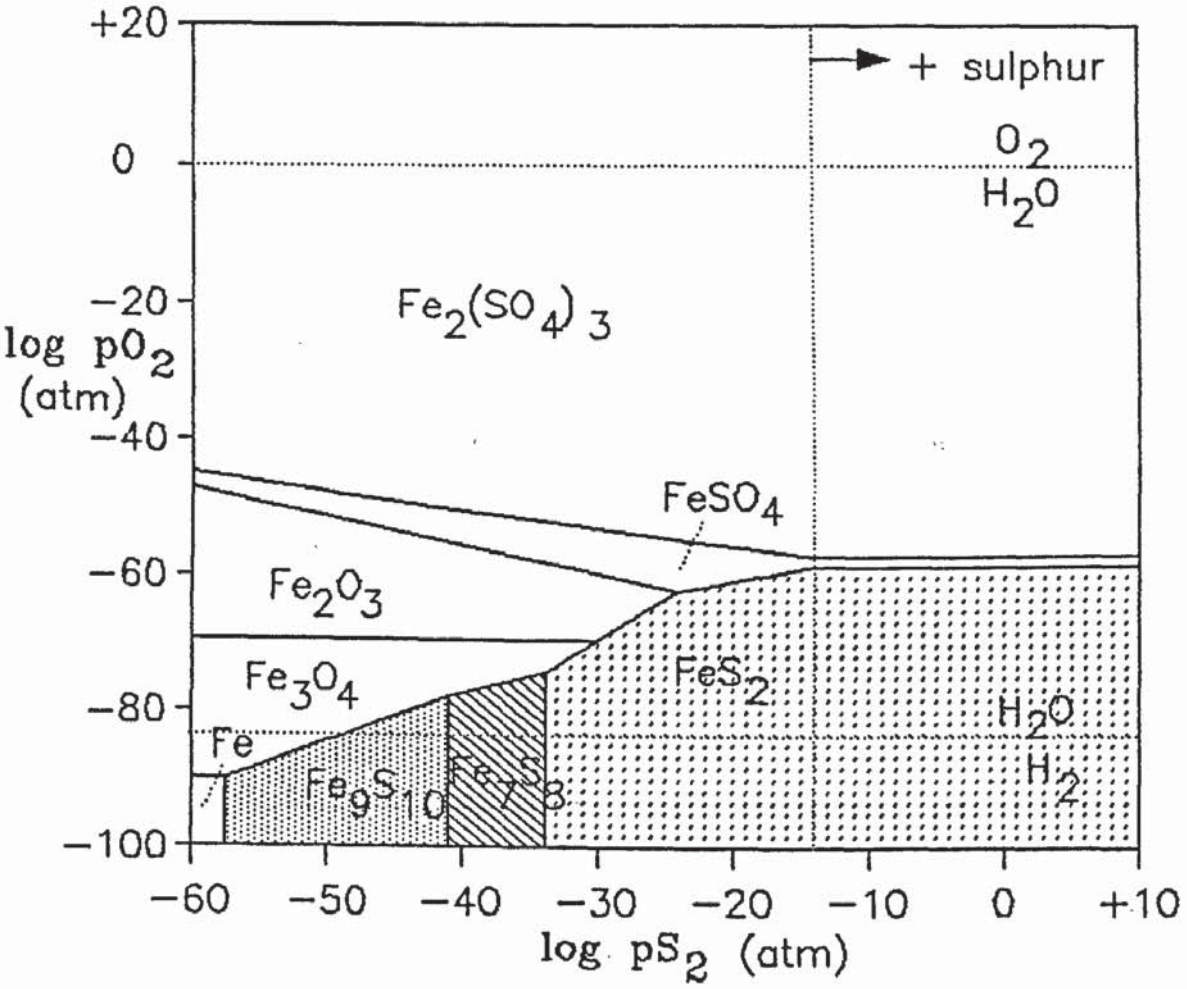

Figure 5.15. Partial pressure diagram (log pO_2/log pS_2) for oxidised hexagonal and monoclinic pyrrhotine, with respect to pyrite. (Equations and free energies of formation for the component phases contained in Appendix 4.)

suggests a greater oxidation for the pyrrhotine since the anodic reaction will be associated with the cathodic reaction of water;

$$O_2 + 2H_2O + 4e \rightarrow 4OH^-$$

The cathodic reduction of water is probably the major driving force at the surface of electrochemical oxidation cells in natural orebodies, and for this reason will affect the electrochemistry of iron sulphide oxidation in natural environments. Applying other equations for the alteration to hydroxides and FeOOH, their formation can also be estimated.

$$Fe_nS_m + (2m-ny)H^+ + nyH_2O + (2m-ny)e \rightarrow nFe(OH)_y + mH_2S$$

$$Fe_nS_m + nyOH^- + mH^+ + (2m-ny)e \rightarrow nFe(OH)_y + mHS^-$$

$$Fe_nS_m + (2m-3n)H^+ + 2nH_2O + (2m-3n)e \rightarrow nFeOOH + mH_2S$$

$$Fe_nS_m + 2nOH^- + (m-n)H^+ + (2m-3n)e \rightarrow nFeOOH + mHS^-$$

For the formation of ferric hydroxide, the reactions of both pyrite and pyrrhotine are anodic in acid solution and the hydroxide would be expected to form. Conversely, in alkaline solutions the oxidation of pyrite is cathodic, whereas the oxidation of pyrrhotine is anodic. The formation of FeOOH would be expected to be cathodic for pyrite and anodic for pyrrhotine.

A further examination of the relative oxidation of hexagonal and monoclinic pyrrhotine to pyrite and other iron-containing sulphides is presented in chapter 10, with respect to the mechanisms of oxidation.

CHAPTER 6.

VIOLARITE

6. Violarite.

6.1. Introduction.

Violarite ($FeNi_2S_4$) is commonly found in the alteration zones of nickeliferous ores, as a secondary sulphide mineral (Ramdohr, 1980; Craig & Vaughan, 1981). Since it exists in supergene environments, violarite can be considered to be stable with respect to the primary sulphides in oxidising conditions. In this investigation it is shown that violarite exhibits a limited surface oxidation, a process that may be further related to the alteration of pentlandite considered in chapter 7. As violarite is present in equilibrated supergene assemblages, showing stability to oxidation, its own oxidation characteristics have not previously been the subject of specific investigation. In this work explanations are proposed, based on surface studies, for the limited oxidation of violarite. This is important from thermochemical considerations because the mineral is predicted to show an instability in aqueous environments as shown in in Eh/pH diagrams.

6.2. Natural Violarites.

In the Fe-Ni-S system violarite is stable in low temperature assemblages, (Misra & Fleet, 1974). Violarite is not found as a primary sulphide, and it has been inferred to form as a result of pentlandite/pyrrhotine alteration, an alteration resulting in nickel enrichment (Nickel et al., 1974; Keele & Nickel, 1974; Watmuff, 1974; Nickel et al., 1977; Thornber et al., 1981). The violarite itself has been reported to show increased nickel concentration towards the top of the supergene profile (up to 40 atomic % Ni). Significantly, in the oxide zone above the water table, violarite becomes unstable and has been reported to break down to iron oxides and goethite.

Thornber (1975a) showed that violarite-pyrite assemblages could be replaced by sulphates and 'gossanous' oxides, in shallow oxidative anodic reactions. Thornber (1975b) also reported that in groundwater electrochemical oxidation-cells, violarite is stable as an anodic

sulphide, but is replaced in the oxide zone by oxides and goethite pseudomorphing violarite.

The reports indicate violarite to have a stability comparable to pyrite, inferred from the co-existence of these minerals in secondary assemblages, and which could be reflected in the surface oxidation characteristics.

6.3. Characterisation of the violarite.

The violarite used in this investigation was produced synthetically using the techniques outlined in chapter 3. A fine-grained violarite was produced by sulphurisation at 400°C of an MSS (Mono-sulphide solid solution → FeS-NiS) phase produced by a direct combination of the elements at 700°C. The primary violarite was too fine-grained for surface analysis, but was used to initiate a synthesis with stoichiometric violarite (of composition $FeNi_2S_4$) at 450°C for several weeks (below the maximum thermal stability of 461 +/- 3°C determined by Craig, 1971).

The resultant phase, although skeletal, had areas large enough to provide surface information. The violarite was characterised largely using XRD and SEM (EDS). XRD analysis showed the sample to be a single phase. Attempts to analyse the sulphide by electron microprobe were unsuccessful. However, the sample comprised a single homogeneous phase, so the violarite was inferred to have an average composition in accordance with the original synthesis starting composition.

6.4. Optical Properties.

The spectral reflectance spectrum obtained for unoxidised violarite agrees with the spectrum described in the IMA/COM data file (Stanley & Criddle, 1986). Table 6.1. shows reflectance data for unaltered and oxidised violarite surfaces. The data shown are average values for five points on the sample surface.

Table 6.1. Reflectance measurements for unoxidised violarite and for violarite surfaces oxidised by various methods.

Oxidation method	Reflectance (R%) 470nm	546nm	589nm	650nm	ΔR(*)
Unoxidised (R^o)	43.2	45.1	46.3	49.8	
Steam	40.4	42.5	43.7	47.0	5.9
H_2O_2	39.5	41.3	42.3	44.9	8.9
NH_4OH	39.5	41.1	42.2	44.6	9.2
Air/oxygen (150°C)	37.9	39.8	41.9	44.4	11.1
Electrochemical (0.8V)	37.5	39.3	41.2	43.8	12.3
H_2SO_4	35.6	37.3	39.4	42.1	16.3

* ΔR = average change in reflectance = $(R^o-R^1)/R^o$ x 100

The reflectance spectra for the oxidised violarite surfaces indicated only small changes from reflectance spectrum of unoxidised material. The limited average changes in reflectance are indicative of the very small oxidation extent observed on the violarite surfaces, when compared to the changes in reflectance observed for other sulphides. The changes indicate that the surfaces have not been altered significantly, and this is also shown by the determination of the chemical compositions of the surfaces by spectroscopic analyses. The physical effects of the oxidation are shown in photomicrographs (figures 6.5. and 6.6.) and SEM photographs (figures 6.7. and 6.8.), discussed with respect to the determined chemical characteristics in section 6.9.

6.5. Auger Electron Spectroscopy.

The elemental compositions of the oxidised violarite surfaces were derived from differentiated Auger spectra. The expected elemental proportions for unoxidised violarite, assuming the synthesis composition of $FeNi_2S_4$, are 14.3% Fe, 28.6% Ni and 57.1% S.

The Auger profiles in figure 6.1. are indicative of the limited oxidation observed on the altered violarite surfaces, as indicated

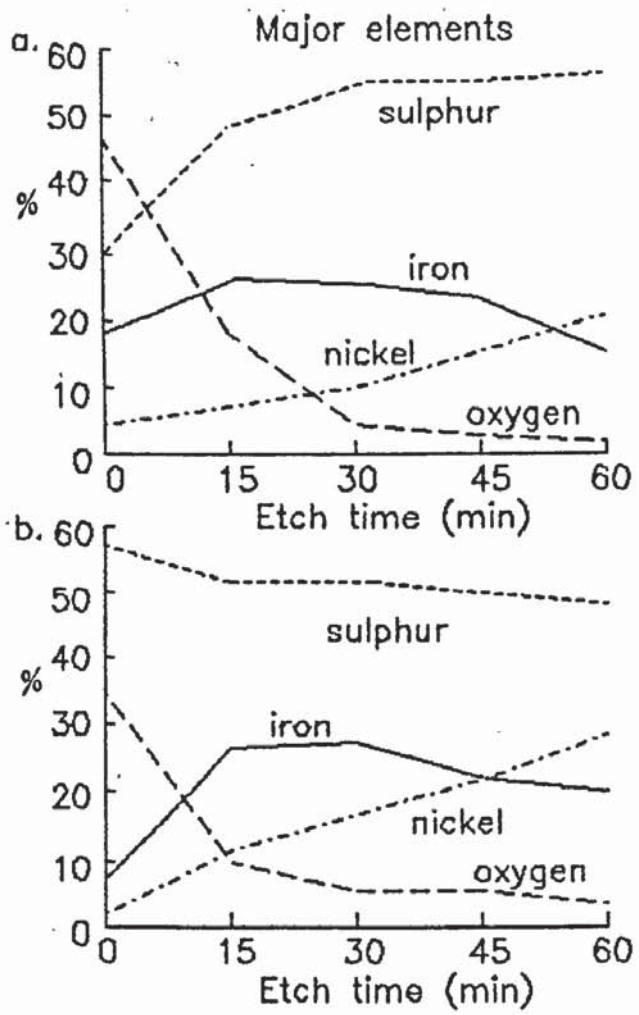

Figure 6.1. Auger depth profiles for violarite oxidised by (a) steam and (b) sulphuric acid, showing the major elements only. Carbon contamination was a major factor in the primary surface, but diminished rapidly with depth. (The etch rate is approimately 1Å per minute, thus the scale can be interpreted as a depth scale in Angstroms).

by the oxygen curves, which show a rapid decrease with depth into the altered surfaces. From the evidence provided by the Auger spectra alone, it could be inferred that the surfaces show evidence of layering in some profiles, especially from the iron curves. However, as shown in the x-ray photoelectron spectra, the change in elemental composition with depth may be more indicative of a general change in the proportions of the compounds present with depth.

Figure 6.1a., an Auger profile for violarite oxidised by steam, shows a noticeable depletion in nickel with respect to iron at the immediate surface. The almost complete disappearance of a peak attributable to oxygen after 60 minutes etching is evidence (assuming an approximate etch rate of 1Å per minute) of an oxidised surface limited to about 60Å.

A more extensive oxidation is shown by figure 6.1b. for oxidation by sulphuric acid. The Auger profile shows a large proportion of sulphur at the surface, decreasing with depth (contrary to the generally observed increase) indicative of sulphur-containing compounds at the surface. This phenomenon is explained by the XPS analyses (section 6.6.). Similarly to the steam oxidised sample, the nickel concentration is depleted at the surface with respect to iron, a factor consistent for all of the Auger profiles of oxidised violarite.

As observed for other minerals, the values obtained for the violarite at depth are consistent, for the most part, with the expected elemental compositions for pure violarite, suggesting that any sputter damage to the mineral (in terms of elemental chemistry) is limited.

6.6. X-ray Photoelectron Spectroscopy.

The oxidation products at the violarite surfaces, estimated to extend approximately 60Å in depth as indicated from the Auger analyses, are ideally suited to XPS analysis because of the depth of analysis using this technique (10-15Å).

As for pyrite, the limited oxidation observed on the violarite surfaces results in a large relative proportion of contaminants,

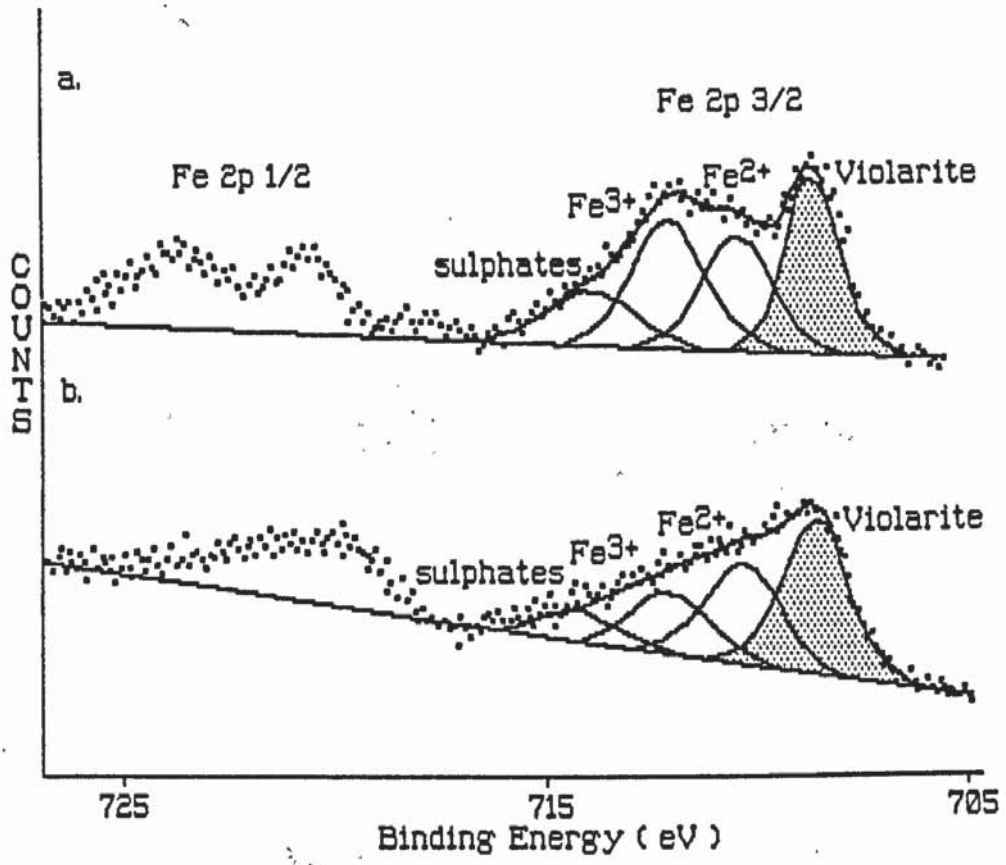

Figure 6.2. Iron 2p (1/2 and 3/2) x-ray photoelectron spectra obtained for violarite oxidised by (a) steam and (b) sulphuric acid.

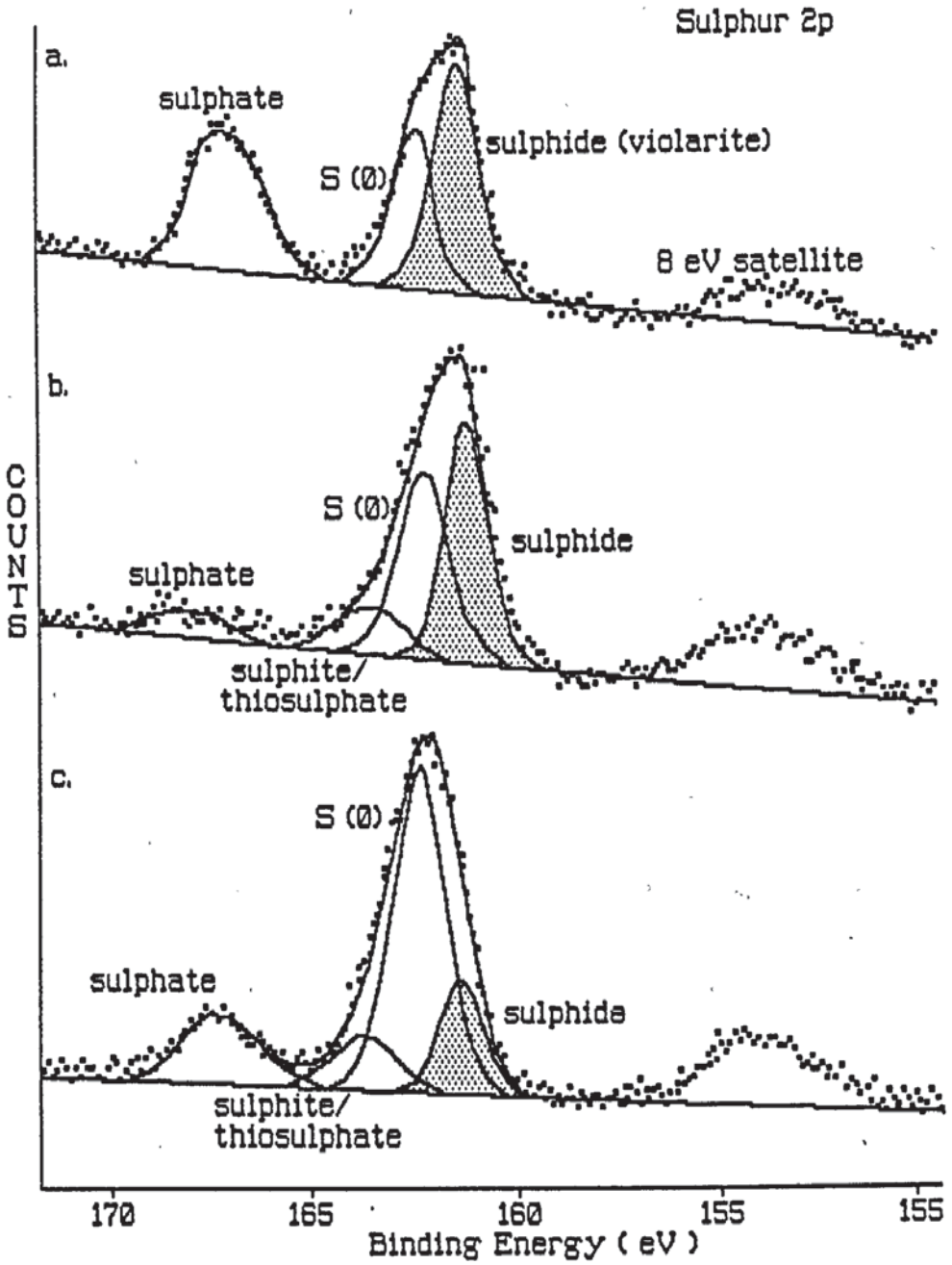

Figure 6.3. Sulphur 2p x-ray photoelectron spectra obtained for violarite surfaces oxidised by (a) air/oxygen (150°C), (b) steam and (c) sulphuric acid.

produced by adsorbed carbon, carbon monoxide etc. The contamination was removed by a few seconds of etching. Determination of the oxygen 1s peak envelopes for the oxidised surfaces indicated, in comparison to spectra from unetched surfaces, that there was little or no sputter reduction.

The binding energies of relevant electrons in violarite were determined in a preliminary investigation. New data were obtained for the violarite binding energies for the relevant peaks (708.4eV for Fe 2p(3/2), 853.2 eV for Ni 2p(3/2), and 161.2eV for sulphur 2p energy levels).

The fitted Fe 2p(3/2) spectra, shown in figure 6.2., indicate the presence of a large component of the original violarite in the oxidised surfaces, shown in these spectra by the shaded areas. The Fe^{2+} and Fe^{3+} peak area determinations indicate that the oxidised phases in the violarite surfaces show a greater proportion of Fe^{3+} compared to Fe^{2+} for most of the oxidation methods used, with the exception of sulphuric acid. From the Fe 2p(3/2) spectra the peaks attributable to sulphates are less well-defined and to a certain extent, may be masked by shake-up effects (although these have been inferred to be minimal for other sulphides and the situation could be similar for violarite). These problems may be overcome by the accurate determination of sulphate proportions from the sulphur 2p spectra.

Nickel 2p 3/2 spectra for the oxidised violarites show little alteration from the unoxidised spectrum, although it is possible to fit peaks for nickel oxide as a high binding energy shoulder on the sulphide peaks at 853.5eV. Generally the nickel oxide only forms a small component of the nickel spectra.

The sulphur 2p spectra for oxidised violarite surfaces indicate the lack of oxidation on most of the surfaces, evident from the remaining sulphide, and showing agreement with the Fe 2p(3/2) spectra. An important feature in the sulphur 2p spectra of oxidised violarite surfaces is the predominance of peaks attributable to sulphur (0). Additional sources of information (Auger profile figure 6.1b. and the SEM photograph in figure 6.5.) suggest that the S (0) peak may be due to elemental sulphur. The proportion of sulphur

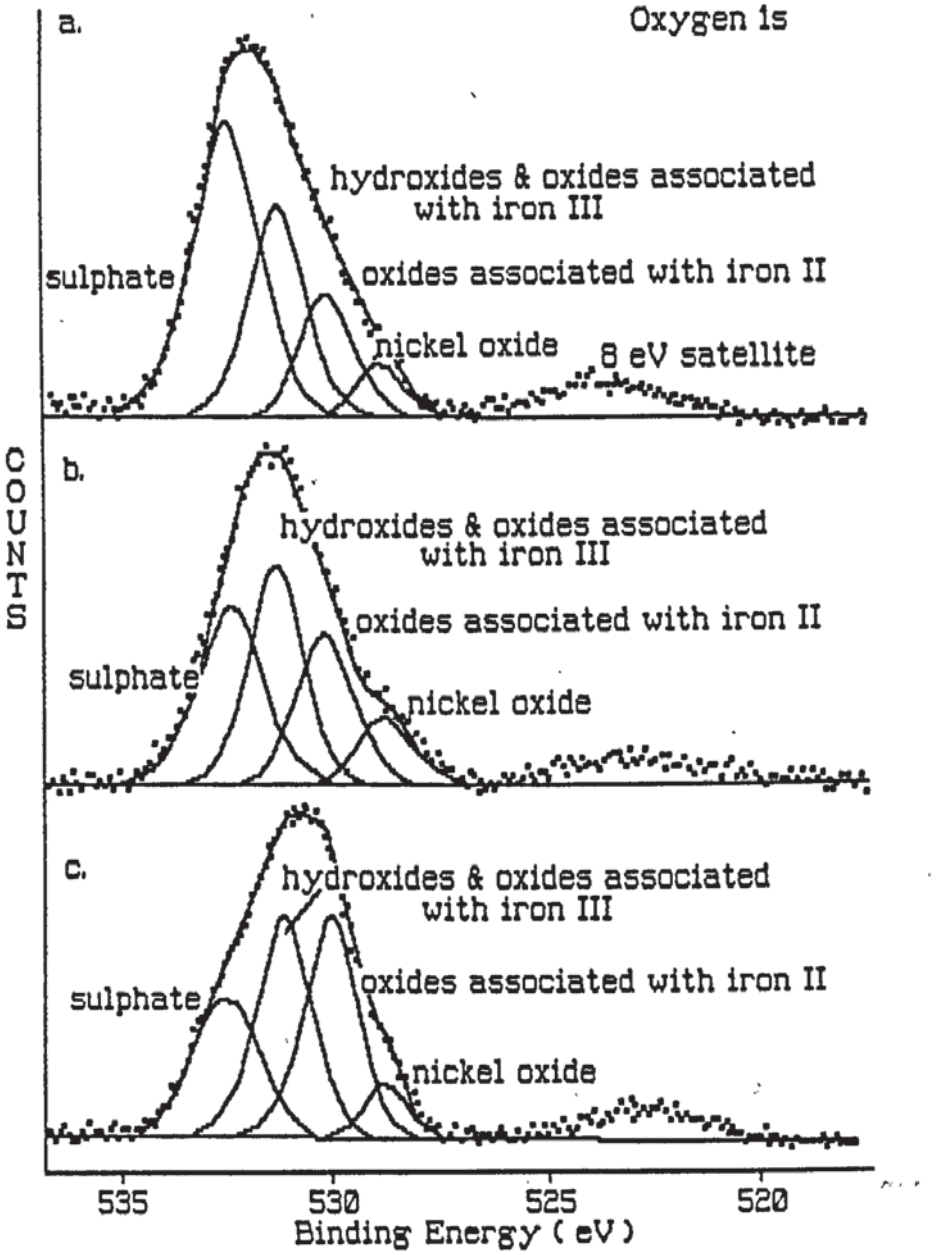

Figure 6.4. Oxygen 1s x-ray photoelectron spectra for violarite surfaces oxidised by (a) hydrogen peroxide, (b) steam and (c) air/oxygen (at 150°C).

determined (table 6.2.) is significant because it is far greater than that observed on other sulphide surfaces, and this suggests that sulphur formation is a major factor in inhibiting violarite oxidation. The presence of oxy-sulphate phases is also inferred from the sulphur 2p spectra. The peak envelopes determined for the oxy-sulphates show variable peak centres which may indicate a variable oxidation state in the oxy-sulphates. An interpretation of the oxy-sulphates present is included in table 6.2. in terms of sulphates or sulphites (including thiosulphates etc.).

The oxidation products can also be determined from the oxygen 1s spectra; these provide a more detailed estimate of the proportions of the oxides, hydroxides and oxy-sulphate phases. In figure 6.4. the variation in oxygen-containing phases on violarite surfaces oxidised by different methods is evident. An important factor in these spectra is the fitting of nickel oxide on the low binding energy shoulder.

The oxygen 1s spectra for violarite oxidised by various methods show that the components are variable and are largely indicative of the oxidising power of the oxidants. The presence of a greater Fe^{2+} oxide component with respect to the Fe^{3+} oxide/hydroxide component for the sulphuric acid oxidation is unexpected, and may be due to the incorporation of a larger Fe^{3+} component in the sulphates. The implications of these variations can be seen in table 6.2.

6.7. Compositional interpretation of XPS and Auger spectra.

The fitted XPS spectra and the elemental compositions inferred from the differentiated Auger electron spectra were used to estimate the surface compositions. Overall bulk compositions, were calculated (table 6.2.) for a surface layer of approximately 10-15Å depth, determined by the depth resolution of the XPS.

The detection of elemental sulphur as identified by the sulphur (0) peak in the sulphur 2p x-ray photoelectron spectra, and the large proportion of sulphur at the surface determined from the Auger spectra has been noted in sections 6.5. and 6.6. The possibility of polysulphide or thionate formation to account for the sulphur (0)

peak has been considered, although the lack of supporting evidence for these species from the x-ray photoelectron spectra is further evidence of elemental sulphur formation being the major cause of the sulphur (0) peak. From the results shown in table 6.2. it appears that sulphur is an important product of oxidation.

Table 6.2. General surface compositions from XPS/AES analyses (estimated molecular percentages).

	Method of Oxidation					
Phase	H_2O_2	steam	NH_4OH	air/oxygen	elec.	H_2SO_4
Fe II/III sulphate	21.8	7.7	11.1	16.7	16.2	15.4
Fe II sulphite etc.	-	10.5	7.0	-	8.4	5.4
Fe III (oxides &	17.8	18.8	19.7	22.8	14.1	8.4
Fe II hydroxides)	12.4	15.5	14.4	22.8	12.2	10.3
S (0)	18.1	20.5	19.8	13.4	26.5	42.8
NiO	2.6	3.7	4.8	5.4	5.3	4.9
Violarite ($FeNi_2S_4$)	27.3	23.3	23.2	18.9	17.3	12.8

As discussed in previous chapters, the Fe II and Fe III sulphates were difficult to characterise, due to problems in accurately fitting the resultant oxy-sulphate peaks in the sulphur 2p spectra, and the problems encountered with shake-up phenomena in the Fe 2p(3/2) spectra (discussed in chapter 2, section 2.2.3.). The sulphates were therefore determined as a single compound.

The deconvolution of the peaks comprising the Fe II and Fe III hydroxides and oxides is complicated by the number of possible compounds that could be present. The potential phases and the binding energies for these compounds are contained in Appendix 2 and the problem further discussed in section 6.10.

6.8. Conversion Electron Mössbauer Spectroscopy.

The unoxidised violarite was analysed by conversion electron Mössbauer spectroscopy. A quadrupole doublet was observed with parameters of 0.320 mms^{-1} for the isomer shift and 0.610 mms^{-1} for the quadrupole splitting. This is in agreement with previous work on violarite indicating iron in octahedral sites (Vaughan & Craig, 1985).

After oxidation of the violarite surfaces, no further contributions were observed to the CEM spectra. This is in agreement with the 60Å oxidation depth inferred from the Auger profiles, since the CEM spectra analyse depths of approximately 1000Å.

Although CEMS does not provide any information directly of relevance to the oxidation of violarite, the parameters determined are important in discussing pentlandite oxidation (chapter 7, section 7.8.).

6.9. Physical observations from SEM and optical microscopy.

The skeletal texture of synthetic violarite is evident in the photomicrographs shown in figures 6.5. and 6.6. Some grains in the 'violarite' show slightly different oxidation characteristics, and these may indicate a compositional variation in the bulk sample, although these are a minor constituent.

Figure 6.5. is typical of most of the surfaces produced in aqueous oxidants in that they show a surface that is largely obscured by thin films (creating the thin-film interference effects observed). This photomicrograph also shows a cracking of the surface (on a 1μm to 2μm scale) that may be caused by etching out of the grain boundaries in the violarite.

In figure 6.6. the thin films on the surface are more pronounced and the dispersion of the oxidation products across the whole surface is seen. The mobility of the oxidation products may be important in limiting the extent of oxidation. As on most oxidised sulphides, this interference limits any interpretation of the surface chemistry. From spectroscopic analyses it is determined that sulphur is a major component in the surfaces, although it is not evident in the

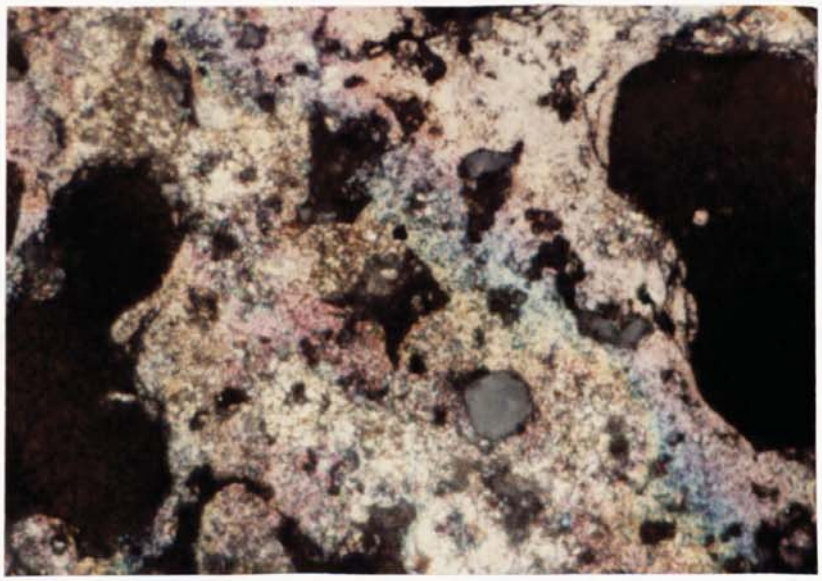

Figure 6.5. Reflected light photomicrograph of a violarite surface oxidised by ammonium hydroxide. (Width of field = 1.5mm, magnification = 67x)

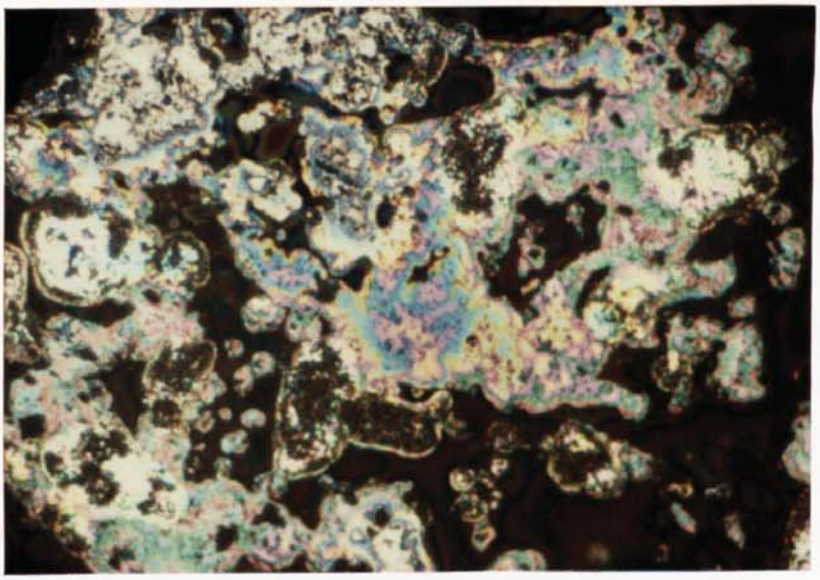

Figure 6.6. Photomicrograph of a violarite surface oxidised by steam. (Width of field = 1.5mm, magnification = 67x)

photomicrographs. Although nickel oxide is determined in low proportions, it is a green compound and may be indicated in figure 6.6., but the surface reflectance properties are distorted by interference effects.

SEM photographs indicate the formation of phases on the violarite surfaces. In figure 6.7., aggregates, with needle-like crystal forms, are detected on surfaces oxidised by sulphuric acid. The forms may be elemental sulphur, since violarite has a high elemental sulphur content, and the forms are not seen on other sulphides.

Figure 6.8. shows an SEM photograph of violarite oxidised electrochemically. The presence of oxidation products forming aggregates is evident, as on all violarite surfaces. The surface oxidation products, after alteration in all oxidants, show similar oxidised forms, with the number of oxidised spots on the surface increasing with the increased degree of oxidation.

6.10. Interpretation and Discussion.

The compounds suggested from the XPS/AES spectra and the extent of the surface oxidation are largely in agreement with interpretations of the reflectance spectra of the altered surfaces. These techniques indicate the limited extent to which the surfaces are altered in comparison to other sulphides, showing the relative stability to oxidation of violarite. As expected for a slightly oxidised surface, the oxidation products did not provide a significant contribution to the conversion electron Mössbauer spectra.

The compounds formed on the violarite surfaces may be considered using partial pressure (figure 6.9.) and Eh/pH diagrams (figure 6.10.) which relate, in simpified systems, the relative stability of violarite to its oxidation products.

Using the partial pressure diagram, the thermochemically stable phases can be estimated and the conditions of their stability used to interpret the alteration products. As noted for other sulphides, in these diagrams FeOOH is unstable with respect to Fe_2O_3, but is likely to form on the oxidised surface. Both partial pressure and Eh/pH

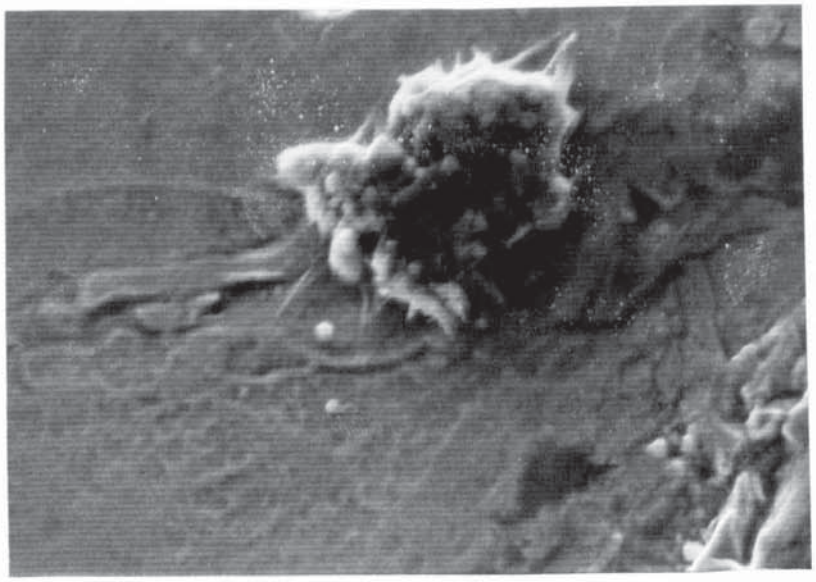

Figure 6.7. SEM photograph of an oxidised phase on the surface of violarite oxidised by sulphuric acid. (Width of field = 60μm, magnification = 1680x)

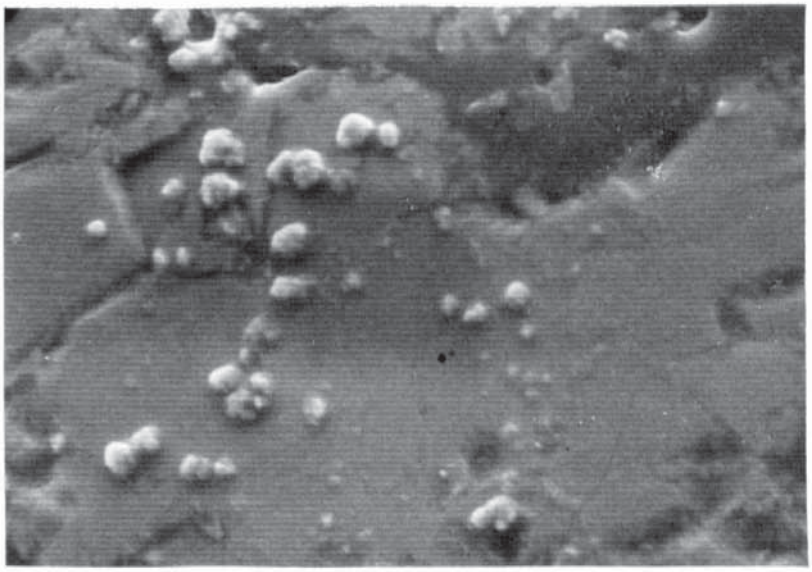

Figure 6.8. SEM evidence for the formation of oxidised phases on the surfaces of violarite oxidised electrochemically. (Width of field = 240μm, magnification = 420x)

diagrams have to be used in conjunction since, for example, magnetite (Fe_3O_4) is inferred from the Eh/pH diagram to be unstable in acid environments. However, in the immediate sub-surface, pH may not have an effect on the components, so magnetite could be stable.

The XPS analyses indicate a significant Fe^{2+} component in the iron oxides and hydroxides for most oxidants, and this is suggested to result from magnetite. A component of FeOOH may be present in most surfaces. Oxidation in sulphuric acid produces a surface with a greater Fe^{2+} component than Fe^{3+}, possibly indicating $Fe_{1-x}O$ (wüstite). The slightly oxidised sulphide surfaces, as exemplified by violarite, suggest, from the lack of clearly defined oxides on the surface, that the oxides present in the surface are an amorphous oxide mixture, which introduces the possibility of mixed iron-nickel oxides being present.

The lack of nickel in the surface components, present in only the original violarite and nickel oxide (or mixed iron-nickel oxide), is due to the high solubility of nickel, indicated by the stability of Ni^{2+} in solution as shown by the Eh/pH diagram in figure 6.10.

The sulphur-containing phases are probably responsible for controlling, at least partially, the rates of oxidation. The formation of elemental sulphur is directly linked to the extent of oxidation (with the exception of furnace oxidation) and shows that in the aqueous environment the more oxidised the surface, the greater the sulphur proportion. As sulphur is a major component in all of the surfaces, it may suppress oxidation by protecting the sub-surface. Sulphates apparently play no role in this. Another possibility is that the violarite is becoming nickel-enriched. Although violarite is part of a solid solution series with end-member polydymite (Ni_3S_4), the enrichment observed in natural deposits during oxidation is up to 40 atomic % of nickel (as outlined in section 6.2.). Therefore the contributions determined from the Ni 2p(3/2) spectra for violarite (with the formula $FeNi_2S_4$, compared to the enriched $Fe_{1-x}Ni_{2+x}S_4$) are over-estimated, and that of Fe 2p(3/2) spectra are under-estimated. Thus, if nickel enrichment is a major factor, the peak area fits give a false representation of the 'violarite' proportion.

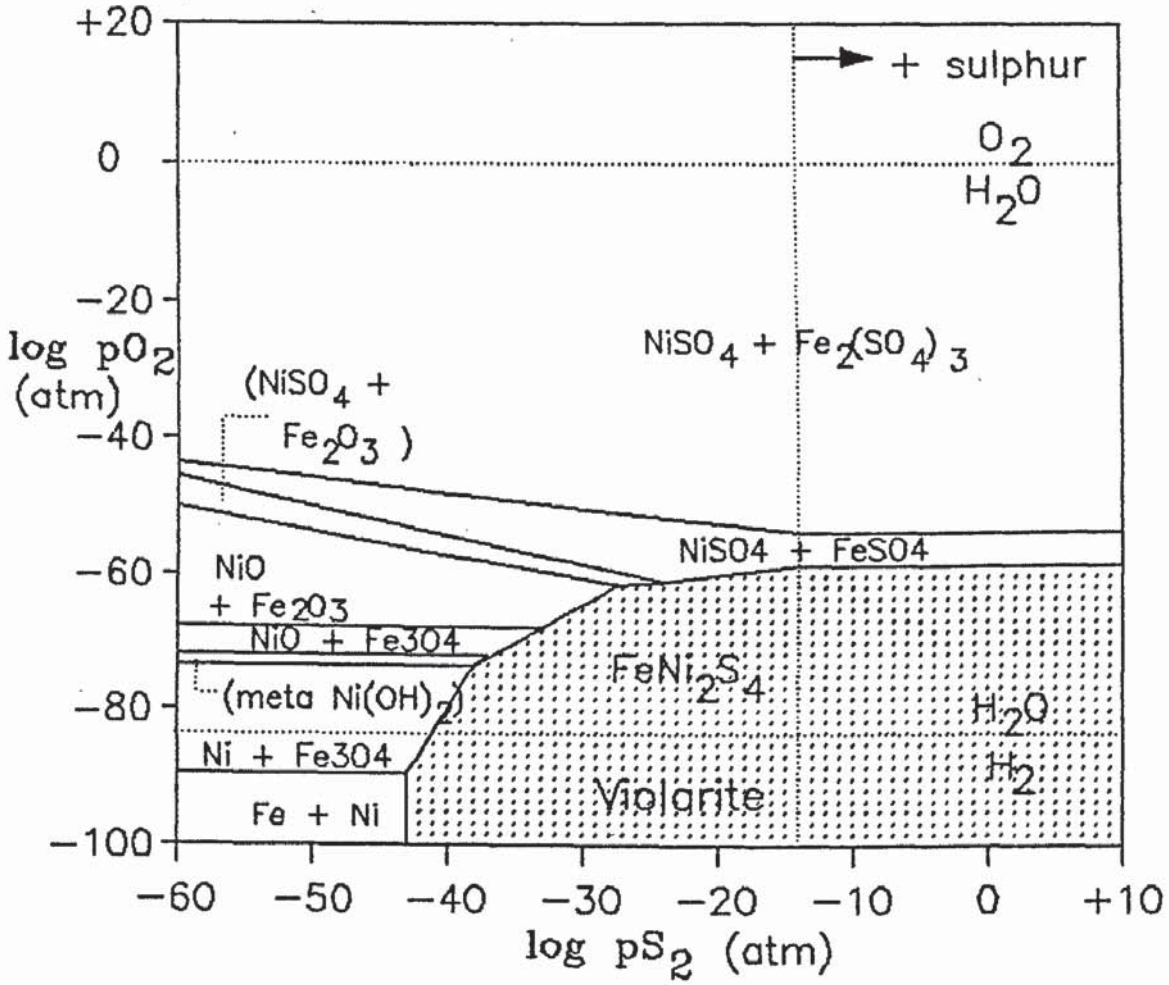

Figure 6.9. Partial pressure diagram (log pO_2/log pS_2) for oxidised violarite. (Equations and free energies of formation for the component phases contained in Appendix 4.)

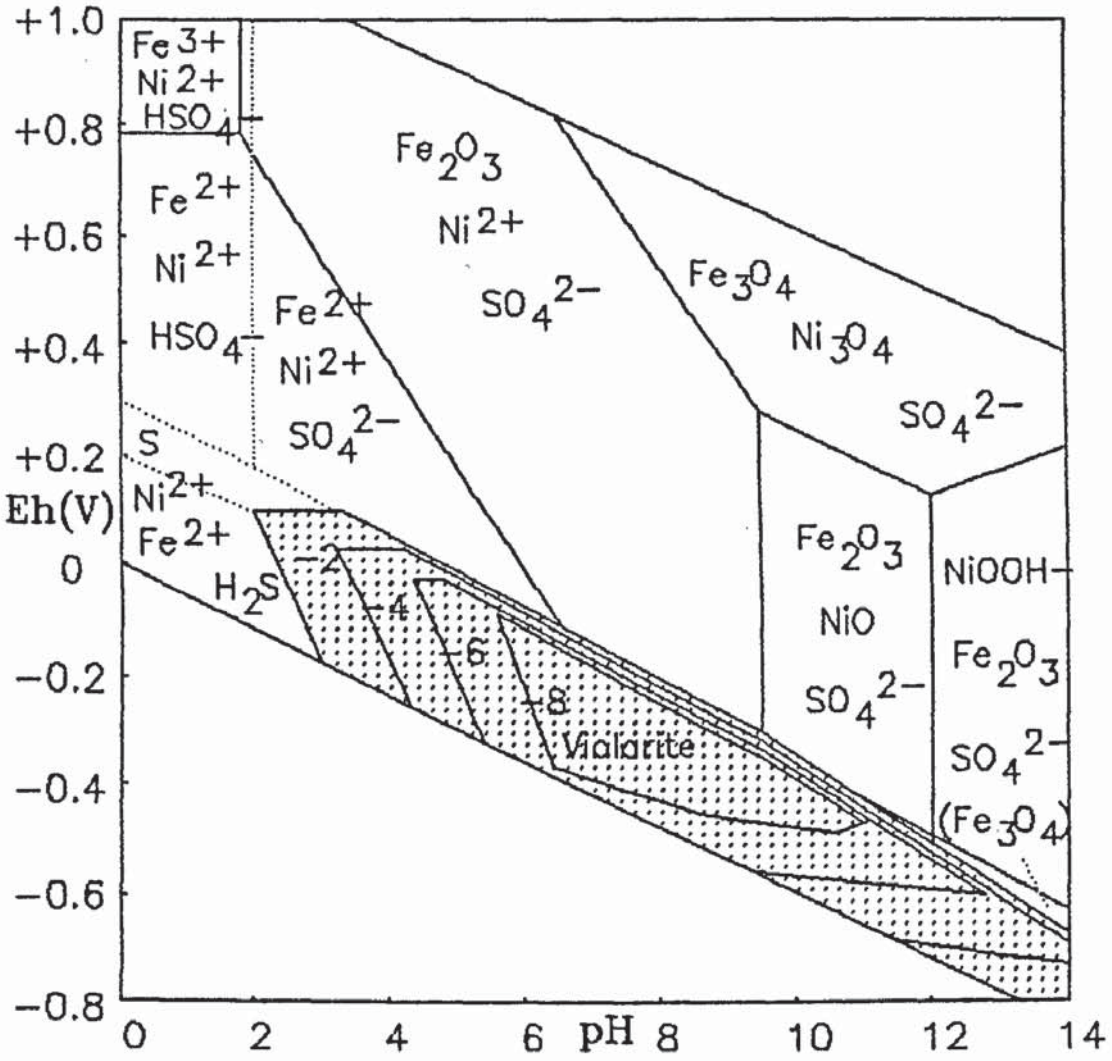

Figure 6.10. Simplified Eh/pH diagram for oxidised violarite. The phases boundaries were determined for log[S] = -2 and for log[Fe] (= log[Ni]) as shown on the diagram. (Equilibria and free energies for the phases contained in Appendix 4.)

In most of the oxidation methods used the oxidation occurs in aqueous solutions. In the air/oxygen (150°C) oxidation method the oxidation products would be largely anhydrous, therefore in determining the nature of the iron oxides/hydroxides, this factor, and the similar Fe^{2+} and Fe^{3+} concentrations, suggests the major component to be magnetite (Fe_3O_4).

Using a partial pressure diagram (figure 6.9.) it may be predicted that, in strongly oxidising environments, the end-products of oxidation would be nickel and iron sulphates.

$$4FeNi_2S_4 + 28O_2 \rightarrow 8NiSO_4 + 2Fe_2(SO_4)_3 + 2S$$

The equation given above shows that sulphatisation of the sulphide surface can be assumed to be accompanied by the formation of elemental sulphur, as detected in the XPS analyses. This will be enhanced where oxides form.

In aqueous oxidation, the general oxidation (inferred from figure 6.12.) is more complex, since nickel is readily taken into solution, as are sulphates, leaving the iron oxides etc. and sulphur as the major surface components.

Considering the oxidation in acidic solutions;

$$xFeNi_2S_4 + (2x+y)H_2O + (4x-2y)H^+ + (4x-2y)e \rightarrow Fe_xO_y + 2xNiO + 4xH_2S$$

$$FeNi_2S_4 + yH_2O + (8-y)H^+ + (8-y)e \rightarrow Fe(OH)_y + 2NiO + 4H_2S$$

$$FeNi_2S_4 + 4H_2O + H^+ + e \rightarrow FeOOH + 2NiO + 4H_2S$$

- and in alkaline solution;

$$xFeNi_2S_4 + (2x+y)OH^- + (2x-y)H^+ + (4x-2y)e \rightarrow Fe_xO_y + 2xNiO + 4xHS^-$$

$$FeNi_2S_4 + yOH^- + 4H^+ + (8-y)e \rightarrow Fe(OH)_y + 2NiO + 4HS^-$$

$$FeNi_2S_4 + 4OH^- + H^+ + e \rightarrow FeOOH + 2NiO + 4HS^-$$

A notable feature of these equations are their cathodic nature. In natural ores, and on the small scale, reactions would proceed via a coupled cathodic reduction of the solution (or water) and an anodic oxidation of the sulphide. Thus the cathodic nature of these reactions would be expected to be a major factor in the lack of reactivity of violarite.

A more detailed discussion on the mechanisms and characteristics of violarite oxidation is presented in chapter 10.

CHAPTER 7.

PENTLANDITE

7. Pentlandite.

7.1. Introduction.

Pentlandite, $(Fe,Ni)_9S_8$, is the major source of the world's supplies of nickel (Ramdohr, 1980; Craig & Vaughan, 1981). For this reason, the alteration (and in particular the oxidation) of the mineral, both in ore deposits and during the extraction process, is important with regard to the nickel yield from the ore.

As it is the major nickel-containing sulphide in the primary ore assemblage, pentlandite alteration is a controlling factor in the distribution of nickel in the weathering zones of the deposits. The mechanisms and nature of supergene alteration in these ores has been the subject of numerous investigations. By comparing the alteration of pentlandite in both supergene and oxide zones it may be possible to relate these to the determined surface characteristics.

7.2. Previous work concerning pentlandite and nickel ore alteration.

Watmuff (1974) and Nickel et al. (1974) reported that pentlandite/pyrrhotine assemblages alter to violarite/pyrite assemblages in supergene environments. The solution chemistry is suggested to involve the removal of Fe^{2+} ions from ore, while dissolved nickel and sulphur are redeposited in the supergene zone. At, or above, the water table, sulphates and hydroxides predominate with relict goethite, while nickel is leached. Nickel et al. (1974) also noted an enrichment in nickel towards the top of the supergene zone. An electrochemical process was suggested as an ore alteration model, linking the anodic oxidation of the ore to the coupled cathodic oxidation of water. Secondary enrichment of the violarite was inferred to proceed by a downward transportation of nickel and sulphur from the oxide zone.

The formation of nickel-rich violarite after the oxidation of pentlandite ores was also reported by Keele & Nickel (1974) and Nickel et al. (1977). In the latter study it was suggested that the nickel enrichment in these ores is not economically significant.

A model for the alteration was proposed by Thornber (1975a), in which conductivity was suggested to be a controlling factor in a galvanic corrosion cell within the supergene profile. This was assumed to be the driving force in the alteration of primary ore (rich in pentlandite) to the violarite/pyrite assemblage. In a chemical study of this "corrosion", Thornber (1975b) reported that the violarite, altered from pentlandite, enriched in nickel near to the cathode in natural oxidation cells, and that nickel was lost away from this zone. It was inferred that although the nickel loss might produce problems in flotation, the easy loss of nickel in anodic zones and in the oxide zone above the water table introduced the possibility of economic leaching.

In a laboratory study of nickel ore alteration, Thornber & Wildman (1979) reported the absence of violarite, but the release of Fe^{2+} and base metals were noted with associated sulphates and acidification of the solutions.

Boateng & Phillips (1978) reviewed the hydrometallurgy of nickel extraction from nickel sulphide (mainly pentlandite) ores. It was reported that most oxidants (ammonia, water, acid, Fe^{3+}, oxygen, Cl^-, SO_2 and anodic dissolution) resulted in nickel leaching, but were not always selective. The remaining pentlandite grains were demonstrated to show an unaltered pentlandite core with a hydrated ferric oxide outer layer.

7.3. Pentlandite characterisation.

In order to minimise any possible effects of minor contaminant elements on the rates and products of oxidation, a synthetic pentlandite was used. The pentlandite was synthesized by direct combination of the elements, using evacuated silica tube methods (chapter 3, section 3.2.). to produce a phase with equal proportions of iron and nickel. Primary homogenisation at 150°C, was followed by several weeks of homogenisation at 600°C, below the maximum thermal stability of pentlandite at 610°C (Kullerud, 1963).

Subsequent examination in polished section and by x-ray diffraction, indicated the presence of homogeneous pentlandite,

although with a granular texture. The grains were in random orientation, giving an average interpretation of the oxidation of the surfaces, which is advantageous since the surface alteration may be affected by crystallographic orientation, even in a cubic mineral such as pentlandite.

The phase did not exhibit any cracking that might have been expected as a consequence of quenching when examined in polished section, which is important with regard to observed oxidation characteristics discussed later.

Electron microprobe data for several points on the pentlandite surface were determined, and assuming the formula $Fe_mNi_nS_8$, the atomic composition of iron varies from 3.74 to 4.77 and that of nickel from 3.50 to 4.93. The average compositions are given in table 7.1.

Table 7.1. Average electron microprobe analyses for pentlandite.

	Fe	Ni	S
Pentlandite (At %)	27.50 +/- 4.34	27.15 +/- 6.92	49.90 +/- 2.56
Average composition (atomic proportions)	4.409	4.353	8.000

The electron microprobe analyses show considerable variation in the proportions of nickel and iron in the pentlandite. Both iron and nickel are present in concentrations less than the initial synthesis compositions. These compositional variations may result in oxidation rates and characteristics that differ slightly across the surfaces.

7.4. Optical Properties.

The spectral reflectance spectrum obtained for unoxidised pentlandite agrees with the spectrum described in the IMA/COM data file (Stanley & Criddle, 1986). Table 7.2. shows reflectance data for

pentlandite surfaces, before and after oxidation. The reflectance data are an average of several points on the sample surface.

Table 7.2. Reflectance measurements for unoxidised pentlandite and pentlandite surfaces oxidised by various methods.

Oxidation method	Reflectance (R%) 470nm	546nm	589nm	650nm	ΔR(*)
Unoxidised (R^o)	40.2	43.8	48.6	52.2	
Air/oxygen (150°C)	28.7	37.1	41.3	44.2	18.1
Steam	28.3	36.2	40.4	43.7	19.6
NH_4OH	26.9	30.2	33.5	35.8	31.6
H_2SO_4	23.6	28.3	31.6	34.7	36.0
H_2O_2	13.3	14.1	15.4	16.4	68.0
Electrochemical (0.8V)	13.1	13.9	15.2	15.4	68.8

* ΔR = average change in reflectance = $(R^o-R^1)/R^o$ x 100

The reflectance data were used to give preliminary indications as to the alteration caused by various methods of oxidation. These indications are fairly consistent with the depths of oxidation determined by other methods as outlined in the following sections. Reasons for discrepancies between the reflectance changes and the determined chemical depths of oxidation are considered in section 7.9., along with an appreciation of the observed oxidation, indicated by both photomicrographs and SEM photographs, with respect to the chemical data determined.

7.5. Auger Electron Spectroscopy.

Differentiated Auger spectra were used, in combination with argon ion etching, to determine elemental concentrations with depth. The expected composition of the unoxidised pentlandite, that would be applicable after sputter removal of the oxidised layer, may be taken from the probe data to be 27.5% Fe, 27.2% Ni and 49.9% S.

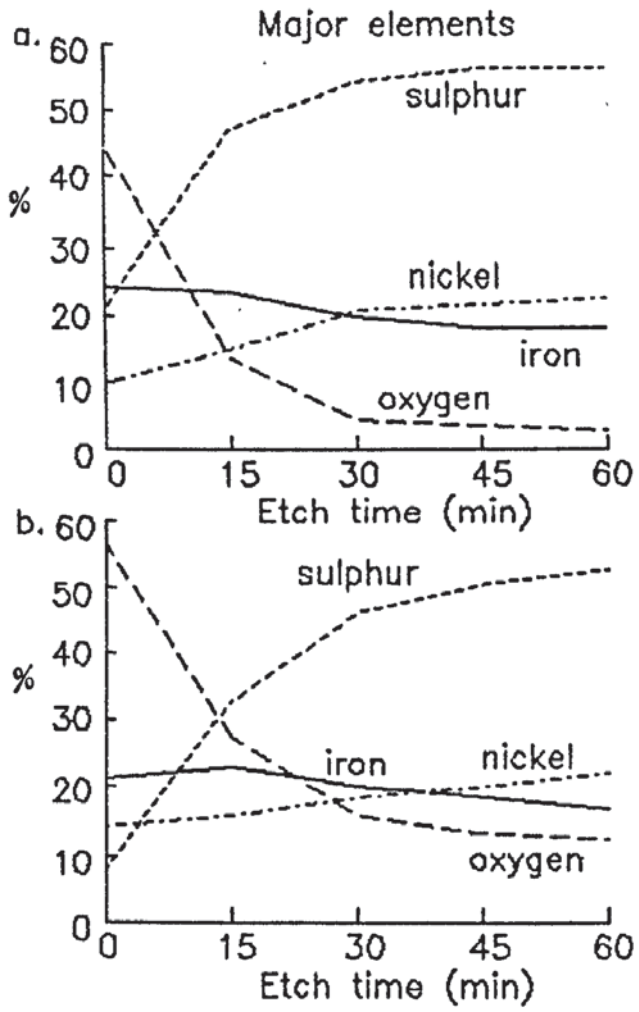

Figure 7.1. Auger depth profile for pentlandite oxidised (a) by steam and (b) electrochemically, showing the major elements only. Carbon contamination was not an important factor in these surfaces. (The etch rate is approximately 1Å per minute, thus the scale can be interpreted as a depth scale in Angstroms).

Typical Auger depth profiles are shown in figure 7.1. for pentlandite surfaces oxidised by steam and electrochemically. These profiles are typical of pentlandite oxidation and show a decrease in oxygen that is inversely proportional to the increase in sulphur in all of the surfaces. In most of the profiles, sulphur is extremely depleted at the surface, with the steam oxidised profile (figure 7.1a.) showing a comparatively large sulphur component. After oxidation in a low temperature (150°C) furnace, and by ammonium hydroxide and hydrogen peroxide, sulphur is absent from the immediate surface.

A major feature in all of these profiles is an increase in nickel with respect to iron at depth, below the immediate surface (this was determined by analysis of an unoxidised pentlandite not to be a sputter effect). This enrichment of nickel in the sub-surface, and reasons for its development, are substantiated and explained in more detail in the following sections.

7.6. X-ray Photoelectron Spectroscopy.

Pentlandite exhibits extensive alteration after oxidation by all of the methods used, and the carbon contamination of the surface was observed to be a minor factor not requiring any preliminary etching. New data were recorded during this work for the pentlandite Fe 2p(3/2) and Ni 2p(3/2) binding energies, of 707.3eV and 853.0eV respectively, obtained by the fitting of the peaks to the spectra of unaltered pentlandite surfaces. Similarly, a peak position of 161.2eV for the sulphur 2p energy level was obtained.

Figure 7.2. shows the alteration on the pentlandite surfaces resulting from oxidation by air/oxygen (at 150°C in a furnace) as evidenced by the Ni 2p(3/2) spectra and the alteration by steam as evidenced the Fe 2p(3/2) spectra.

The nickel x-ray photoelectron spectra of the oxidised surfaces (for example figure 7.2c for furnace oxidation) show that the occurrence of secondary nickel-containing compounds in the surfaces is limited to nickel oxide. In most of the oxidised pentlandite Ni 2p(3/2) spectra, the nickel oxide component is only a minor peak. The

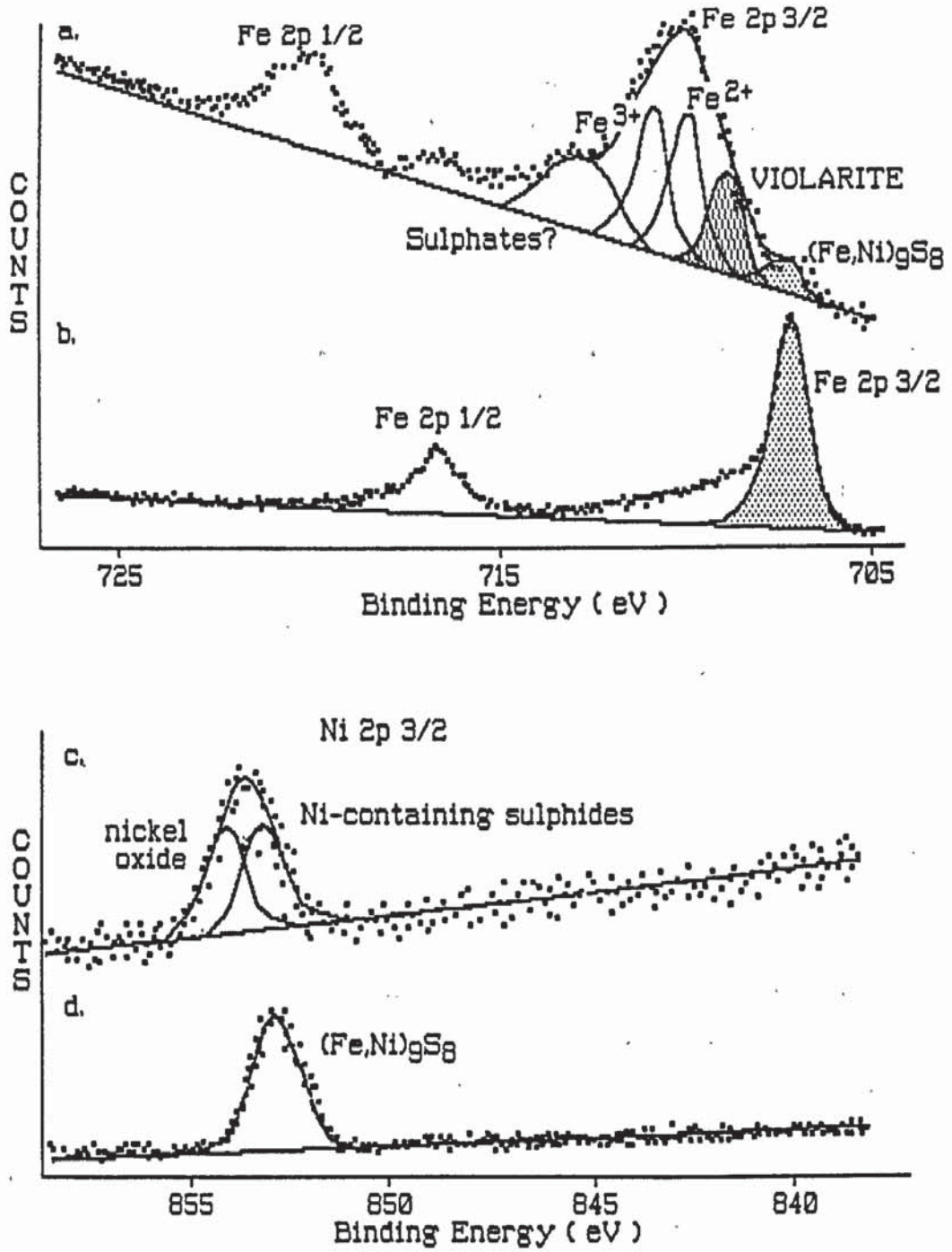

Figure 7.2. Fe 2p(3/2) x-ray photoelectron spectra (top) of pentlandite oxidised by (a) steam with respect to a spectrum for unaltered pentlandite (b). Ni 2p(3/2) x-ray photoelectron spectra (bottom) for a (c) furnace oxidised pentlandite in comparison to (d) the unaltered surface.

nickel peak determined for sulphide broadens slightly after oxidation, but does not allow the determination of a second phase. Evidence for nickel sulphate in the surfaces is not found. On comparison with other analysed elements, there is a depletion in nickel-containing alteration products in the surface.

The Fe 2p(3/2) spectra of the altered surfaces are more complex. In figure 7.2. a spectrum for steam oxidised pentlandite is shown in comparison to an unaltered pentlandite (after quartic-quintic smoothing, discussed in chapter 2, section 2.2.2.). The Fe 2p3/2 spectra of the altered pentlandite surfaces indicate the formation of several iron-containg compounds with binding energies consistent with a range of iron II and iron III oxides and hydroxides, with associated oxy-sulphates. As with the other suphides studied, the iron oxide and hydroxide peaks were fitted in terms of the iron II and III oxidation states, rather than specific iron oxides and hydroxides.

In these spectra, shake-up lines (chapter 2, section 2.2.3.) may be a problem, as indicated by figure 7.2. where the unoxidised pentlandite indicates a shoulder developed on the high binding energy side of the sulphide peak. The error in determining the peak area due to oxidised phases is overcome by also using the peak area information from the sulphur 2p and the oxygen 1s spectra.

During fitting of the iron 2p spectra, it was evident that there was a contribution to the spectrum from a compound with a binding energy slightly greater than that of pentlandite. In addition, most of the surfaces studied showed a considerable contribution from sulphides to the sulphur 2p spectra. This also suggests, in combination with the minimal Fe 2p(3/2) pentlandite peak for the altered surfaces, that a second sulphide is present.

Previous mineralogical studies of the oxidation of pentlandite surfaces (section 7.2.) have indicated that the secondary sulphide is likely to be violarite. In the analyses of the synthetic violarite (used in chapter 6, section 6.6.), values of 708.4eV for the Fe 2p(3/2) binding energies and 853.2eV for the Ni 2p(3/2) binding energies were obtained. Fitting these values to the spectra of altered pentlandite surfaces produced accurate fits to the Fe 2p(3/2) spectra

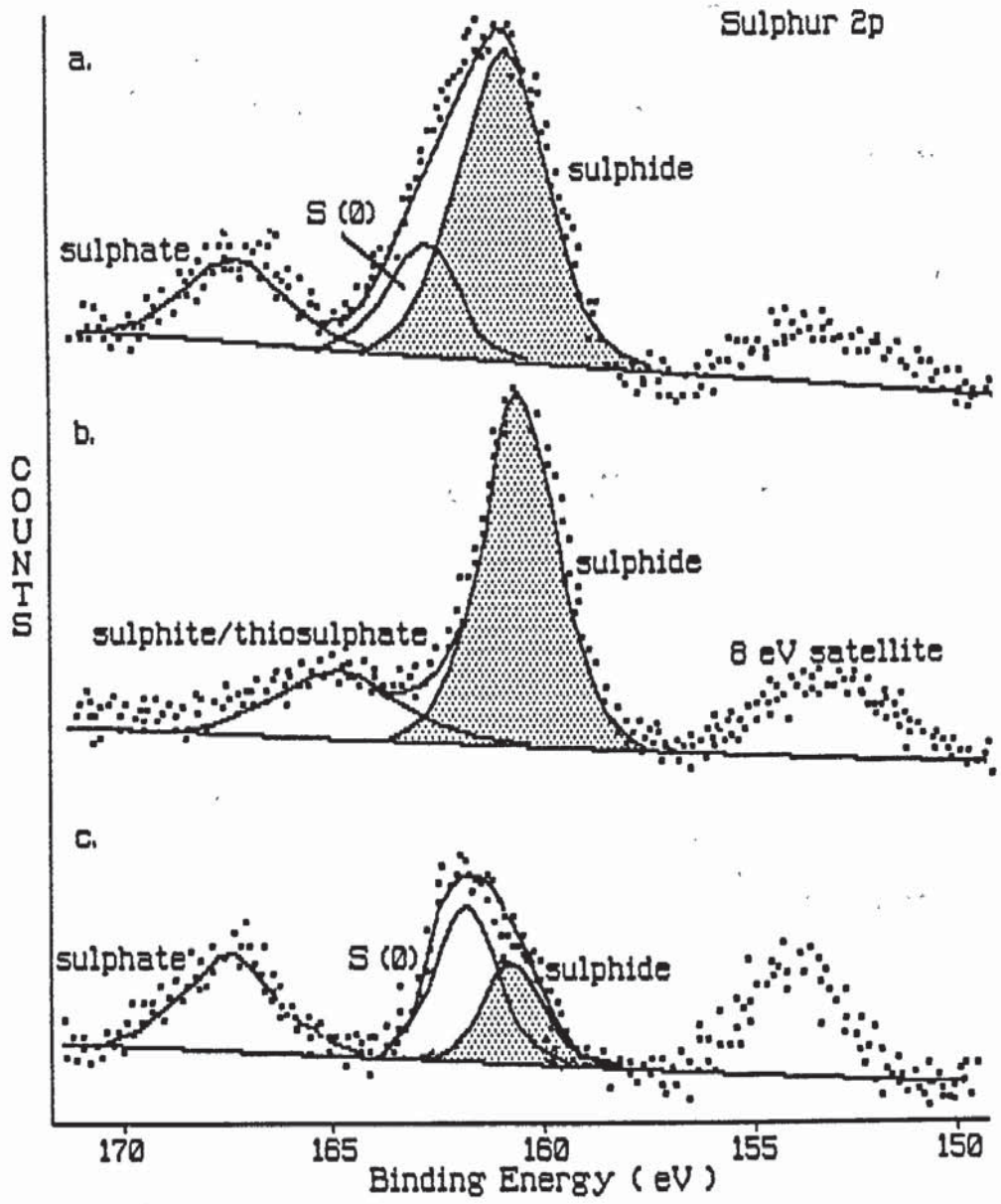

Figure 7.3. Sulphur 2p x-ray photoelectron spectra obtained for pentlandite surfaces oxidised by (a) sulphuric acid, (b) steam and (c) hydrogen peroxide.

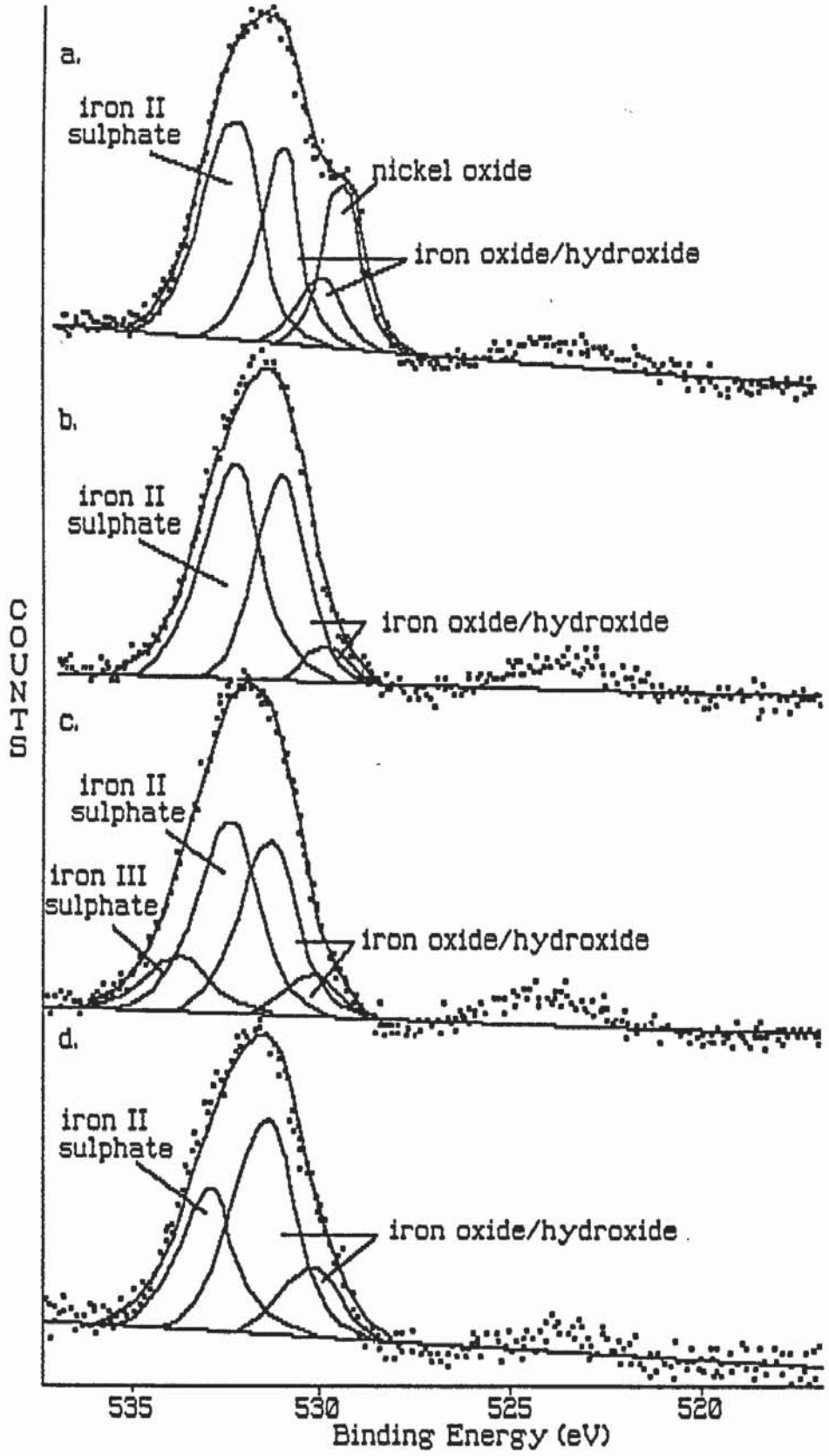

Figure 7.4. Oxygen 1s x-ray photoelectron spectra obtained for pentlandite surfaces oxidised by (a) air/oxygen (150°C), (b) sulphuric acid, (c) hydrogen peroxide and (d) ammonium hydroxide.

and accounted for the broadening of the sulphide peak in the Ni 2p(3/2) spectra, that were not sufficiently separated to otherwise allow accurate fitting. The possible presence of other secondary sulphides was considered, but the binding energies were not consistent with the data from the oxidised pentlandite spectra.

In assessing the pentlandite oxidation, much information is derived from the volatile elements, sulphur and oxygen. The sulphur 2p spectra (figure 7.3.) indicate that the sulphur species at the surface can vary considerably. The presence of a contribution to the spectra from sulphides is evident from most surfaces, and as shown in the Fe 2p(3/2) spectra, the presence of violarite is suggested to accompany the pentlandite. Although the S 2p binding energy in both pentlandite and violarite is determined to be 161.2eV, the broader peak widths obtained in fits for some spectra do suggest slightly differing values.

Oxygen 1s spectra for several oxidised pentlandite surfaces are shown in figure 7.4. and from these the relative proportions of sulphates, and the iron and nickel oxides may be determined. Only the furnace oxidised spectrum shows evidence of nickel oxide formation. Excepting the suggestion that nickel is enriched in violarite after pentlandite oxidation, and that nickel oxide is present in minor quantities, the nickel compounds are depleted in the oxidised pentlandite surfaces.

7.7. Compositional Interpretation of XPS and Auger spectra.

The determination of elemental concentrations at the surface from the differentiated Auger spectra and the chemical compositions inferred from the XPS spectra were used to estimate the proportions of the phases present in the oxidised surfaces. Overall bulk compositions are presented in table 7.3. of a surface layer of approximately 10-15Å depth (determined by the depth resolution of the XPS).

Additional information from conversion electron Mössbauer spectroscopy, photomicrographs, SEM photographs, and appreciation of

possible structural transformations in the surfaces, are necessary to provide more detailed interpretations of the chemical compositions given in table 7.3; such interpretations are undertaken in section 7.11.

Table 7.3. General surface compositions from XPS/AES analyses (estimated molecular percentages).

Phase	Method of Oxidation					
	elec.	H_2SO_4	steam	air/oxygen	NH_4OH	H_2O_2
Fe II/III sulphate	12.4	26.7	-	29.7	28.3	32.0
Fe II sulphite etc.	12.4	-	27.6	-	-	-
Fe III (oxides &	14.2	16.3	24.6	25.0	39.6	20.4
Fe II hydroxides)	15.5	7.3	22.8	14.6	7.3	12.2
NiO	9.4	-	-	12.3	-	-
S (0)	-	22.6	-	6.2	13.7	26.8
Violarite - $FeNi_2S_4$	23.7	20.9	19.1	10.8	8.8	8.6
Pentlandite - $(Fe,Ni)_9S_8$	12.4	6.2	5.9	1.4	2.3	-

7.8. Conversion electron Mössbauer spectroscopy.

A CEMS analysis of unaltered pentlandite surfaces produced a quadrupole doublet spectrum with parameters of 0.333 mms^{-1} for the isomer shift and 0.336 mms^{-1} for the quadrupole splitting, indicating iron in tetrahedral sites. Previous work (Vaughan & Ridout, 1971) indicated that pentlandite can have iron present in both tetrahedral and octahedral sites. However, as reported by Knop et al. (1970), the iron diffuses into tetrahedral sites during annealing. The pentlandite used in this study (which was annealed during synthesis) shows similar parameters to those reported by Knop et al. (1970).

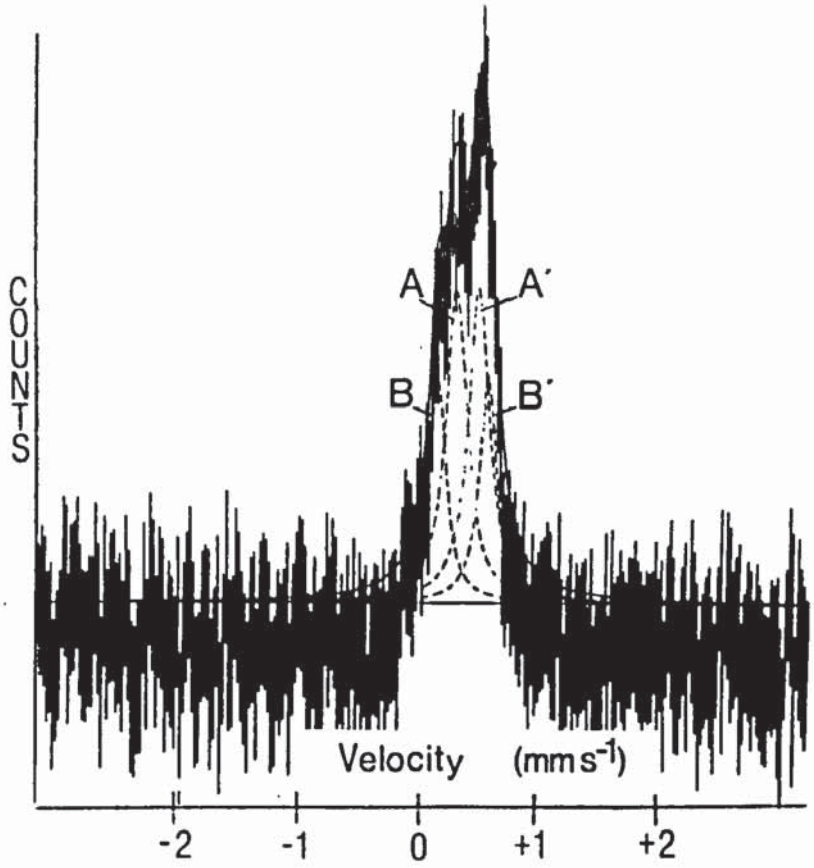

Figure 7.5. Conversion electron Mössbauer spectrum for pentlandite oxidised by hydrogen peroxide. The quadrupole doublet AA' corresponds to iron in pentlandite tetrahedral sites. The quadrupole doublet BB' is fitted after oxidation corresponding to octahedral sites in violarite.

After oxidation with any of the oxidants used, a second quadrupole doublet was observed, as shown in figure 7.5. Fitted parameters for the second doublet are 0.320 mms^{-1} for the isomer shift and 0.610 mms^{-1} for the quadrupole splitting, in agreement with the assignment to Fe in octahedral sites in violarite (see chapter 6 and Vaughan & Craig, 1985). The other surface oxidation products suggested from the XPS interpretations were not present in sufficient quantities to be detected by CEMS.

7.9. Observations from SEM and optical microscopy.

The photomicrographs presented as figures 7.6. and 7.7. show typical features of pentlandite oxidation. The granular texture of the pentlandite produced as a result of the synthesis procedures is evident in these figures. In most of the oxidised pentlandite surfaces investigated there is evidence of an induced cracking in the sample surface. This phenomenon is suggested to be related to the structural transformation of pentlandite to violarite, and is considered in more detail in section 7.10.

Of the two photomicrographs shown, that for the electrochemically oxidised surface (figure 7.6.) is more typical of pentlandite oxidation in general. Overlying the cracked sub-surface are oxidation products (labelled B) which have not been positively identified, although the spectroscopic analyses suggest the formation of iron hydroxides and sulphates. The cracked surface is considerably tarnished with respect to the unoxidised surface, a factor that is difficult to quantify from reflectance measurements due to the additional reduction in reflectance as a result of the surface cracking.

The photomicrograph in figure 7.7. illustrates the effect of extensive oxidation in hydrogen peroxide, and although the cracking of the sub-surface is observed in certain areas, the overlying oxidation products largely obscure this. The variation in thickness of the oxidised layers is evident from the thin film interference effects.

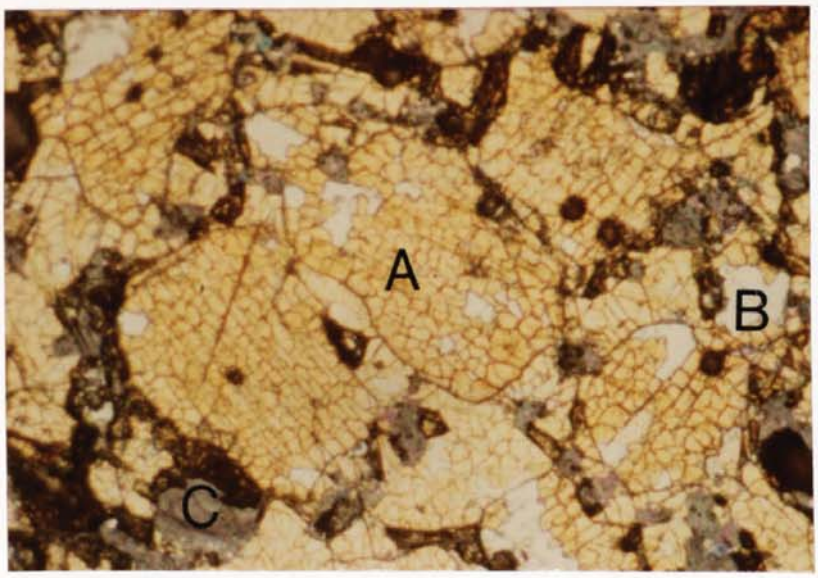

Figure 7.6. Photomicrograph of electrochemically oxidised pentlandite with evidence of shrinkage cracks (A). Overlaying these are thin oxidation layers (B). The granular nature of the pentlandite is evident from the partially infilled holes (C). (Width of field = 1.5mm, magnification = 67x)

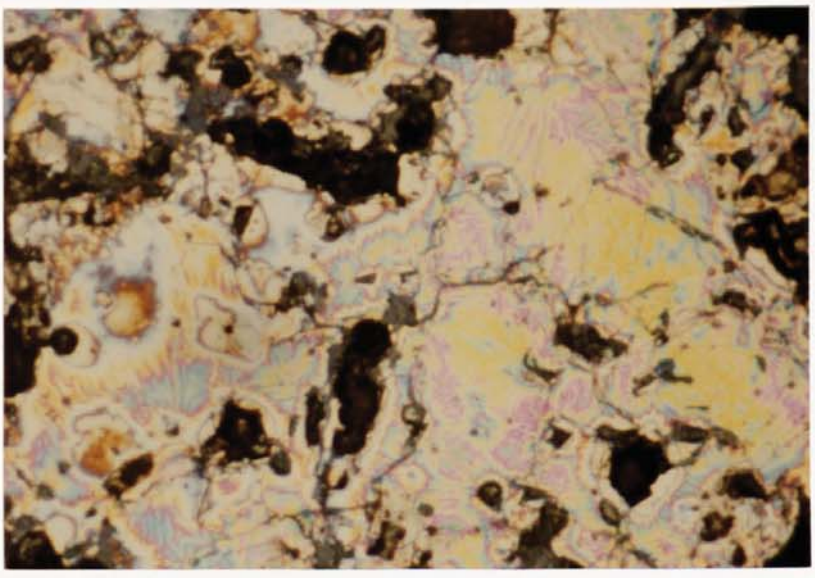

Figure 7.7. Photomicrograph of a pentlandite surface oxidised by ammonium hydroxide. The change of depth in the oxidation products is evident from thin film interference patterns. (Width of field = 1.5mm, magnification = 67x)

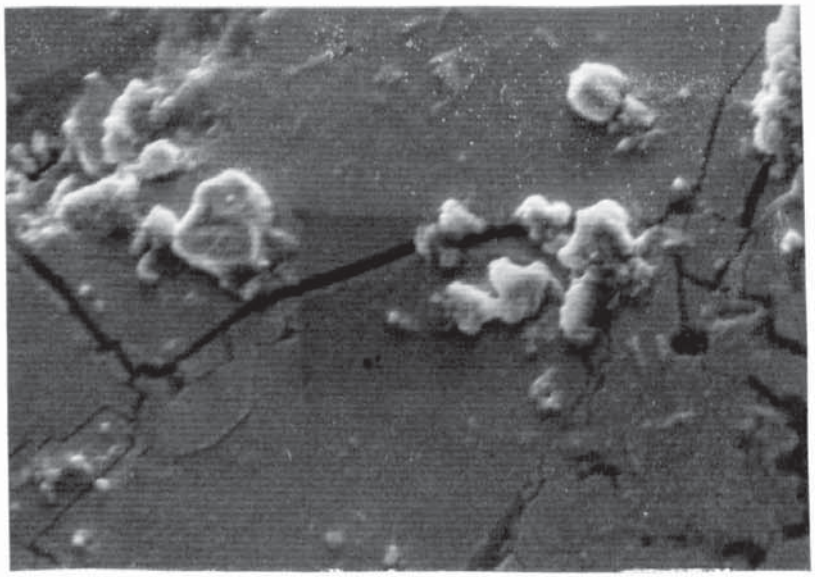

Figure 7.8. SEM photograph of a pentlandite surface oxidised electrochemically showing shrinkage cracks and the formation of amorphous oxidation products. (Width of field = 60μm, magnification = 1680x)

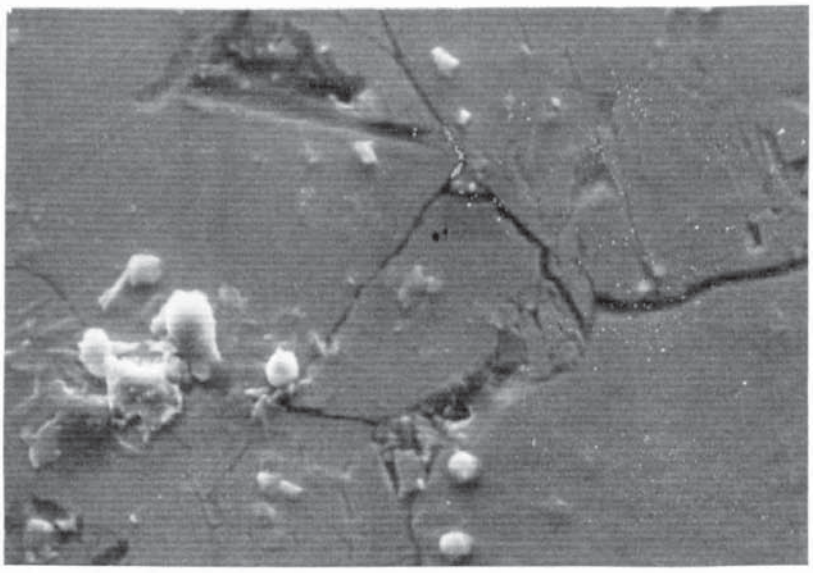

Figure 7.9. SEM photograph of a hydrogen peroxide oxidised pentlandite surface, showing 60° joints between cracks and similar amorphous oxidation products to those in figure 7.8. (Width of field = 60μm, magnification = 1680x)

In SEM photographs (figures 7.8. and 7.9.) further evidence for the formation of surface cracking is observed. None of the products of surface oxidation show any discernable crystal form, and are probably a very fine grained mixture of compounds.

There is additional evidence in these photographs for a structural relationship causing the cracking of the surface, since the intersects of the cracks range from 90° (clearly shown in figure 7.6.) to 60° (evident in figure 7.9.), as identified in both photomicrographs and SEM photographs, indicative of the cleavages of cubic minerals intersecting the surface.

7.10. Structural Transformation.

The observed characteristics of pentlandite oxidation suggest the alteration to violarite occurs via a sub-surface enrichment of nickel. The rapid formation of violarite is promoted by the instability of pentlandite, and more importantly, by the similarity between the crystal structures. Misra & Fleet (1974) investigated the pentlandite transformation in ore samples from nickel deposits and concluded that the alteration could be caused by the removal of excess metal atoms, largely iron, and the formation of violarite around the similar, face-centred cubic, sulphur atom sub-structure. The unit cells for the two sulphides are shown in figure 7.10. These show that each sulphide has 32 sulphur atoms in their unit cells, which suggests that if the transformation occurs there is no sulphur loss. The presence of elemental sulphur in the surface indicates that the oxidation of pentlandite does not proceed solely via violarite formation.

The transformation from pentlandite to violarite involves a reduction in cell size from 10.07Å to 9.46Å, an overall volume reduction of 17%. The cracking observed on the oxidised pentlandite surfaces is suggested to result from the volume reduction associated with violarite formation.

It has also been reported that the cracking of pentlandite is evidence of the loss of metals as sulphates (Ramdohr, 1980). Although sulphate formation definitely occurs (as determined by spectroscopic

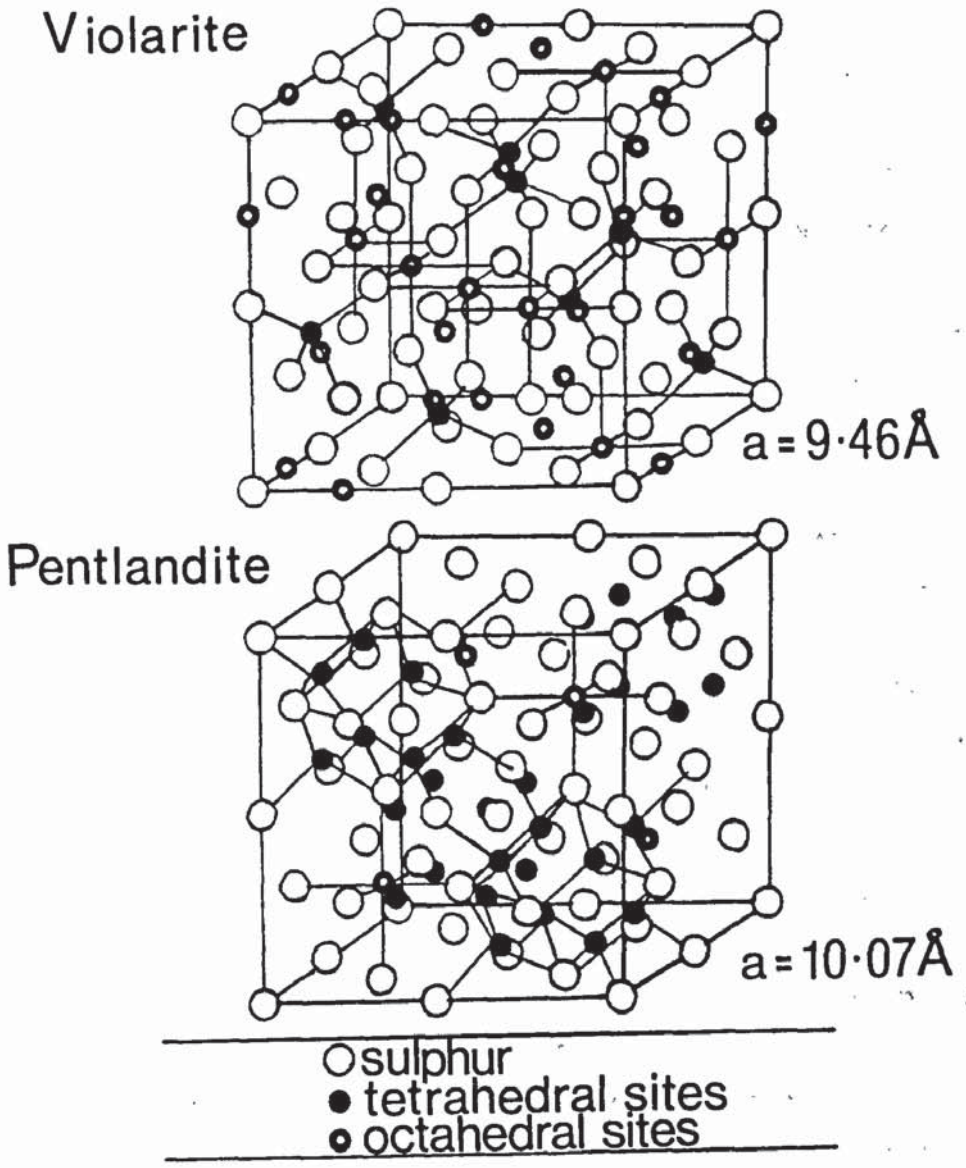

Figure 7.10. Comparison of the unit cells of violarite (with selected bonds to show the structure) and pentlandite (showing the tetrahedral-bonded cube clusters in the front half of the cell), illustrating the similarity between the sulphur sub-structures.

methods) it is unlikely to account for the surface cracking observed since it is a uniform effect across the surface unlikely to cause deformation.

7.11. Results and Discussion.

The results of the XPS/Auger analyses shown in table 7.3. can now be interpreted with additional evidence from CEMS, photomicrographs, and SEM photographs. The compounds suggested to be present on the surfaces of oxidised pentlandite can also be related thermochemically using partial pressure diagrams (figure 7.11.) and Eh/pH diagrams (figure 7.12.).

In general, the spectroscopic methods used suggest an iron-rich surface with iron oxides, hydroxides and sulphates, and a depletion of iron at depth with respect to nickel, leading to the formation of violarite. Although the alteration to violarite appears rapid, the extent of the oxide layer is limited to about 10 to 50Å, which indicates relatively little extensive oxidation. The lack of further violarite oxidation is not surprising, considering the oxidation characteristics determined in chapter 6. After oxidation of the pentlandite surfaces, compositional variations are detected that depend on the oxidants used.

Prominent on all of the surfaces studied are iron sulphates and iron oxides and hydroxides, with a ratio of Fe^{2+} to Fe^{3+} which, in general, decreases with the effective strength of the oxidant used. The formation of these compounds is important to the oxidation of pentlandite, since this is probably linked to the initial stages of iron depletion in the surface.

The partial pressure diagram (figure 7.11.) shows the stabilities of Fe_3O_4 (magnetite), Fe_2O_3 (hematite), and iron sulphates after pentlandite oxidation. Similarly, with respect to Eh/pH diagrams (figure 7.12.) the same oxides are also suggested to be stable, although sulphates may be expected to be taken into solution. In interpreting the spectroscopic information, the principal Fe^{2+}-bearing compound is probably magnetite. The Fe^{3+}-bearing compounds

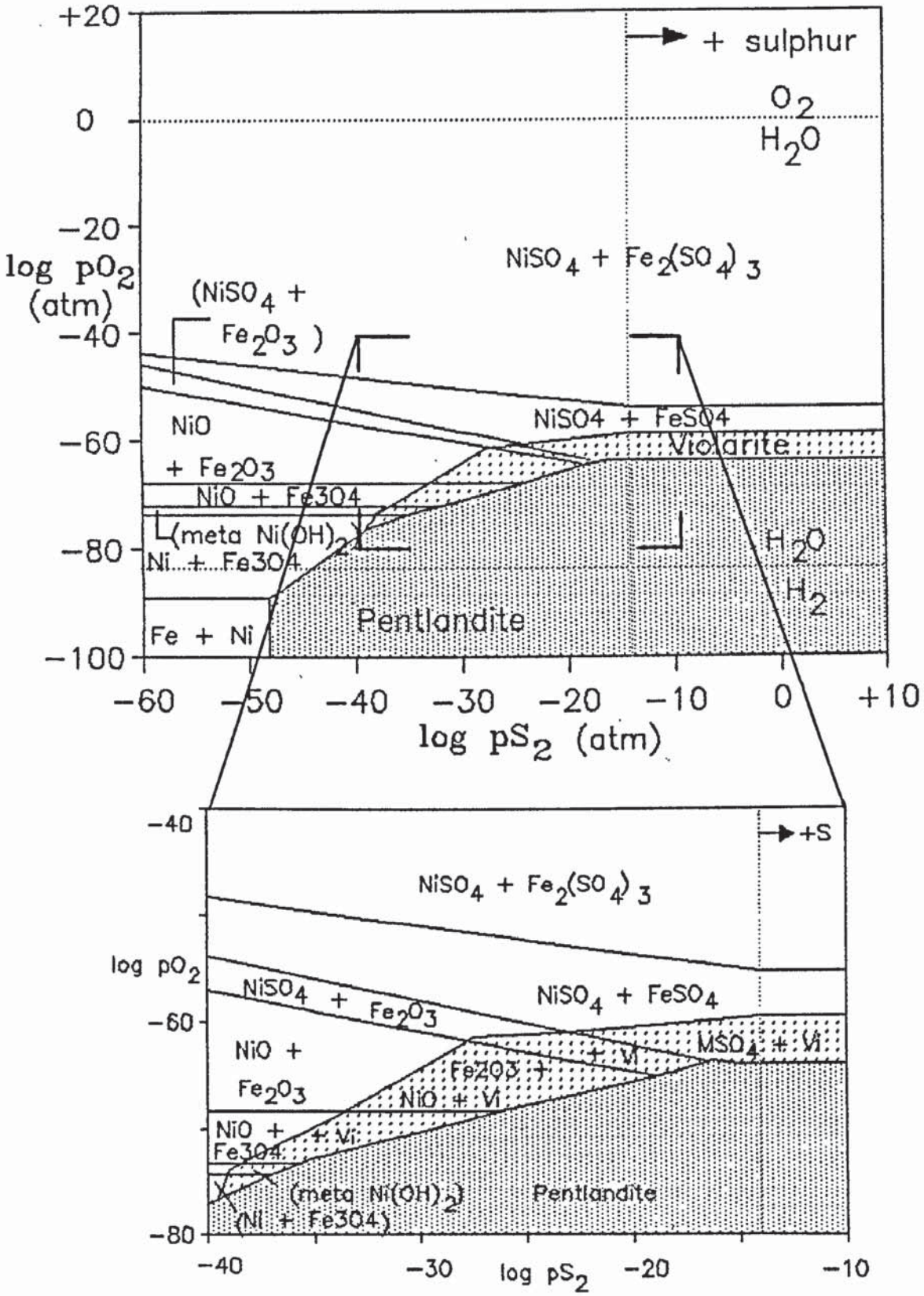

Figure 7.11. Partial pressure diagram (log pO_2/log pS_2) for pentlandite oxidation. (Equations and free energies of formation for the component phases contained in Appendix 4.)

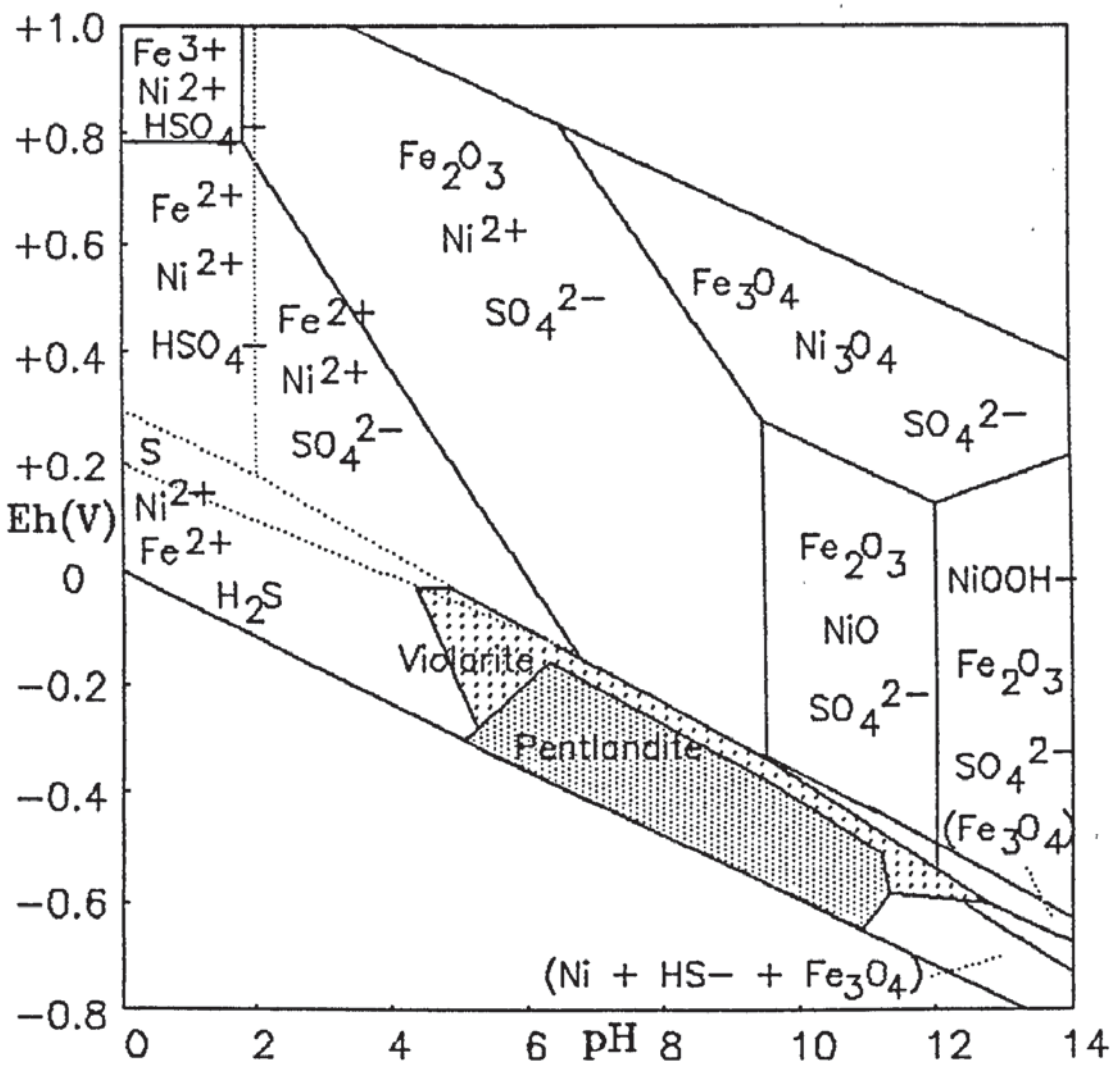

Figure 7.12. Eh/pH diagram for pentlandite oxidation with respect to violarite. The phase boundaries were determined for log [S] = -2 and for log [Fe] (log [Ni]) = -6. (Equilibria and free energies for the phases contained in Appendix 4.

occur in a number of forms, with hematite, FeOOH, $Fe(OH)_3$ as possible components. FeOOH is unstable in the thermochemical diagrams with respect to hematite, although as suggested for other sulphides, and from natural oxidation, FeOOH is expected to be the dominant Fe^{3+} phase in aqueous oxidation.

Apart from the nickel-enrichment in the pentlandite surfaces, leading to the formation of violarite, nickel-containing compounds are largely absent from the oxide-rich immediate surface, being detected in the electrochemically and furnace oxidised samples only. This may be as a result of dissolution rates, where the nickel compounds are formed in the surface and then dissolved. Considering this possibility, dissolution would play no part in the furnace oxidation, and the presence of nickel oxide in the electrochemically oxidised surfaces is probably due to an oxidation rate that supersedes the rate of dissolution.

In considering the nature of the nickel species in the surface region, it has been inferred that the nickel is either present as sulphides or nickel oxide. The nickel-containing oxides developed after oxidation may also be interpreted as either nickel oxide or iron-nickel oxides, for example trevorite, $NiFe_2O_4$. Since the spectroscopic methods used cannot differentiate between the phases, the oxide of nickel detected is reported as NiO.

The sulphur (0), detected by XPS may be interpreted as elemental sulphur since there is no evidence for the formation of either polysulphides or thionates, other compounds that would possibly account for the sulphur (0). Considering that the pentlandite to violarite transformation occurs without a sulphur loss, the formation of sulphur and sulphates indicates that pentlandite is altering directly, or ultimately via violarite, to more-oxidised phases.

In considering the oxidation of pentlandite and subsequent violarite formation, a simplified half-cell equation may be used;

$$Fe_{4.4}Ni_{4.4}S_8 \rightarrow 2FeNi_2S_4 + 2.4Fe^{2+} + 0.4Ni^{2+} + 5.6e$$

- which suggests an anodic reaction and the leaching of metal ions from the surface, favourable in the oxidising environments. The

transformation indicates loss of iron as a major factor in the oxidation, which probably promotes the reaction.

Reactions relating to the stability of pentlandite, with respect to violarite, are given in Appendix 4, and used for the construction of partial pressure and Eh/pH diagrams. However the actual alteration taking place is too complex to explain by simple equations, as has been attempted for other minerals in this work.

The oxidation of pentlandite surfaces can be summarised as follows. Primary alteration of the surfaces proceeds rapidly with the oxidised surface developing iron compounds at a faster rate than nickel compounds. This phenomenon is shown in the analyses of furnace oxidised pentlandite where no dissolution process can take place, and nickel oxide is detected. Where dissolution is a factor, the nickel compounds are further depleted. Variations in the surface compositions are a consequence of the thermochemical stability of the various oxidation products in the oxidising media.

After initial rapid oxidation, an iron-rich oxidised layer is developed. This layer may act as an inert barrier preventing further rapid oxidation into the surface. Subsequent oxidation would then proceed by diffusion through the oxidised layer, resulting in further preferential iron loss. Consequently, the iron-deficient sub-surface sulphide transforms from pentlandite to violarite. This is comparable to the Buckley & Woods (1983) model for the sub-surface copper enrichment of bornite (Cu_5FeS_4) to copper sulphides.

CHAPTER 8.

CHALCOPYRITE

8. Chalcopyrite.

8.1. Introduction.

Chalcopyrite ($CuFeS_2$) is a major sulphide mineral and is also the main source of the world's supplies of copper (Habashi, 1978; Ramdohr, 1980; Craig and Vaughan, 1981). As such, chalcopyrite has been the subject of numerous investigations concerning its alteration in the supergene environment, during mineral processing and laboratory oxidation.

The spectroscopic analysis of oxidised chalcopyrite surfaces has also been the focus of several studies. However, in the context of this work, further investigations are necessary in order to determine the effects of different oxidants and to compare the oxidation phenomena observed relative to those observed in other sulphide minerals.

As a major copper-containing mineral in primary ore assemblages, the alteration of chalcopyrite is a controlling factor in the distribution of copper in the weathered ores. In this respect, it is similar to pentlandite, the phase controlling the distribution of nickel in weathered ores (chapter 7). Indeed, as will be shown later, the observed characteristics of chalcopyrite and pentlandite oxidation show similar phenomena.

The nature of the alteration of chalcopyrite in supergene environments, as investigated by previous workers, is outlined in section 8.2. Previous spectroscopic studies of chalcopyrite oxidation are discussed in the light of the present work in section 8.7.

8.2. Previous work on chalcopyrite oxidation.

As a major ore mineral and source of copper, the oxidation characteristics of chalcopyrite have been studied extensively. Concerning natural occurrences, a comprehensive review of chalcopyrite replacement and alteration is given by Ramdohr (1980).

Ramdohr (1980) reports that the alteration of chalcopyrite due to oxidation may take a number of forms, of which the replacement

by hematite (Fe_2O_3) and magnetite (Fe_3O_4), associated with the formation of bornite (Cu_5FeS_4) or chalcocite (Cu_2S) are common. Weathering may proceed directly to limonite (hydrated ferric oxide); however, a thin layer of chalcocite or covelline (CuS) may precede this. In supergene zones Ramdohr (1980) reports a zone passing from minerals poor in copper to minerals rich in copper (ie. chalcopyrite → bornite → covelline → chalcocite). The presence of chalcopyrite as overgrowths in hypogene environments, although found rarely, also indicates some stability in copper-rich solutions, indicating that chalcopyrite may be stable in both primary and hypogene assemblages.

Steger (1977) and Steger & Desjardins (1978) reported the results of laboratory oxidation of chalcopyrite in humidity chambers, and the analysed surfaces were characterised chemically. Steger (1977) suggested that iron sulphate, thiosulphate, and to some extent, goethite (FeOOH) were the main oxidation products. Steger & Desjardins (1978) reported the dominant oxidation products to be metal sulphates (both iron and copper), with metal thiosulphate forming as an intermediary product. Minor quantities of goethite and elemental sulphur were also determined.

Numerous authors investigating the effects of chalcopyrite leaching as a method for concentrating copper during extraction, have also determined the alteration products of chalcopyrite. Forward & Mackiw (1955) noted that the use of ammonia to leach chalcopyrite, resulted in copper enrichment forming covelline, with the dissolution of sulphates and thiosulphates. Majima & Peters (1966) reported the enhanced oxidation of chalcopyrite in caustic solutions (NaOH) and suggested that covelline and chalcocite were major copper-containing products, and inferred that the low elemental sulphur yield was due to the reduction of cupric ions by sulphur forming the copper sulphide products. A comprehensive review of copper sulphide leaching was presented by Wadsworth (1972).

Peters (1976) outlined the importance of Eh/pH diagrams in determining the products of chalcopyrite oxidation, especially with respect to the sulphur species present, in varying pH conditions, and the effect this has on the copper-enrichment of the sulphides formed. Ferreira & Burkin (1975) reported a gradual copper enrichment of the

'chalcopyrite' during acid leaching, with the formation of non-stoichiometric copper-iron sulphides. Letowski (1979) has also shown that although copper becomes enriched in the remaining solid phases, it is also taken into solution as sulphates. The activity of both ferric and ferrous ions in the acid leaching environment was also suggested to be important in the oxidation of the chalcopyrite.

8.3. Chalcopyrite characterisation.

Attempts to produce a homogeneous synthetic chalcopyrite were unsuccessful, largely due to the formation of reaction rims showing both copper-iron sulphides and copper sulphides. For this reason, a natural chalcopyrite sample was chosen that contained as few contaminants as possible.

The chalcopyrite used in this work was from the collection of the Geology Dept. of Aston University, and is of unknown origin. A sample of chalcopyrite was selected and sliced into parallel layers, such that the crystallographic orientation was, as far as possible, unchanged during the oxidation of the surfaces; however, the chalcopyrite probably contains several crystals and as such, this preparation may be unnecessary. The mineral was analysed using XRD, SEM (EDS) and by electron microprobe analysis. All of these showed the sample to be very pure chalcopyrite. The electron microprobe results are given in table 8.1.

Table 8.1. Electron microprobe data for the chalcopyrite used in this investigation.

	Cu	Fe	S
Chalcopyrite (At%)	21.52 +/- 0.25	22.01 +/- 0.11	45.02 +/- 0.17
Formula	0.96	0.98	2.00
Impurities	0.02% Sb	0.01% As	(0.003% Ag)

The formula determined in table 8.1. shows agreement with the expected composition of chalcopyrite. The lack of any indication, by electron microprobe and the other analytical methods, of other elements suggests a reasonably pure chalcopyrite sample.

8.4. Reflectance data.

Spectral reflectance measurements of unoxidised chalcopyrite surfaces are in agreement with the spectrum described in the IMA/COM data file (Stanley & Criddle, 1986). Data for the unoxidised chalcopyrite surface and for surfaces after oxidation in various media are shown in table 8.2. The surfaces are moderately bireflectant and the data given are both an average of the minimum and maximum reflectance values obtained for each point, and of several points on the sample surface.

Table 8.2. Reflectance measurements for unoxidised chalcopyrite and for chalcopyrite surfaces after oxidation by a range of oxidants.

	Reflectance (R%)				
Oxidation method	470nm	546nm	589nm	650nm	ΔR(*)
Unoxidised (R^o)	32.7	44.4	46.2	46.7	
Air/oxygen (150°C)	31.2	42.8	44.9	45.3	3.4
Steam	28.9	40.9	42.5	43.0	8.6
NH_4OH	23.2	34.6	36.9	37.3	22.4
H_2O_2	12.4	16.5	18.2	20.6	60.2
Electrochemical (0.8V)	10.7	13.8	15.3	17.8	66.1
H_2SO_4	9.5	12.1	14.2	15.4	69.9

* ΔR = average change in reflectance = $(R^o-R^1)/R^o \times 100$

The different methods of oxidation, as observed from the reflectance data, show a considerable range of effectiveness. The reflectance changes may be used as indicators of the extent of oxidation, since these are roughly proportional to the depths of

oxidation determined using chemical spectroscopic methods. The physical effects of oxidation are shown by photomicrographs (figures 8.7. to 8.9.) and an SEM photograph (figure 8.10.), that are discussed in section 8.9. with respect to the determined chemical characteristics of the surfaces.

8.5. Auger Electron Spectroscopy.

It was evident from the differentiated Auger spectra of the unsputtered chalcopyrite surface and of the surfaces after depth profiling, that the extent of chalcopyrite oxidation by different methods is variable. The oxygen content of the surfaces, as shown in depth profiles, appears to be proportional to the extent of oxidation indicated by the reflectance spectra. As observed during the analysis of other sulphides, the oxygen content of chalcopyrite surfaces is inversely proportional to the sulphur concentration.

The depth profiles of chalcopyrite surfaces oxidised by air/oxygen (at 150°C in a furnace) and by steam show a rapid decrease in oxygen with depth, indicating an estimated depth of oxidation of approximately 30Å. After 45 minutes of sputtering, these surfaces indicate elemental concentrations that are in accordance with the expected elemental ratios in unoxidised chalcopyrite. The ammonium hydroxide oxidised surface shows a greater oxidation depth, estimated to be in the order of 60Å.

In contrast to this limited oxidation, several oxidised surfaces show very large oxidation depths (H_2O_2, electrochemical and sulphuric acid oxidation). A factor apparent in the Auger depth profiles of these more oxidised surfaces, shown in figure 8.1., is the relative enrichment in copper with depth. It could be expected that copper would be depleted due to 'knock-on' effects as a result of sputtering (outlined in chapter 2, section 2.1.3.), so the copper enrichment may well be even greater than that suggested from the depth profiles.

An AES study of chalcopyrite oxidation was performed by Eadington (1977). Surfaces were oxidised by both oxygen (under

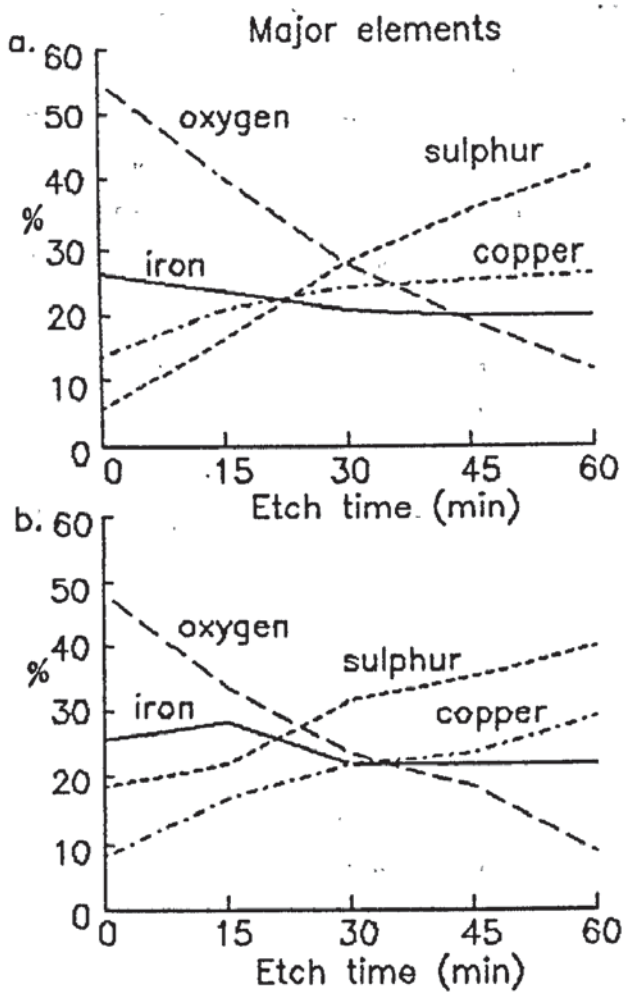

Figure 8.1. Auger depth profiles for chalcopyrite surfaces oxidised by (a) hydrogen peroxide and (b) sulphuric acid. The etch rate is estimated to be approximately 1Å min^{-1} so the etch time scale may also be used as an estmated depth scale in Angstroms.

pressure) and by water. In both oxidation methods, an increase in copper with respect to iron was suggested. The results determined by Eadington (1977) are comparable to those determined for aqueous oxidants, but are not in agreement with those from air/oxygen (150°C) oxidation. Surface compositions were not proposed by Eadington, however, with the additional evidence available from XPS, the copper-enrichment of oxidised chalcopyrite surfaces may be explained in terms of their chemical compositions as suggested in section 8.6.

A study of a chemically similar mineral, bornite (Cu_5FeS_4), undertaken by Losch & Monhemius (1976), suggested a reduction of the copper peak intensities after argon ion sputtering, inferred to be due, all or in part, to knock-on effects (and the effect on copper, and, in particular, the reduced copper in the surface, is discussed in chapter 2, section 2.1.3). With reference to the copper concentration observed in this work, it may be that knock-on effects are not a major factor in this case, or that the copper-enrichment is larger than suggested.

8.6. X-ray Photoelectron Spectroscopy.

The interpretation of the x-ray photoelectron spectra of oxidised chalcopyrite surfaces introduces problems in determining the chemical compositions of the surfaces, due to the masking of potentially relevant information by peak overlaps, and also due to apparently contradictory evidence from spectra obtained from the same oxidised surface. To illustrate this problem, the Fe 2p, S 2p and Cu 2p 3/2 x-ray photoelectron spectra (figures 8.2 to 8.4.) are presented for unoxidised, steam oxidised and sulphuric acid oxidised surfaces. The oxidised chalcopyrite surfaces did not require any preliminary argon ion sputtering to remove contaminants, eliminating the possibility of any artifacts forming in the sample surfaces.

The spectra of unoxidised chalcopyrite were used to fit standard peaks at 707.4eV for Fe 2p 3/2, 932.6eV for Cu 2p 3/2 and 161.4eV for sulphur 2p. Previous determinations of chalcopyrite binding energies (Clifford et al., 1975; Nakai et al., 1978; Brion, 1980; Holloway et

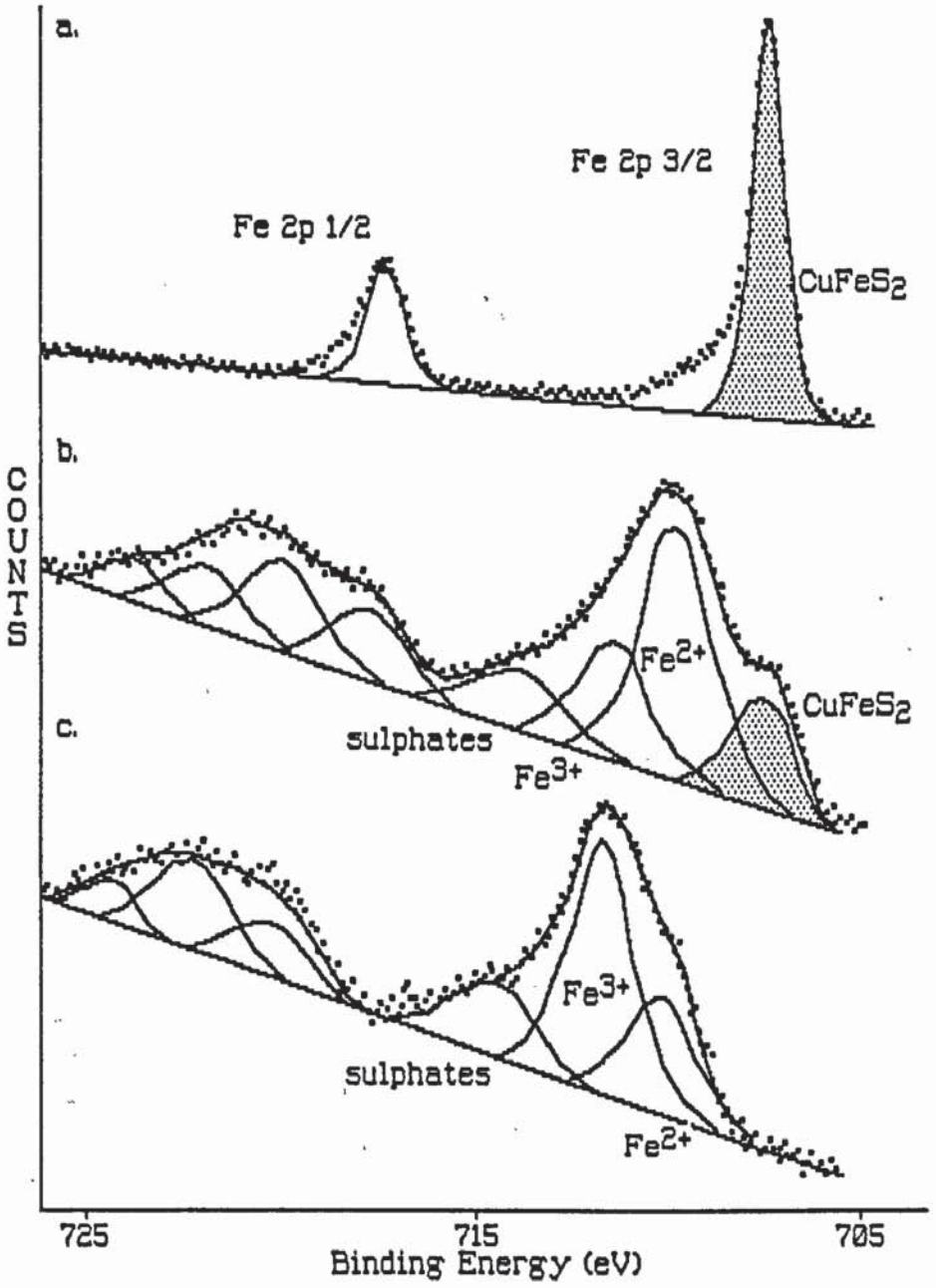

Figure 8.2. Iron 2p (1/2 and 3/2) x-ray photoelectron spectra obtained for (a) unoxidised chalcopyrite and for chalcopyrite oxidised by (b) steam and (c) sulphuric acid.

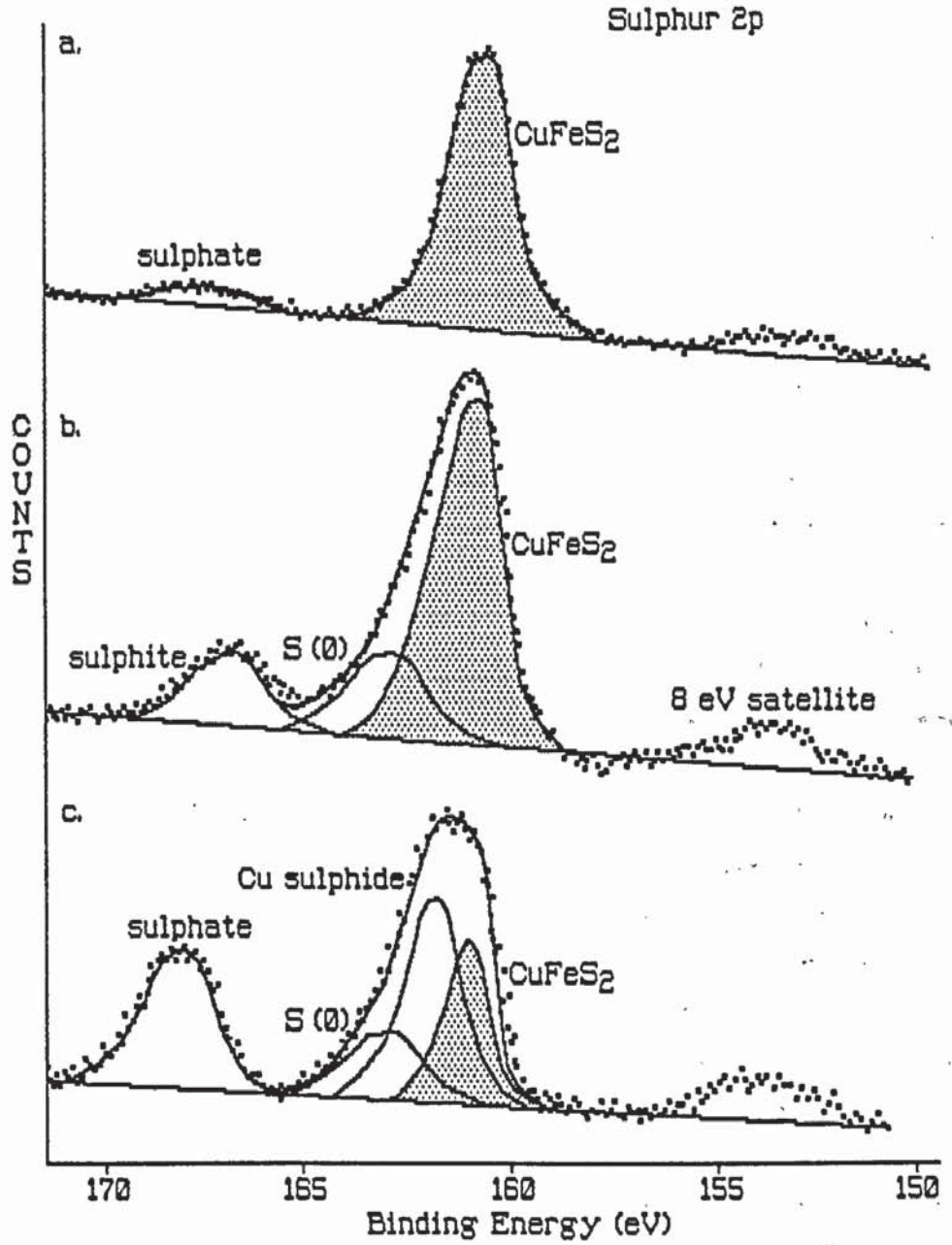

Figure 8.3. Sulphur 2p x-ray photoelectron spectra obtained for (a) unoxidised chalcopyrite and for chalcopyrite oxidised by (b) steam and (c) sulphuric acid.

al., 1981; Tossell et al., 1982; Buckley and Woods, 1984a&b) are numerous, and are either in agreement or show close values to those determined in this work.

The Fe 2p 3/2 x-ray photoelectron spectra illustrate the variation in oxidation effects (figure 8.2). The unoxidised spectrum shows that shake-up effects (discussed in chapter 2, section 2.2.2.) are a minor phenomenon, but considering the depths of oxidation determined, and the number of compounds present, the effect on the peak area calculation is likely to be minimal. The peaks were fitted to iron in different valence states, rather than specific iron compounds, to avoid the problems of overlap, as discussed in previous chapters.

After oxidation by air/oxygen (150°C) and steam oxidation, chalcopyrite is still a major component in the surfaces, less so after ammonium hydroxide oxidation. After oxidation in hydrogen peroxide, sulphuric acid and after electrochemical oxidation, the Fe 2p 3/2 spectra show no evidence of chalcopyrite, although this is only the case for the Fe 2p spectra. In all the oxidised surfaces a minor component of iron oxy-sulphate was fitted to the spectra.

The sulphur 2p spectra reflect the degree of oxidation of the surface as shown by the Fe 2p 3/2 spectra; however, the fitting of these spectra is more complex due to peak overlaps. A minor component of oxysulphates can be fitted to the spectra of all the oxidised chalcopyrite surfaces, and the peak position in steam oxidation, show in figure 8.3. suggests the formation of sulphites. A proportion of the oxysulphates detected in furnace and NH_4OH oxidation is also due to sulphites, whilst sulphates are the only oxy-sulphate compounds of the heavily oxidised surfaces. Sulphur (0) is a minor component, and is suggested to be due to elemental sulphur, although the potential for a contribution from polysulphides to this peak cannot be ruled out, as discussed later.

For the heavily oxidised surfaces, it was not possible to obtain accurate fits to the spectra, assuming oxysulphates, sulphur (0), and chalcopyrite to be present. Accurate fits have been obtained by adding a contribution from 'copper sulphides', although their exact compositions are difficult to determine from the spectra. An

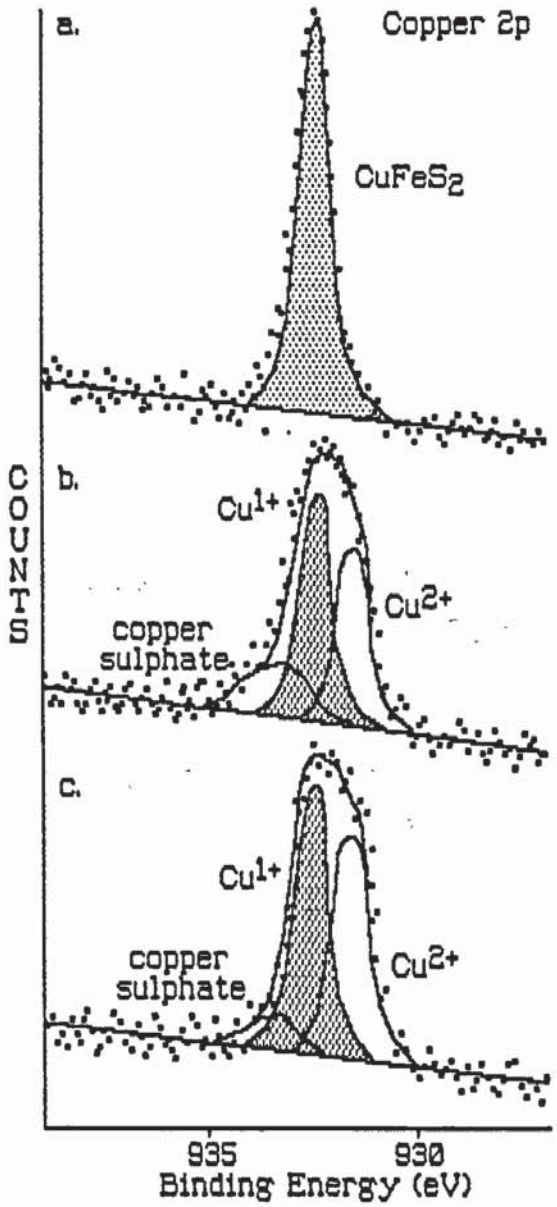

Figure 8.4. Copper 2p 3/2 x-ray photoelectron spectra obtained for (a) unoxidised chalcopyrite and for chalcopyrite oxidised by (b) steam and (c) sulphuric acid.

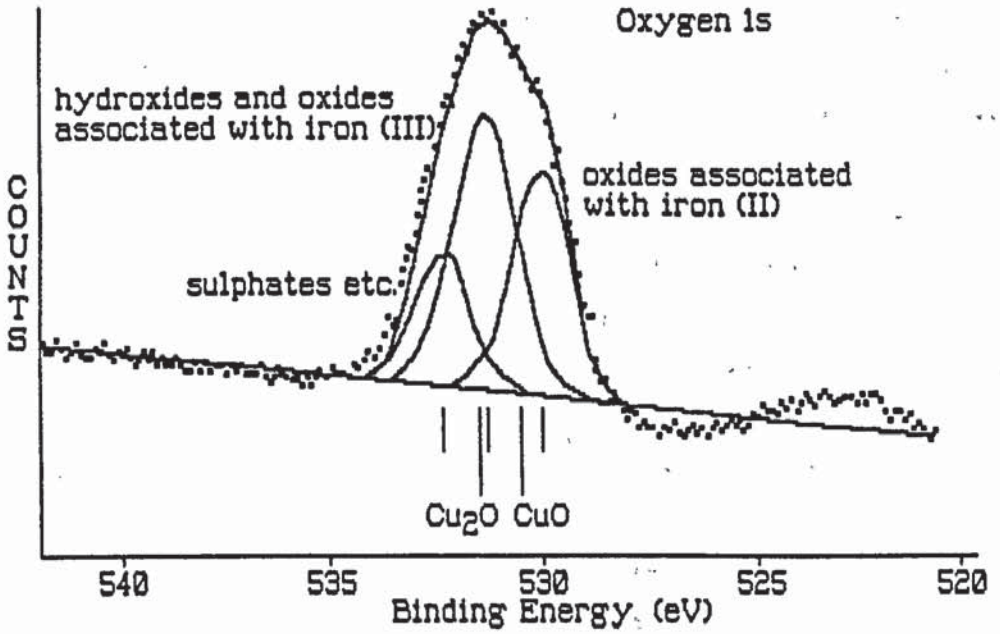

Figure 8.5. Oxygen 1s x-ray photoelectron spectrum for chalcopyrite oxidised by sulphuric acid, showing the problems encountered where possible contributory peaks overlap.

additional problem is the presence of a peak due to chalcopyrite, contrary to the evidence of the Fe 2p 3/2 spectra, and with a peak area that is greater than that expected if the peak is purely an effect of the greater escape depth of the sulphur 2p electrons (with greater kinetic energies). A possibility is the formation of a copper-rich sulphide, such as bornite, but since there is no Fe 2p 3/2 contribution, copper sulphides seem more likely.

The copper 2p spectra, shown in figure 8.4., are less well resolved, but it is possible to determine, in general, the composition of the copper-containing oxidation products. Important here, is the presence of copper sulphates, which are not completely dissolved from the surface, as might be expected when considering their high solubility. The sulphide component, to which chalcopyrite produces a contribution may also be fitted as copper (I) in other sulphides. The broadening on oxidation evident in figure 8.4. may be due to the presence of both copper (I) and copper (II) sulphides. This would account for the sulphide contribution to the sulphur 2p spectra. However, the possibility of copper (I) and copper (II) oxide formation must also be considered.

The use of oxygen 1s spectra cannot resolve the problem since the copper oxides overlap with the iron oxides and hydroxides. The situation is shown in figure 8.5., where the spectrum for a sulphuric acid oxidised surface is fitted accurately using the iron compounds only. It would also be possible to fit copper oxides to this spectrum, with the binding energies shown, and produce an accurate fit. For this reason, the oxygen 1s spectra are unreliable for the analysis of chalcopyrite surfaces.

8.7. Interpretation of the spectroscopic results.

The fitted x-ray photoelectron spectra and the elemental compositions inferred from the differentiated Auger spectra were used to estimate the surface compositions of the oxidised chalcopyrite. The deconvolution of the x-ray photoelectron spectra is incomplete for some surfaces, leading to possible inaccuracies. In table 8.3.

general surface compositions are presented, restricted in terms of the valence states determined, for a surface layer of approximately 10-15Å depth, as determined by the depth resolution of the XPS.

Table 8.3. General surface compositions from XPS/AES analyses (estimated molecular percentages).

Phase	Method of Oxidation					
	air/oxygen	steam	NH_4OH	H_2O_2	elec.	H_2SO_4
Fe II/III sulphate	4.8	-	6.3	15.6	14.3	15.3
Fe II sulphite	4.8	7.6	7.1	-	-	-
Cu I/II sulphate	-	1.9	-	-	4.5	3.8
Fe III (oxides &	26.0	23.8	40.2	27.5	29.5	35.5
Fe II hydroxides)	33.7	33.3	22.3	27.5	25.0	22.5
S (0)	3.8	4.8	2.7	3.7	2.7	3.1
Cu_2S - chalcocite **	-	1.9	3.6	11.9	13.4	11.4
CuS - covelline **	-	7.6	4.5	11.9	8.9	7.6
$CuFeS_2$ *	26.9	19.0	13.4	1.8	1.8	0.7

* The determination of chalcopyrite is hindered by the incomplete deconvolution of the Fe 2p 3/2, Cu 2p 3/2 and S 2p x-ray photoelectron peaks, and the inconsistent information obtained. This may suggest the formation of bornite (Cu_5FeS_4), accounting for the weak Fe 2p 3/2 response and strong responses from the Cu 2p 3/2 and S 2p in the chalcopyrite fits.

** A component of this may need to be attributed to copper I & II oxides.

It appears that copper sulphides are a major component of the altered surface, and although determinations of their proportions are presented in table 8.3., they may be inaccurate due to the possibility

of bornite forming in the oxidised surface and a possible underestimate of the extent of copper oxide formation.

The sulphur (0) detected may be attributed to elemental sulphur, although a proportion of it may be due to copper polysulphide formation (since the copper sulphides are not specifically identified).

Major surface components are suggested to be iron II & III oxides and hydroxides. Identification of the actual phases present is not possible, although certain phases may be predicted from the proportions determined. In the case of ammonium hydroxide oxidation, the large $Fe^{3+}:Fe^{2+}$ ratio may be attributed to hydroxyl ion oxidation, forming iron III hydroxides. Discounting the NH_4OH oxidation, the extent of oxidation is reflected by the increased presence of iron III oxides and hydroxides.

8.8. Conversion electron Mössbauer spectroscopy.

A conversion electron Mössbauer spectrum of unaltered chalcopyrite was fitted with a six-peak spectrum showing an isomer shift of 0.219 mms^{-1} and a magnetic splitting caused by an internal field of 323kOe.

After oxidation, as shown in figure 8.6., a quadrupole doublet with parameters of 0.410mms^{-1} for the isomer shift and 0.68mms^{-1} for the quadrupole splitting is observed. In considering possible surface components, the quadrupole doublet may be attributed to βFeOOH or γFeOOH. The percentage contribution from unaltered chalcopyrite compared with the β or γFeOOH is less than expected considering the data from XPS and AES, and a possible reason for this, as part of a model of oxidation, is proposed in section 8.11. The outer region of the spectra suggest an unfitted contribution from magnetite.

8.9. SEM and optical microscopy.

The chemical characterisation of the surfaces described in previous sections can be related to the physical nature of the surfaces as seen in photomicrographs and SEM photographs.

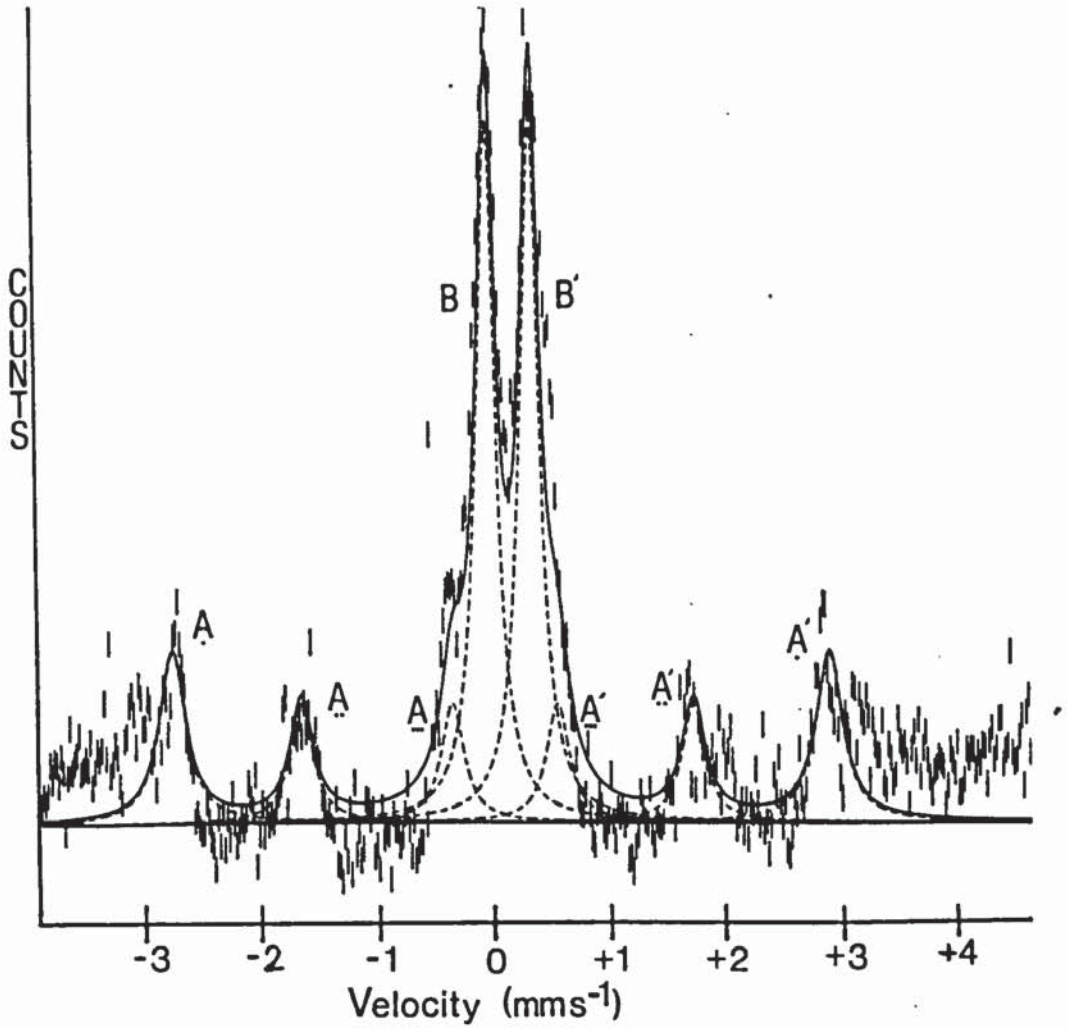

Figure 8.6. Conversion electron Mössbauer spectrum for chalcopyrite oxidised by sulphuric acid. The six peak magnetically split chalcopyrite spectrum (A) is evident, along with an oxidation product (B), suggested to be due to γFeOOH.

After oxidation by air/oxygen (150°C), the chalcopyrite is altered only slightly. A similar altered surface is obtained after steam oxidation (figure 8.7.), and shows the development of a brown tarnish. Ammonium hydroxide also shows an increased tarnish (relative to steam oxidation). These three less oxidised surfaces all show differing degrees of fairly uniform brown tarnishing across the surfaces, and with respect to the spectroscopically determined phases present in the altered surfaces (table 8.3.), the main components are suggested to be iron II and III oxides and hydroxides, which in the case of furnace oxidation is possibly magnetite (Fe_3O_4), and in the steam and hydroxide oxidation the major components are probably iron oxy-hydroxides and hydroxides.

After extensive oxidation by electrochemical methods, and by hydrogen peroxide and sulphuric acid, pitting of the sample surface is observed and the formation of blue and red zones on the sample surface (shown in figures 8.8. and 8.9.). The brown tarnishing is also observed, but is masked by the overlying coloured oxidation products. In figure 8.8, the hydrogen peroxide oxidised surface shows red alteration, which has evidence of dendritic growth across the surface, with blue zones overlying this. It could be inferred that the blue colouration is induced by the optical effects of a thickening oxidised layer. This may not be the case, since in comparison to figure 8.9., which shows sulphuric acid oxidation, the blue zones form directly on the slightly tarnished chalcopyrite surface, whilst also producing dendritic growths, suggesting that the red and blue colours may be caused by specific alteration products.

Considering the chemical phases present on the oxidised surfaces, the blue/red zones could result from a combination of iron sulphates and the copper sulphide enrichment determined spectroscopically.

SEM photographs only exhibit alteration on the heavily oxidised surfaces, in which amorphous alteration products are observed that tend to form flakes on the surfaces. This is shown in figure 8.10. for an electrochemically oxidised surface, which is also characteristic of the oxidation produced by both hydrogen peroxide and sulphuric acid.

Figure 8.7. Photomicrograph of a chalcopyrite surface after steam oxidation. (Width of field = 1.5mm, magnification = 67x)

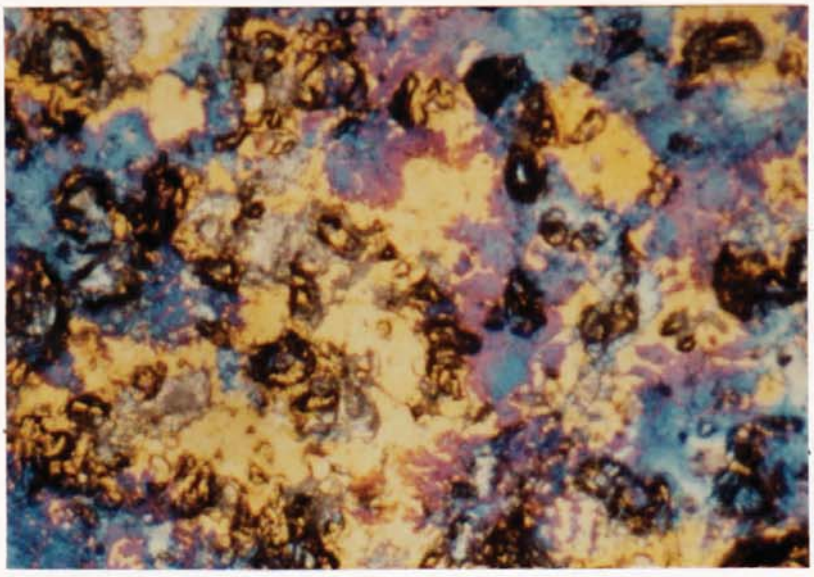

Figure 8.8. Photomicrograph of a chalcopyrite surface oxidised by hydrogen peroxide. (Width of field = 1.5mm, magnification = 67x)

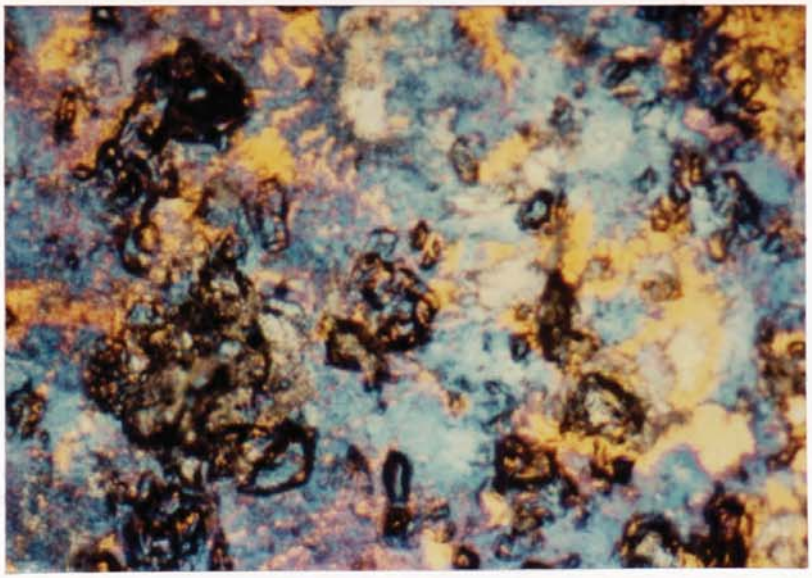

Figure 8.9. Photomicrograph of a chalcopyrite surface oxidised by sulphuric acid. (Width of field = 1.5mm, magnification = 67x)

Figure 8.10. SEM photograph of an electrochemically oxidised chalcopyrite surface. (Width of field = 120μm, magnification = 840x)

8.10. Previous spectroscopic analysis of chalcopyrite oxidation.

The study of chalcopyrite oxidation using x-ray photoelectron spectroscopy has been the focus of several previously published works. These are briefly reviewed in order to compare them with this work.

Holloway et al. (1981) studied polishing effects on chalcopyrite surfaces using XPS, AES and microreflectometry. It was suggested that the chemical alteration of chalcopyrite, produced a copper enrichment of the sulphide (forming bornite), an iron oxide (suggested to be mainly magnetite), FeOOH and hydrated iron sulphate. A reaction mechanism was considered in which it was inferred that the copper in the sulphide sub-surface remains bonded to sulphur during the alteration.

Buckley & Woods (1984a&b) investigated the nature of chalcopyrite oxidation by a range of oxidants and suggested an iron enrichment at the surface resulting in the formation of iron oxy-hydroxide. The alteration of the chalcopyrite was suggested to lead to the formation of a copper-enriched species, suggested to be CuS_2 (or $Cu_{0.8}S_2$). It was considered that the CuS_x phase could be interpreted as copper polysulphide, and that this may result from a loss of some copper and, more importantly iron, forming a metal-deficient sulphide with a similar sulphur lattice to that of chalcopyrite. Buckley et al. (1985) further extended this model to include the suggested formation of iron III hydroxides in the iron-rich immediate surface.

These interpretations are generally in agreement with the data obtained in the present work and are discussed in the next section.

8.11. Results and discussion of chalcopyrite oxidation.

The oxidation products formed on the surface of chalcopyrite can be inferred to be mainly a function of the strength and pH of the oxidant used. However, the extensively oxidised surfaces show

characteristics that may be controlled by the sub-surface copper-enrichment of chalcopyrite to form copper sulphides.

The characterisation of oxidised chalcopyrite surfaces may be re-assessed in terms of thermochemically stable phases. This is necessary in order to suggest specific phases present for the iron II and iron III compounds and to show the stability relations of the copper sulphides with respect to chalcopyrite. The stability relations in the system Cu-Fe-S-O-H are represented by a partial pressure diagram (figure 8.11.) and an Eh/pH diagram (figure 8.12.). Although the Eh/pH diagram is limited in terms of the fixed conditions shown in this diagram, the inter-relationship between the compounds suggested is still relevant.

The stable iron III oxide component in these diagrams is determined to be hematite (Fe_2O_3), although FeOOH may be considered to be stable in aqueous environments. Similarly, magnetite (Fe_3O_4) is unstable in acid environments, although it may form in the sub-surface where it is protected from the effects of oxidising solutions. The proportions of iron II and III species in the altered chalcopyrite surfaces indicate that in the extensively oxidised surfaces (H_2SO_4, H_2O_2 and electrochemical) the major components are probably FeOOH, (and possibly minor Fe_2O_3) and magnetite (Fe_3O_4) as indicated by the greater concentration of iron III phases. After NH_4OH oxidation the formation of iron III hydroxide or FeOOH would account for the increased proportion of iron III phases. The formation of FeOOH is also indicated by the CEMS spectra. In air/oxygen (150°C in a furnace) and steam oxidation the chalcopyrite surfaces show iron II phases to be dominant which probably indicates the formation of magnetite and wüstite ($Fe_{1-x}O$).

The spectroscopic data show the less oxidised surfaces to contain iron oxy-sulphate phases, in particular sulphites, whereas for the more oxidised surfaces, sulphates are the major phases. Copper sulphates are only a minor component in the oxidised surfaces, due to their high solubility.

The alteration of chalcopyrite to copper sulphides can be considered in the light of the thermochemical diagrams. The diagrams have been simplified, and do not show the zones of stability of

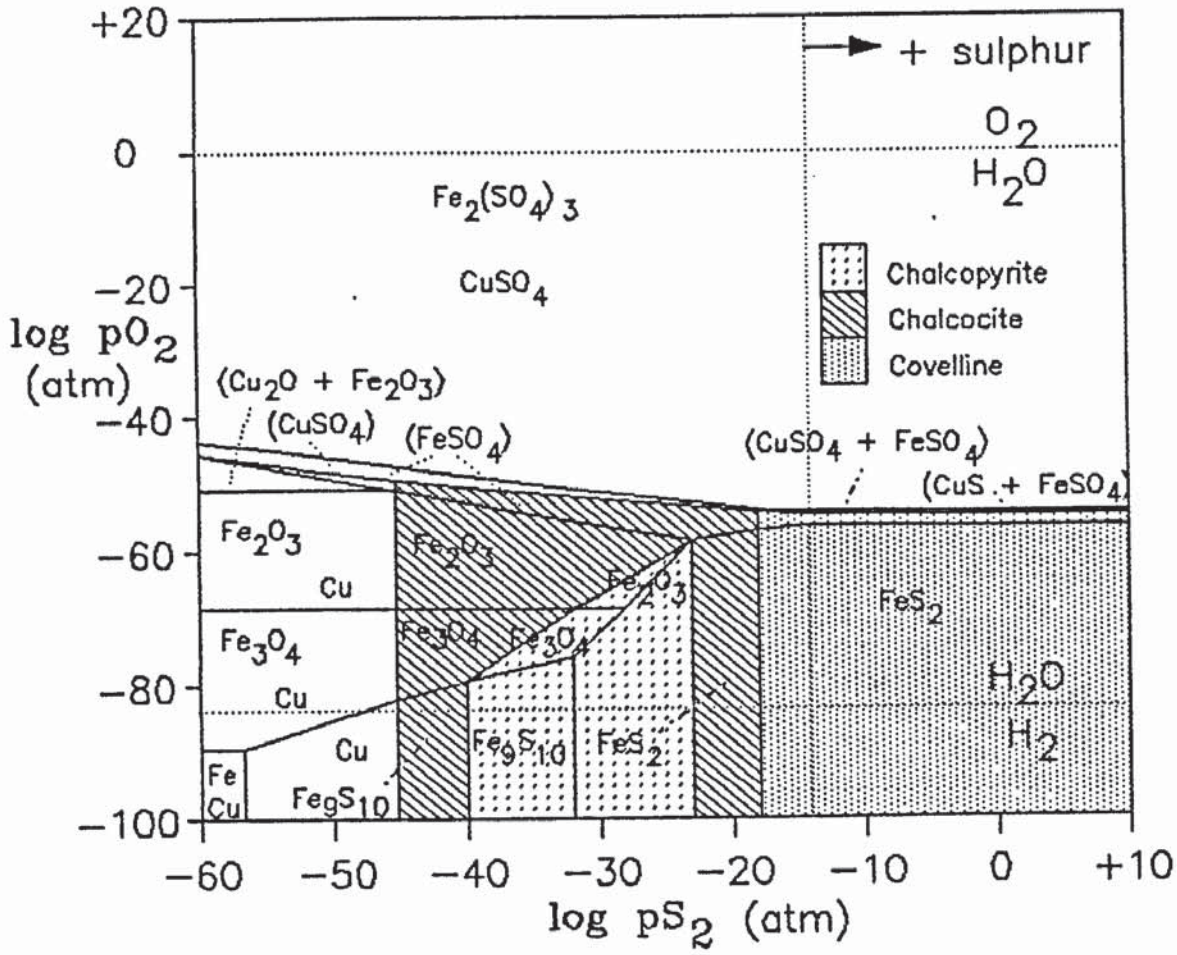

Figure 8.11. Partial pressure diagram (log pO_2/log pS_2) for oxidised chalcopyrite. This is simplified by not showing some copper-iron sulphides such as bornite. (Equations and free energies of formation for the component phases contained in Appendix 4.)

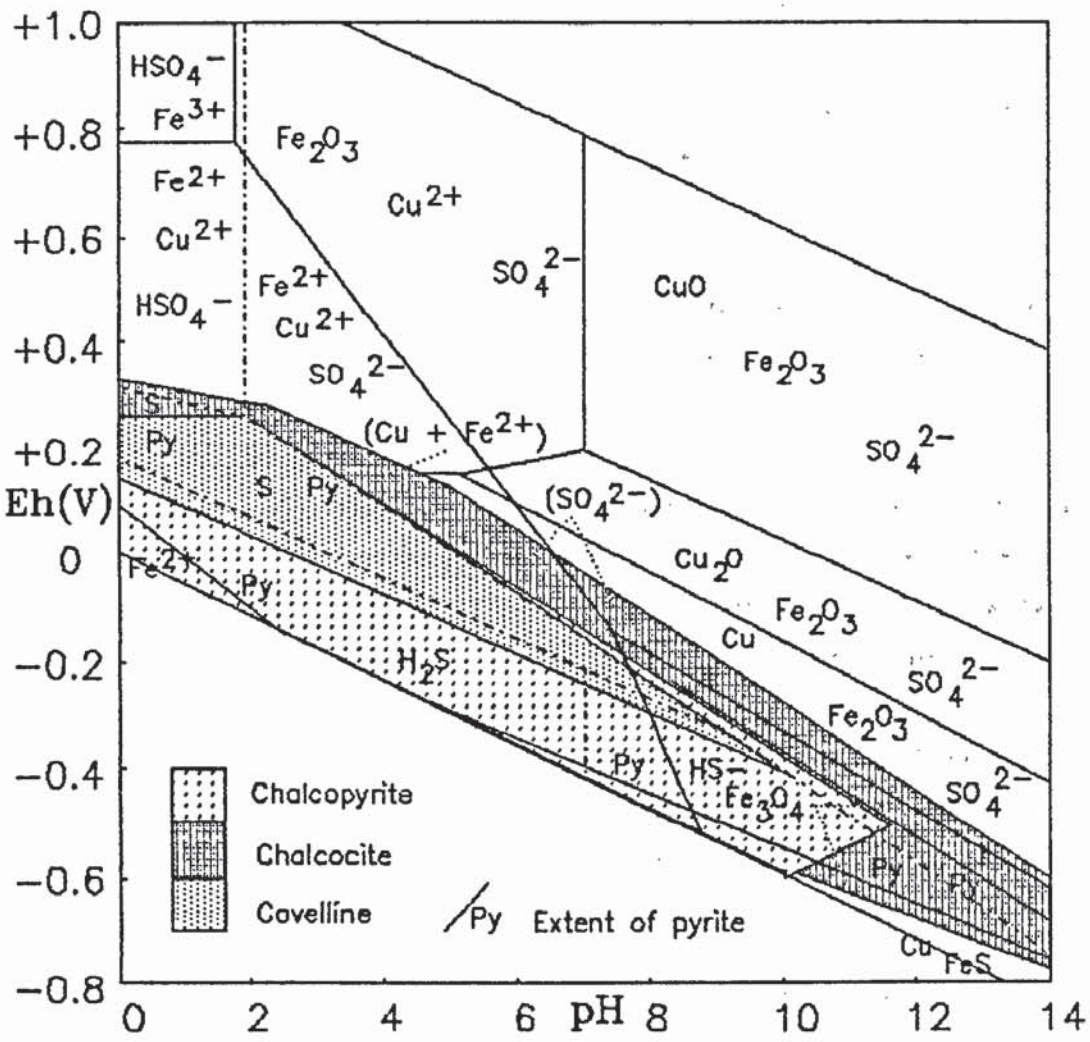

Figure 8.12. Eh/pH diagram for oxidised chalcopyrite with respect to the copper sulphides. A zone of stability of bornite can be inferred between those of chalcopyrite and the copper sulphides. The phase boundaries were determined for log [Fe]=-6, log [Cu]=-6 and log [S]=-1. (Equilibria and free energies for the phases contained in Appendix 4.)

bornite and other copper-iron sulphides that would have an intermediate stability between that of chalcopyrite and the copper sulphides. In the partial pressure diagram, the fields of stability of the copper sulphides suggest that chalcocite would be present as the major copper sulphide forming after oxidation. In the Eh/pH diagram, this is further indicated by the zone of chalcopyrite stability proceeding to covelline and then chalcocite, as the oxidation potential and the pH increases.

Elemental sulphur formation may account for most of the sulphur (0) in the surfaces, and the low concentration may be linked to the formation of copper sulphides by the reduction of cupric ions as suggested by Majima & Peters (1966).

Considering the nature of the formation of copper sulphides from the point of view of any possible structural transformation, it can be inferred that although the crystal structures are dissimilar, the process of conversion from chalcopyrite to copper sulphides may occur around a slightly changed sulphur sub-structure.

The observed oxidation is in agreement with the model proposed by Buckley & Woods (section 8.10), for a metal-deficient sulphide, or more importantly, an iron-deficient sulphide. The following model was proposed by Buckley & Woods (1984b);-

> "...surface oxidation of sulphide minerals involves progressive removal of metal atoms from the sulphide lattice....the product is a metal-deficient sulphide with a higher sulphur content than established, stable phases within the respective metal-sulphur systems..."

This model would explain the strong peak determined for chalcopyrite (now iron-deficient) in the copper 2p 3/2 spectra, and the lack of a chalcopyrite Fe 2p 3/2 peak. Linked to this evidence, the Mössbauer data show only a small chalcopyrite contribution with predominant FeOOH. This suggests, in connection with the XPS data, that the immediate surface consists of iron oxides and hydroxides (largely FeOOH) and copper sulphides, with an iron-leached metastable chalcopyrite in the sub-surface (thus accounting for the low

chalcopyrite detection in the Mössbauer spectra due to the loss of iron from the structure).

The iron, being readily leached from the chalcopyrite surface, would lead to the formation of a copper-rich zone in the sub-surface. The instability of this zone would also lead to the dissolution of copper which could react with the sulphur in the altered surface and result in the formation of copper sulphides.

$$CuFeS_2 \rightarrow Fe^{3+} + \text{metastable } CuS_x + (2-x)S + 3e$$

$$CuS_x \rightarrow Cu^{2+} + xS + 2e$$

$$2Cu^{2+} + S + 4e \rightarrow Cu_2S \qquad Cu^{2+} + S + 2e \rightarrow CuS$$

Since copper I & II sulphides are detected in the surface (showing binding energies differing from chalcopyrite), it is possibly a combination of the two processes that result in the observed characteristics.

Considering the alteration of chalcopyrite in acid and neutral solutions and the compounds formed, the following equations relate to possible oxidation.

In acid solution;

$$xCuFeS_2 + yH_2O + (4x-2y-2)H^+ + (2x-2y+2)e \rightarrow Fe_xO_y + Cu_2S + (x-2)Cu^{2+} + (2x-1)H_2S$$

$$2CuFeS_2 + 6H_2O \rightarrow 2Fe(OH)_3 + Cu_2S + 3H_2S$$

$$2CuFeS_2 + 4H_2O \rightarrow 2FeOOH + Cu_2S + 3H_2S$$

In alkaline solution;

$$xCuFeS_2 + yOH^- + (2x-y-1)H^+ + (2x-2y)e \rightarrow Fe_xO_y + CuS + (x-1)Cu^{2+} + (2x-1)HS^-$$

$$CuFeS_2 + 3OH^- + H^+ \rightarrow Fe(OH)_3 + CuS + HS^- + e$$

$$CuFeS_2 + 2OH^- \rightarrow FeOOH + CuS + HS^- + e$$

These equations show specific alteration assuming the major copper sulphide product of acid oxidation to be chalcocite, and of alkaline oxidation to be covelline, as indicated by the x-ray photoelectron spectra. The actual mechanism of alteration is far more complex and is controlled by both the oxidant and the mechanism of sub-surface alteration.

The oxidation of chalcopyrite surfaces is discussed further with respect to the oxidation observed on other sulphide surfaces in chapter 10.

CHAPTER 9.

ARSENOPYRITE

9. Arsenopyrite.

9.1. Introduction.

Arsenopyrite (FeAsS) is a major mineral in several ore associations, and a minor component in many others (Ramdohr, 1980; Craig & Vaughan, 1981). However, the demand for arsenopyrite as an ore is limited, since the arsenic production requirement of most countries is met by extraction from the flue dusts of smelters. From the viewpoint of both contamination of the products of processing, and environmental considerations, arsenopyrite is more often an unwanted mineral.

The processes involved in arsenopyrite extraction and their efficiency are therefore important from both commercial and environmental standpoints and foremost amongst these processes is froth flotation. The leaching of arsenopyrite in tailings dumps may create environmental problems and lead to the contamination of water systems by soluble arsenic species. The surface characteristics of arsenopyrite are important in understanding its behaviour during ore processing and in oxidation in the natural environment.

9.2. Previous work concerning arsenopyrite oxidation.

There is little information on arsenopyrite oxidation in the mineralogical literature. This may be partially because arsenopyrite is rapidly replaced in hypogene zones by other sulphides, eg. galena, chalcopyrite, chalcocite, stannite and sphalerite (Ramdohr, 1980). The intergrowths and replacement textures of arsenopyrite are complex due to the involvement of many replacing elements, which interact with the mineral in both hypogene and supergene oxidising environments.

Spectroscopic investigation undertaken in this work suggests possible chemical alteration products of arsenopyrite from analyses of the surface components.

9.3. Arsenopyrite characterisation.

Due to problems encountered in producing synthetic arsenopyrite, a natural sample of the mineral was used, selected from several arsenopyrite samples for its purity. The arsenopyrite was supplied from the collection of the British Museum (Natural History), catalogue number BM 1927,1624. The sample appeared to be comprised of several arsenopyrite crystals, of which one 'crystal' of approximately 1 cm^3 was sliced such that the analysed surfaces were all cut in the same orientation. Subsequent examination indicated the sample to be far from homogeneous (as shown in figure 9.6.), and the surfaces showed extensive twinning. For this reason, the use of similarly orientated surfaces is not a necessity in this case.

Careful examination in polished section, along with x-ray diffraction and electron microprobe analyses show the sample to be of high purity as shown in table 9.1. The electron microprobe analysis of several points on the sample surface was undertaken to provide an average composition for the arsenopyrite (given in table 9.1.), however the compositional changes as a result of zoning and twinning were not determined.

Table 9.1. Electron microprobe characterisation of the arsenopyrite.

	Fe	As	S
Arsenopyrite (At %)	32.80 +/- 0.26	31.13 +/- 0.37	36.02 +/- 0.30
Average composition	0.911	0.864	1.000

The electron microprobe analyses show consistent values for the atomic percentages of the arsenopyrite. The arsenopyrite is very pure, apart from a minor antimony content (Sb = 0.05 At %).

9.4. Optical properties.

Arsenopyrite is moderately bireflectant in most orientations in plane polarised light. However, the sections were prepared in orientations that show no measurable bireflectance. The spectral reflectance spectrum obtained for the unoxidised arsenopyrite agrees with the spectrum described in the IMA/COM data file (Stanley & Criddle, 1986). Reflectance data for arsenopyrite surfaces, before and after oxidation, are included in table 9.2. The reflectance data are an average of the maximum reflectance for several points on the sample surface.

Table 9.2. Reflectance measurements for unoxidised arsenopyrite and arsenopyrite surfaces oxidised by various methods.

	Reflectance (R%)				
Oxidation method	470nm	546nm	589nm	650nm	ΔR(*)
Unoxidised (R^o)	49.5	51.8	53.2	53.4	
Air/oxygen (150°C)	44.6	46.2	47.7	47.8	10.4
Steam	40.5	43.2	44.4	44.1	17.2
NH_4OH	35.1	38.3	39.7	39.5	26.6
H_2SO_4	23.4	28.3	30.9	34.3	43.8
H_2O_2	18.3	23.1	26.6	29.5	53.1
Electrochemical (0.8V)	17.9	23.0	24.3	26.8	55.7

* ΔR = average change in reflectance = $(R^o-R^1)/R^o \times 100$

The reflectance data give a preliminary indication of the extent of oxidation and are in agreement overall with the extent of oxidation determined from the spectroscopic data as outlined in the following sections. An assessment of these data, supported by photomicrographs and SEM photographs, is presented in section 9.9. with respect to the determined chemical compositions of the surfaces.

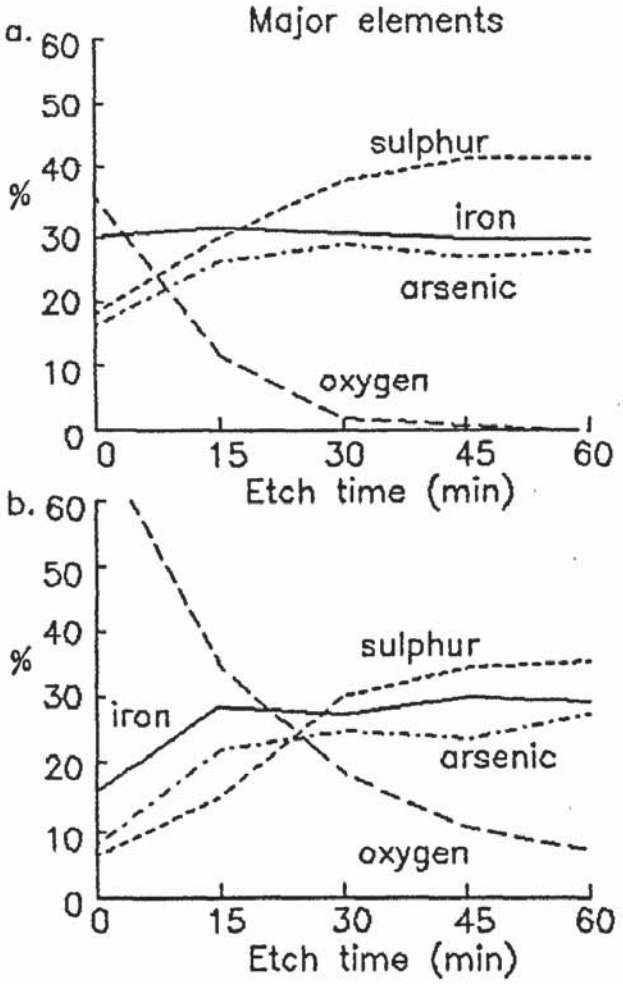

Figure 9.1. Auger depth profiles of arsenopyrite surfaces oxidised by (a) air/oxygen (at 150°C in a furnace) and (b) sulphuric acid.

9.5 Auger Electron Spectroscopy (AES).

Differentiated Auger spectra were used, in combination with argon ion sputtering, to determine elemental concentrations with depth. After sputtering away the oxidised layers, the expected proportions of the elements comprising arsenopyrite, as determined from the probe data, can be assumed to be 33% Fe, 31% As, and 36% S.

Auger depth profiles, exhibiting the typical oxidation observed on arsenopyrite surfaces, are shown in figure 9.1. The surfaces show, in general, a slight increase in sulphur with respect to iron and arsenic, which could be indicative of a sulphur-rich compound, however no supporting evidence for this is available from the other techniques used.

The oxidation depth of the arsenopyrite surfaces can be estimated from the oxygen curves. The oxidation of the surface by air/oxygen (at 150°C), as shown by figure 9.1a., has a rapidly diminishing concentration of oxygen with depth. The complete absence of oxygen detected in the spectra after 60 minutes of sputtering suggests that sputter-mixing (chapter 2, section 2.1.3.) of the surface components is limited, and, as such, is not a problem. The sulphur concentration is shown by these profiles to be inversely proportional to the oxygen concentration width depth. However, the presence of elemental sulphur as an oxidation product, in addition to sulphides and oxy-sulphates, suggested in the following sections, suggests that the relationship between the oxygen and sulphur concentration curves is not a simple inverse one.

No evidence of layering in any of the arsenopyrite surfaces can be inferred from the depth profiles. The rapid convergence with depth of the iron, arsenic, and sulphur concentrations to the expected elemental proportions for arsenopyrite, is also evidence of a limited oxidation, as well as indicating a lack of sputter reduction.

9.6. X-ray Photoelectron Spectroscopy (XPS).

The arsenopyrite exhibits variable degrees of oxidation, and certain oxidation products, depending on the oxidants used, as

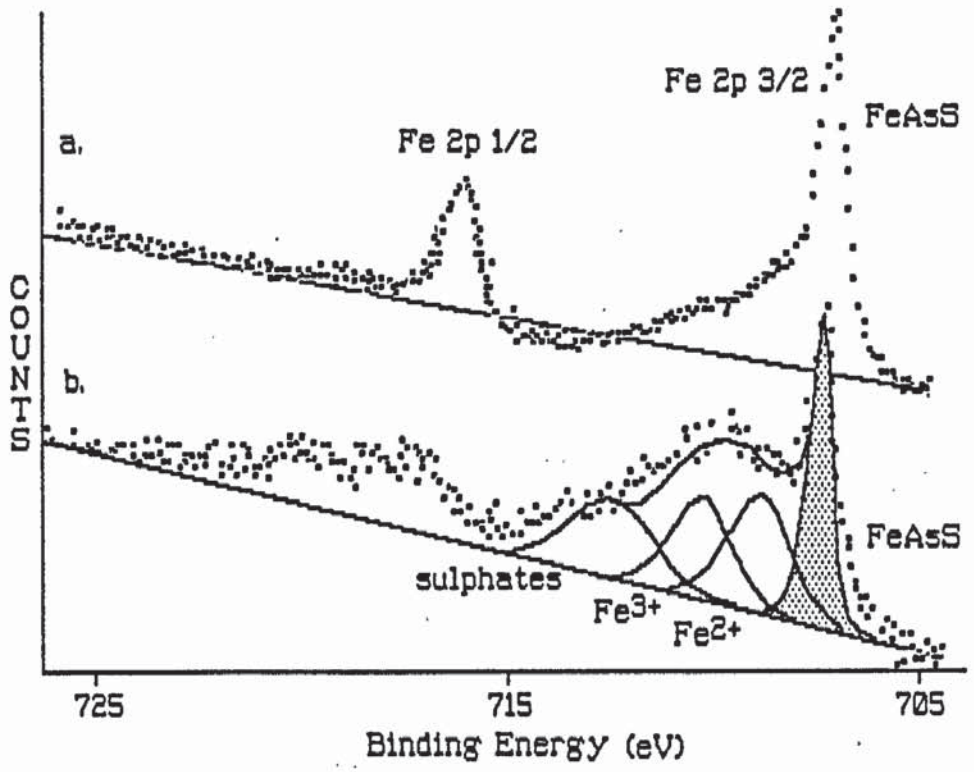

Figure 9.2. Fe 2p (1/2 & 3/2) x-ray photoelectron spectra for (a) an unoxidised arsenopyrite surface and (b) an arsenopyrite surface oxidised by steam

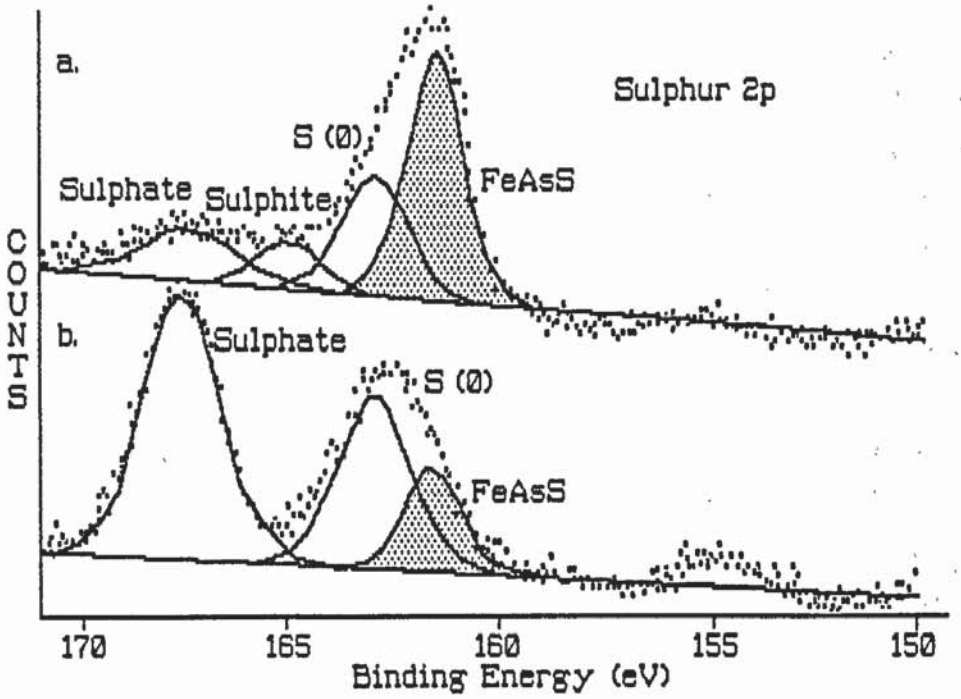

Figure 9.3. Sulphur 2p x-ray photoelectron spectra obtained for arsenopyrite following oxidation by (a) air/oxygen (at 150°C in a furnace) and (b) sulphuric acid.

determined from both the reflectance and the Auger spectra. The chemical characteristics of the observed oxidation products may be interpreted from the x-ray photoelectron spectra.

New data were recorded for the binding energies of specific electrons in arsenopyrite. Binding energies of 706.9eV for Fe 2p(3/2), 40.7eV for As 3d and 161.2eV for S 2p were determined by fitting peaks to the spectra of unoxidised arsenopyrite surfaces.

Figure 9.2. shows the effect of steam oxidation as observed in the Fe 2p x-ray photoelectron spectra compared to a spectrum from an unoxidised surface. The spectrum of unoxidised arsenopyrite exhibits shake-up, which could affect the determination of peak areas for the oxidised surfaces. This affects the assessment of the iron II and III oxides and hydroxides and the oxy-sulphates, but the oxygen 1s and sulphur 2p peaks provide better resolution for these compounds.

The resolution available from the sulphur 2p spectra is shown in figure 9.3. From these spectra the presence of sulphur (0) has been established. Since the other x-ray photoelectron spectra show no indication of the formation of thionates or polysulphides, the sulphur (0) must be due to elemental sulphur. The determination of oxysulphates from the sulphur 2p spectra, shows that sulphates are the major phases in most of the oxidised surfaces, except for steam oxidation where sulphites predominate and oxidation in air/oxygen (at 150°C) where there is a minor sulphite component (shown in figure 9.3.).

The arsenic 3d spectra, shown in figure 9.4., indicate the formation of arsenic III species in the altered surfaces, and in the case of sulphuric acid oxidation, the additional presence of arsenic V species. The occurrence of arsenic III and V in the surfaces is attributed to the presence of oxides. The formation of arsenic oxides after oxidation by air/oxygen (at 150°C) could be expected. However, the formation of arsenic oxides during oxidation in solutions in the proportions detected is surprising, considering their very high solubilities. Wedepohl (1978) cites solubility values of 20.5 gl^{-1} for arsenic III oxide, and an even higher solubility for arsenic V oxide. A possible explanation for the unexpected insolubility of arsenic compounds is the potential for arsenate and arsenite formation.

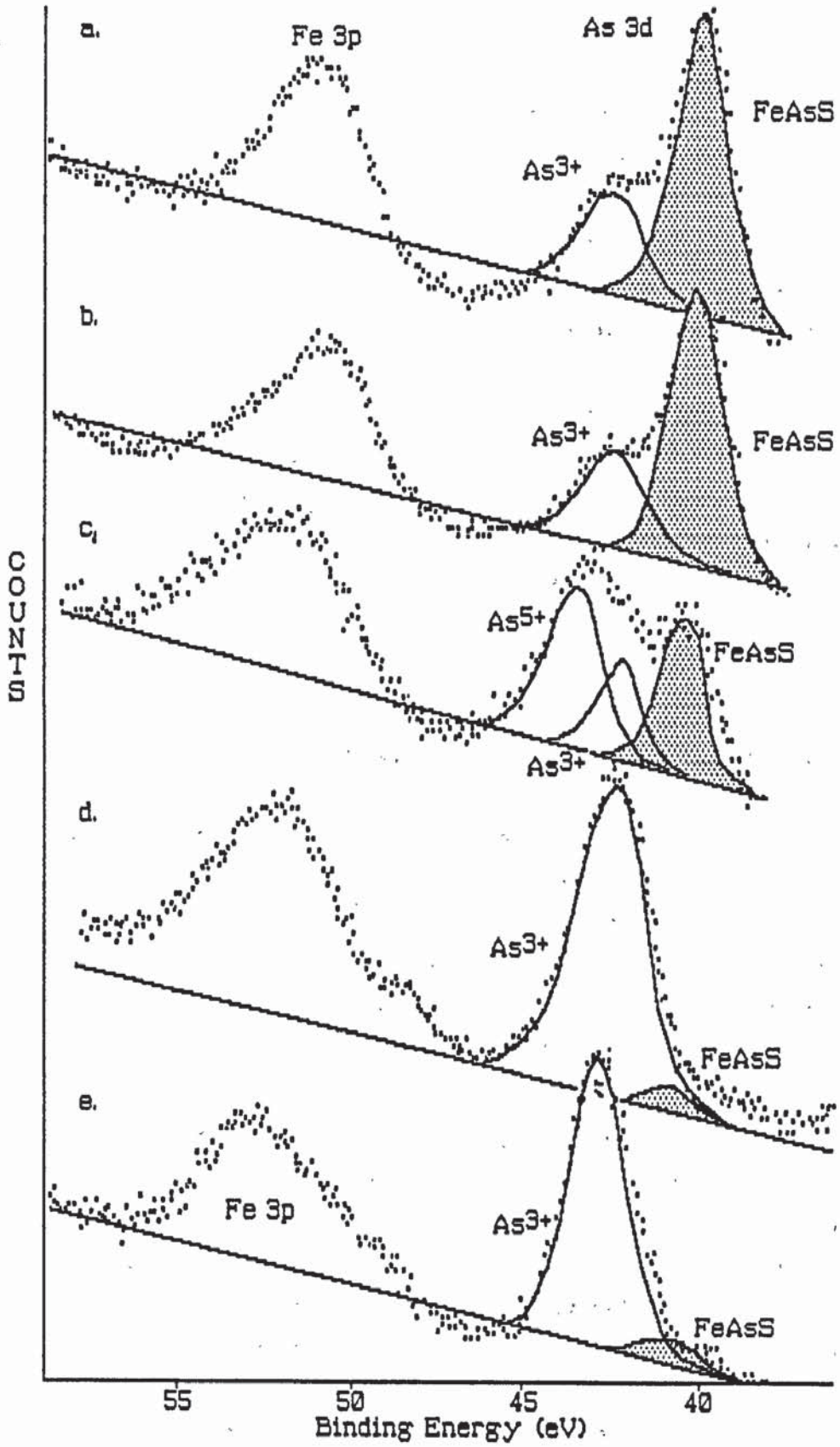

Figure 9.4. Arsenic 3d (with Fe 3p) x-ray photoelectron spectra for arsenopyrite surfaces obtained following oxidation by (a) air/oxygen (150°C in a furnace), (b) steam, (c) sulphuric acid, (d) electrochemical methods and (e) hydrogen peroxide.

Also shown in figure 9.4. are the Fe 3p photoelectron peaks. As oxidation increases, indicated by the increased proportion of arsenic oxides, there is a shift in the Fe 3p peak maximum to higher binding energies, consistent with the oxidation of iron. The resolution of the Fe 3p electron binding energies is less defined than that of the Fe 2p(3/2) binding energies and peaks have not been fitted to these spectra.

The oxygen 1s binding energies of the oxidised arsenopyrite surfaces are consistent, for the most part, with the proportions of the oxidised compounds determined in the other spectra. An assessment of the proportions of the oxygen-containing phases and of the other compounds present in the surfaces is suggested in section 9.7.

9.7. Compositional Interpretation of the XPS and Auger spectra.

The compositions of the oxidised arsenopyrite surfaces are suggested from the differentiated Auger spectra and the chemical compositions inferred from the XPS spectra. Estimated proportions of the phases present in the oxidised surfaces are presented in table 9.3., showing the phases present for the bulk composition in a surface layer of approximately 10-15Å depth, determined by the depth resolution of the XPS.

As explained in previous chapters, the likely Fe^{2+} component is from magnetite (Fe_3O_4). In the less oxidised surfaces the Fe^{2+} is in greater concentration than that of Fe^{3+}, suggesting the presence of wüstite ($Fe_{1-x}O$, a metastable product). Where the Fe^{3+} predominates in an aqueous environment, it is easily hydrated and is likely to form iron III hydroxides and FeOOH, rather than hematite (Fe_2O_3), although this is the most stable phase suggested thermochemically. Iron III oxide would be expected as an iron III phase in the arsenopyrite surfaces after oxidation by air/oxygen (at 150°C), along with a component of magnetite.

Table 9.3. General surface compositions from XPS/AES analyses (estimated molecular percentages).

Phase	Method of Oxidation					
	air/oxygen	steam	NH_4OH	H_2O_2	H_2SO_4	elec.
Fe (II/III) sulphate	5.9	-	9.4	18.3	13.6	17.6
Fe (II) sulphite	3.8	13.1	-	-	-	-
Fe (III) (oxides & Fe (II) hydroxides)	13.1	17.6	22.3	26.7	23.7	25.1
	15.6	22.4	23.2	17.4	17.2	18.4
As (V)	-	-	-	-	21.3	-
As (III)	7.8	10.7	14.7	17.6	10.4	25.7
S (0)	19.6	15.4	11.8	10.8	9.4	8.9
Arsenopyrite (FeAsS)	34.2	20.8	18.6	9.2	4.4	4.3

In the oxidised surfaces arsenic III phases are major components, indicating that the rate of formation of the arsenic phases is greater than the dissolution of arsenic from the surface. The presence of arsenic V phases is limited to the oxidation by sulphuric acid, and reasons for this are given, with respect to the thermochemical stabilities, in section 9.10.

A major phenomenon in the surface oxidation concerns the inter-relationship between the sulphur species. In general, the formation of oxy-sulphates increases with the apparent depth of oxidation as determined by Auger depth profiles and reflectance techniques. Conversely the presence of sulphur (0), interpreted as elemental sulphur, is inversely proportional to the depth of oxidation. It could be inferred that sulphur is an initial product of arsenopyrite oxidation and that the sulphur is being progressively oxidised, although sulphites would be expected in greater quantities than those detected. The precise Eh/pH conditions of oxidation appear to have a considerable effect on the sulphur species forming in the surface,

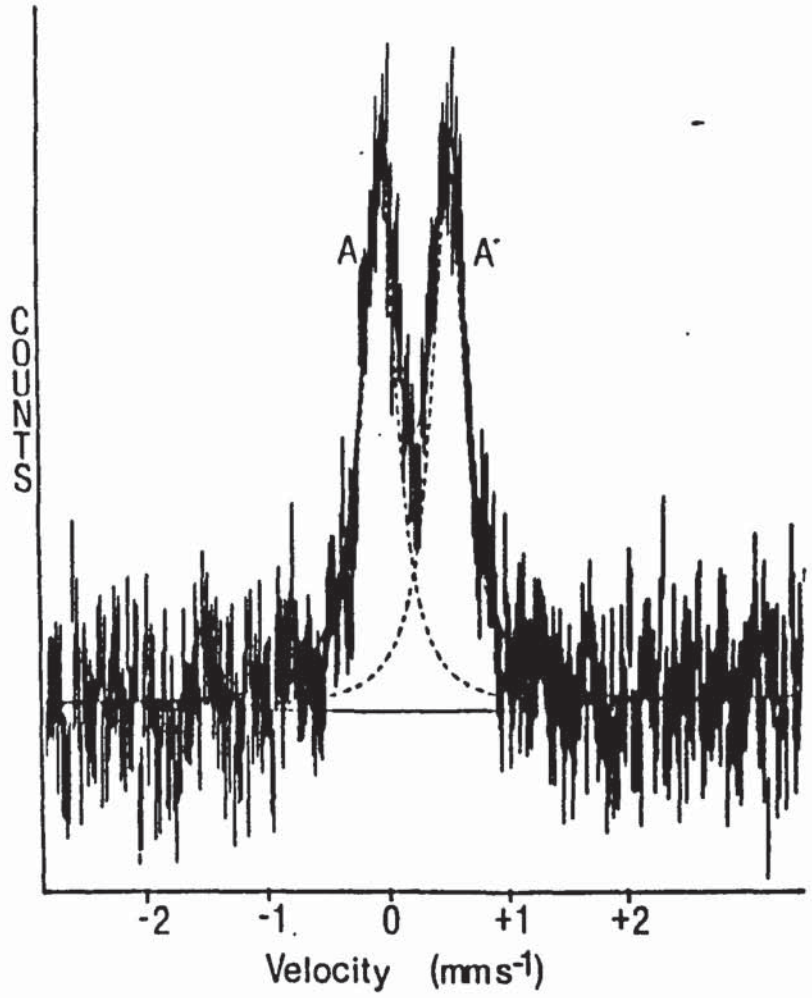

Figure 9.5. Conversion electron Mössbauer spectrum for an arsenopyrite surface oxidised by sulphuric acid.

and the effect on the surface composition of the oxidation conditions are further discussed in section 9.10.

9.8. Conversion Electron Mössbauer Spectroscopy (CEMS).

The unoxidised arsenopyrite gave a Mössbauer spectrum with a single quadrupole doublet having 0.214 mms^{-1} for the isomer shift and 1.084 mms^{-1} for the quadrupole splitting. After oxidation of the surface by sulphuric acid, shown in figure 9.5.,the peaks comprising the quadrupole doublet are still the only fitted peaks. It is not possible to determine oxidised phases from the spectra.

The apparent lack of alteration observed by CEMS is to be expected considering the limited depth of oxidation determined by Auger depth profiles.

9.9. SEM and photomicrographs.

The chemical characterisation of the arsenopyrite surfaces may be related to the data from reflectance spectra, and the surfaces observed in photomicrographs and SEM photographs.

Microscopic examination of oxidised arsenopyrite surfaces reveals a large variation of surface textures. Figure 9.6. shows a surface oxidised by hydrogen peroxide. It is evident in this surface that the hydrogen peroxide has etched out textural features, including lamellar (and possibly zonal) twinning and cleavage textures. This photomicrograph is useful since it outlines the problems of crystallographic orientation on the oxidation reactions. Since the twinning is present, a regular alignment of a certain crystallographic orientation of the arsenopyrite is not possible.

The reflectance data for the surface oxidised by hydrogen peroxide indicates a relatively intense degree of oxidation, as recorded in table 9.2., these data are given for an average of several points on the surface. Considering the proposed chemical composition of the surface given in table 9.3., the surface is depleted in arsenopyrite

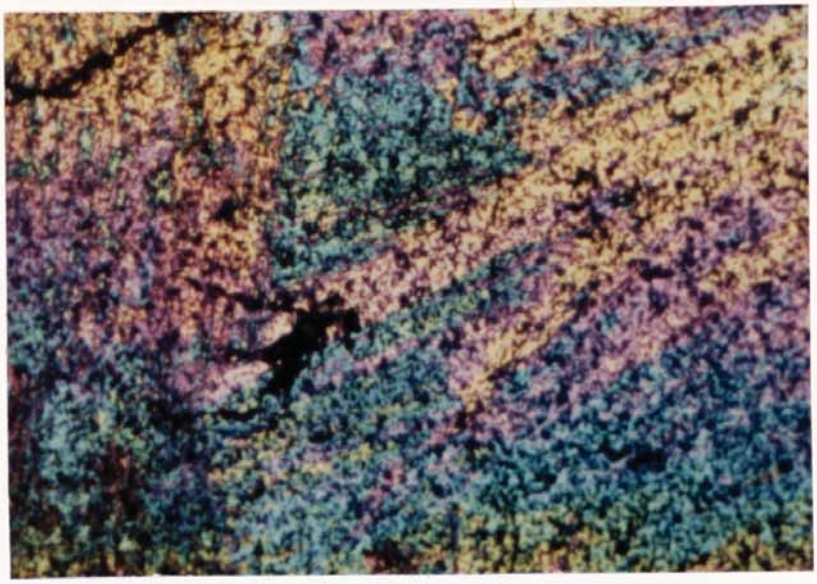

Figure 9.6. Photomicrograph of an arsenopyrite surface oxidised by hydrogen peroxide showing the twinning textures. (Width of field = 1.5mm, magnification = 67x)

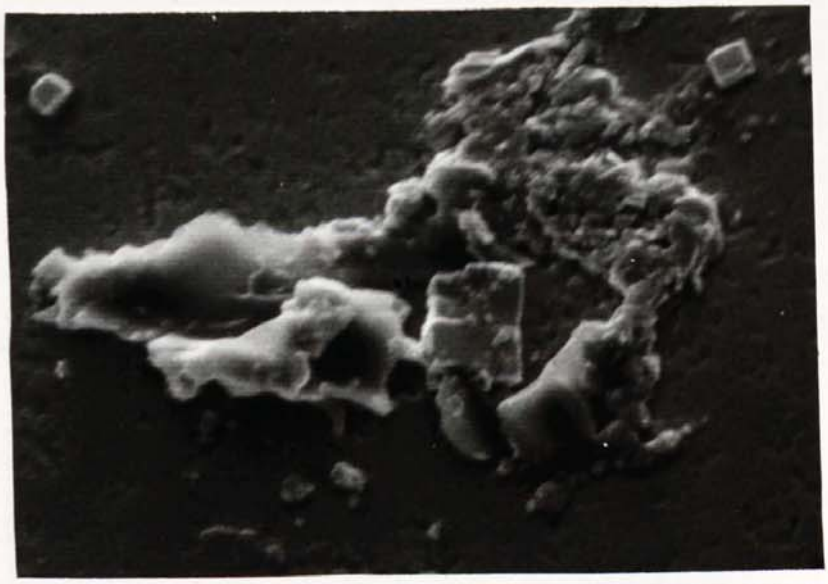

Figure 9.7. SEM photograph of an arsenopyrite surface oxidised by hydrogen peroxide with evidence of both amorphous and crystalline oxidation products. (Width of field = 24μm, magnification = 4200x)

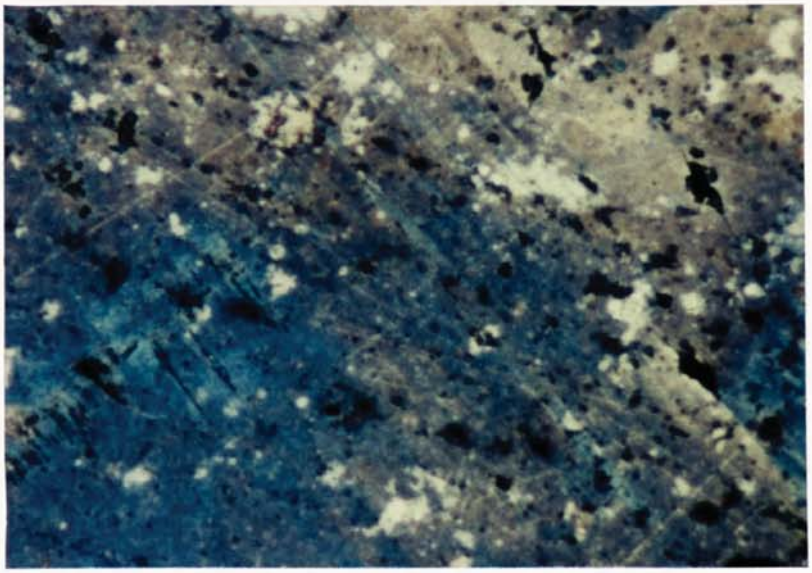

Figure 9.8. Photomicrograph of an arsenopyrite surface oxidised by sulphuric acid. (Width of field = 1.5mm, magnification = 67x)

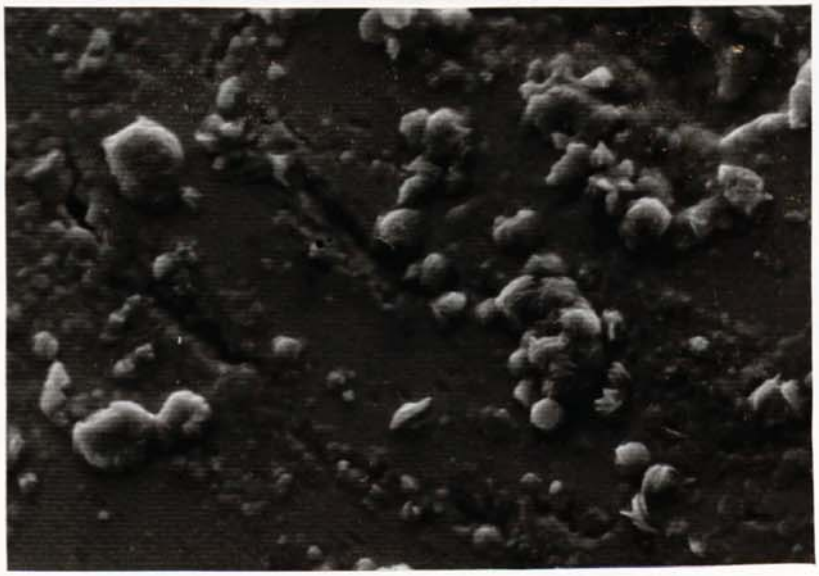

Figure 9.9. SEM photograph of an arsenopyrite surface oxidised electrochemically. (Width of field = 60μm, magnification = 1680x)

and has relatively little sulphur compared to other surfaces. The oxidised layer is suggested to consist predominantly of sulphates, iron oxides & hydroxides and arsenic III (oxide?).

An SEM photograph (figure 9.7.) of the same surface shows the presence of crystalline forms. These are not present on the other oxidised arsenopyrite surfaces, or on any of the other sulphide mineral surfaces studied, and are also suggested to be an arsenic phase. However, this does not aid the determination of the actual arsenic compounds since, by considering the crystal forms of possible arsenic compounds, it could possibly be hydrated iron arsenate (scorodite, orthorhombic) or arsenic III oxide (arsenolite, cubic). This could be resolved by EDAX analysis of the crystals, however this facility was not available on the SEM used.

Another effect of the oxidation of arsenopyrite is shown in figure 9.8., where the oxidation has resulted in a predominantly blue tarnish of the the surface. The oxidation, extensive in this case, is more typical of arsenopyrite oxidation. SEM photographs of this surface shows crystal forms similar to those shown in figure 9.9. for electrochemical oxidation. The nature of the forms seen in figure 9.9. may be considered in the light of previous chemical characterisation of the surface. Possible compounds are either γ-FeOOH, which has been reported to form "thin stringers" (Ramdohr, 1980) with a ropy to needle-like morphology similar to those observed, or a form of sulphur.

Overall, any determination of such phases by their morphology as observed in SEM photographs must be tenuous, since it is not possible to analyse these phases, and the crystals are too small to be separated for XRD analysis.

9.10. Interpretation and Discussion.

The compounds suggested to form following the oxidation of arsenopyrite surfaces may be related to thermochemically predicted compounds as shown in partial pressure (figure 9.10.) and Eh/pH diagrams (figure 9.11.). The partial pressure diagram is more

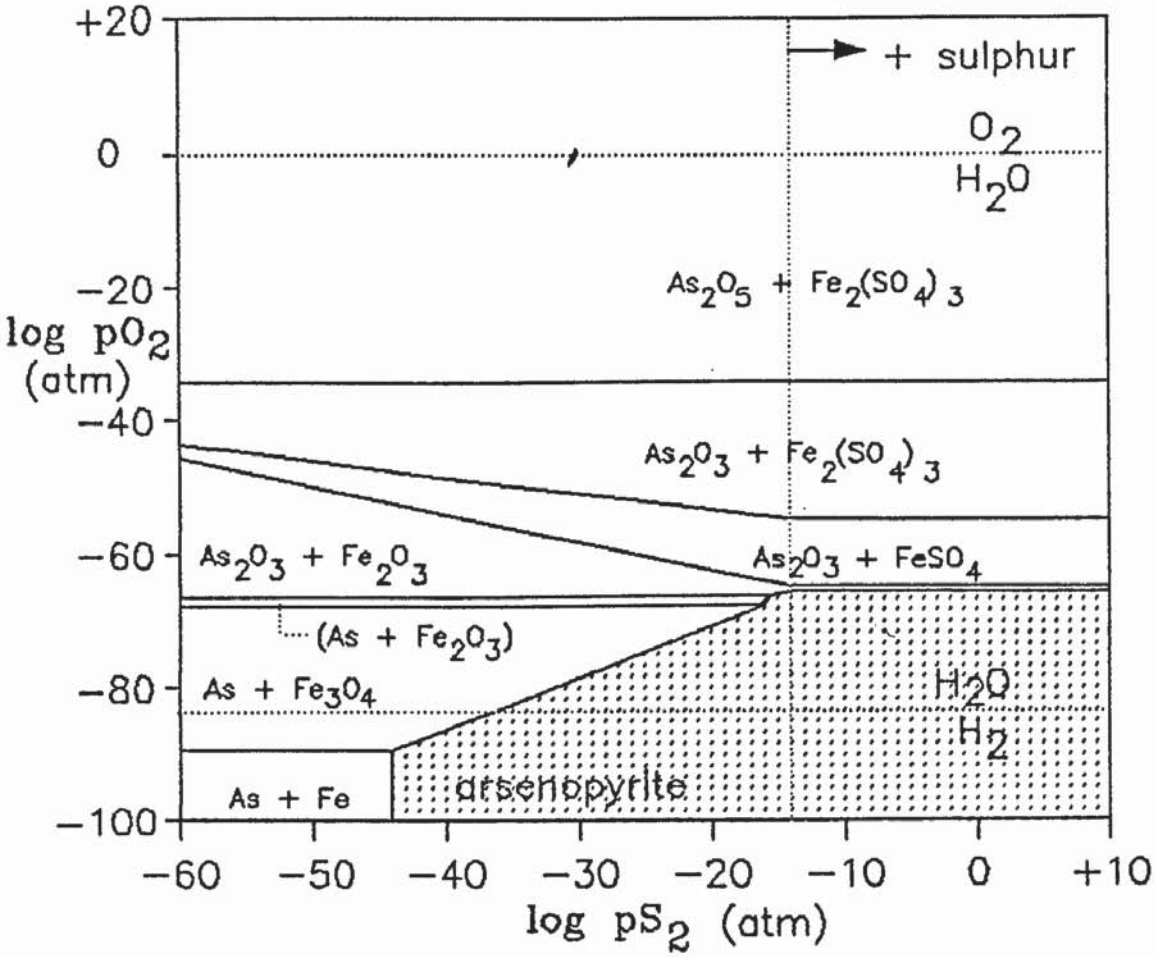

Figure 9.10. Partial pressure diagram (log pO_2/log pS_2) for oxidised arsenopyrite. (Equations and free energies of formation for the component phases contained in Appendix 4.)

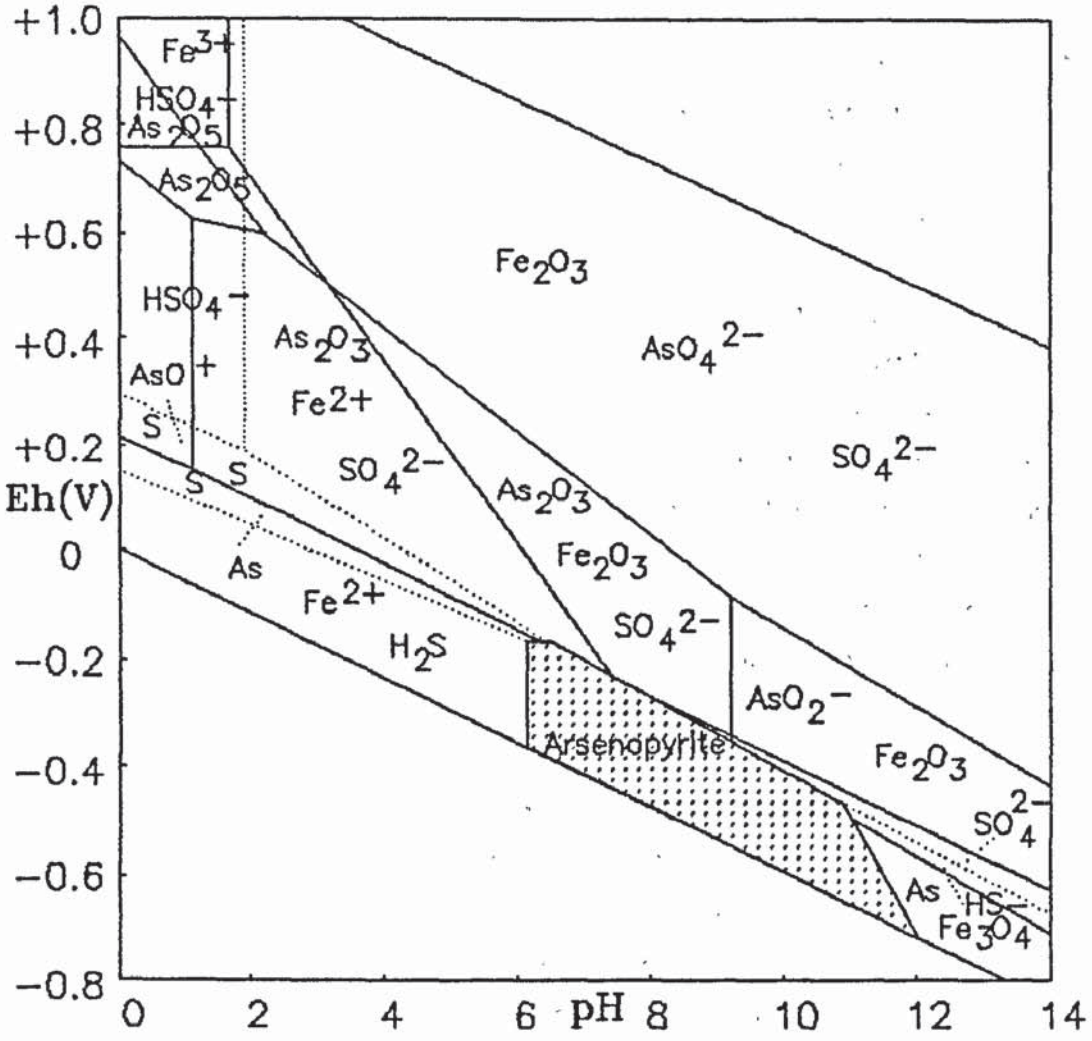

Figure 9.11. Eh/pH diagram for oxidised arsenopyrite. The phase boundaries were determined for log[S] = -1, log[Fe] = -6 and log[As] = -5. (Equilibria and free energies for the phases contained in Appendix 4.)

applicable to conditions immediately below the surface, whereas the Eh/pH diagram shows the stability in aqueous environments, although under fixed conditions.

The products of oxidation determined are for the most part uniform, although variations in surface compositions (particularly the arsenic-containing phases), are a result of the particular Eh/pH conditions of the aqueous oxidants. The surface compositions discussed in section 9.7. may be related to thermochemical data. The arsenic species show a pH control on their oxidation, where most surfaces show only arsenic III compounds, except in sulphuric acid where arsenic V compounds are also found, a factor supported by the stability fields outlined in figure 9.11. Although the arsenic oxides have high solubility, they are prevalent in the altered surfaces. This may be due to a reaction rate faster than the rate of dissolution, or it could be due to arsenic compounds forming in the sub-surface below the oxidising interface. In section 9.7. the formation of ferric and ferrous arsenates was considered, and these phases may account for the unexpected solution characteristics.

The nature of the iron-containing oxidised phases at the surface is considered in section 9.7., and the difficulty in determining the nature of the iron oxides, hydroxides or oxy-hydroxides is similar to that encountered with other sulphide surfaces as discussed in detail previously (for example chapter 4, sections 4.7. and 4.10).

The following equations show possible reactions in varying oxidising conditions. Since the arsenic species have only been defined accurately in terms of their valence states, the equations represent only such arsenic species, although the analysed surfaces suggest the presence of arsenic compounds.

In acid solutions (assuming As^{5+} forming);

$$xFeAsS + yH_2O \rightarrow Fe_xO_y + xAs^{5+} + xH_2S + (2y-2x)H^+ + (3x+2y)e$$

$$FeAsS + yH_2O \rightarrow Fe(OH)_y + As^{5+} + H_2S + (y-2)H^+ + (3+y)e$$

$$FeAsS + 2H_2O \rightarrow FeOOH + As^{5+} + H_2S + 2H^+ + 7e$$

- and in alkaline solutions (with As^{3+});

$$xFeAsS + yOH^- \rightarrow Fe_xO_y + xAs^{3+} + xHS^- + (y-x)H^+ + (x+2y)e$$

$$FeAsS + yOH^- + H^+ \rightarrow Fe(OH)_y + As^{3+} + HS^- + (1+y)e$$

$$FeAsS + 2OH^- \rightarrow FeOOH + As^{5+} + HS^- + 6e$$

In both acid and alkaline solutions the oxidation of arsenopyrite is anodic, which is important in terms of the alteration in natural environments, since anodic oxidation would increase the rates of oxidation when linked to the cathodic oxidation of water. Additional equations relating to the stability of arsenopyrite as shown in figures 9.10. and 9.11. are included in appendix 4.

Further discussion of the oxidation of arsenopyrite relative to the oxidation observed on other sulphide surfaces is presented in chapter 10.

Surface characterisation shows that arsenic species are a major part of the arsenopyrite oxidation process, although the exact extent of their formation and dissolution from the surface during oxidation is uncertain. Careful consideration must be given to the disposal of arsenopyrite tailings, since in most cases, especially those involving solutions of low pH such as those found in tailings dumps, there will be dissolution of soluble arsenic species by percolating meteoric and ground waters. The involvement of arsenopyrite and other sulphides in the dump materials will be important in the generation of sulphuric acid and lowering of the pH, thus further increasing the potential for the formation of oxidised arsenic species. For this reason, if the run-off from mine dumps containing arsenopyrite enters the drainage system it is likely to result in serious local pollution of the environment.

CHAPTER 10.

DISCUSSION

10. Discussion.

10.1. General introduction.

The effects of oxidation on the particular mineral surfaces studied have been discussed in chapters 4 to 9. This chapter is aimed at contrasting the relative effects of oxidation by different methods and considering the implications of the results obtained with respect to various oxidising environments.

The oxidation phenomena observed on the altered surfaces of iron-containing sulphides are of importance in understanding the stability of these minerals to oxidation in natural environments. It is observed that surface stability and characteristic oxidation phenomena are affected by the oxidation methods used and these phenomena are discussed with respect to specific oxidants in section 10.2.

Using the observed oxidation characteristics, determined using spectroscopic methods, it is possible to suggest the relative stability of the sulphides studied to oxidation, and to infer a general order of oxidation stability. This order and the factors controlling the oxidation and products forming on the sample surface, are considered in section 10.3.

The relative oxidation stability under various pH and oxidising conditions may be related to the Eh/pH regimes of natural groundwater systems (section 10.4.) and may be used to infer the characteristics of oxidation in natural environments. The oxidation of sulphides during mineral processing is also considered. Possible topics for further research are outlined in section 10.5.

10.2. The mechanisms of alteration by specific oxidants.

By considering the nature of the oxidant, and the oxidising processes involved, it is sometimes possible to suggest the nature of certain phases forming on the sulphide surfaces, eg. the iron oxides or hydroxides. The following sections outline the stability of the sulphides in response to various oxidising conditions.

Originally an attempt was made to use oxidants which would cause similar amounts of alteration on each sulphide surface (controlled by the oxidant strength and the time of exposure), however this does not allow for the assessment of the relative effects of different oxidants on a particular sulphide. Of more importance are the resultant alteration products and the extent of alteration caused by each oxidant, allowing an assessment of the relative oxidation of the sulphide minerals.

In the following sections, chemical equations are used to show the overall reactions. These equations show the end-products of oxidation, and the proportions of the oxidised phases shown in these equations are similar to those determined from the spectroscopic data; however, it is suggested that the oxidation of the surfaces may occur via several reaction paths. In the chemical formulae presented in this chapter, FeS_x is used to represent pyrite and the pyrrhotines.

For each oxidation method, a sequence is presented showing the relative stability of the sulphides. These sequences are based on the proportion of the original sulphide remaining in the surface analysed by AES and XPS after oxidation.

10.2.1. Air/oxygen oxidation at 150°C in a furnace.

The relative stabilities of sulphide surfaces to furnace oxidation are considered in table 10.1., which shows the order of stabilities of the minerals, along with their maximum thermal stabilities.

As shown in table 10.1., the maximum thermal stabilities of most of the minerals are well above the oxidation temperature employed in the experiments, with the exception of hexagonal pyrrhotine. Notably, pyrite and arsenopyrite, with high thermal stabilities, are the most stable in their response to this method of oxidation. Considering the observed order of stability in relation to the thermal stabilities, the oxidation is consistent, apart from that determined for the iron-nickel sulphides, which show an oxidation greater than that expected.

Table 10.1. The order of stability of the sulphides to air/oxygen (150°C) oxidation.

Sulphide	Observed stability	Max. T (°C)	%Sulphide
Pyrite	MOST STABLE	743 (a)	39.0
Arsenopyrite		702 (b)	34.2
Chalcopyrite		557 (c)	26.9
Monoclinic Pyrrhotine ($\simeq Fe_7S_8$) 4C		254 (d)	26.6
Hexagonal Pyrrhotine ($\simeq Fe_9S_{10}$) 5C		$\simeq$100 (e)	25.9
Violarite		461 (f)	18.9
Pentlandite	LEAST STABLE	610 (g)	1.4

Max. T (°C) = maximum thermal stability. As reported by; (a) Kullerud & Yoder (1959), (b) Clark (1960), (c) Cabri (1973), (d) Kissin (1974), (e) Nakazawa & Morimoto (1971), (f) Craig (1971) and (g) Kullerud (1963).
%Sulphide = the percentage of the primary sulphide remaining in the oxidised ($\simeq$15Å) surface, determined from XPS/AES spectra.

The oxidation process (involving filling the furnace with oxygen) is anhydrous, and for this reason it would be expected that the phases produced would be largely pure oxides. The spectroscopic determination of the iron-containing oxidised phases on the sulphide surfaces shows a greater Fe^{2+} component than Fe^{3+}. The iron-containing oxidised phases are therefore suggested to be mainly wüstite ($Fe_{1-x}O$) and magnetite (Fe_3O_4). Considering the stable iron oxide to be magnetite the following oxygenation reactions are suggested for the sulphides;

Iron sulphides:

$$3FeS_x + 2O_2 \rightarrow Fe_3O_4 + 3xS$$
$$FeS_x + 2O_2 \rightarrow FeSO_4 + (x-1)S$$

Arsenopyrite:

$$6FeAsS + 8.5O_2 \rightarrow 2Fe_3O_4 + 3As_2O_3 + 6S$$
$$2FeAsS + 5.5O_2 \rightarrow 2FeSO_4 + As_2O_3$$

Chalcopyrite: Since the sub-surface sulphide formed is suggested (chapter 8) to be an iron-deficient copper-containing phase, the metastable sub-surface is shown as $CuS_{(2-x)}$

$$3CuFeS_2 + 2O_2 \rightarrow Fe_3O_4 + 3CuS_{(2-x)} + 3xS$$
$$3CuFeS_2 + (4x+2)O_2 \rightarrow (1-x)Fe_3O_4 + 3xFeSO_4 + 3CuS_{(2-x)}$$

Violarite:

$$3FeNi_2S_4 + 5O_2 \rightarrow Fe_3O_4 + 6NiO + 12S$$
$$FeNi_2S_4 + 3O_2 \rightarrow FeSO_4 + 2NiO + 3S$$

Pentlandite: showing the formation of violarite as suggested for the nickel-enriched pentlandite sub-surface.

$$2Fe_{4.5}Ni_{4.5}S_8 + 3.83O_2 \rightarrow 4FeNi_2S_4 + 1.67Fe_3O_4 + NiO$$
$$2Fe_{4.5}Ni_{4.5}S_8 + 16.5O_2 \rightarrow 2FeNi_2S_4 + 7FeSO_4 + 5NiO + S$$

The iron-nickel sulphides have already been shown to form iron sulphates and sulphur as major components of their surface layers after air/oxygen oxidation which, along with the nickel enrichment of the pentlandite sub-surface resulted in the formation of secondary violarite (proposed in chapter 7). The proportion of nickel oxide determined spectroscopically in the oxidised violarite surface is less than that expected and may indicate a nickel enrichment of the violarite. This phenomenon (discussed in chapter 6, section 6.2.) has been observed in natural environments, where the atomic proportions of the nickel in violarites may increase from 29% to 40% ($FeNi_2S_4$ to $Fe_{0.2}Ni_{2.8}S_4$).

All of the iron-containing sulphides show similar iron-containing oxidation products and for this reason the extent of oxidation determined for the sulphides may be related to the ease of formation of the associated oxides (defined by their thermochemical stabilities). In an environment with an increased oxygen partial pressure, as indicated in the partial pressure diagrams in chapters 4

to 9 (discussion sections), the ease of formation of NiO (with respect to arsenic and copper oxides) would account for the greater alteration of the iron-nickel sulphides relative to the arsenic-iron and copper-iron sulphides.

The oxidation of the iron sulphides, as expected, demonstrates the stability of pyrite with respect to monoclinic and hexagonal pyrrhotine. The relative stability of the iron sulphides during oxidation by air/oxygen (at 150°C) is comparable to that shown in partial pressure diagrams (chapter 5, figure 5.15.).

10.2.2. Steam oxidation.

During oxidation, the temperature at the mineral surfaces was measured as 75 - 95°C, which does not exceed the maximum thermal stability of any of the sulphides. However, this is fairly close to the maximum thermal stability of hexagonal pyrrhotine (presented in table 10.1). This factor may be indicated in the order of stability. The fact that pentlandite, with a high thermal stability oxidises more than hexagonal pyrrhotine suggests a more complex reason for the extent of oxidation observed. A sequence of sulphides showing their stability relative to steam oxidation is given in table 10.2.

Table 10.2. The order of stability of the sulphides to steam oxidation.

Sulphide	Observed Stability	%Sulphide
Pyrite	MOST STABLE	37.9
Violarite		23.3
Arsenopyrite		20.8
Chalcopyrite		19.0
Monoclinic Pyrrhotine		14.9
Hexagonal Pyrrhotine		14.8
Pentlandite	LEAST STABLE	4.9

%Sulphide = the percentage of the primary sulphide remaining in the oxidised (≈15Å) surface, determined from XPS/AES spectra.

In considering the nature of the iron oxides and hydroxides produced, these generally show variable proportions of Fe^{2+} and Fe^{3+}. The Fe^{3+}:Fe^{2+} ratios vary from 1:1 to 2:1. The oxidation process may proceed via hydration of the surface leading to the formation of FeOOH. The Fe ratios suggest that, in addition to FeOOH, a major component of the surface may be magnetite (Fe_3O_4).

The oxy-sulphate phases forming on the sulphide surfaces are generally determined to be iron sulphites, as suggested by fitting the sulphur 2p x-ray photoelectron spectra, although a smaller concentration of iron sulphates was also determined. Major proportions of elemental sulphur are found from the data for the pyrite and violarite surfaces.

The following reactions are proposed;

Iron sulphides:

$$3FeS_x + 4H_2O \rightarrow Fe_3O_4 + 4H_2S + (3x-4)S$$
$$FeS_x + 3H_2O \rightarrow FeSO_3 + (x-1)H_2S + (8-2x)H^+ + (8-2x)e$$

Violarite:

$$3FeNi_2S_4 + 10H_2O \rightarrow Fe_3O_4 + 6NiO + 10H_2S + 2S$$
$$FeNi_2S_4 + 5H_2O \rightarrow FeSO_3 + 2NiO + 3H_2S + 4H^+ + 4e$$

Pentlandite:

$$2Fe_{4.5}Ni_{4.5}S_8 + 11H_2O \rightarrow$$
$$3FeNi_2S_4 + 2Fe_3O_4 + 3NiO + 4H_2S + 14H^+ + 14e$$
$$2Fe_{4.5}Ni_{4.5}S_8 + 26H_2O \rightarrow$$
$$2FeNi_2S_4 + 7FeSO_3 + 5NiO + H_2S + 50H^+ + 50e$$

Chalcopyrite:

$$3CuFeS_2 + 4H_2O \rightarrow 3CuS + Fe_3O_4 + 3H_2S + 2H^+ + 2e$$
$$CuFeS_2 + 3H_2O \rightarrow CuS + FeSO_3 + 6H^+ + 6e$$

Arsenopyrite:

$$6FeAsS + 17H_2O \rightarrow 2Fe_3O_4 + 3As_2O_3 + 6H_2S + 22H^+ + 22e$$
$$2FeAsS + 9H_2O \rightarrow 2FeSO_3 + As_2O_3 + 18H^+ + 18e$$

An important relationship is shown by the above equations regarding the formation of elemental sulphur in the oxidised surfaces. For both pyrite and violarite, the above equations indicate that sulphur should form in the altered surfaces, in agreement with the large sulphur concentration detected. An effect of the sulphur forming in the surfaces may be a limitation of the degree of oxidation of the surface due to protection of the sub-surface.

The order of stability of the other sulphides is influenced by a combination of effects including sub-surface enrichment (chalcopyrite and pentlandite), structural instability (pyrrhotines) and the ease of formation of the oxidised phases.

10.2.3. Oxidation by hydrogen peroxide.

The nature of oxidation using hydrogen peroxide is complex and involves many reaction paths. Firstly, hydrogen peroxide breaks down to water and oxygen, and the oxygen forming at the mineral/water interface promotes oxygenation leading to oxidation of the surface.

$$2H_2O_2 \rightarrow 2H_2O + O_2$$

Another reaction process may involve the presence of free radicals (excited forms of $HO_2^\bullet$ and $OH^\bullet$), which participate in the free radical catalysis of hydrogen peroxide breaking down to water and oxygen. It has been reported (Ardon, 1965; Cotton & Wilkinson, 1980) that in acidic solutions, the presence of Fe^{3+} may act as a catalyst in the breakdown of hydrogen peroxide. This process may involve the leaching of iron from the surface and the oxidation of the iron in solution from Fe^{2+} to Fe^{3+}.

An investigation of the surface characteristics after slight oxidation reveals that the oxidation of the surfaces tends to start

where oxygen forms (as bubbles) on the sulphide surface, with oxidation initiated at the (H_2O_2 + H_2O)/O_2/sulphide interfaces.

The order of stability of the sulphides determined after hydrogen peroxide oxidation is listed below. The order is identical to the overall stability for sulphide oxidation, suggesting that although the reactions may be complex, the overall stability of the sulphides remains unchanged from that observed using hydrogen peroxide.

Table 10.3. Order of stability of the sulphides to oxidation by hydrogen peroxide.

Sulphide	Observed stability	%Sulphide
Pyrite	MOST STABLE	35.6
Violarite		27.3
Monoclinic Pyrrhotine		15.3
Arsenopyrite		9.2
Hexagonal Pyrrhotine		2.5
Chalcopyrite		1.8
Pentlandite	LEAST STABLE	0.0

%Sulphide = the percentage of the primary sulphide remaining in the oxidised (≈15Å) surface, determined from XPS/AES spectra.

In considering the process of oxidation it may be valid to consider the oxidation as a result of water/oxygen reactions at the mineral surface, since it has been observed that the initiation of oxidation is a result of oxygen bubbles forming on the surfaces. The proportions of Fe^{2+} and Fe^{3+} determined in the surfaces suggest that the iron oxides and hydroxides are a combination of Fe_3O_4 and FeOOH. Thus for;

Iron sulphides;

$$3FeS_x + 2O_2 \rightarrow Fe_3O_4 + 3xS$$

$$2FeS_x + 2H_2O + O_2 \rightarrow 2FeOOH + H_2S + (2x-1)S$$

$$FeS_x + 2H_2O + O_2 \rightarrow FeSO_4 + (x-1)H_2S + (6-2x)H^+ + (6-2x)e$$

Violarite:

$$3FeNi_2S_4 + 5O_2 \rightarrow Fe_3O_4 + 6NiO + 12S$$
$$FeNi_2S_4 + 0.5H_2O + 1.75O_2 \rightarrow FeOOH + 2NiO + 4S$$
$$FeNi_2S_4 + 3O_2 \rightarrow FeSO_4 + 2NiO + 4S$$

Pentlandite:

$$2Fe_{4.5}Ni_{4.5}S_8 + 3.83O_2 \rightarrow 4FeNi_2S_4 + 1.67Fe_3O_4 + NiO$$
$$2Fe_{4.5}Ni_{4.5}S_8 + 3.5H_2O + 7.75O_2 \rightarrow 2FeNi_2S_4 + 7FeOOH + 5NiO + 8S$$
$$2Fe_{4.5}Ni_{4.5}S_8 + H_2O + 11O_2 \rightarrow 3FeNi_2S_4 + 4FeSO_4 + 2FeOOH + 3NiO$$

Chalcopyrite:

$$3CuFeS_2 + 2O_2 \rightarrow Cu_2S + CuS + Fe_3O_4 + 4S$$
$$3CuFeS_2 + 1.5H_2O + 2.25O_2 \rightarrow Cu_2S + CuS + 3FeOOH + 4S$$
$$3CuFeS_2 + 6O_2 \rightarrow Cu_2S + CuS + 3FeSO_4 + S$$

Arsenopyrite:

$$6FeAsS + 8.5O_2 \rightarrow 2Fe_3O_4 + 3As_2O_3 + 6S$$
$$2FeAsS + H_2O + 3O_2 \rightarrow 2FeOOH + As_2O_3 + 2S$$
$$2FeAsS + 5.5O_2 \rightarrow 2FeSO_4 + As_2O_3$$

The apparent concentration of elemental sulphur in the oxidised surfaces is less than expected considering possible reactions. This may be due to the removal of sulphur species from the surface in the form of dissolved sulphates. Although most of the surfaces show the oxy-sulphate phase to be sulphate, the less oxidised pyrite surfaces also contain sulphite.

10.2.4. Electrochemical oxidation.

In initial experiments carried out in order to determine whether to use the mineral as the anode or the cathode (with reference to previous work by Peters & Majima, 1968 and Biegler & Swift, 1979) it

was observed with initial oxidation experiments that both methods produced like results if similar oxidising potentials were used. In this work it was decided to use anodic oxidation since this should promote the formation of cations at the sulphide surface. The operating voltage used was approximately 15V, the exact value depending on the mineral. However, much of this potential is required to polarise the carbon cathode and overcome the resistance of the water. Potentials monitored at the start of oxidation maintained a voltage of 0.8V at the mineral surface. Attempts to measure current reduction with time through the circuit were consistent with an increased resistance through the sulphide, as a result of a non-conducting surface forming. However, the time/current results could not be replicated with an accuracy sufficient for quantitative analysis.

The spectroscopic analyses of the oxidised surfaces allowed determination of the following order of oxidation stability for the electrochemically oxidised surfaces.

Table 10.4. The order of stability of the sulphides to electrochemical oxidation.

Sulphide	Observed stability	%Sulphide
Violarite	MOST STABLE	17.3
Pentlandite		12.4
Pyrite		7.8
Monoclinic Pyrrhotine		6.3
Arsenopyrite		4.3
Hexagonal Pyrrhotine		3.0
Chalcopyrite	LEAST STABLE	1.8

%Sulphide = the percentage of the primary sulphide remaining in the oxidised (≈15Å) surface, determined from XPS/AES spectra.

The noticeable feature of electrochemical oxidation is that the general order of stability of the sulphides determined using the other oxidation methods is observed, with the exception of the pentlandite. It has been determined spectroscopically that the

pentlandite surface alters rapidly to violarite when oxidised electrochemically, and as such the characteristics of pentlandite alteration are similar to those of violarite.

The oxidation characteristics of the surfaces are similar to those observed after oxidation by other methods. The Fe^{3+} concentration is greater than that of Fe^{2+} and indicates the formation of FeOOH and Fe_3O_4. From the oxy-sulphate phases it was suggested that sulphates are the major phases in the oxidised surfaces, with additional sulphites determined in the iron-nickel sulphide surfaces. Sulphur is a minor constituent of the surfaces.

10.2.5. Alkaline oxidation (ammonium hydroxide).

The oxidation of the sulphides by ammonium hydroxide (pH = 10.5) gives an indication of the characteristics of alteration produced in alkaline solutions. The order of stability to oxidation (given in table 10.5.) was determined for the sulphides studied.

Table 10.5. The order of stability of the sulphides to oxidation by ammonium hydroxide.

Sulphide	Observed stability	%Sulphide
Monoclinic Pyrrhotine	MOST STABLE	25.2
Hexagonal Pyrrhotine		24.3
Violarite		23.2
Arsenopyrite		18.6
Chalcopyrite		13.4
Pyrite		5.8
Pentlandite	LEAST STABLE	2.3

%Sulphide = the percentage of the primary sulphide remaining in the oxidised (≈15Å) surface, determined from XPS/AES spectra.

The reactions suggested for the alkaline oxidation of sulphides have been presented in the discussion sections of the mineral chapters. From these, it is seen that the oxidation at the surface may be cathodic or anodic. The cathodic or anodic nature of the

reactions on the different mineral surfaces does not appear to affect the order of stability of the sulphides.

General observations regarding the sulphide surfaces include; a) a greater proportion of Fe^{3+} is present compared to Fe^{2+}, b) sulphates are present in all surfaces with additional (or remaining) sulphite in the less oxidised surfaces, and c) the sulphur content is variable and not proportional to the extent of oxidation.

The Fe^{3+} present is probably due to the formation of $Fe(OH)_3$ and FeOOH as a direct consequence of oxidation by hydroxyl ions. A less direct effect of oxidation is the formation of the oxy-sulphate phases, with incomplete oxidation to sulphites and sulphates in the slightly oxidised surfaces, and only sulphates in the more extensively oxidised surfaces. Since the time of exposure of each surface to the oxidant is the same, the difference in oxy-sulphates must be directly related to the rate of oxygenation of the sulphides.

The stability of the sulphides, and their oxidation products, can be considered with respect to Eh/pH diagrams (presented in the discussion sections of the mineral chapters). It may be predicted from these diagrams that the minerals with stability fields in high pH regions should be more stable. This explains the relative stability of monoclinic and hexagonal pyrrhotine, violarite and arsenopyrite. In the cases of chalcopyrite and pentlandite, also stable in high pH solutions, the consequences of sub-surface enrichment are important since the secondary compounds are more stable in high pH solutions than the primary sulphide, increasing the extent of alteration.

The reason for the extensive alteration of pyrite observed (and reproduced on several pyrite surfaces), is uncertain since, both from thermochemical considerations, and the observed stability of pyrite to other oxidants, the instability is greater than that expected.

10.2.6. Acid oxidation (sulphuric acid).

The oxidation of sulphides by acids is relevant to numerous natural environments and to metallurgical processing. The effect of sulphuric acid (pH = 1.9) illustrates the effect of low pH solutions

on sulphide surfaces. The oxidation by sulphuric acid produces the order of stability for the sulphides presented in table 10.6.

Table 10.6. The order of stability of the sulphides to oxidation by sulphuric acid.

Sulphide	Observed stability	%Sulphide
Pyrite	MOST STABLE	20.3
Monoclinic Pyrrhotine		16.3
Violarite		12.8
Pentlandite		6.2
Arsenopyrite		4.4
Hexagonal Pyrrhotine		2.0
Chalcopyrite	LEAST STABLE	1.8

%Sulphide = the percentage of the primary sulphide remaining in the oxidised (≈15Å) surface, determined from XPS/AES spectra.

Suggested reactions for the acid oxidation of sulphides are included in the discussion sections of chapters 4 to 9. In considering the order of stability, with the exception of pentlandite, acid oxidation produces results that are comparable to the overall order of stability determined in section 10.3.

Reasons for the differing extents of oxidation observed are difficult to determine since there are considerable variations in the oxidation products observed. The main factor apparently causing these variations is the leaching of metals from the surface and their dissolution as metals (as suggested in the Eh/pH diagrams) as opposed to the formation of compounds in other aqueous media.

Oxy-sulphates are a large component of all of the sulphide surfaces, of which sulphates predominate (only violarite shows evidence of some sulphite). The presence of sulphite is an indication that the sulphuric acid does not wholly produce oxy-sulphates by a direct combination of sulphate ions with surface cations. The formation of elemental sulphur, as with alkaline oxidation, is variable. The largest sulphur concentration is determined for

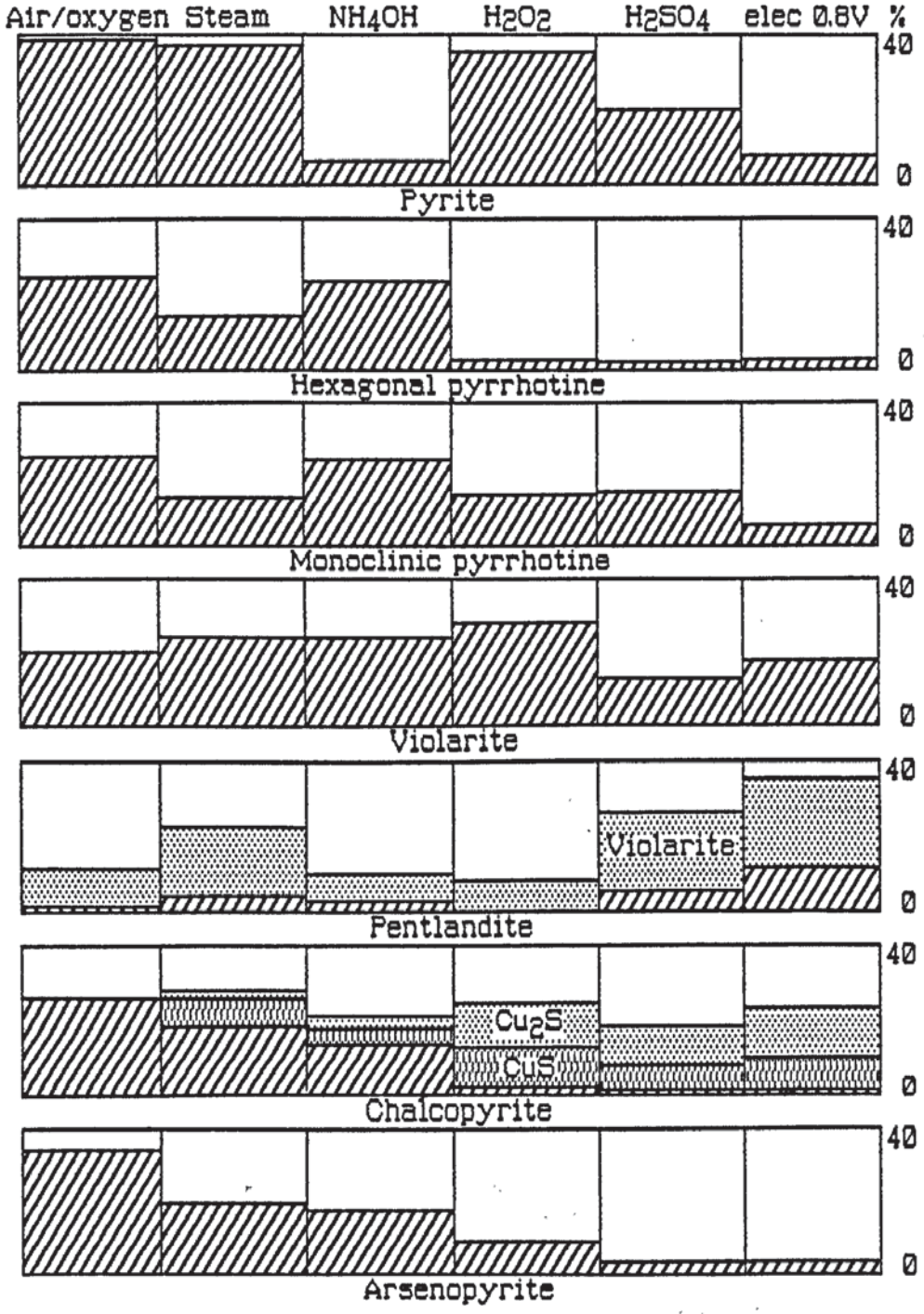

Figure 10.1. Relative sulphide oxidation: A schematic representation of the extent of oxidation in terms of the percentage of sulphides remaining in the 15Å surface layer after oxidation (as determined by XPS/Auger analyses).

pentlandite surfaces and this may inhibit surface oxidation, accounting for the reduced oxidation of pentlandite observed.

10.3. General model of sulphide oxidation.

In the above sections and the previous chapters, reactions have been proposed to account for the oxidation characteristics observed. The general extent of oxidation observed in particular cases (from the XPS/Auger data) is considered in section 10.3.1. and suggestions as to the major controlling processes involved in the oxidation of the sulphide surfaces are discussed in section 10.3.2., with the effect of metal:sulphur ratios considered in section 10.3.3.

10.3.1. The general effects of oxidation.

The relative effects of oxidation on the different sulphide surfaces are shown in figure 10.1., which indicates variable oxidation, both in terms of the mineral stability and the oxidant used. By an assessment of the remaining sulphides present in the 15Å surface (the estimated depth studied using x-ray photoelectron and Auger electron spectroscopies), an overall sequence of mineral oxidation is suggested for the the sulphides investigated;

Most stable:	Pyrite
	Violarite
	Monoclinic pyrrhotine
	Arsenopyrite
	Hexagonal pyrrhotine
	Chalcopyrite
Least stable:	Pentlandite

This sequence is determined from an average of the oxidation characteristics observed on all of the oxidised surfaces, although particular oxidants may cause oxidation characteristics that are not in agreement with the above suggested order of stability.

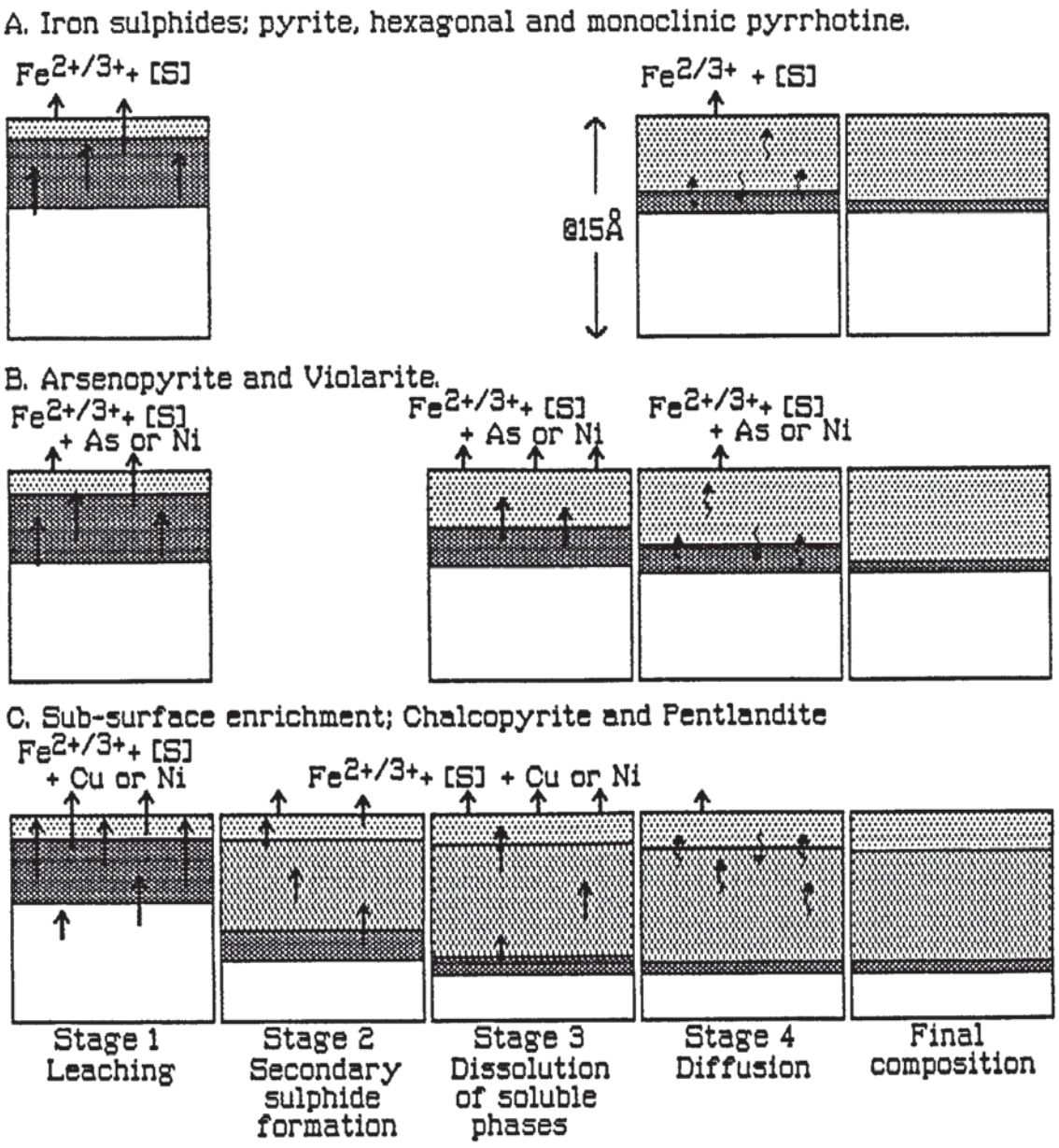

Figure 10.2. Schematic representation of sulphide oxidation; involving leaching (mainly of iron), sub-surface enrichment, dissolution (of soluble compounds) and diffusion in the sub-surface, as discussed in section 10.3.2. No specific thicknesses of oxidation products should be inferred from these diagrams.

10.3.2. A Model of sulphide oxidation.

Several controlling factors are suggested to account for the chemical alteration determined in the altered surfaces. The stages of alteration suggested below are referred to in figure 10.2., and are treated as being interconnected processes.

Stage 1. The primary oxidation process is suggested to be the leaching of iron (and to a lesser extent other cations) from the sulphide surfaces. This is promoted by the ease of formation of Fe^{2+} and Fe^{3+} ions in solution. Also, considering the oxidation, iron oxides/hydroxides may, from thermochemical considerations, form in preference to the oxides of nickel, copper or arsenic. The primary oxidation of the surface may be related to the number of metal sites at the surface, as discussed in the next section.

Stage 2. As a result of the leaching of iron and other cations from the sample surface, a sub-surface enrichment may be exhibited, as observed for chalcopyrite and pentlandite (showing enrichment in copper and nickel respectively). The model of sub-surface enrichment was first proposed for chalcopyrite by Buckley & Woods (1984a). They also suggested that the sub-surface could be regarded as a metal deficient sulphide in agreement with the observed characteristics of the altered chalcopyrite and pentlandite surfaces. The sulphides that do not show sub-surface enrichment in certain elements may nevertheless, through a process of metal leaching, become metal-deficient. The alteration of the immediate surface may be increased by the instability of the sulphide layer. Considering the suggested order of stability to oxidation proposed in section 10.3.1., the phenomenon of sub-surface enrichment appears to result in an increase in the extent of alteration.

Stage 3. Dissolution is expected to be a major factor in the oxidation of the surfaces, although the amount of material removed from the surface is uncertain. The effects of dissolution are most evident in the alteration shown by arsenopyrite (comparing the

air/oxygen (150°C) to solution oxidation). The effects of dissolution could be expected to be large in the initial stages of oxidation; however, dissolution may be expected to decrease as a relatively inert (oxide/hydroxide/sulphate) layer develops on the surface.

Stage 4. The formation of an inert layer on the sample surface should eventually limit the alteration by limiting the rapid transfer of ions to and from the oxidising media. Further oxidation and re-equilibration of the sulphide surface may then be controlled by diffusive processes. The limits imposed on the surface oxidation by the 'oxide' layer can be appreciated in the representation of the sulphide oxidation shown in figure 10.1, in which it is shown that the oxidation of even the most reactive sulphide is limited to ∝15Å into the surface.

10.3.3. Metal:sulphur ratios and the sulphide stability.

Table 10.7. Metal:sulphur ratios of the sulphides (in order of increasing alteration).

Sulphide	Formula	Ratio of metal to sulphur
Pyrite	FeS_2	1 : 2.00
Violarite	$FeNi_2S_4$	1 : 1.33
Monoclinic pyrrhotine	Fe_7S_8	1 : 1.14
Arsenopyrite	FeAsS	*
Hexagonal pyrrhotine	Fe_9S_{10}	1 : 1.11
Chalcopyrite	$CuFeS_2$	1 : 1.00
Pentlandite	$(Fe,Ni)_9S_8$	1 : 0.88

* The metal:sulphur ratio of arsenopyrite is complicated by the involvement of the arsenic.

The overall relative stabilities of the sulphides may be related to the metal:sulphur ratio of the bulk sulphide. This is shown in table 10.2. With the exception of arsenopyrite, due perhaps to the differing chemistry of arsenic, an increase in the metal:sulphur ratio

appears to be associated with an increase in the extent of alteration observed.

The less oxidised sulphides contain a lower proportion of metals. The lower proportion of metals will result in a lower concentration of metals in surface sites. In the sequence of general oxidation predicted (section 10.3.2.) it was suggested that the initial oxidation is promoted by a leaching of cations from the surface, from which it can be inferred that a lowering of the concentration of metal sites at the surface would result in relatively decreased oxidation.

10.4. Sulphide oxidation in ores and during mineral processing.

The alteration of sulphide minerals can also be considered by comparison with the alteration of naturally occurring ores (section 10.4.1.), and the effects of surface oxidation can be considered with respect to the flotation and leaching processes of importance to the metallurgical industry (section 10.4.2.).

10.4.1. Natural alteration of sulphides: Effects of surface alteration.

The oxidation of sulphides is affected by the Eh/pH conditions prevailing in the oxidising solutions. The range of Eh/pH conditions measured in natural waters is summarised in figure 10.3. In meteoric, stream and groundwaters, pH values are determined to be approximately neutral, which contrasts with mine waters which exhibit low pH values and tend to be highly oxidising.

The high acidity observed in mine waters is a consequence of the alteration of sulphides. Sulphates are dissolved as the sulphides oxidise, and the production of hydrogen ions during the oxidation process increases the acidity; generally -

$$MS + 5H_2O \rightarrow MO + SO_4^{2-} + 10H^+ + 8e$$

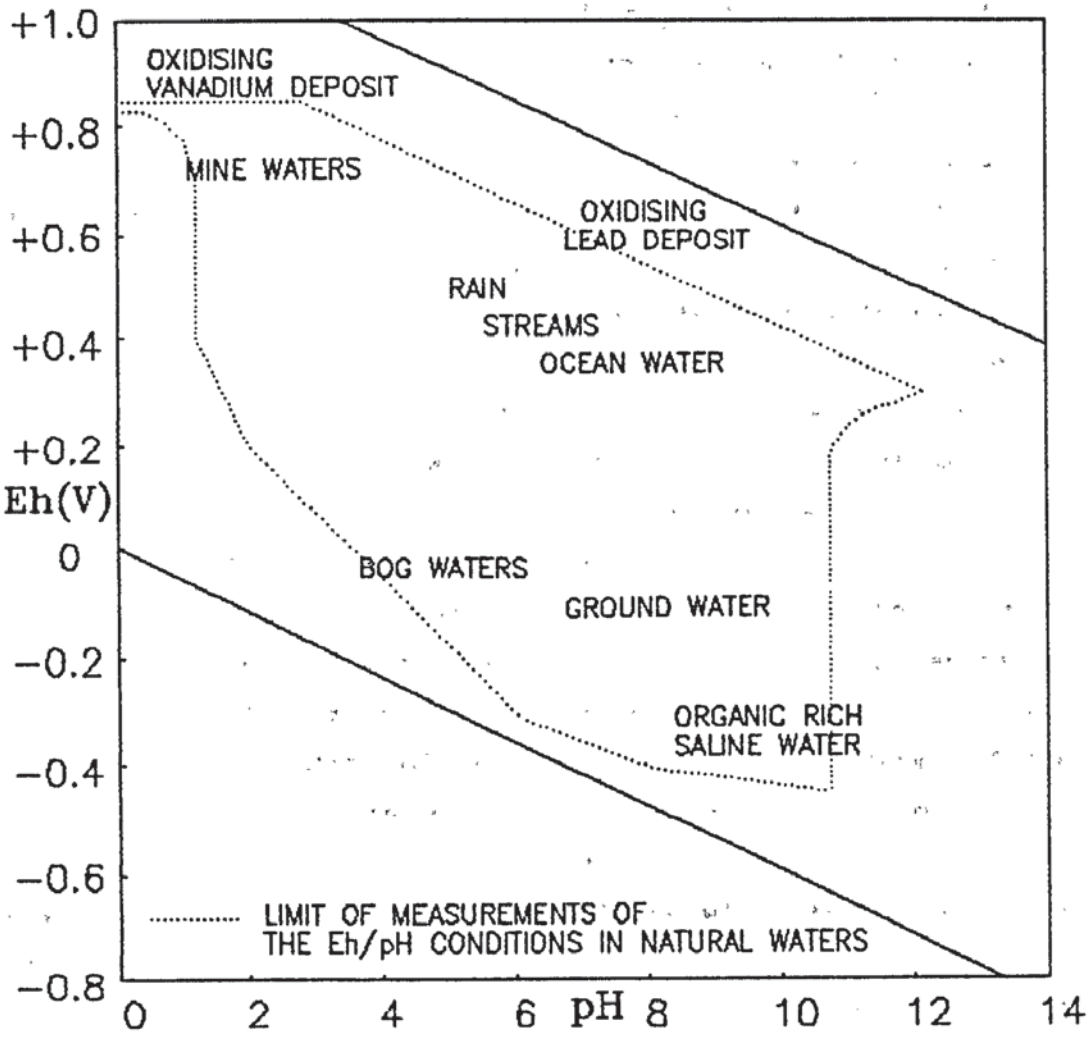

Figure 10.3. The Eh/pH conditions of specific environments in natural water systems (after Garrels & Christ, 1965), with the extent of a study of natural waters shown by the dotted line (after Baas Becking et al., 1960).

The equation above explains the formation of sulphate ions, a factor that has not been considered in much detail in previous chapters since analyses of the chemical compositions of the oxidising solutions were not undertaken. According to the Eh/pH diagrams, sulphate ions are likely to be major dissolved products.

In mine waters, the oxidation is self-promoting since the lowering of the pH, as a result of the dissolution of oxidised phases, effectively increases the oxidation. For this reason, the oxidation in the natural environment can be assumed to be largely in neutral to acid solutions, with a trend towards acid environments. Considering this, the order of stability of the sulphides can be assumed to be similar to the order shown in section 10.3.1. (although acid environments such as those found in mine waters would suggest pentlandite to be relatively more stable).

Of concern from an environmental standpoint, is the effect of run-off from mines and mine dumps, and the resulting contamination of the drainage system by dissolved species. Important among these effects are acidification of the groundwater and, in terms of the sulphides studied, an increase in the concentration of dissolved ions such as copper and nickel. More importantly, mines and mine dumps containing arsenic minerals would oxidise with the formation of soluble arsenic oxides, which may be leached out by the low pH and, as suggested in chapter 9, the run-off from such dumps could result in serious local pollution of the environment.

10.4.2. Surface chemistry in relation to mineral processing.

The direct application of this study of the oxidation of sulphide surfaces to mineral processing is limited, and in section 10.5. further research proposals linking the fields of study are presented. However, it may be possible to infer some of the consequences of the oxidation of the sulphide surfaces in terms of flotation and leaching.

In the beneficiation of ores for the extraction of metals, the minerals of importance in this investigation are chalcopyrite and pentlandite (and less importantly violarite), major ores of copper

and nickel respectively. Arsenopyrite is a hindrance (as a contaminant) in the processing of some ores, and since the required production of arsenic is met by extraction from the flue dusts of smelters as a by-product of the processing of other metals, it is not required as an ore mineral.

Considering nickel extraction (Peters, 1976), oxidation by acids has no application to nickel-containing sulphide processing; however, the alteration by alkalis is important in the oxidation of the ores prior to ammonia pressure leaching. Wills (1985) reports the optimum pH for the flotation of nickel ores to be 8 to 9. The observed oxidation of pentlandite shows that sub-surface enrichment and eventually a limited oxidation of the surface, partly protected by violarite formation, restricts the amount of nickel present as nickel oxide. Since ammonia leaching is effective for the extraction of nickel from NiO, into solution as ammines, the lack of NiO in the surfaces of alkaline oxidised sulphides may limit extraction efficiency.

Chalcopyrite is the main source of the world's supplies of copper and, as such, its oxidation in extraction procedures is important. Several processes are used to decompose chalcopyrite for the extraction of copper, and of relevance to this work, are the use of both acids and alkalis. Both methods are reported (Peters, 1976) to proceed via the leaching of iron from the mineral and the gradual enrichment in copper of the residue, which is extracted before final reduction of the copper ore.

The importance of surface chemistry is evident in the flotation of metal ores, in which the flotation agents become attached to certain sites on the mineral surfaces. Briefly, the froth flotation process used in mineral separation involves the use of collectors, chemically attached to the mineral surface, such that the mineral is rendered either hydrophobic or aerophobic, and in such states, the mineral can be concentrated by separation into froth or aqueous media respectively. The sulphides investigated in this work, and sulphides in general, tend to be naturally hydrophobic and can be concentrated in the froth: however, as outlined by Wills (1985, in a classification

table), sulphates can be considered less hydrophobic, and oxides/hydroxides to be hydrophilic.

The complex interactions caused as a result of surface alteration (an inevitable consequence in preliminary crushing and grinding of these ore minerals) complicates the flotation process, and it is often necessary to use activators (compounds which alter the surface such that it is accessible to flotation reagents).

Considering the surfaces examined in this investigation, the flotation capability of the economic ore fraction during processing could be inferred to decrease as oxidation increases (hence increasing the hydrophilic character). For this reason, a characterisation of the surface components in oxidising environments and their relative proportions is of importance in determining potential activators and collectors, and in improving extraction efficiency. In addition, recognition of those environments that would cause alteration or a particular form of alteration, eg. sulphatisation, may be of economic benefit when considering the cost of extraction reagents.

10.5. Proposals for further research concerning sulphide surfaces.

During the course of this investigation, three potential areas for further research into the surface chemistry of sulphides were noted, and are briefly outlined below.

a) The metal:sulphur model for the stability of the sulphides appears to be a useful model and a further development of this at the molecular level is needed. In addition, the study of further sulphides (including the major economic minerals) would expand on this theory and as well as characterising the chemical compositions of other mineral surfaces.

b) Of industrial importance, an application of the surface chemical data determined in this study, would be useful in the study of the effects of flotation reagents, collectors, modifiers etc. on the mineral surfaces, and their efficiency after various oxidative pre-treatments.

c) In natural deposits, the effect of electrical oxidation cells is important (such as those suggested by Thornber (1975b) and discussed in chapters 6 and 7). It is recognised that the driving force in electrical oxidation cells is the cathodic reduction of water, allowing the anodic oxidation of orebodies (over a scale of tens to hundreds of metres). Since the reactions proposed for the minerals in this investigation show both anodic and cathodic characters, it may be possible that smaller scale oxidation cells (of a few centimetres or less) are formed between these minerals. From a study of the effects of oxidation and, in particular, the rates of reaction on the surfaces of certain important minerals from specific deposits, it may be possible to determine the effect of electrical coupling between these minerals, and the effect this has on the alteration of orebodies.

REFERENCES

References.

ARDON, M.
Oxygen. Chapter 4; Hydrogen Peroxide.
Pub. Benjamin. 1965.

ARMSTRONG, R.J., MORRISH, A.H. and SAWATSKI, G.A.
A Mössbauer study of ferric ions in a spinel.
Physics Letters. 23 pp 414-416. 1966.

ARNOLD, R.G.
Equilibrium relations between pyrrhotite and pyrite from 325°C to 743°C.
Economic Geology. 57 pp 72-90. 1962.

ARNOLD, R.G.
Pyrrhotite phase relations below 304 +/- 6°C at <1 atm total pressure.
Economic Geology. 64 pp 405-419. 1969.

BAAS-BECKING, L.G.M., KAPLAN, I.R. and MOORE, D.
Limits of the natural environment in terms of pH and oxidation-reduction potentials.
Journal of Geology. 68 pp 243-284. 1960.

BAHL, M.K., WOODALL, R.O., WATSON, R.L. and IRGOLIC, K.J.
Relaxation during photoemission and LMM Auger decay in arsenic and some of its compounds.
Journal of Chemical Physics. 64 (3) pp 1210-1218. 1976.

BANCROFT, G.M.
Mössbauer spectroscopy: An introduction for inorganic chemists and geochemists.
Pub. McGraw-Hill, England. 1973.

BANCROFT, G.M., MADDOCK, A.G., ONG, W.K., PRINCE, R.H. and STONE, A.J.
Mössbauer spectra of iron III diketone complexes.
Journal of the Chemical Society. A1976 pp 1966-1971. 1967.

BANERJEE, A.C.
Mechanism of oxidation of iron pyrites.
Chemical Communications. pp 1006-1007. 1971.

BIEGLER, T. and SWIFT, D.A.
Anodic behaviour of pyrite in acid solutions.
Electrochemica Acta. 24 (4) pp 415-420. 1979.

BOATENG, D.A.D. and PHILLIPS, C.R.
The hydrometallurgy of nickel extraction from sulphide ores.
Part 1. Feed preparation and leaching systems.
Mining Science and Engineering. 10 (3) pp 151-171. 1978.

BRIGGS, D. and SEAH, M.P.
Practical surface analysis by Auger and x-ray photoelectron spectroscopy.
Pub. Wiley, England. 1983.

BRION, D.
Etude par spectroscopie de photoelectrons de la degradation superficielle de FeS_2, $CuFeS_2$, ZnS et PbS a l'air et dans l'eau.
Aplications of Surface Science. 5 pp 133-152. 1980.

BRION, D., HAYER, J. and PREDALI, J.J.
Characterisation by ESCA of surface compounds of pyrite during the flotation process.
Fine Particles Processing. Proceedings of the International Symposium. 1 pp 544-547. 1980.

BRUNDLE, C.R., CHUANG T.J., and WANDELT K.
Core and valence photo-emission studies of iron oxide surfaces and the oxidation of iron.
Surface Science 68 pp 459-468. 1977.

BUCKLEY, A.N. and WOODS, R.
An x-ray photoelectron spectroscopic investigation of the tarnishing of bornite.
Australian Journal of Chemistry. 36 pp 1793-1804. 1983.

BUCKLEY, A.N. and WOODS, R.
An x-ray photoelectron spectroscopic study of the oxidation of chalcopyrite.
Australian Journal of Chemistry. 37 pp 2403-2413. 1984a.

BUCKLEY, A.N. and WOODS, R.
An x-ray photoelectron spectroscopic investigation of the surface oxidation of sulphide minerals.
Proceedings of the International Symposium on Electrochemistry. Mineralogical and Metallurgical Processing. pp 286-302. 1984b.

BUCKLEY, A.N. and WOODS, R.
X-ray photoelectron spectroscopy of oxidised pyrrhotite surfaces. I. Exposure to air.
Applications of Surface Science. 22/23 pp 280-287. 1985.

BUCKLEY, A.N. and WOODS, R.
X-ray photoelectron spectroscopy of oxidised pyrrhotite surfaces. II. Exposure to aqueous solutions.
Applications of Surface Science. 20 pp 472-480. 1985.

BUCKLEY, A.N., HAMILTON, I.C. and WOODS, R.
Investigation of the surface oxidation of sulphide minerals by linear potential sweep voltammetry and x-ray photoelectron spectroscopy.
Developments in Mineral Processing. 6 pp 41-60. 1985.

BURHOP, E.H.S.
The Auger effect and other radiationless transitions.
Cambridge monographs on physics.
Cambridge University Press, England. 1952.

BURKIN, A.R.
The chemistry of hydrometallurgical processes.
Pub. E. & F.N. Spon Ltd., England. 1966.

CABRI, J.L.
New data on phase relations in the Cu-Fe-S system.
Economic Geology. 68 pp 443-454. 1973.

CARPENTER, R.H. and DESBOROUGH, G.A.
Range in solid solution and structure of naturally occurring troilite and pyrrhotite.
American Mineralogist. 49 pp 1350-1365. 1964.

CLARK, A.H.
Stability field of monoclinic pyrrhotite.
Transactions of the Institute of Mining and Metallurgy. 75B pp 232-235. 1960.

CLIFFORD, R.K., PURDY, K.L. and MILLER J.D.
Characterisation of sulphide mineral surfaces in froth flotation systems using electron spectroscopy for chemical analysis.
Americal Institute of Chemical Engineering (AIChE) symposium series. 71 (150) pp 138-147. 1975.

COCHRAN, S.J. and LARKINS, F.P.
Surface reduction in some transition metal oxides. An x-ray photoelectron spectroscopic study of iron, copper, nickel and zinc oxides.
Journal of the Chemical Society, Faraday Transactions. 81 2179-2190. 1985.

COMPTON, D.M.J. and SCHOEN, A.H.
The Mössbauer effect: Proceedings of the second international conference on Mössbauer spectroscopy.
Wiley and Sons, England. 1962.

COTTON, F.A. and WILKINSON, G.
Advanced Inorganic Chemistry (An Inorganic Text). 2nd ed.
Pub. Interscience Publishers. 1980.

CRAIG, J.R.
Violarite stability relations.
American Mineralogist. 56 pp 1303-1311. 1971.

CRAIG, J.R. and VAUGHAN, D.J.
Ore microscopy and ore petrography.
Pub. Wiley, England. 1981.

DAVIS, L.E. ed.
Handbook of Auger electron spectroscopy.
Pub. Physical Electronics Industries, USA. 1976.

DESBOROUGH, G.A. and CARPENTER, R.H.
Phase relations of pyrrhotite.
Economic Geology. 60 pp 1431-1450. 1965.

DUTRIZAC, J.E. and MACDONALD, R.J.C.
Ferric ion as a leaching medium.
Mining Science Engineering. 6 (2) pp 59-100. 1974.

EADINGTON, P.
Study of oxidation layers of surfaces of chalcopyrite by use of Auger electron spectroscopy.
Transactions of the Insitute of Mining and Metallurgy C. 1977 pp 186-189.

EVANS, B.J., JOHNSON, R.G., SENFTLE, F.E., BLAINE CECIL, C. and DULONG, F.
The Fe Mössbauer parameters of pyrite and marcasite with different provenances.
Geochemica et Cosmochemica Acta. 46 pp 761-775. 1982.

FERREIRA, R.C.H. and BURKIN, A.R.
Acid leaching of chalcopyrite. In "Leaching and reduction in hydrometallurgy". ed. Burkin, A.R.
Pub. The Institute of Mining and Metallurgy, England. 1975.

FINKLEA, S.L. and CATHEY, L.
Investigation of the bonding mechanism in pyrite using the Mössbauer effect and x-ray crystallography.
Acta Crystallographica. A32 pp 529 - 537 1976

FLUCK, E.
The Mössbauer effect and its application in chemistry.
Advances in Inorganic Chemistry and Radiochemistry. 6 pp 433-489. 1963.

FORWARD, F.A. and MACKIW, V.I.
Chemistry of the ammonia process for leaching Ni, Cu and Co from Sherritt Gordon sulphide concentrates.
Journal of Metals. 7 pp 457-463. 1955.

FYSH, S.A. and OSTWALD, J.
A Mössbauer study of some Australian iron ore minerals.
Mineralogical Magazine. 47 pp 209-217. 1983.

GARRELS, R.M. and CHRIST, C.L.
Solutions, minerals, and equilibria.
Pub. Harper and Row, England. 1965.

GONSER, U., GRANT, R.W., MUIR, A.H. and WIEDERSICH, H.
Precipitation and oxidation studies in the Cu-Fe system using the Mössbauer effect.
Acta Metallurgica. 14 (3) pp 259-264. 1966.

GOPALAKRISHNAN, J., MURUGESAN, T., HEGDE, M.S. and RAO, C.N.R.
Study of transition metal monosulphides by photoelectron spectroscopy.
Journal of Physics C. (Solid State Physics). 12 pp 5255-5261. 1979.

GRAHAM, A.R.
Quantitative determination of hexagonal and monoclinic pyrrhotite by x-ray diffraction.
Canadian Mineralogist. 10 pp 4-24. 1969.

HABASHI, F.
Chalcopyrite its chemistry and metallurgy.
Pub. McGraw-Hill, USA. 1978.

HARVEY, D.T. and LINTON, R.W.
Chemical characterisation of hydrous ferric oxides by x-ray photoelectron spectroscopy.
Analytical Chemistry. 53 (11) pp 1684-1688. 1981.

HIROKAWA, K. and OKU, M.
Application of ESCA to semi-quantitative surface and state analysis.
Talanta. 26 (9) pp 855-859. 1979.

HOBSON, M.C.
Mössbauer spectroscopy. Chapter 13 in "Characterization of solid surfaces". eds. Kane, P.F. and Larrabee, G.B.
Pub. Plenum Press, USA. 1974.

HOLLOWAY, P.H., REMOND, G. and SWARTZ, W.E.
Surface composition and reflectance of polished $CuFeS_2$.
Meeting of the Engineering Foundation (USA). Interfacial Phenomena in Mineral Processing. pp 93-117. 1981.

KEELE, R. and NICKEL, E.H.
The geology of a primary millerite bearing sulphide assemblage and supergene alteration at the Otter Shoot, Kambalda, Western Australia.
Economic Geology. 69 pp 1102-1117. 1974.

KISSIN, S.A.
Phase relations in a portion of the Fe-S system.
PhD. thesis, University of Toronto, Canada. 1974.

KISSIN, S.A. and SCOTT, S.D.
Phase relations involving pyrrhotite below 350°C.
Economic Geology. 77 pp 1739-1754. 1982.

KNOP, O., HUANG C-H, and WOODHAMS, F.W.D.
Chalcogenides of the transition elements. VII. A Mössbauer study of pentlandite.
American Mineralogist. 55 pp 1115-1130. 1970.

KULLERUD, G.
Thermal stability of pentlandite.
Canadian Mineralogist. 7 pp 353-366. 1963.

KULLERUD, G. and YODER, H.S.
Pyrite stability relations in the Fe-S system.
Economic Geology. 54 pp 533-572. 1959.

LARSON, P.E.
ESCA studies of some copper and silver selenides.
Journal of Electron Spectroscopy and Related Phenomena. 4 (3) pp 213-218. 1974.

LEFELHOCZ, J.F., FRIEDEL, R.A. and KOHMAN, T.P.
Mössbauer spectroscopy of iron in coal.
Geochemica et Cosmochemica Acta. 31 pp 2261-2273. 1967

LETOWSKI, F.
Acid hydrometallurgical leaching of copper and other metals from complex Polish copper concentrates.
Developments in Mineral Processing. Procedings of the Warsaw conference on mineral processing. 1979.

LIMOUZIN-MAIRE, Y.
Etude par spectroscopie ESCA de sulfures et sulfates de manganese, fer, cobalt, nickel, cuivre et zinc.
Bulletin of the Chemical Society (France). Pt.1 pp 340-343. 1981.

LOSCH W. and MONHEMIUS A.J.
An AES study of a copper-iron sulphide mineral.
Surface Science. 60 pp 196-210. 1976.

LOWSON, R.T.
Aqueous oxidation of pyrite by molecular oxygen.
Chemical Reviews. 82 (5) pp 461-497. 1982.

MADDOCK, A.G.
Mössbauer spectroscopy in mineral chemistry. Chapter 5 in "Chemical bonding and spectroscopy in mineral chemistry".
eds. Berry, F.J. and Vaughan, D.J.
Pub. Chapman and Hall Ltd., England. 1985.

MAJIMA, H. and PETERS, E.
Oxidation rates of sulphide minerals by aqueous oxidation at elevated temperatures.
Transactions of the metallurgical Society of AIME. 236 pp 1409-1413. 1966.

MATHEWS, C.T. and ROBINS, R.G.
The oxidation of iron sulphide by ferric sulphate.
Australian Chemical Engineering. 50 pp 21-25. 1972.

McINTYRE, N.S. and COOK, M.G.
X-ray photoelectron studies on some oxides and hydroxides of cobalt, nickel and copper.
Analytical Chemistry. 47 (13) pp 2208-2213. 1976.

McINTYRE, N.S. and ZETARUK D.G.
X-ray photoelectron spectroscopic studies of iron oxides.
Analytical Chemistry. 49 (11) pp 1521-1529. 1977.

MILLS, K.C.
Thermodynamic data for inorganic sulphides, selenides and tellurides.
Pub. Butterworths, London. 1974.

MILLS, P. and SULLIVAN, J.
An XPS study of the bonding of core level electrons in iron oxides.
Journal of Physics D. (Applied Physics) 16 pp 723-732. 1983.

MISRA, K.C. and FLEET, M.E.
Chemical composition and stability of violarite.
Economic Geology. 69 pp 391-403. 1974.

MITCHELL, D.F., SPROULE, G.I. and GRAHAM, M.J.
Quantitative analysis of iron oxides using Auger electron spectroscopy combined with ion sputtering.
Journal of Vacuum Science Technology. 18 (3) pp. 690-695. 1981.

MOLCHANOV, A.
Pyrite activation.
Geol. Geofiz. (translated from Russ.) 10 pp 142-144. 1982.

MONTANO, P.A. and SEEHRA, M.S.
Magnetism of iron pyrite (FeS_2)- A Mössbauer study in an external magnetic field.
Solid State Communications. 20 pp 897-898. 1976.

MORICE, J.A., REES, L.V.C. and RICKARD, D.T.
Mössbauer studies of iron sulphides.
Journal of Inorganic and Nuclear Chemistry. 31 pp. 3797-3802. 1969.

MORIMOTO, N., GYOBU, A., MUKAIYAMA, H. and IZAWA, E.
Crystallography and stability of pyrrhotites.
Economic Geology. 70 pp 824-833. 1975.

MUIR, A.H. and WIEDERSICH, H.
Investigation of $CuFeO_2$ by the Mössbauer effect.
Journal of the Physics and Chemistry of Solids. 28 (1) pp 65-71. 1966.

MURAD, E.
Mössbauer spectra of goethite: Evidence for structural imperfections.
Mineralogical Magazine. 43 pp 355-361. 1979.

NAKAI, I., SUGITANI, Y., NAGASHIMA, K. and NIWA, Y.
XPS study of copper minerals.
Journal of Inorganic and Nuclear Chemistry. 40 pp 789-791. 1978.

NAKAZAWA, H. and MORIMOTO, N.
Phase relations and superstructures of pyrrhotites $Fe_{1-x}S$.
Material Resources Bulletin. 6 pp 345-358. 1971.

NEFEDOV, V.I., ZHUMADILOV, E.K. and KOPYTOVA, T.Y.
Comparison of the chemical shifts of x-ray electrons and Auger lines.
Journal of Structural Chemistry. 1977vol./Pt.18 pp 549-553.

NICKEL, E.H.
Structural stability of minerals with the pyrite, marcasite, arsenopyrite and loellingite structures.
Canadian Mineralogist. 9 pp 311-321. 1967.

NICKEL, E.H., ROSS, J.R. and THORNBER, M.R.
The supergene alteration of pyrrhotite-pentlandite ore at Kambalda, Western Australia.
Economic Geology. 69 pp 93-107. 1974.

NICKEL, E.H., ALLCHURCH, P.D., MASON, M.G. and WILMSHURST, J.R.
Supergene alteration at the Perseverance Nickel Deposit, Agnew, Western Australia.
Economic Geology. 72 pp 184-203. 1977.

NOVAKOV, T.
X-ray photoelectron spectroscopy of solids; Evidence of band structure.
Physical Review B. 3 (8) pp 2693-2697. 1971.

NOVAKOV, T. and PRINS R.
Band structure and the shake-up photoelectron spectra of copper and nickel halides and oxides.
Solid State Communications. 9 pp 1975-1979. 1971.

PANZNER, G., EGERT, B., and SCHMIDT, H.P.
The stability of CuO and Cu_2O surfaces during argon ion sputtering studied by XPS and AES.
Surface Science 151 pp 400-408. 1985.

PETERS, E.
Direct leaching of sulphides: Chemistry and applications.
Metallurgical Transactions B. 7 pp 505-517. 1976.

PETERS, E. and MAJIMA, H.
Electrochemical reactions of pyrite in acid perchlorate solutions.
Canadian Metallurgy Quarterly. 7 (3) pp 111-117. 1968.

POWER, L.F. and FINE H.A.
The iron-sulphur system. Part 1. The structures and properties of the compounds of the low-temperature phase fields.
Mineral Science Engineering. 8 (2) pp 106-128. 1976.

PRITCHARD A.M. and DOBSON C.M.
Mössbauer effect and iron corrosion kinetics.
Nature. 224 p. 1295. 1969.

PRITCHARD A.M. and MOULD, B.T.
Mössbauer spectra of some iron compounds formed in alkaline solutions.
Corrosion Science. 11 pp 1-9. 1971.

PUTNIS, A. and McCONNELL, J.D.C.
Principles of mineral behaviour.
Pub. Blackwell Scientific, England. 1980.

RAMDOHR, P.
The ore minerals and their intergrowths.
Pub. Pergamon Press, England. 1980.

REMOND, G., HOLLOWAY, P.H. and LeGRESSUS, C.
Electron spectroscopy and microscopy for studying surface changes in mechanically prepared pyrite and quartz.
Scanning electron microscopy. 1 pp 483-492. 1981.

ROBIE, R.A., HEMINGWAY, B.S. and FISHER J.R.
Thermodynamic properties of minerals and related substances at 298.15K and 1 bar (10^5 Pascals) pressure and at higher temperatures.
Geol. Survey Bulletin (1452), U.S. Government Printing Office, Washington, USA. 1978.

ROMAND, M., ROUBIN, M. and DELOUME, J.P.
X-ray induced photoelectron and Auger spectra of copper, copper II oxide, copper I oxide and copper I sulphide thin films.
Journal of Electron Spectroscopy and Related Phenomena. 13 (4) pp 229-242. 1978.

ROSSITER, M.J. and HODGSON, A.E.M.
A Mössbauer study of ferric oxy-hydroxide.
Journal of Inorganic and Nuclear Chemistry. 27 pp 63-71 1965.

RUSSELL, P.E. and MONTANO, P.E.
Magnetic hyperfine parameters of iron containing minerals in coal.
Journal of Applied Physics. 49 pp 4615-4617. 1978.

SAPOROSCHENKO, M., HINCKLEY, C.C., SMITH, G.V., TWARDOWSKA, H., SHILEY, R.H., GRIFFIN, R.A. and RUSSELL, S.J.
Mössbauer spectroscopic studies of the mineralogical changes in coal as a function of cleaning, pyrolysis, combustion and coal-conversion processes.
Fuel. 59 pp 567-574. 1980.

SCOTT, S.D.
Experimental methods in sulphide synthesis.
Chapter 4 of "Sulphide mineralogy". Ed. Ribbe, P.H.
Reviews in Mineralogy, Volume 1. Mineralogical Society of America. 1976.

SHIRANE, G., COX, D.E., TAKEI, W.J. and RUBY, S.L.
A study of the magnetic properties of the $FeTiO_3$-αFe_2O_3 system by neutron diffraction and the Mössbauer effect.
Journal of the Physics Society of Japan. 17 pp 1598-1611. 1962

SIEGBAHN, K.
ESCA: Atomic, molecular and solid state structure studied by means of electron spectroscopy.
Pub. Almqvist and Wiksells, Sweden. 1967.

STANLEY, C.J. and CRIDDLE, A.J.
Quantitative data file for the ore minerals of the Commission on Ore Microscopy of the International Mineralogical Association.
Pub. British Museum (Natural History), England. 1986.

STEGER, H.F.
Oxidation of sulphide minerals, 1. Determination of ferrous and ferric iron in samples of pyrrhotite, pyrite and chalcopyrite.
Talanta. 24 pp 251-254. 1977.

STEGER, H.F.
Oxidation of sulphide minerals, VII. Effect of temperature and relative humidity on the oxidation of pyrrhotite.
Chemical Geology. 35 pp 281-295. 1980.

STEGER, H.F. and DESJARDINS, L.E.
Oxidation of sulphide minerals, 4. Pyrite, chalcopyrite and pyrrhotite.
Chemical Geology. 23 pp 225-237. 1978.

STOUT, D.A., GAVELLI, G., LUMSDEN, G.B. and STAEHLE, R.W.
In situ AES and XPS analysis of iron oxides formed by a galvanic cell.
Applications of Surface Analysis. ASTM special technical publication (STP 699). pp 42-53. 1980.

TERRELL, J.H. and SPIJKERMAN, J.J.
Determination of surface compound formation by backscatter Mössbauer spectroscopy.
Applied Physics Letters. 13 (1) pp 11-13. 1968.

THOMPSON, M., BAKER, M.D., CHRISTIE, A., and TYSON J.F.
Auger electron spectroscopy.
Pub. Wiley and Sons, England. 1985.

THORNBER, M.R.
Supergene alteration of sulphides. I. A chemical model based on massive nickel sulphide deposits at Kambalda, Western Australia.
Chemical Geology. 15 pp 1-14. 1975a.

THORNBER, M.R.
Supergene alteration of sulphides. II. A chemical study of the Kambalda nickel sulphide deposits.
Chemical Geology. 15 pp 117-144. 1975b.

THORNBER, M.R., ALLCHURCH, P.D. and NICKEL, E.H.
Variations in gossan geochemistry at the Preseverance Nickel Sulphide Deposit, Western Australia: A descriptive and experimental study.
Economic Geology. 76 pp 1764-1774. 1981.

THORNBER, M.R. and WILDMAN, J.E.
Supergene alteration of sulphides. VI. The binding of copper, nickel, zinc, cobalt and lead with gossan (iron-bearing) minerals.
Chemical Geology. 44 pp 399-434. 1979.

TOSSELL, J.A., VAUGHAN D.J. and BURDETT, J.K.
Pyrite, marcasite and arsenopyrite type minerals. Crystal chemical and structural principles.
Physics and Chemistry of Minerals. 7 pp 177-184. 1981.

TOSSELL, J.A., URCH, D.S., VAUGHAN, D.J. and WIECH, G.
The electronic structure of $CuFeS_2$, chalcopyrite, from x-ray emission and x-ray photoelectron spectroscopy and $X\alpha$ calculations.
Journal of Chemical Physics. 77 pp 77-82. 1982.

TRICKER, M.J.
Conversion electron Mössbauer spectroscopy and its recent development. In "Mössbauer spectroscopy and its chemical applications", Ch 3. eds. Stevens, J.G. and Shenoy, G.K.
American Chemical Society, USA. 1985.

TSANG, T., COYLE, G.J., ADLER, I., and YIN L.
XPS studies of ion bombardment damage of iron-sulphur compounds.
Journal of Electron Spectroscopy and Related Phenomena. 16 pp 389-396. 1979.

URCH, D.S.
X-ray spectroscopy and chemical bonding in minerals. In chapter 2 of "Chemical bonding and spectroscopy in mineral chemistry". eds. Berry, F.J. and Vaughan, D.J. Chapman and Hall Ltd., England. 1985.

VANYUKOV, A.V., RAZUMOVSKAYA, N.N., VOITKOVSKII, Y.B. and BRUEN, V.N.
Study of the low-temperature oxidation of pyrrhotites. Untranslated abstract. Chemical Abstracts. 87 87.88377h 1977.

VANYUKOV, A.V., RAZUMOVSKAYA, N.N. and VOITKOVSKII, Y.B.
Oxidation of pyrrhotites in aqueous pulps. Untranslated abstract. Chemical Abstracts. 88 88.195156c 1978.

VANYUKOV, A.V. and VOITKOVSKII, Y.B.
Study of the iron monosulphides by a Mössbauer spectroscopic method. Untranslated abstract. Chemical Abstracts. 89 89.97515v 1978.

VANYUKOV, A.V. and RAZUMOVSKAYA, N.N.
Hydrothermal oxidation of pyrrhotites. Untranslated abstract. Chemical Abstracts. 92 92.92283e 1979.

VAUGHAN, D.J. and CRAIG, J.R.
Mineral chemistry of metal sulphides. Pub. Cambridge University Press, England. 1978.

VAUGHAN, D.J. and CRAIG, J.R.
The crystal chemistry of iron-nickel thiospinels. American Mineralogist. 70 pp 1036-1043. 1985.

VAUGHAN, D.J. and RIDOUT, M.S.
Mössbauer study of some sulphide minerals. Journal of Inorganic and Nuclear Chemistry. 33 pp 741-746. 1971.

VAUGHAN, D.J. and TOSSELL, J.A.
Interpretation of the Auger electron spectra (AES) of sulphide minerals. Physics and Chemistry of minerals. 13 (5) pp 347-350. 1986.

WADSWORTH, M.E.
Advances in the leaching of sulphide minerals. Minerals Science and Engineering. 4 (4) pp 36-47. 1972.

WAGNER, C.D.
Handbook of x-ray photoelectron spectroscopy. Pub. Perkin-Elmer, USA. 1979.

WAGNER, C.D., GALE, L.H. and RAYMOND R.H.
Two dimensional chemical state plots: A standardised data set for use in identifying chemical states in x-ray photoelectron spectroscopy. Analytical Chemistry. 51 pp 466-482. 1979.

WALL, F.T.
Chemical thermodynamics.
Pub. W.H.Freeman and Co., USA. 1974.

WARN, J.R.W.
Concise chemical thermodynamics.
Pub. Van Nostrand Reinhold, England. 1969.

WATMUFF, I.G.
Supergene alteration of the Mt. Windarra nickel sulphide ore deposit, Western Australia.
Mineralium Deposita. 9 pp 199-221. 1974.

WEDEPOHL, K.H. ed.
Handbook of Geochemistry.
Pub. Springer, West Germany. 1978.

WERTHEIM, G.K.
Mössbauer effect: Principles and applications.
Pub. Academic Press, USA. 1964.

WILLS, B.A.
Mineral Processing Technology (An introduction to the practical aspects of ore treatment and mineral recovery). 3rd edition.
Pub. Pergamon Press, England. 1985.

APPENDICES.

Appendix 1.

Auger transitions, peak positions, and relative sensitivity factors (S_x), for the measurement of element concentrations from differentiated Auger spectra.

Table A1.1.

Element	Auger Transition	Auger K.E. (eV)	(S_x)
Sulphur	$L_3M_{2,3}M_{2,3}$	152	0.85
Chlorine	$L_3M_{2,3}M_{2,3}$	181	1.05
Argon	$L_3M_{2,3}M_{2,3}$	215	1.05
Carbon	KL_1L_1	272	0.20
Nitrogen	KL_1L_2	379	0.33
Oxygen	KL_1L_2	503	0.50
Iron	($L_3M_{2,3}M_{2,3}$)	598	
	($L_3M_{2,3}M_{4,5}$)	651	
	$L_3M_{4,5}M_{4,5}$	703	0.20
Nickel	($L_3M_{2,3}M_{2,3}$)	716	
	($L_3M_{2,3}M_{4,5}$)	783	
	$L_3M_{4,5}M_{4,5}$	848	0.28
Copper	($L_3M_{2,3}M_{2,3}$)	776	
	($L_3M_{2,3}M_{4,5}$)	849	
	$L_3M_{4,5}M_{4,5}$	920	0.32
Arsenic	($L_3M_{2,3}M_{2,3}$)	1030	
	$L_3M_{2,3}M_{4,5}$	1117	0.03
	($L_3M_{4,5}M_{4,5}$)	1228	0.09

The transitions shown in brackets are prominent features of the differentiated spectra, but are not used in measurements.

Appendix 2.

A2.1. X-ray Photoelectron Data.

Review of binding energy data for compounds forming potential components of oxidised sulphide mineral surfaces. References to previous work and comparative peak values are given.

The sensitivity of the spectrometer to different elements varies as a consequence of the relative escape depths of the photoelectrons, operating voltages, and the energy levels investigated. Table A2.1. shows sensitivity factors in terms of relative peak areas, after Wagner et al. (1979).

Table A2.1.

Element	Energy level	Sensitivity factor
C	1s	0.25
O	1s	0.66
S	2p	0.54
Fe	2p (3/2)	2.00
Ni	2p (3/2)	3.00
Cu	2p (3/2)	4.20
As	3d	0.53

Table A2.2.

Element	Phase	Level	B.E. (eV)	Γ (eV) (Linewidth)	References
Carbon	Adsorbed	1s	284.3	0.7	(1)
	Organic	1s	285+	variable	(1)

Element	Phase	Level	B.E. (eV)	Γ (eV)	References
Oxygen	As_2O_3	1s	531.0	1.1	(2)
	As_2O_5	1s	531.4	1.1	(2)
	CuO	1s	530.7	0.9	(3,4,5,6,8)
	Cu_2O	1s	531.5	0.7	"
	$CuSO_4$	1s	532.8	1.3	(7)
	$Fe_{1-x}O$	1s	530.0	0.7	(9,10,11,12)
	Fe_3O_4 (2+)	1s	530.0	0.7	"
	Fe_3O_4 (3+)	1s	531.4	1.1	"
	Fe_2O_3	1s	531.4	1.1	"
	FeOOH (O)	1s	530.0	0.7	(9,13)
	FeOOH (OH)	1s	531.4	1.1	"
	$Fe(OH)_3$	1s	531.4	1.1	"
	$FeSO_4$	1s	532.6	1.3	(7)
	$Fe_2(SO_4)_3$	1s	532.9	1.3	(7)
	NiO	1s	529.6	0.7	(5)
	NiOOH (O)	1s	530.3	0.7	(5)
	NiOOH (OH)	1s	531.5	1.1	(5)
	$Ni(OH)_2$	1s	531.5	1.1	(5)
	$NiSO_4$	1s	532.0	1.3	(7)
Sulphur	S	2p	162.5	1.2	(Ch. 4-9)
	FeS_2	2p	161.5	0.9	(Ch. 4)
	Fe_7S_8	2p	161.1	0.9	(Ch. 5)
	Fe_9S_{10}	2p	161.1	0.9	(Ch. 5)
	$FeNi_2S_4$	2p	161.2	0.9	(Ch. 6)
	$(Fe,Ni)_9S_8$	2p	161.2	0.9	(Ch. 7)
	$CuFeS_2$	2p	161.4	0.9	(Ch. 8)
	FeAsS	2p	161.2	0.9	(Ch. 9)
	AsS	2p	161.2	0.9	(2)
	As_2S_3	2p	161.2	0.9	(2)
	Cu_2S	2p	161.9	0.9	(14)
	CuS	2p	162.0	0.9	(14)
	NiS_2	2p	161.1	0.9	(1,18)
	NiS	2p	161.2	0.9	(1,18)

Element	Phase	Level	B.E. (eV)	Γ (eV)	References
Sulphur	$CuSO_4$	2p	169.8	1.4	(7)
	$NiSO_4$	2p	167.4	1.4	(7)
	$FeSO_3$ etc.	2p	165-6	1.4	(7)
	$FeSO_4$	2p	168.0	1.4	(7,1)
	$Fe_2(SO_4)_3$	2p	168.2	1.4	(7,1)
Iron	FeS_2	2p(3/2)	707.1	0.9	(Ch. 4)
	Fe_7S_8	2p(3/2)	707.2	0.9	(Ch. 5)
	Fe_9S_{10}	2p(3/2)	707.2	0.9	(Ch. 5)
	$FeNi_2S_4$	2p(3/2)	708.4	0.9	(Ch. 6)
	$(Fe,Ni)_9S_8$	2p(3/2)	707.3	0.9	(Ch. 7)
	$CuFeS_2$	2p(3/2)	707.4	0.9	(Ch. 8)
	FeAsS	2p(3/2)	706.9	0.9	(Ch. 9)
	$Fe_{1-x}O$	2p(3/2)	709.5	1.3	(9,10,11, 12,15,19)
	Fe_3O_4 (2+)	2p(3/2)	709.5	1.3	"
	Fe_3O_4 (3+)	2p(3/2)	710.8	1.5	"
	Fe_2O_3	2p(3/2)	711.0	1.5	"
	FeOOH	2p(3/2)	711.0	1.5	(1,9,13)
	$Fe(OH)_3$	2p(3/2)	711.0	1.5	"
	$FeSO_4$	2p(3/2)	712.3	1.8	(7)
	$Fe_2(SO_4)_3$	2p(3/2)	714.6	1.8	(7)
	Fe (2+)	2p(3/2)	709.8	1.4	valence fit
	Fe (3+)	2p(3/2)	711.0	1.6	valence fit
Nickel	$FeNi_2S_4$	2p(3/2)	853.2	0.9	(Ch. 6)
	$(Fe,Ni)_9S_8$	2p(3/2)	853.0	0.9	(Ch. 7)
	NiS_2	2p(3/2)	853.1	0.9	(1,14)
	NiS	2p(3/2)	853.9	0.9	"
	NiO	2p(3/2)	853.5	1.3	(1,5)
	NiOOH	2p(3/2)	856.0	1.5	(5)
	$Ni(OH)_2$	2p(3/2)	856.0	1.5	(1,5)
	$NiSO_4$	2p(3/2)	858.0	1.8	(1,7)

Element	Phase	Level	B.E. (eV)	Γ (eV)	References
Nickel	Ni (2+)	2p(3/2)	853.5	1.3	valence fit
	Ni (3+)	2p(3/2)	856.0	1.5	valence fit
Copper	$CuFeS_2$	2p(3/2)	932.6	0.9	(Ch. 8)
	Cu_2S	2p(3/2)	932.6	0.9	(17)
	CuS	2p(3/2)	931.8	0.9	(14)
	Cu_2O	2p(3/2)	932.4	1.3	(3,4,5,6,8)
	CuO	2p(3/2)	932.7	1.3	"
	Cu_2SO_4	2p(3/2)	933.8	1.8	(16)
	$CuSO_4$	2p(3/2)	933.7	1.8	(4,7,16)
	Cu (1+)	2p(3/2)	932.6	1.3	valence fit
	Cu (2+)	2p(3/2)	931.8	1.3	valence fit
Arsenic	FeAsS	3d	40.7	1.2	(Ch. 9)
	As_2O_3	3d	42.7	1.4	(1,2)
	As_2O_5	3d	44.3	1.4	(1,2)
	As (3+)	3d	42.7	1.4	valence fit
	As (5+)	3d	44.0	1.4	valence fit

References: (1) Wagner (ed.), (1979); (2) Bahl et al., (1976); (3) Novakov, (1971); (4) Novakov & Prins, (1971); (5) McIntyre & Cook, (1976); (6) Nakai et al., (1978); (7) Limouzin-Maire, (1981); (8) Panzner et al., (1985); (9) McIntyre & Zetaruk, (1977); (10) Brundle et al., (1977); (11) Mills & Sullivan, (1983); (12) Cochran & Larkins, (1985); (13) Harvey & Linton, (1981); (14) Romand et al., (1978); (15) Wagner et al., (1979); (16) Nefedov et al., (1977); (17) Larson, (1974); (18) Gopalakrishnan et al., (1979); (19) Hirokawa & Oku, (1979).

Appendix 3.

A3.1. Mössbauer parameters.

Table A3.1: Mössbauer (Fe^{57}) parameters for the sulphides analysed, and for the iron-containing oxidised phases.

Phase		I.S. (mms^{-1})	Q.S. (mms^{-1})	H (kOe)	references
Sulphides.					
FeS_2	pyrite	0.262	0.638	0	(Ch. 4)
Fe_7S_8	monoclinic pyrrhotine	0.69	0.43	287	(Ch. 5)
		0.35	0.26	0	
Fe_9S_{10}	hexagonal pyrrhotine	0.82	0.45	330	(Ch. 5)
		0.75	0.42	305	
$FeNi_2S_4$	violarite	0.320	0.610	0	(Ch. 6)
$(Fe,Ni)_9S$	pentlandite	0.333	0.336	0	(Ch. 7)
$CuFeS_2$	chalcopyrite	0.219	-	323	(Ch. 8)
FeAsS	arsenopyrite	0.214	1.084	0	(Ch. 9)
Sulphates.					
$FeSO_4.7H_2O$		1.29	3.12	0	(1,2)
$FeSO_4.H_2O$		1.18	2.69	0	(3)
$FeSO_4$		1.18	2.92	0	(4)
Oxides.					
$Fe_{1-x}O$	wüstite	1.11	0.6	0	(5,6)
Fe_3O_4	magnetite	-	-	486	(5,7,8)
		-	-	456	
		-	-	(427)	

Phase		I.S. (mms^{-1})	Q.S. (mms^{-1})	H (kOe)	references
αFe_2O_3	haematite	0.49	-0.18	536	(9,10)
		0.49	0.35	543	
γFe_2O_3	maghemite	0.27	0	488	(11)
		0.41	0	499	
Iron oxy-hydroxides.					
$\alpha FeOOH$	goethite (variable data)	0.36	0.27	359	(12,13)
$\beta FeOOH$	akaganeite "	0.43	0.62	0	(13,14)
$\gamma FeOOH$	lepidocrocite "	0.48	0.54	0	(13,14)
$Fe(OH)_2$		1.18	2.92	0	(8)

References; (1) Fluck et al. (1963), (2) Lefelhocz et al. (1967), (3) Russell & Montano (1978), (4) Saporoschenko et al. (1980), (5) Gonser et al. (1966), (6) Shirane et al. (1962), (7) Pritchard & Dobson (1969), (8) Pritchard & Mould (1971), (9) Fysh & Ostwald (1983), (10) Muir & Wiedersich (1966), (11) Armstrong et al. (1966), (12) Murad (1979), (13) Rossiter & Hodgson (1965), and (14) Terrell & Spijkerman (1968).

Appendix 4.

Free energies of formation of the possible component phases in the surfaces of oxidised sulphide minerals are given in section A4.1. Thermodynamic equations relating to the construction of partial pressure diagrams and equilibria relating to the construction of Eh/pH diagrams are presented in sections A4.2. and A4.3. respectively.

A4.1 Free energies of formation (25°C).

The free energies of formation cited in the table below were derived from the following source references ; (1) Garrels & Christ (1965), (2) Robie et al. (1978), (3) Mills (1974), (4) Warn (1969), (5) Wall (1974). Estimated values (6) are based on the free energies of simple sulphides.

Phase	State	ΔG(kJmol^{-1})	ref.	Phase	State	ΔG(kJmol^{-1})	ref.
Arsenic							
AsO^{+}	aq	-163.6	1	AsO_2^{-}	aq	-350.2	1
AsO_4^{2-}	aq	-636.0	1	As_2O_3	c	-575.55	2
As_2O_5	c	-772.4	1	$As_2O_5.4H_2O$	c	-1720.0	1
As_4O_6	c	-1152.1	1	AsS	c	-70.32	2
As_2S_2	c	-126.78	3	As_2S_3	c	-168.41	2
FeAsS	c	-86.0	6				
Copper							
Cu^{+}	aq	52.2	1	Cu^{2+}	aq	64.98	4
CuO	c	-129.56	2	Cu_2O	c	-146.03	2
$Cu(OH)_2$	c	-356.90	1	CuS	c	-49.08	2
Cu_2S	c	-86.87	2	$CuFeS_2$	c	-150.41	6
Cu_2SO_4	c	-652.7	1	$CuSO_4$	c	-662.31	2
$CuSO_4.H_2O$	c	-917.1	1	$CuSO_4.3H_2O$	c	-1399.97	1
$CuSO_4.5H_2O$	c	-1879.9	1				
Iron							
Fe^{2+}	aq	-84.94	4	Fe^{3+}	aq	-10.54	1
FeO	c	-244.3	4	Fe_2O_3	c	-741.0	4
Fe_3O_4	c	-1014.2	1	$Fe(OH)_2$	c	-483.5	1
$Fe(OH)_3$	c	-694.5	1	FeS	c	-101.33	2

Phase	State	ΔG(kJmol^{-1})	ref.	Phase	State	ΔG(kJmol^{-1})	ref.
Fe_9S_{10}	c	-965.07	6	Fe_7S_8	c	-768.25	6
FeS_2	c	-160.23	2	$FeSO_4$	c	-829.69	1
$FeSO_4.7H_2O$	c	-2509.64	2	$Fe_2(SO_4)_3$	c	-2249.56	2
Hydrogen							
H^+	aq	0	-	H_2	g	0	-
Nickel							
Ni^{2+}	aq	-45.6	5	NiO	c	-211.58	2
NiO_2	c	-198.74	1	$NiO_2.2H_2O$	c	-689.52	1
$Ni_3O_4.2H_2O$	c	-1186.29	1	$Ni_2O_3.H_2O$	c	-711.11	1
$NiOOH^-$	aq	-349.2	1	$Ni(OH)_2$	c	-447.27	5
$Ni(OH)_3$	c	-541.83	1	NiS	c	-86.19	2
Ni_3S_2	c	-197.07	2	$(Fe,Ni)_9S_8$	c	-780.0	6
$FeNi_2S_4$	c	-330.0	6	$NiSO_4$	c	-773.62	1
$NiSO_4.6H_2O$	c	-2224.54	2	$NiSO_4.7H_2O$	c	-2461.74	2
Oxygen							
O_2	g	0	-	OH^-	aq	-157.29	5
H_2O	g	-228.59	5	H_2O	l	-237.18	5
H_2O_2	l	-134.10	5	O_2^-	aq	54.4	1
HO_2^-	aq	-65.31	1				
Sulphur							
S	c	0	-	S_2	g	80.04	1
S^{2-}	aq	85.77	5	S_2^{2-}	aq	82.63	1
SO_2	g	-300.19	5	SO_2	aq	-300.71	5
SO_3	g	-371.08	5	$S_2O_3^{2-}$	aq	-532.21	1
SO_3^{2-}	aq	-486.60	5	SO_4^{2-}	aq	-744.63	5
HS^-	aq	12.05	5	H_2S	g	-33.56	5
H_2S	aq	-27.86	5	HSO_3^-	aq	-527.81	5
HSO_4^-	aq	-756.01	5	H_2SO_3	l	-537.90	5
H_2SO_4	l	-690.10	5				

A4.2 Thermodynamic equations for Partial Pressure Diagrams.

These equilibria relate to the construction of log pO_2 / log pS_2 partial pressure diagrams and are in order of appearance in the text. Equilibria from some systems may relate to other systems as well, and for clarity these are only referred to once. (Free energies for the reactions are in kJmol^{-1})

A4.2.1. General equilibria (25°C).

$$2H_2O \rightarrow 2H_2 + O_2$$

$$\Delta Gr = 474.36 \quad \log k = -83.1$$

The upper stability of water is defined by a partial pressure of oxygen equal to 1 atm, ie. log pO_2 = 0, and the lower by a partial pressure of hydrogen of 1 atm, ie. log pO_2 = -83.1.

$$S_2 \rightarrow 2S$$

$$\Delta Gr = -80.04 \quad \log k = -\log pS_2 = 14.02 \quad \log pS_2 = -14.02$$

This boundary defines the maximum vapour pressure of sulphur (gas), since at higher vapour pressures sulphur (solid) can be added to the system.

In the following general equilibria the metastable reactions have been omitted, except where they may be relevant to the system.

$2As + 1.5O_2 \rightarrow As_2O_3$	ΔGr =	-575.6	$\log pO_2$ =	-67.2
$As_2O_3 + O_2 \rightarrow As_2O_5$	ΔGr =	-196.9	$\log pO_2$ =	-34.5
$2Cu + 0.5O_2 \rightarrow Cu_2O$	ΔGr =	-146.0	$\log pO_2$ =	-51.2
$Cu_2O + 0.5O_2 \rightarrow 2CuO$	ΔGr =	-113.1	$\log pO_2$ =	-39.6
$3Fe + 2O_2 \rightarrow Fe_3O_4$	ΔGr =	-1014.2	$\log pO_2$ =	-88.8
$2Fe_3O_4 + 0.5O_2 \rightarrow 3Fe_2O_3$	ΔGr =	-194.6	$\log pO_2$ =	-68.1
$Ni + 0.5O_2 \rightarrow NiO$	ΔGr =	-211.6	$\log pO_2$ =	-74.1
$3NiO + 0.5O_2 \rightarrow Ni_3O_4$	ΔGr =	-77.2	$\log pO_2$ =	-27.0
$2Ni_3O_4 + 0.5O_2 \rightarrow 3Ni_2O_3$	ΔGr =	2.3	$\log pO_2$ =	0.8
$Ni_2O_3 + 0.5O_2 \rightarrow 2NiO_2$	ΔGr =	152.9	$\log pO_2$ =	53.6
$Ni + H_2O + 0.5O_2 \rightarrow Ni(OH)_2$	ΔGr =	-210.1	$\log pO_2$ =	-73.6
$3Ni(OH)_2 + 0.5O_2 \rightarrow Ni_3O_4 + 3H_2O$	ΔGr =	-81.7	$\log pO_2$ =	-28.6
$Cu + 0.5S_2 + 2O_2 \rightarrow CuSO_4$	ΔGr =	-702.3	log K =	123.0

$123.0 = -0.5 \log pS_2 - 2 \log pO_2$

$Cu_2O + S_2 + 3.5O_2 \rightarrow 2CuSO_4$ $\Delta Gr = -1258.6$ log K = 220.5
$220.5 = -1 \log pS_2 - 3.5 \log pO_2$

$Fe_2O_3 + S_2 + 2.5O_2 \rightarrow 2FeSO_4$ $\Delta Gr = -998.4$ log K = 174.9
$174.9 = -1 \log pS_2 - 2.5 \log pO_2$

$2FeSO_4 + 0.5S_2 + 2O_2 \rightarrow Fe_2(SO_4)_3$ $\Delta Gr = -670.2$ log K = 117.4
$117.4 = -0.5 \log pS_2 - 2 \log pO_2$

$NiO + 0.5S_2 + 1.5O_2 \rightarrow NiSO_4$ $\Delta Gr = -602.1$ log K = 105.5
$105.5 = -0.5 \log pS_2 - 1.5 \log pO_2$

$Ni(OH)_2 + 0.5S_2 + 1.5O_2 \rightarrow NiSO_4 + H_2O$ $\Delta Gr = -603.5$ log K = 105.9
$105.9 = -0.5 \log pS_2 - 1.5 \log pO_2$

A4.2.2. Pyrite equilibria.

$Fe + S_2 \rightarrow FeS_2$ $\Delta Gr = -240.2$ log $pS_2 = -42.1$

$Fe_3O_4 + 3S_2 \rightarrow 3FeS_2 + 2O_2$ $\Delta Gr = 293.4$ log K = -51.4
$-51.4 = 2 \log pO_2 - 3 \log pS_2$

$Fe_2O_3 + 2S_2 \rightarrow 2FeS_2 + 1.5O_2$ $\Delta Gr = 260.4$ log K = -45.6
$-45.6 = 1.5 \log pO_2 - 2 \log pS_2$

$FeS_2 + 2O_2 \rightarrow FeSO_4 + 0.5S_2$ $\Delta Gr = -629.4$ log K = 110.3
$110.3 = -2 \log pO_2 + 0.5 \log pS_2$

$2FeS_2 + 6O_2 \rightarrow Fe_2(SO_4)_3 + 0.5S_2$ $\Delta Gr = -1889.1$ log K = 330.9
$330.9 = -6 \log pO_2 + 0.5 \log pS_2$

A4.2.3. Hexagonal and Monoclinic Pyrrhotine equilibria.

$7Fe_3O_4 + 12S_2 \rightarrow 3Fe_7S_8 + 14O_2$ $\Delta Gr = 3834.2$ log K = -671.6
$-671.6 = -12 \log pS_2 + 14 \log pO_2$

$Fe_3O_4 + 5S_2 \rightarrow Fe_3S_{10} + 6O_2$ $\Delta Gr = 1677.3$ log K = -293.8
$-293.8 = -5 \log pS_2 + 6 \log pO_2$

$7Fe_2O_3 + 8S_2 \rightarrow 2Fe_7S_8 + 10.5O_2$ $\Delta Gr = 3010.2$ log K = -527.3
$-527.3 = -8 \log pS_2 + 10.5 \log pO_2$

$9Fe_2O_3 + 10S_2 \rightarrow 2Fe_9S_{10} + 13.5O_2$ $\Delta Gr = 4098.5$ log K = -717.9
$-717.9 = -10 \log pS_2 + 13.5 \log pO_2$

$7FeSO_4 + 0.5S_2 \rightarrow Fe_7S_8 + 14O_2$ $\Delta Gr = 4999.6$ log K = -875.7
$-875.7 = -0.5 \log pS_2 + 14 \log pO_2$

$9FeSO_4 + 0.5S_2 \rightarrow Fe_9S_{10} + 18O_2$ $\Delta Gr = 6462.1$ log K =-1131.9

$-1131.9 = -0.5\log pS_2 + 18\log pO_2$

$2Fe_7S_8 + 42O_2 + 2.5S_2 \rightarrow 7Fe_2(SO_4)_3$ $\Delta Gr = -14410.5$ log K = 2524.2

$2524.18 = -42\log pO_2 - 2.5\log pS_2$

$2Fe_9S_{10} + 54O_2 + 3.5S_2 \rightarrow 9Fe_2(SO_4)_3$ $\Delta Gr = -18596.0$ log K = 3257.3

$3257.3 = -54\log pO_2 - 3.5\log pS_2$

$7Fe_9S_{10} + S_2 \rightarrow 9Fe_7S_8$ $\Delta Gr = -238.8$ $\log pS_2 = -41.8$

$Fe_7S_8 + 3S_2 \rightarrow 7FeS_2$ $\Delta Gr = -593.5$ $\log pS_2 = -34.7$

A4.2.4. Violarite.

$Fe + 2Ni + 2S_2 \rightarrow FeNi_2S_4$ $\Delta Gr = -492.1$ $\log pS_2 = -43.1$

$FeNi_2S_4 + 0.667O_2 \rightarrow 0.333Fe_3O_4 + 2Ni + 2S_2$ $\Delta Gr = 154.0$ log K = -27.0

$-26.98 = 2\log pS_2 - 0.667\log pO_2$

$FeNi_2S_4 + 2H_2O + 1.667O_2 \rightarrow 0.333Fe_3O_4 + 2Ni(OH)_2 + 2S_2$ $\Delta Gr = -267.8$ log K = 46.9

$46.9 = 2\log pS_2 - 1.667\log pO_2$

$FeNi_2S_4 + 2H_2O + 1.75O_2 \rightarrow 0.5Fe_2O_3 + 2Ni(OH)_2 + 2S_2$ $\Delta Gr = -298.0$ log K = 52.2

$52.2 = 2\log pS_2 - 1.75\log pO_2$

$FeNi_2S_4 + 2.083O_2 \rightarrow 0.5Fe_2O_3 + 0.667Ni_3O_4 + 2S_2$ $\Delta Gr = -352.1$ log K = 61.7

$61.7 = 2\log pS_2 - 2.083\log pO_2$

$FeNi_2S_4 + 4.75O_2 \rightarrow 2NiSO_4 + 0.5Fe_2O_3 + S_2$ $\Delta Gr = -1505.7$ log K = 263.7

$263.7 = \log pS_2 - 4.75\log pO_2$

$FeNi_2S_4 + 6O_2 \rightarrow 2NiSO_4 + FeSO_4 + 0.5S_2$ $\Delta Gr = -2004.9$ log K = 351.2

$351.2 = 0.5\log pS_2 - 6\log pO_2$

$FeNi_2S_4 + 7O_2 \rightarrow 2NiSO_4 + 0.5Fe_2(SO_4)_3 + 0.25S_2$ $\Delta Gr = -2320.0$ log K = 406.4

$406.4 = 0.25\log pS_2 - 7\log pO_2$

A4.2.5 Pentlandite (and stability with respect to violarite).

$4.5Fe + 4.5Ni + 4S_2 \rightarrow (Fe,Ni)_9S_8$ $\Delta Gr = -1101.7$ $\log pS_2 = -48.2$

$(Fe,Ni)_9S_8 + 3O_2 \rightarrow 1.5Fe_3O_4 + 4.5Ni + 4S_2$ $\Delta Gr = -418.9$ log K = 73.4

$73.4 = 4\log pS_2 - 3\log pO_2$

$(Fe,Ni)_9S_8 + 4.5H_2O + 5.25O_2 \rightarrow 1.5Fe_3O_4 + 4.5Ni(OH)_2 + 4S_2$

$\Delta Gr = -1364.6$ log K = 239.0

$239.0 = 4 \log pS_2 - 5.25 \log pO_2$

$(Fe,Ni)_9S_8 + 4.5H_2O + 5.625O_2 \rightarrow 2.25Fe_2O_3 + 4.5Ni(OH)_2 + 4S_2$

$\Delta Gr = -1510.5$ log K = 264.6

$264.6 = 4 \log pS_2 - 5.625 \log pO_2$

$(Fe,Ni)_9S_8 + 12.375O_2 \rightarrow 4.5NiSO_4 + 2.25Fe_2O_3 + 1.75S_2$

$\Delta Gr = -4226.5$ log K = 740.3

$740.3 = 1.75 \log pS_2 - 12.375 \log pO_2$

$(Fe,Ni)_9S_8 + 18O_2 + 0.5S_2 \rightarrow 4.5NiSO_4 + 4.5FeSO_4$

$\Delta Gr = -6472.9$ log K = 1133.8

$1133.8 = -0.5 \log pS_2 - 18 \log pO_2$

$(Fe,Ni)_9S_8 + 22.5O_2 + 1.625S_2 \rightarrow 4.5NiSO_4 + 2.25Fe_2(SO_4)_3$

$\Delta Gr = -7890.9$ log K = 1382.2

$1382.2 = -1.625 \log pS_2 - 22.5 \log pO_2$

$FeNi_2S_4 + 1.167Fe_3O_4 + 2.5Ni + 2S_2 \rightarrow (Fe,Ni)_9S_8 + 2.333O_2$

$\Delta Gr = 573.2$ log K = -100.4

$-100.4 = 2.333 \log pO_2 - 2 \log pS_2$

$FeNi_2S_4 + 1.167Fe_3O_4 + 2.5NiO + 2S_2 \rightarrow (Fe,Ni)_9S_8 + 3.584O_2$

$\Delta Gr = 1262.2$ log K = -221.1

$-221.1 = 3.584 \log pO_2 - 2 \log pS_2$

$FeNi_2S_4 + 1.167Fe_3O_4 + 2.5Ni(OH)_2 + 2S_2 \rightarrow (Fe,Ni)_9S_8 + 3.584O_2 + 2.5H_2O$

$\Delta Gr = 1120.2$ log K = -196.2

$-196.2 = 3.584 \log pO_2 - 2 \log pS_2$

$FeNi_2S_4 + 1.75Fe_2O_3 + 2.5Ni(OH)_2 + 2S_2 \rightarrow (Fe,Ni)_9S_8 + 2.5H_2O + 3.875O_2$

$\Delta Gr = 1211.9$ log K = -212.3

$-212.3 = 3.875 \log pO_2 - 2 \log pS_2$

$FeNi_2S_4 + 1.75Fe_2O_3 + 2.5NiSO_4 + 0.75S_2 \rightarrow (Fe,Ni)_9S_8 + 7.625O_2$

$\Delta Gr = 2390.8$ log K = -418.8

$-418.8 = 7.625 \log pO_2 - 0.75 \log pS_2$

$FeNi_2S_4 + 3.5FeSO_4 + 2.5NiSO_4 \rightarrow S_2 + (Fe,Ni)_9S_8 + 12O_2$

$\Delta Gr = 2720.8$ log K = -476.6

$-476.6 = 12 \log pO_2 - \log pS_2$

A4.2.6. Chalcopyrite (and stability with respect to CuS and Cu_2S).

$2Cu + 0.5S_2 \rightarrow Cu_2S$ $\Delta Gr = -126.9$ $\log pS_2 = -44.5$

$Cu_2S + 0.5S_2 \rightarrow 2CuS$ $\Delta Gr = -51.3$ $\log pS_2 = -18.0$

$2CuS + 0.5O_2 \rightarrow Cu_2O + S_2$ $\Delta Gr = 32.2$ log K = -5.6

$-5.6 = \log pS_2 - \log pO_2$

$CuS + 2O_2 \rightarrow CuSO_4$ $\Delta Gr = -613.2$ log K = 107.4

$107.4 = -2\log pO_2$

$Cu_2S + 4O_2 + 0.5S_2 \rightarrow 2CuSO_4$ $\Delta Gr = -1258.6$ log K = 220.5

$220.5 = -0.5\log pS_2 - 4\log pO_2$

$3CuFeS_2 + 2.75O_2 \rightarrow 3Cu_2O + Fe_3O_4 + 3S_2$ $\Delta Gr = -731.0$ log K = 128.0

$128.0 = 3\log pS_2 - 2.75\log pO_2$

$3CuFeS_2 + 2O_2 \rightarrow 3CuS + Fe_3O_4 + 1.5S_2$ $\Delta Gr = -560.2$ log K = 98.1

$98.1 = 1.5\log pS_2 - 2\log pO_2$

$6CuFeS_2 + 4O_2 \rightarrow 3Cu_2S + 2Fe_3O_4 + 1.5S_2$ $\Delta Gr = -1093.2$ log K = 191.5

$191.5 = 1.5\log pS_2 - 4\log pO_2$

$2CuFeS_2 + 2O_2 \rightarrow Cu_2O + Fe_2O_3 + 2S_2$ $\Delta Gr = -406.2$ log K = 71.1

$71.1 = 2\log pS_2 - 2\log pO_2$

$2CuFeS_2 + 1.5O_2 \rightarrow 2CuS + Fe_2O_3 + S_2$ $\Delta Gr = -438.3$ log K = 76.8

$76.8 = \log pS_2 - 1.5\log pO_2$

$2CuFeS_2 + 1.5O_2 \rightarrow Cu_2S + Fe_2O_3 + 2S_2$ $\Delta Gr = -347.0$ log K = 60.8

$60.8 = 2\log pS_2 - 1.5\log pO_2$

$2CuFeS_2 + 4.5O_2 \rightarrow Cu_2O + 2FeSO_4 + S_2$ $\Delta Gr = -1432.3$ log K = 250.9

$250.9 = \log pS_2 - 4.5\log pO_2$

$CuFeS_2 + 4O_2 \rightarrow CuSO_4 + FeSO_4$ $\Delta Gr = -1331.6$ log K = 233.2

$233.2 = -4\log pO_2$

$CuFeS_2 + 2O_2 \rightarrow CuS + FeSO_4 + 0.5S_2$ $\Delta Gr = -678.4$ log K = 118.8

$118.8 = 0.5\log pS_2 - 2\log pO_2$

$2CuFeS_2 + 4O_2 \rightarrow Cu_2S + 2FeSO_4 + 0.5S_2$ $\Delta Gr = -1385.4$ log K = 242.7

$242.7 = 0.5\log pS_2 - 4\log pO_2$

$2CuFeS_2 + 10O_2 + 2.5S_2 \rightarrow 2CuSO_4 + Fe_2(SO_4)_3$ $\Delta Gr = -3453.5$ log K = 604.9

$604.9 = -2.5\log pS_2 - 10\log pO_2$

A4.2.7. Arsenopyrite.

$Fe + As + 0.5S_2 \rightarrow FeAsS$ $\Delta Gr = -125.8$ $\log pS_2 = -44.1$

$$FeAsS + 0.667O_2 \rightarrow 0.333Fe_3O_4 + As + 0.5S_2$$
$\Delta Gr = -217.9$ log K = 38.2
$38.2 = 0.5\log pS_2 - 0.667\log pO_2$

$$FeAsS + 0.75O_2 \rightarrow 0.5Fe_2O_3 + As + 0.5S_2$$
$\Delta Gr = -244.7$ log K = 42.9
$42.9 = 0.5\log pS_2 - 0.75\log pO_2$

$$FeAsS + 1.417O_2 \rightarrow 0.333Fe_3O_4 + 0.5As_2O_3 + 0.5S_2$$
$\Delta Gr = -496.1$ log K = 86.9
$86.9 = 0.5\log pS_2 - 1.417\log pO_2$

$$FeAsS + 1.5O_2 \rightarrow 0.5Fe_2O_3 + 0.5As_2O_3 + 0.5S_2$$
$\Delta Gr = -538.1$ log K = 94.3
$94.3 = 0.5\log pS_2 - 1.5\log pO_2$

$$FeAsS + 2.75O_2 \rightarrow 0.5As_2O_3 + FeSO_4$$
$\Delta Gr = -1031.7$ log K = 180.7
$180.7 = -2.75\log pO_2$

$$FeAsS + 3.75O_2 + 0.5S_2 \rightarrow 0.5As_2O_3 + 0.5Fe_2(SO_4)_3$$
$\Delta Gr = -656.8$ log K = 115.1
$115.1 = -0.5\log pS_2 - 3.75\log pO_2$

A4.3. Chemical equations in aqueous environments: - Construction of Eh/pH diagrams relating the stability of the sulphides to the oxidised phases.

The potential difference for the reactions, E (Eh relative to the hydrogen electrode), is related to the free energy for the reaction by the Nernst equation;-

$$E = E^{\circ} + (RT/n\mathfrak{f})\ln K$$

and at room temperature - $= (\Delta Gr/n\mathfrak{f}) + (0.0592/n)\log K$

(where R and $\mathfrak{f}$ are the Universal gas constant and the Faraday constant respectively.)

The following sections list aqueous equilibria of relevance to sulphide oxidation. As in the previous section, the equilibria relating to more than one system are only referred to once. (In the equilibria (determined for 25°C), the free energy for the reaction is given in $kJmol^{-1}$ and the electrode potential is in volts).

A4.3.1. General aqueous equilibria.

Upper and lower limits of water stability.

$2H_2O \rightarrow O_2 + 4H^+ + 4e$ $\Delta Gr = 474.36$

$E = 1.229 - 0.0592pH$

$H_2 \rightarrow 2H^+ + 2e$ $\Delta Gr = 0$

$E = -0.0592pH - 0.0296\log pH_2$, and since $pH_2 = 1$

$E = -0.0592pH$

Sulphur species stability.

$HSO_4^- = H^+ + SO_4^{2-}$	log K = -1.9	pH =	1.9
$H_2S = H^+ + HS^-$	" -7.0	pH =	7.0
$HS^- = H^+ + S^{2-}$	" -14.0	pH =	14.0

$S + 4H_2O \rightarrow HSO_4^- + 7H^+ + 6e$ $\Delta Gr = 192.71$

$E = 0.333 - 0.0691pH + 0.0099\log[HSO_4^-]$

$S + 4H_2O \rightarrow SO_4^{2-} + 8H^+ + 6e$ $\Delta Gr = 204.09$

$E = 0.353 - 0.079pH + 0.0099\log[SO_4^{2-}]$

$H_2S \rightarrow S + 2H^+ + 2e$ $\Delta Gr = 27.86$

$E = 0.144 - 0.059pH - 0.0296\log[H_2S]$

$HS^- \rightarrow S + H^+ + 2e$ $\Delta Gr = -12.05$

$E = -0.062 - 0.0296pH - 0.0296\log[HS^-]$

$HS^- + 4H_2O \rightarrow SO_4^{2-} + 9H^+ + 8e$ $\Delta Gr = 192.04$

$E = 0.249 - 0.0592pH + 0.0074\log[SO_4^{2-}/HS^-]$

$S^{2-} + 4H_2O \rightarrow SO_4^{2-} + 8H^+ + 8e$ $\Delta Gr = 118.32$

$E = 0.153 - 0.0592pH + 0.0074\log[SO_4^{2-}/S^{2-}]$

$H_2S + 4H_2O \rightarrow SO_4^{2-} + 10H^+ + 8e$ $\Delta Gr = 231.95$

$E = 0.300 - 0.0715pH + 0.0074\log[SO_4^{2-}/H_2S]$

$H_2S + 4H_2O \rightarrow HSO_4^- + 9H^+ + 8e$ $\Delta Gr = 220.57$

$E = 0.286 - 0.0666pH + 0.0074\log[HSO_4^-/H_2S]$

Stable arsenic oxides.

$2AsO^+ + H_2O \rightarrow As_2O_3 + 2H^+$ $\Delta Gr = -11.17$

$pH = -0.978 - \log[AsO^+]$

$As_2O_3 + H_2O \rightarrow 2AsO_2^- + 2H^+$ $\Delta Gr = 112.33$

$pH = 11.035 + \log[AsO_2^-]$

$As + H_2O \rightarrow AsO^+ + 2H^+ + 3e$ $\Delta Gr = 73.58$

$E = 0.254 - 0.0395pH + 0.0197\log[AsO^+]$

$2As + 3H_2O \rightarrow As_2O_3 + 6H^+ + 6e$ $\Delta Gr = 135.99$

$E = 0.235 - 0.0592pH$

$As + 2H_2O \rightarrow AsO_2^- + 4H^+ + 3e$ $\Delta Gr = 124.16$

$E = 0.429 - 0.0789pH + 0.0197\log[AsO_2^-]$

$2AsO^+ + 3H_2O \rightarrow As_2O_5 + 6H^+ + 4e$ $\Delta Gr = 266.34$

$E = 0.690 - 0.0888pH - 0.0296\log[AsO^+]$

$As_2O_3 + 2H_2O \rightarrow As_2O_5 + 4H^+ + 4e$ $\Delta Gr = 277.51$

$E = 0.719 - 0.0592pH$

$As_2O_3 + 5H_2O \rightarrow 2AsO_4^{2-} + 10H^+ + 6e$ $\Delta Gr = 489.45$

$E = 0.846 - 0.0987pH + 0.0197\log[AsO_4^{2-}]$

$AsO_2^- + 2H_2O \rightarrow AsO_4^{2-} + 4H^+ + 3e$ $\Delta Gr = 188.56$

$E = 0.651 - 0.0789pH + 0.0197\log([AsO_4^{2-}]/[AsO_2^-])$

$As_2O_5 + 3H_2O \rightarrow 2AsO_4^{2-} + 6H^+ + 2e$ $\Delta Gr = 211.94$

$E = 1.098 - 0.178pH + 0.0592\log[AsO_4^{2-}]$

$AsO^+ + 3H_2O \rightarrow AsO_4^{2-} + 6H^+ + 3e$ $\Delta Gr = 239.14$

$E = 0.826 - 0.118pH + 0.0197\log([AsO_4^{2-}]/[AsO^+])$

Stable copper oxides.

$2Cu + H_2O \rightarrow Cu_2O + 2H^+ + 2e$ $\Delta Gr = 91.15$

$E = 0.472 - 0.059pH$

$Cu_2O + H_2O \rightarrow 2CuO + 2H^+ + 2e$ $\Delta Gr = 124.08$

$E = 0.643 - 0.059pH$

$Cu \rightarrow Cu^{2+} + 2e$ $\Delta Gr = 14.78$

$E = 0.153$

$Cu_2O + 2H^+ \rightarrow 2Cu^{2+} + H_2O + 2e$ $\Delta Gr = 38.81$

$E = 0.201 + 0.0592pH + 0.0592\log[Cu^{2+}]$

$Cu^{2+} + H_2O \rightarrow CuO + 2H^+$ $\Delta Gr = 42.64$

$pH = 4.188 - 0.5\log[Cu^{2+}]$

Stable iron oxides.

$3Fe + 4H_2O \rightarrow Fe_3O_4 + 8H^+ + 8e$ $\Delta Gr = -65.48$

$E = -0.085 - 0.0592pH$

$2Fe_3O_4 + H_2O \rightarrow 3Fe_2O_3 + 2H^+ + 2e$ $\Delta Gr = 42.58$

$E = 0.221 - 0.0592pH$

$2Fe^{2+} + 3H_2O \rightarrow Fe_2O_3 + 6H^+ + 2e$ $\Delta Gr = 140.42$

$E = 0.728 - 0.178pH - 0.0592\log[Fe^{2+}]$

$3Fe^{2+} + 4H_2O \rightarrow Fe_3O_4 + 8H^+ + 2e$ $\Delta Gr = 189.13$

$E = 0.980 - 0.237pH - 0.0888\log[Fe^{2+}]$

$2Fe(OH)_3 \rightarrow Fe_2O_3 + 3H_2O$ (stable products) $\Delta Gr = -63.54$

$Fe^{2+} \rightarrow Fe^{3+} + e$ $\Delta Gr = 74.4$

$E = 0.771$

Stable nickel oxides.

$NiO + H_2O \rightarrow Ni(OH)_2$ $\Delta Gr = 1.5$

$Ni \rightarrow Ni^{2+} + 2e$ $\Delta Gr = -45.6$

$E = -0.236 + 0.0296\log[Ni^{2+}]$

$Ni + H_2O \rightarrow NiO + 2H^+ + 2e$ $\Delta Gr = 25.60$

$E = 0.133 - 0.0592pH$

$Ni + 2H_2O \rightarrow NiOOH^- + 3H^+ + 2e$ $\Delta Gr = 125.16$

$E = 0.649 - 0.0888pH + 0.0296\log[NiOOH^-]$

$3NiO + 3H_2O \rightarrow Ni_3O_4 + 6H^+ + 6e$ $\Delta Gr = 634.35$

$E = 1.096 - 0.0592pH$

$Ni^{2+} + H_2O \rightarrow NiO + 2H^+$ $\Delta Gr = 71.20$

$pH = 7.07 - 0.5\log[Ni^{2+}]$

$NiO + H_2O \rightarrow NiOOH^- + H^+$ $\Delta Gr = 99.56$

$pH = 17.34 + \log[NiOOH^-]$

$Ni_3O_4 + 2H_2O \rightarrow 3NiOOH^- + H^+ + 2e$ $\Delta Gr = 138.69$

$E = 0.719 - 0.0296pH + 0.0888\log[NiOOH^-]$

A4.3.2. Pyrite.

$Fe_7S_8 + 6H_2S \rightarrow 7FeS_2 + 12H^+ + 12e$ $\Delta Gr = -186.19$

$E = -0.161 - 0.0592pH - 0.0296\log[H_2S]$

$Fe_7S_8 + 6HS^- \rightarrow 7FeS_2 + 6H^+ + 12e$ $\Delta Gr = -425.65$

$E = -0.368 - 0.0296pH - 0.0296\log[HS^-]$

$Fe_3O_4 + 6H_2S \rightarrow 3FeS_2 + 4H_2O + 4H^+ + 4e$ $\Delta Gr = -248.05$

$E = -0.643 - 0.0592pH - 0.0888\log[H_2S]$

$Fe_2O_3 + 4H_2S \rightarrow 2FeS_2 + 3H_2O + 2H^+ + 2e$ $\Delta Gr = -179.56$

$E = -0.930 - 0.0592pH - 0.1184\log[H_2S]$

$2FeS_2 + 19H_2O \rightarrow Fe_2O_3 + 4SO_4^{2-} + 38H^+ + 30e$ $\Delta Gr = 1107.36$

$E = 0.383 + 0.075pH + 0.0079\log[SO_4^{2-}]$

$3FeS_2 + 28H_2O \rightarrow Fe_3O_4 + 6SO_4^{2-} + 56H^+ + 44e$ $\Delta Gr = 1639.75$

$E = 0.386 + 0.0753pH + 0.0081\log[SO_4^{2-}]$

$2FeS_2 + 19H_2O \rightarrow 4HSO_4^- + Fe_2O_3 + 34H^+ + 30e$ $\Delta Gr = 1061.84$

$E = 0.367 + 0.0671pH + 0.0079\log[HSO_4^-]$

$2H_2S + Fe^{2+} \rightarrow FeS_2 + 4H^+ + 2e$ $\Delta Gr = -19.57$

$E = - 0.101 - 0.118pH - 0.0296\log\{[H_2S]^2[Fe^{2+}]\}$

$FeS_2 + 8H_2O \rightarrow 2HSO_4^- + Fe^{2+} + 14H^+ + 14e$ $\Delta Gr = 460.71$

$E = 0.341 - 0.0592pH + 0.0085\log[HSO_4^-] + 0.0042\log[Fe^{2+}]$

$FeS_2 + 8H_2O \rightarrow 2SO_4^{2-} + Fe^{2+} + 16H^+ + 14e$ $\Delta Gr = 483.47$

$E = 0.358 - 0.0677pH + 0.0085\log[SO_4^{2-}] + 0.0042\log[Fe^{2+}]$

$2HS^- + Fe^{2+} \rightarrow FeS_2 + 2H^+ + 2e$ $\Delta Gr = -99.39$

$E = - 0.515 - 0.0592pH - 0.0592\log[HS^-] - 0.0296\log[Fe^{2+}]$

$FeS_2 \rightarrow Fe^{2+} + 2S + 2e$ $\Delta Gr = 75.29$

$E = 0.390 + 0.296\log[Fe^{2+}]$

$Fe_3O_4 + 6HS^- + 2H^+ \rightarrow 3FeS_2 + 4H_2O + 4e$ $\Delta Gr = -487.51$

$E = - 1.263 + 0.0296pH - 0.0888\log[HS^-]$

$3Fe_7S_8 + 28H_2O \rightarrow 7Fe_3O_4 + 24HS^- + 32H^+ + 8e$ $\Delta Gr = 1557.19$

$E = 2.017 - 0.236pH + 0.177\log[HS^-]$

A4.3.3. Hexagonal and monoclinic pyrrhotine.

$9Fe + 10H_2S \rightarrow Fe_9S_{10} + 20H^+ + 20e$ $\Delta Gr = -686.47$

$E = - 0.356 - 0.0592pH - 0.0296\log[H_2S]$

$7Fe + 8H_2S \rightarrow Fe_7S_8 + 16H^+ + 16e$ $\Delta Gr = -545.37$

$E = - 0.353 - 0.0592pH - 0.0296\log[H_2S]$

$Fe_9S_{10} + 12H_2O \rightarrow 3Fe_3O_4 + 10HS^- + 14H^+ + 4e$ $\Delta Gr = 889.13$

$E = 2.304 - 0.207pH + 0.148\log[HS^-]$

$3Fe_7S_8 + 28H_2O \rightarrow 7Fe_3O_4 + 24HS^- + 32H^+ + 8e$ $\Delta Gr = 2135.59$

$E = 2.766 - 0.237pH + 0.178\log[HS^-]$

$Fe_9S_{10} + 52H_2O \rightarrow 3Fe_3O_4 + 10SO_4^{2-} + 104H^+ + 84e$ $\Delta Gr = 2809.53$

$E = 0.347 - 0.0733pH + 0.007\log[SO_4^{2-}]$

$3Fe_7S_8 + 124H_2O \rightarrow 7Fe_3O_4 + 24SO_4^{2-} + 248H^+ + 200e$ $\Delta Gr = 6744.55$

$E = 0.349 - 0.0734pH + 0.0071\log[SO_4^{2-}]$

$2Fe_9S_{10} + 107H_2O \rightarrow 9Fe_2O_3 + 20SO_4^{2-} + 214H^+ + 174e$ $\Delta Gr = 5746.80$

$E = 0.342 - 0.0728pH + 0.0068\log[SO_4^{2-}]$

$2Fe_7S_8 + 85H_2O \rightarrow 7Fe_2O_3 + 16SO_4^{2-} + 170H^+ + 138e$ $\Delta Gr = 4595.72$

$E = 0.345 - 0.0729pH + 0.0069\log[SO_4^{2-}]$

$Fe_9S_{10} + 40H_2O \rightarrow 9Fe^{2+} + 10SO_4^{2-} + 80H^+ + 78e$ $\Delta Gr = 2241.51$

$E = 0.298 - 0.0607pH + 0.0068\log[Fe^{2+}] + 0.0076\log[SO_4^{2-}]$

$Fe_7S_8 + 32H_2O \rightarrow 7Fe^{2+} + 8SO_4^{2-} + 64H^+ + 62e$ $\Delta Gr = 1806.39$

$E = 0.302 - 0.0611pH + 0.0067\log[Fe^{2+}] + 0.0076\log[SO_4^{2-}]$

$10H_2S + 9Fe^{2+} \rightarrow Fe_9S_{10} + 20H^+ + 2e$ $\Delta Gr = 77.99$

$E = 0.404 - 0.592pH - 0.266\log[Fe^{2+}]$

$8H_2S + 7Fe^{2+} \rightarrow Fe_7S_8 + 16H^+ + 2e$ $\Delta Gr = 49.21$

$E = 0.255 - 0.474pH - 0.207\log[Fe^{2+}]$

A4.3.4. Violarite.

$3FeNi_2S_4 + 58H_2O \rightarrow 6NiO + Fe_3O_4 + 12SO_4^{2-} + 116H^+ + 78e$ $\Delta Gr = 3527.19$

$E = 0.469 - 0.088pH + 0.009\log[SO_4^{2-}]$

$2FeNi_2S_4 + 39H_2O \rightarrow 4NiO + Fe_2O_3 + 8SO_4^{2-} + 78H^+ + 62e$ $\Delta Gr = 2365.66$

$E = 0.395 - 0.0745pH + 0.007\log[SO_4^{2-}]$

$2FeNi_2S_4 + 35H_2O \rightarrow Fe_2O_3 + 4Ni^{2+} + 8SO_4^{2-} + 70H^+ + 62e$ $\Delta Gr = 2086.08$

$E = 0.347 - 0.0668pH + 0.003\log[Ni^{2+}] + 0.007\log[SO_4^{2-}]$

$3FeNi_2S_4 + 52H_2O \rightarrow Fe_3O_4 + 6Ni^{2+} + 12SO_4^{2-} + 104H^+ + 92e$ $\Delta Gr = 3107.83$

$E = 0.350 - 0.0669pH + 0.003\log[Ni^{2+}] + 0.007\log[SO_4^{2-}]$

$3FeNi_2S_4 + 64H_2O \rightarrow Fe_3O_4 + 6NiOOH^- + 12SO_4^{2-} + 122H^+ + 92e$ $\Delta Gr = 4132.39$

$E = 0.465 - 0.0785pH + 0.003\log[NiOOH^-] + 0.007\log[SO_4^{2-}]$

$FeNi_2S_4 + 16H_2O \rightarrow Fe^{2+} + 2Ni^{2+} + 4SO_4^{2-} + 32H^+ + 30e$ $\Delta Gr = 972.83$

$E = 0.336 - 0.0631pH + 0.002\log[Fe^{2+}] + 0.003\log[Ni^{2+}] + 0.007\log[SO_4^{2-}]$

$FeNi_2S_4 \rightarrow Fe^{2+} + 2Ni^{2+} + 4S + 6e$ $\Delta Gr = 156.47$

$E = 0.270 + 0.009\log[Fe^{2+}] + 0.019\log[Ni^{2+}]$

$Fe^{2+} + 2Ni^{2+} + 4H_2S \rightarrow FeNi_2S_4 + 4H^+ + 2e$ $\Delta Gr = -45.03$

$E = -0.233 - 0.236pH - 0.029\log[Fe^{2+}] - 0.059\log[Ni^{2+}] - 0.118\log[H_2S]$

$Fe_3O_4 + 6Ni + 12HS^- \rightarrow 3FeNi_2S_4 + 4H_2S + 4H^+ + 16e$ $\Delta Gr = -1076.95$

$E = -0.697 - 0.0148pH - 0.044\log[HS^-]$

$Fe^{2+} + 2Ni^{2+} + 4HS^- \rightarrow FeNi_2S_4 + 4H^+ + 2e$ $\Delta Gr = -153.86$

$E = -0.797 - 0.118pH - 0.029\log[Fe^{2+}] - 0.059\log[Ni^{2+}] - 0.118\log[H_2S]$

$Fe^{2+} + 2Ni + 4HS^- \rightarrow FeNi_2S_4 + 4H^+ + 6e$ $\Delta Gr = -295.87$

$E = -0.511 - 0.0395pH - 0.009\log[Fe^{2+}] - 0.039\log[HS^-]$

A4.3.5. Pentlandite (and stability with respect to violarite).

$2(Fe,Ni)_9S_8 + 32H^+ \rightarrow 9Fe^{2+} + 9Ni^{2+} + 16H_2S + 4e$ $\Delta Gr = -55.92$

$E = -0.145 + 0.474pH + 0.133\log[Fe^{2+}][Ni^{2+}] + 0.237\log[H_2S]$

$2(Fe,Ni)_9S_8 \rightarrow 9Ni^{2+} + 9Fe^{2+} + 16S + 36e$ $\Delta Gr = 389.84$

$E = 0.112 + 0.0167\log[Fe^{2+}][Ni^{2+}]$

$4(Fe,Ni)_9S_8 + 155H_2O \rightarrow 18Ni^{2+} + 9Fe_2O_3 + 32SO_4^{2-} + 310H^+ + 282e$ $\Delta Gr = 8574.34$

$E = 0.315 - 0.0651pH + 0.0038\log[Ni^{2+}] + 0.0067\log[SO_4^{2-}]$

$2(Fe,Ni)_9S_8 + 64H_2O \rightarrow 9Ni^{2+} + 9Fe^{2+} + 16SO_4^{2-} + 128H^+ + 134e$ $\Delta Gr = 3655.28$

$E = 0.283 - 0.0565pH + 0,004\log[Fe^{2+}][Ni^{2+}] + 0.007\log[SO_4^{2-}]$

$4(Fe,Ni)_9S_8 + 173H_2O \rightarrow 18NiO + 9Fe_2O_3 + 32SO_4^{2-} + 346H^+ + 282e$ $\Delta Gr = 9846.52$

$E = 0.362 - 0.0726pH + 0.0067\log[SO_4^{2-}]$

$2(Fe,Ni)_9S_8 + 85H_2O \rightarrow 9NiO + 3Fe_3O_4 + 16SO_4^{2-} + 170H^+ + 138e$ $\Delta Gr = 4859.39$

$E = 0.365 - 0.0729pH + 0.0069\log[SO_4^{2-}]$

$2(Fe,Ni)_9S_8 + 21H_2O \rightarrow 9NiO + 3Fe_3O_4 + 16HS^- + 26H^+ + 10e$ $\Delta Gr = 1786.75$

$E = 1.852 - 0.154pH + 0.0947\log[HS^-]$

$2(Fe,Ni)_9S_8 + 76H_2O \rightarrow 3Fe_3O_4 + 9Ni^{2+} + 16SO_4^{2-} + 152H^+ + 138e$ $\Delta Gr = 2658.6$

$E = 0.200 - 0.0652pH + 0.0039\log[Ni^{2+}] + 0.0069\log[SO_4^{2-}]$

$9Fe^{2+} + 9Ni + 16HS^- \rightarrow 2(Fe,Ni)_9S_8 + 16H^+ + 14e$ $\Delta Gr = -993.04$

$E = -0.735 - 0.0677pH - 0.038\log[Fe^{2+}] - 0.0677\log[HS^-]$

$6(Fe,Ni)_9S_8 + 282H_2O \rightarrow 9Fe_3O_4 + 27NiOOH^- + 48SO_4^{2-} + 510H^+ + 387e$ $\Delta Gr = 17280.4$

$E = 0.463 - 0.078pH + 0.0041\log[NiOOH^-] + 0.0073\log[SO_4^{2-}]$

$2(Fe,Ni)_9S_8 + 16H^+ \rightarrow 9Fe^{2+} + 9Ni^{2+} + 16HS^- + 4e$ $\Delta Gr = 582.43$

$E = 1.509 + 0.237pH + 0.133\log[Fe^{2+}][Ni^{2+}] + 0.237\log[HS^-]$

$6(Fe,Ni)_9S_8 + 90H_2O \rightarrow 9Fe_3O_4 + 27NiOOH^- + 48HS^- + 105H^+ + 30e$ $\Delta Gr = 8062.5$

$E = 2.785 - 0.207pH + 0.0947\log[HS^-] + 0.0533\log[NiOOH^-]$

$(Fe,Ni)_9S_8 + 8H^+ \rightarrow FeNi_2S_4 + 3.5Fe^{2+} + 2.5Ni^{2+} + 4H_2S + 4e$ $\Delta Gr = -70.01$

$E = -0.181 + 0.118pH + 0.0592\log[H_2S] + 0.037\log[Ni^{2+}] + 0.0518\log[Fe^{2+}]$

$(Fe,Ni)_9S_8 + 4.667H_2O \rightarrow FeNi_2S_4 + 1.167Fe_3O_4 + 2.5Ni + 4HS^- + 5.336H^+ + 1.336e$ $\Delta Gr = 421.79$

$E = 3.272 - 0.236pH + 0.177\log[HS^-]$

$(Fe,Ni)_9S_8 + 23.167H_2O \rightarrow FeNi_2S_4 + 1.167Fe_3O_4 + 2.5NiO + 4SO_4^{2-}$
$+ 46.336H^+ + 38.336e \quad \Delta Gr = 1253.7$
$E = 0.339 - 0.0716pH + 0.0062\log[SO_4^{2-}]$

$(Fe,Ni)_9S_8 + 20.667H_2O \rightarrow FeNi_2S_4 + 2.5Ni^{2+} + 1.167Fe_3O_4 + 4SO_4^{2-}$
$+ 41.336H^+ + 38.336e \quad \Delta Gr = 1076.6$
$E = 0.291 - 0.0638pH + 0.0039\log[Ni^{2+}] + 0.0062\log[SO_4^{2-}]$

A4.3.6. <u>Chalcopyrite (with respect to chalcocite, covelline, pyrite and pyrrhotine).</u>

$2Cu + H_2S \rightarrow Cu_2S + 2H^+ + 2e \quad \Delta Gr = -59.01$
$E = - 0.305 - 0.0592pH - 0.0296\log[H_2S]$

$2Cu + HS^- \rightarrow Cu_2S + H^+ + 2e \quad \Delta Gr = -98.92$
$E = - 0.513 - 0.0296pH - 0.0296\log[HS^-]$

$Cu_2S + 4H_2O \rightarrow 2Cu + SO_4^{2-} + 8H^+ + 6e \quad \Delta Gr = 290.96$
$E = 0.503 - 0.0789pH + 0.0099\log[SO_4^{2-}]$

$Cu_2S + 5H_2O \rightarrow Cu_2O + SO_4^{2-} + 10H^+ + 8e \quad \Delta Gr = 382.11$
$E = 0.495 - 0.074pH + 0.0074\log[SO_4^{2-}]$

$Cu_2S + 6H_2O \rightarrow 2CuO + SO_4^{2-} + 12H^+ + 10e \quad \Delta Gr = 506.2$
$E = 0.524 - 0.071pH + 0.0059\log[SO_4^{2-}]$

$Cu_2S + 4H_2O \rightarrow 2Cu^{2+} + SO_4^{2-} + 8H^+ + 10e \quad \Delta Gr = 420.92$
$E = 0.436 - 0.0473pH + 0.0059\log[SO_4^{2-}] + 0.0118\log[Cu^{2+}]$

$Cu_2S \rightarrow 2Cu^{2+} + S + 4e \quad \Delta Gr = 216.83$
$E = 0.562 + 0.0296\log[Cu^{2+}]$

$Cu_2S + 4H_2O \rightarrow 2Cu^{2+} + HSO_4^- + 7H^+ + 10e \quad \Delta Gr = 409.58$
$E = 0.424 - 0.0414pH + 0.0118\log[Cu^{2+}] + 0.0059\log[HSO_4^-]$

$Cu + H_2S \rightarrow CuS + 2H^+ + 2e \quad \Delta Gr = -21.22$
$E = - 0.110 - 0.0592pH - 0.0296\log[H_2S]$

$Cu + HS^- \rightarrow CuS + H^+ + 2e \quad \Delta Gr = -61.13$
$E = - 0.317 - 0.0296pH - 0.0296\log[HS^-]$

$CuS + 4H_2O \rightarrow Cu + SO_4^{2-} + 8H^+ + 6e \quad \Delta Gr = 253.17$
$E = 0.437 - 0.0789pH + 0.0099\log[SO_4^{2-}]$

$2CuS + 9H_2O \rightarrow Cu_2O + 2SO_4^{2-} + 18H^+ + 14e \quad \Delta Gr = 597.49$
$E = 0.442 - 0.0761pH + 0.0085\log[SO_4^{2-}]$

$CuS + 5H_2O \rightarrow CuO + SO_4^{2-} + 10H^+ + 8e \quad \Delta Gr = 360.79$
$E = 0.467 - 0.074pH + 0.0074\log[SO_4^{2-}]$

$CuS + 4H_2O \rightarrow Cu^{2+} + SO_4^{2-} + 8H^+ + 6e \quad \Delta Gr = 318.15$
$E = 0.550 - 0.0789pH + 0.0099\log[SO_4^{2-}][Cu^{2+}]$

$CuS \rightarrow Cu^{2+} + S + 2e$ $\Delta Gr = 114.06$

$E = 0.591 + 0.0592\log[Cu^{2+}]$

$CuS + 4H_2O \rightarrow Cu^{2+} + HSO_4^- + 7H^+ + 8e$ $\Delta Gr = 306.77$

$E = 0.397 - 0.0518pH + 0.0074\log[HSO_4^-][Cu^{2+}]$

$Cu_2S + HS^- \rightarrow 2CuS + H^+ + 2e$ $\Delta Gr = -23.34$

$E = -0.121 - 0.0296pH - 0.0296\log[HS^-]$

$Cu_2S + H_2S \rightarrow 2CuS + 2H^+ + 2e$ $\Delta Gr = 16.57$

$E = 0.086 - 0.0592pH - 0.0592\log[H_2S]$

$2CuS + 4H_2O \rightarrow Cu_2S + SO_4^{2-} + 8H^+ + 6e$ $\Delta Gr = 215.38$

$E = 0.372 - 0.0789pH + 0.0099\log[SO_4^{2-}]$

$2CuFeS_2 + 2H^+ \rightarrow Cu_2S + FeS_2 + Fe^{2+} + H_2S$ $\Delta Gr = 25.86$

$-4.529 = 2pH + \log[Fe^{2+}][H_2S]$

$2CuFeS_2 + H^+ \rightarrow Cu_2S + FeS_2 + Fe^{2+} + HS^-$ $\Delta Gr = -19.17$

$3.359 = pH + \log[Fe^{2+}][H_2S]$

$CuFeS_2 + H_2S \rightarrow FeS_2 + CuS + 2H^+ + 2e$ $\Delta Gr = -31.04$

$E = -0.161 - 0.0592pH - 0.0296\log[H_2S]$

$FeS_2 + CuS + 4H_2O \rightarrow CuFeS_2 + SO_4^{2-} + 8H^+ + 6e$ $\Delta Gr = 262.99$

$E = 0.454 - 0.0789pH + 0.0099\log[SO_4^{2-}]$

$2CuFeS_2 + HS^- \rightarrow Cu_2S + 2FeS_2 + H^+ + 2e$ $\Delta Gr = -177.72$

$E = -0.92 - 0.0296pH - 0.0296\log[HS^-]$

A4.3.7. Arsenopyrite.

$As + Fe + H_2S \rightarrow FeAsS + 2H^+ + 2e$ $\Delta Gr = -52.27$

$E = -0.271 - 0.0592pH$

$Fe^{2+} + As + H_2S \rightarrow FeAsS + 2H^+$ $\Delta Gr = 26.97$

$pH = 2.650 - 0.5\log[Fe^{2+}][H_2S]$

$FeAsS + H_2O \rightarrow Fe^{2+} + AsO^+ + S + 2H^+ + 5e$ $\Delta Gr = 74.47$

$E = 0.154 - 0.0237pH + 0.0118\log[Fe^{2+}][AsO^+]$

$2FeAsS + 19H_2O \rightarrow 2SO_4^{2-} + Fe_2O_3 + 2AsO_4^{2-} + 38H^+ + 30e$ $\Delta Gr = 1175.81$

$E = 0.406 - 0.075pH + 0.0039\log[SO_4^{2-}][AsO_4^{2-}]$

$3FeAsS + 4H_2O \rightarrow 3HS^- + Fe_3O_4 + 2As + 5H^+ + 2e$ $\Delta Gr = 228.15$

$E = 1.180 - 0.148pH + 0.0888\log[HS^-]$

$3FeAsS + 16H_2O \rightarrow 3SO_4^{2-} + Fe_3O_4 + 3As + 32H^+ + 26e$ $\Delta Gr = 804.27$

$E = 0.321 - 0.0728pH + 0.0068\log[SO_4^{2-}]$

$3FeAsS + 28H_2O \rightarrow Fe_3O_4 + 3AsO_4^{2-} + 3SO_4^{2-} + 56H^+ + 44e$ $\Delta Gr = 1742.43$

$E = 0.410 - 0.0753pH + 0.0040\log[AsO_4^{2-}][SO_4^{2-}]$

$2FeAsS + 11H_2O \rightarrow Fe_2O_3 + 2As + 2SO_4^{2-} + 22H^+ + 18e$ $\Delta Gr = 550.37$

$E = 0.317 - 0.0724pH + 0.0066\log[SO_4^{2-}]$

$FeAsS + 4H_2O \rightarrow Fe^{2+} + As + SO_4^{2-} + 8H^+ + 8e$ $\Delta Gr = 204.98$

$E = 0.266 - 0.0592pH + 0.0074\log[Fe^{2+}][SO_4^{2-}]$

$2FeAsS + 14H_2O \rightarrow Fe_2O_3 + As_2O_3 + 2SO_4^{2-} + 28H^+ + 24e$ $\Delta Gr = 686.36$

$E = 0.296 - 0.0691pH + 0.0049\log[SO_4^{2-}]$

$2FeAsS + 11H_2O \rightarrow 2Fe^{2+} + As_2O_3 + 2SO_4^{2-} + 22H^+ + 22e$ $\Delta Gr = 545.95$

$E = 0.257 - 0.0592pH + 0.0054\log[Fe^{2+}][SO_4^{2-}]$

$FeAsS + 5H_2O \rightarrow Fe^{2+} + AsO^+ + SO_4^{2-} + 10H^+ + 11e$ $\Delta Gr = 278.56$

$E = 0.262 - 0.0538pH + 0.0054\log[Fe^{2+}][AsO^+][SO_4^{2-}]$